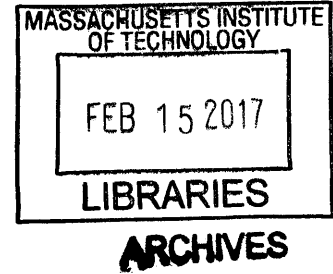# A Multi-scale Model Integrating both Global Ring Pack Behavior and Local Oil Transport in Internal Combustion Engines

by

Yang Liu

B.Sc., Mechanical Engineering
Purdue University, 2011
Shanghai JiaoTong University, 2011

S.M., Mechanical Engineering
Massachusetts Institute of Technology, 2013

Submitted to the Department of Mechanical Engineering
in Partial Fulfillment of the Requirements of the Degree of

Doctor of Philosophy in Mechanical Engineering

at the

MASSACHUSETTS INSTITUTE OF TECHNOLOGY

February 2017

Signature of Author: _____ **Signature redacted**

Department of Mechanical Engineering
January 13, 2017

Certified by: _____ **Signature redacted**

Dr. Tian Tian
Principal Research Engineer, Department of Mechanical Engineering
Thesis Supervisor

Accepted by: _____ **Signature redacted**

Professor Rohan Abeyaratne,
Quentin Berg Professor, Department of Mechanical Engineering
Chairman, Committee on Graduate Studies

A Multi-scale Model Integrating both Global Ring Pack Behavior and Local Oil Transport in Internal Combustion Engines

By

Yang Liu

Abstract

Improving fuel economy of internal combustion engines is one of the major focuses in automotive industry. The piston ring friction contributes as much as 25% of total mechanical loss in internal combustion engines [1] and is an area of great interests to the automotive industry in their overall effort to improve engine efficiency. However, typical methods to reduce friction loss from piston ring pack, such as ring tension reduction, may cause additional oil consumption. A compromise between reduction of friction loss and control of gas leakage and oil consumption needs to be made, which requires a deep understanding of oil transport mechanism. This compromise gives rise to the interest in modeling work. Both experimental results and previous experience showed that oil film distribution on the piston varies significantly along the circumference and the oil leakage occurs locally. Therefore to predict oil transfer across different ring pack regions, one needs to integrate both global and local processes.

This work is aimed at establishing an enduring framework for all the cycle-based processes at different length scales. As a first step, a multi-scale multi-physics piston ring pack model was developed by coupling the structural dynamics of the piston rings with gas flows and local interactions at ring-groove and ring-liner interfaces. A curved beam finite element method was adopted to calculate the ring structural response to interaction between the ring and the liner as well as the ring and the groove. Compared to a traditional straight beam finite element method, the curved beam separates the structural mesh and contact grid by utilizing the shape functions.

In this work, a multi-length-scale ring pack model was, for the first time, successfully assembled. This model bears its fundamental values to truly reflect the integral results of all the relevant mechanisms. The significance of the current work is that it demonstrated such an integration of all the length scales is possible for a cycle model with a reasonable computation cost. With the current model, one can realistically investigate the effects of all kinds of piston and liner distortion, piston secondary motion, bridging, and lube-oil dilution on gas sealing, oil transport and lubrication. As a result, optimization of the ring designs and the part of block design contributing to bore distortion can be coordinated to reduce development costs.

Thesis Supervisor: Dr. Tian Tian

Thesis Committee:
Dr. Tian Tian (Committee Chair)
Prof. Wai K. Cheng
Prof. Pierre Lermusiaux

Acknowledgements

Table of Contents

1. Introduction

1.1. Background and Motivation

1.1.1. Piston Ring Pack System

The piston assembly is an important component in internal combustion engines which is composed of the piston and three piston rings (Figure 1).

①	Compression ring (top ring)
②	Scraper ring (2nd ring)
③	Oil control ring (OCR)
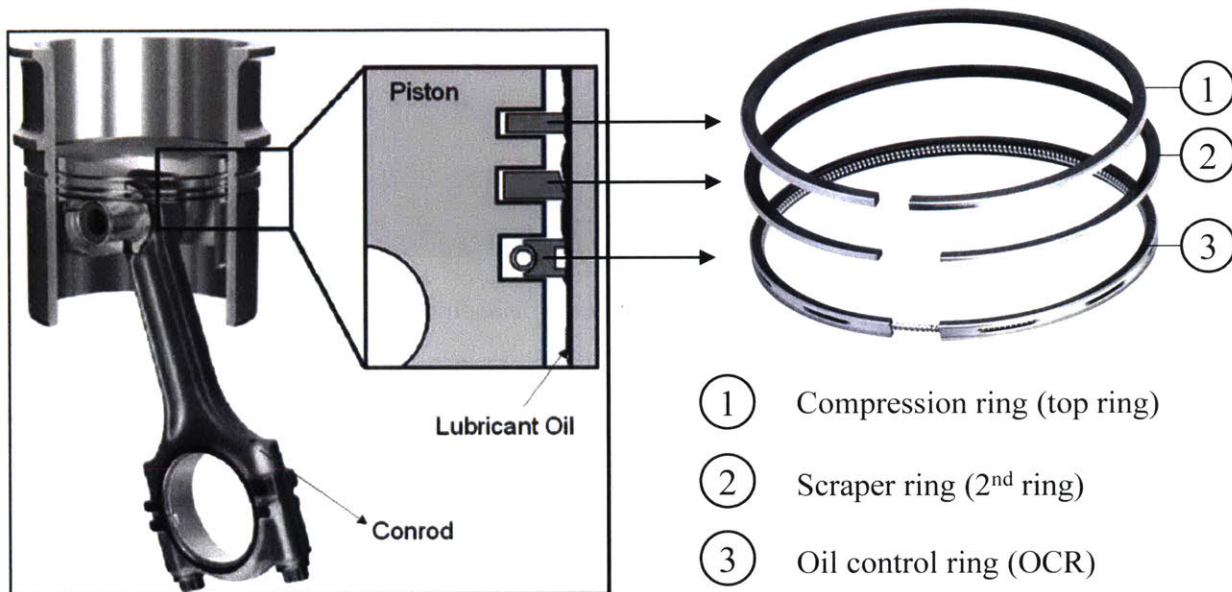
Figure 1 Overview of the Power Cylinder System

The piston primary function is to transmit mechanical work to crankshaft. As shown in Figure 2, three ring grooves are machined on the piston side to assemble the piston rings. There are several drain holes in the 3rd ring groove to allow flow of gas and release of oil to the crankcase. The piston skirt is the surface below the grooves and 90° on both sides of the pin. It is in contact with the liner and constrains the lateral motion of the piston.

Groove

Draining hole

Pin

Piston skirt
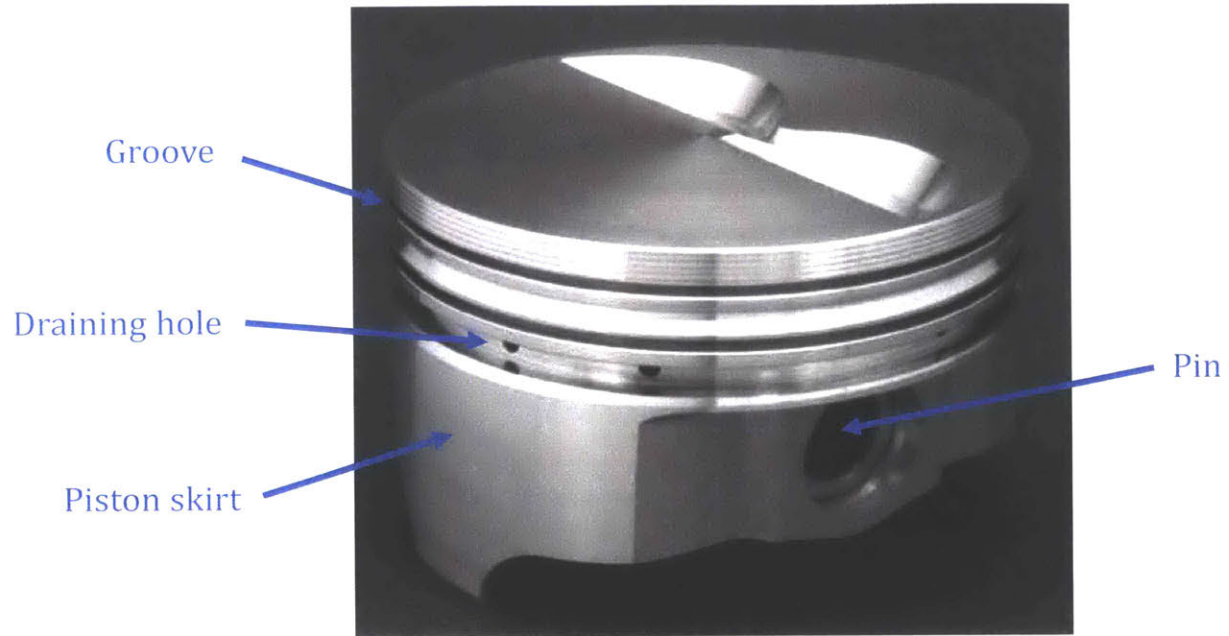
Figure 2 Overview of the Piston Geometry

Each of the piston rings has a specific function. The compression ring or top ring is a gas seal to prevent leakage of high pressure gas from the combustion chamber to the crank case in order to avoid work loss. The piston rings need lubricant to reduce friction and wear and the oil control ring (OCR) is responsible for controlling the amount of the lubricant supplied to the ring pack to limit oil consumption. The second ring or scraper ring is both an oil and gas ring. It acts mainly as a secondary control of the excessive oil on the piston third land. Top two rings are also known as a single piece ring.

The outer piston surfaces between the rings are called piston lands (as shown in Figure 3). Land-liner clearances vary by design to control gas pressure in the various regions of the ring pack. A cut or chamfer can be found at the top of the piston skirt. Its function is to retain oil to lubricate the piston skirt during the up stroke and reduce the pressure in the oil below the OCR to limit oil flow into the OCR groove.
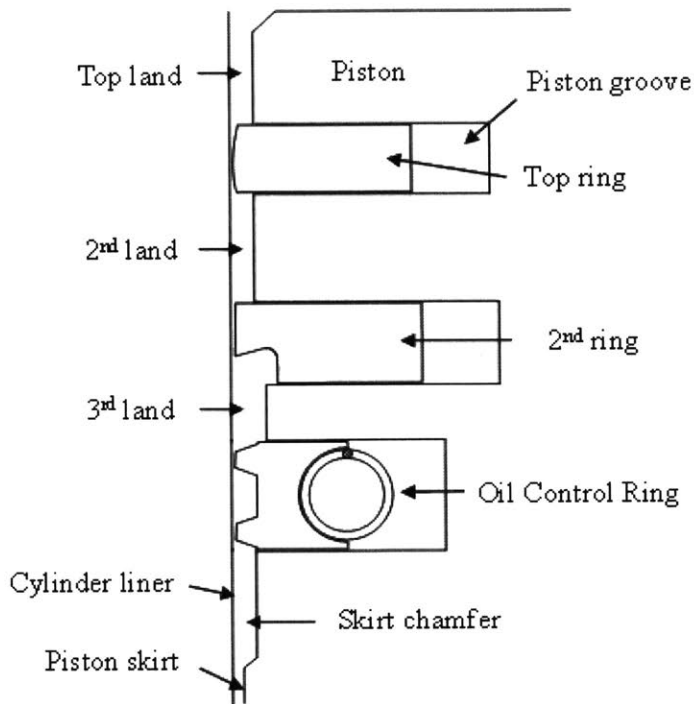
Figure 3 A Cross Section of Piston and Piston Ring Pack

The piston rings have different designs tailored to their function. The top ring section is nearly rectangular. Usually, a cut can be found in the upper ID of the top ring which gives the ring a positive static twist. The top ring with a positive twist contacts the groove at the ID first with a rising cylinder pressure, which leaves the upper flank exposed to cylinder pressure while the lower flank to lower second land pressure. Doing so enhances the top ring stability sitting on the lower flank cutting off the gas flow path [2] [3] [4]. Its running surface has microscopic parabolic profile to favor hydrodynamic pressure and improve lubrication. Some keystone design can be also found for top rings, which introduces relative motion between the ring and the groove to reduce carbon deposit. The second ring shown in Figure 3 is a Napier ring which is a common design for second rings. A hook is cut to act as an oil reservoir to prevent oil flowing from the piston 3rd land to the liner. When the top two rings are assembled into the piston, they are closed from their free shapes and this change of curvature and torsion increases the strain energy thus providing expansion force and static twist sealing the ring-liner and the ring-groove interfaces. The OCR in Figure 3 is a twin-land oil control ring which is widely used in diesel engines and some gasoline engines. It has two components: a metallic ring and a coiled spring. The OCR has a thin cross section with much better flexibility compared top two rings and its spring provides very uniform normal force distribution. As a result, the oil control ring is able to maintain contact with the liner even with relatively large bore distortion. The twin-land oil control ring has two

ring lands that contact with the liner. Their profile is flat and parallel to the liner which limits the oil film thickness to surface roughness level so that the OCR can just provide barely enough oil to lubricate the top two rings and control the oil consumption. Several variations of OCR design exist. Another very common used is the three piece oil control ring (TPOCR). TPOCR is composed of an expander and two rails. The expander is a split ring pushing the two rails against the cylinder and the upper and lower flanks of the OCR groove. In this thesis, we are going to focus on the twin-land oil control ring though the general methodology can be extended to the three piece oil control ring.

1.1.2. Development of Power Cylinder System

Development of modern automotive engines is driven by three major factors: fuel economy, environmental protection and customer satisfaction. For such a complex system as internal combustion engines, satisfying these requirements needs technology advancement in engine components, fuel and oil. The performance of characteristics of the piston ring pack is closely associated with the friction, wear, blow-by gas flow and oil consumption, which are in turn directly related to the listed three factors.

The target of power cylinder system optimization is to improve engine efficiency, namely reducing friction, increasing compression height and cutting cost. As shown in Figure 4, certain constraints have to be satisfied first. For example, the oil consumption and blow-by gas need to be under control over entire engine lifetime. The optimization also needs to consider multiple components and a wide range of engine operating conditions, which make it more difficult. Thus a model that combines variety of important factors can provide engineers more detailed understanding and may provide potential trend to improve the engine system.
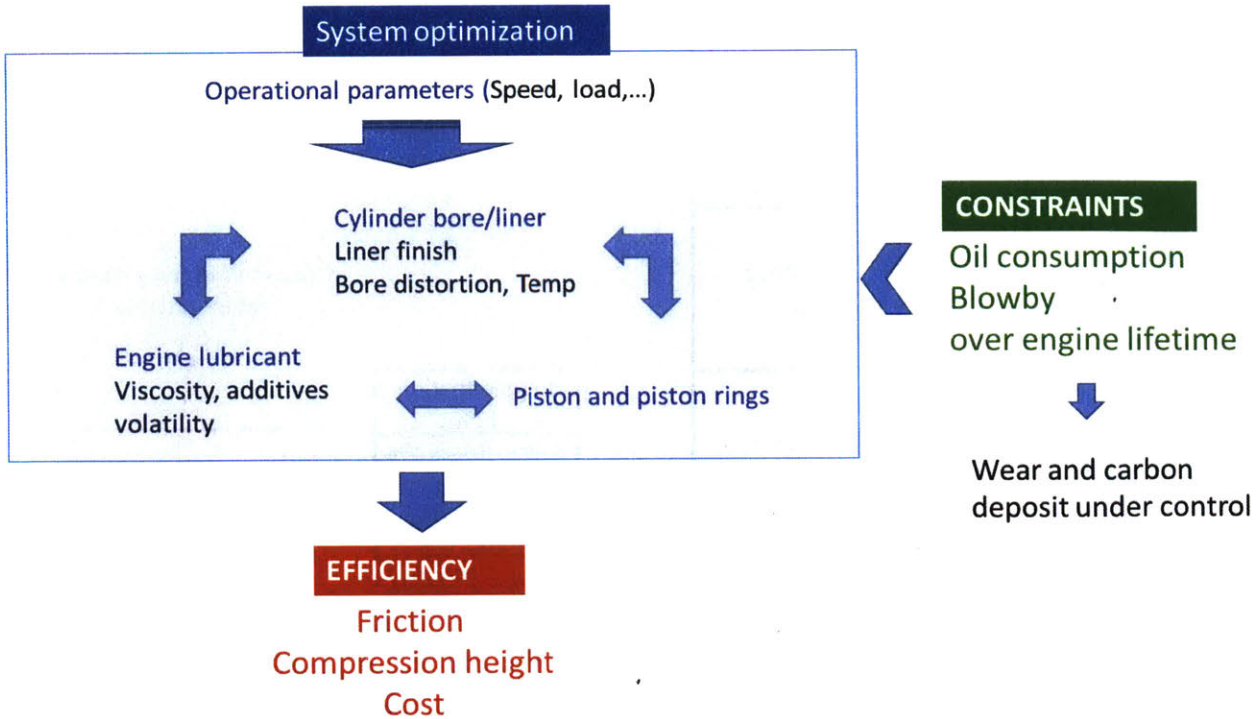
Figure 4 Power Cylinder System Optimization

1.1.3. Friction of Piston Ring Pack System

A significant portion of energy losses in internal combustion engines is from friction losses. Figure 5 shows that most of the fuel energy is lost through the exhaust and the cooling system. Mechanical power only attributes to 38%, among which around 55% or 21% of the total fuel energy is actually used to drive the vehicle. The rest is dissipated due to friction loss either in the engine or the transmission. Friction reduction plays an important role in current effort to increase the efficiency of internal combustion engines. An ambitious but physically achievable reduction of 50% of engine friction would lead to a 6% gain of the useful output. Compared to the current 21% of fuel energy used to move the car, this improvement can reduce almost 29% of fuel consumption which highlights the great contribution that engine friction can have on vehicle fuel economy.
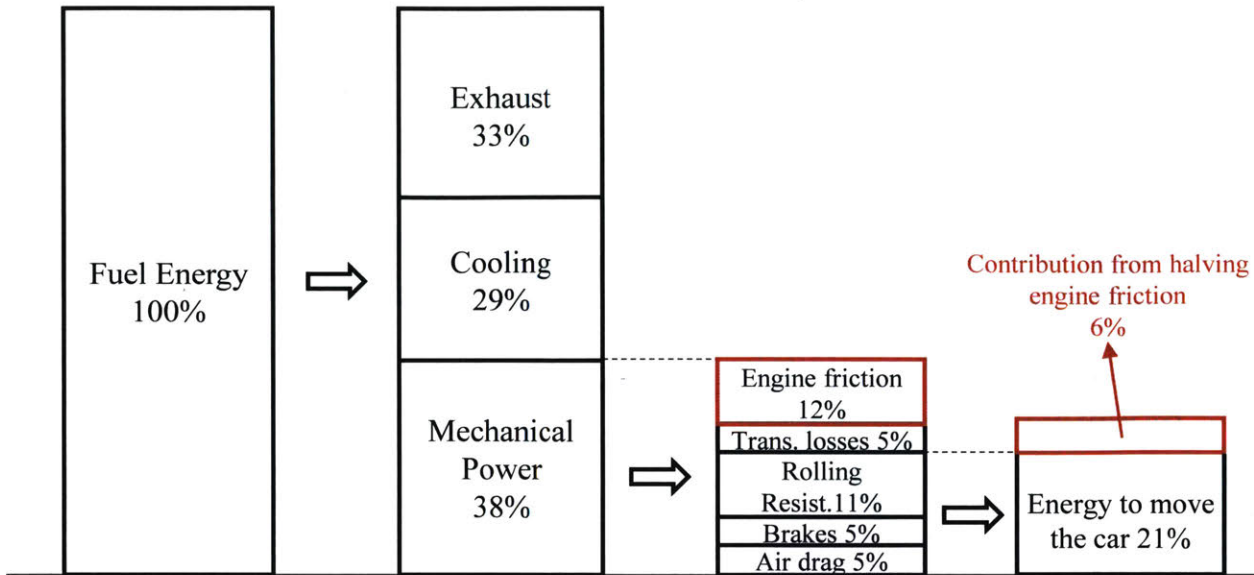
Figure 5 Energy Flow in an Internal Combustion Engine [5]

The piston ring pack system which is studied in this thesis accounts for 25% of the engine mechanical loss [1]. Reducing friction coefficient and ring tension is essential to reduce the friction loss of piston rings. The contact interaction between the piston ring and the liner is characteristic of sliding contact which can be best represented by Stribeck curve [6] [7]. In Figure 6, the y-axis is the combined friction coefficient of hydrodynamic and asperity contact. The x-axis is a dimensionless parameter combining the oil viscosity μ, the sliding speed V, bore radius R and the normal contact load F. This parameter represents engine operating conditions. In the figure, we notice that there exists an optimum point that the friction coefficient reaches its minimum. Stribeck curve is determined by surface material, ring profile and liner roughness structure [8]. With a careful design of these three and lubricant, we are able to have engine operating in most of the time around the optimum point so that the friction coefficient is significantly reduced.
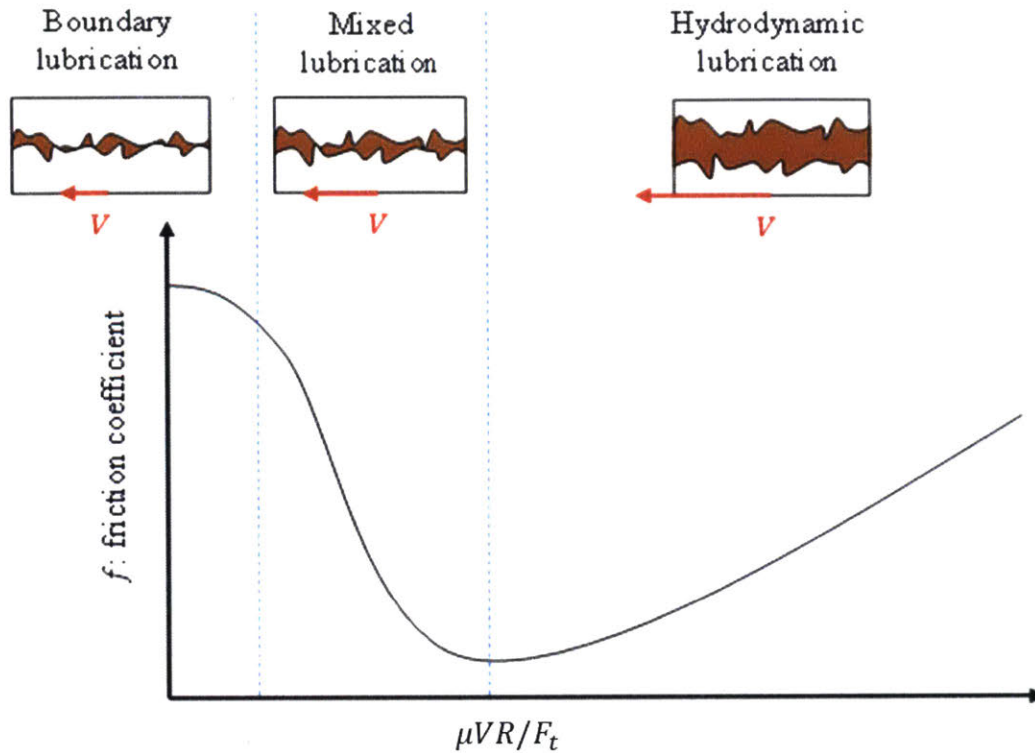
Figure 6 Stribeck Curve of a Sliding Contact

Secondly, the reduction of ring tension can also help have less friction loss from piston ring pack. However, oil consumption is most likely increased by reduction of ring tension [9]. When people are making efforts to reduce ring-liner friction by reducing ring tension, they need to understand ring dynamics and oil transfer of ring pack system and usually need to modify ring or piston design to compensate for the adverse effect on oil consumption and blow-by control.

1.1.4. Oil Consumption from Piston Ring Pack System

Engine oil consumption has a significant contribution on both hydrocarbon and particulate emissions [10] [11] [12]. In addition, some oil additives poison and shorten the lifetime of catalytic converter [13] [14]. As Figure 7 shows, oil is consumed through different sources. The first one is vaporization from the liner. A thin oil film is left on the liner by the piston rings, which is usually on the order of $0.1\mu m$. Due to the high temperature of the liner, approximately 1% of the oil film is vaporized into the combustion chamber every cycle. It is a fairly steady process, since the oil film thickness inside the engine is mainly determined by oil viscosity and engine speed which do not change frequently from cycle to cycle. Secondly, oil may accumulate on the piston top land and form droplets which have possibility to move into the combustion chamber driven by inertial force. The dimension of the oil droplets is usually below

micron. This process is sporadic since oil accumulation on the top land happens rarely. It usually needs excessive oil supply to the top ring via other sources than the oil film passing the OCR such as bridging which happens sporadically (bridging is going to be discussed in detail later). Thirdly, small oil droplets may flow into the combustion chamber carried by recycled blow-by gas. The dimension of the droplets is submicron after they pass through the oil separator.

Direct Oil Consumption Sources (excluding Valves, turbo)

| Vaporization from Liner
Fairly steady cycle-cycle | Passing top of the Piston
In liquid form
Sporadic | Recycled Blowby Gas
Usually only sub-micron droplets
Remain after oil separator |
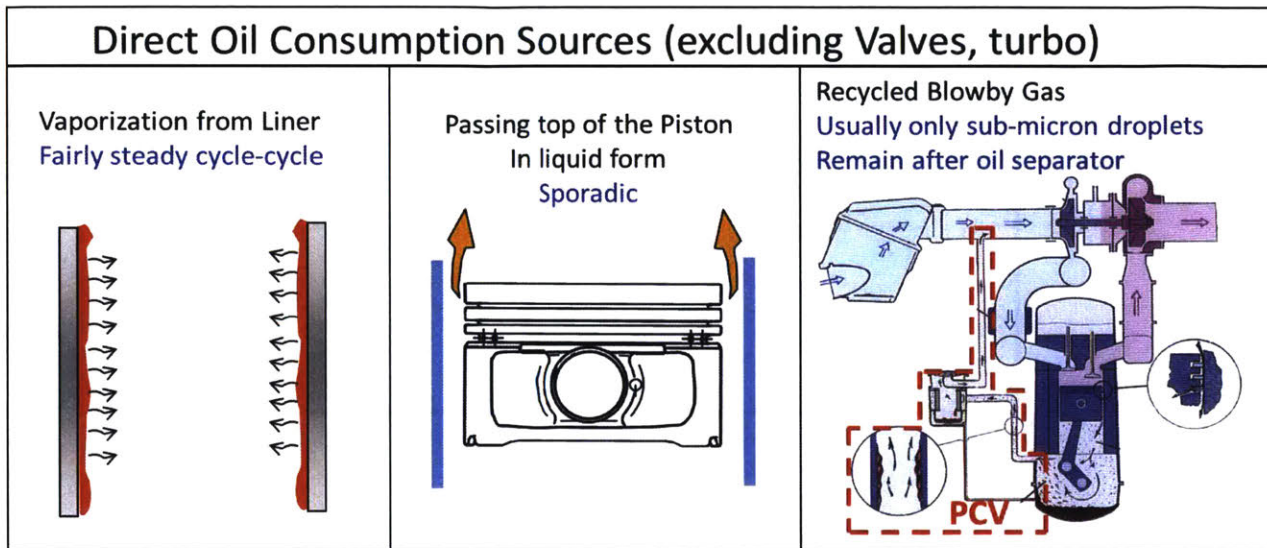
Figure 7 Oil Consumption Sources

A typical value of oil consumption rate for a 4-cylinder 2 liter engine at 2000rpm full load is 10g/hour which is equivalent to 2.5g/hour per cylinder. This value means that per cylinder every cycle only $0.05 mm^3$ of oil is consumed. If this amount of oil is evenly distributed on the liner, the film thickness is only 2nm. If it is accumulated on the top land, the film thickness is around 50nm. If it forms one single droplet, the diameter is only 0.45mm. All the values imply that oil consumption rate is very sensitive and may be significantly affected by a minor change of oil transport. It is part of the reason that oil consumption is arguably the most complicated problem in the piston lubrication system and is still the least understood area although a great deal of effort has been made.

1.2. Oil Transport in the Piston Ring Pack System of IC engines

A better understanding of oil transport can help us optimize the power cylinder system more efficiently. Generally speaking, oil flows from the crank case to the combustion chamber through three major paths: the ring-liner interfaces, the ring-groove interfaces and the ring gaps (as shown in Figure 8). There are three main elements to be resolved to predict oil leakage through different interfaces in the ring pack. First, clearances of the ring-liner interfaces, ring-groove interfaces, and the ring gaps need to be

14

calculated, which are dependent on ring structure dynamics and the distorted geometry of the piston and the liner. Second, the gas pressure distribution in different regions is important to oil flows because it not only deforms the piston rings to adapt to the geometry of the piston and the liner but also redistributes the oil on the piston lands and inside the piston grooves. This redistribution leads to local oil accumulation and a variance of oil supply to the ring-groove interfaces and the ring-liner interfaces [15] [16]. Finally, proper oil flow models are needed to compute the oil flow rates through the ring gaps and the ring-groove interfaces, and the oil film thickness on the liner.
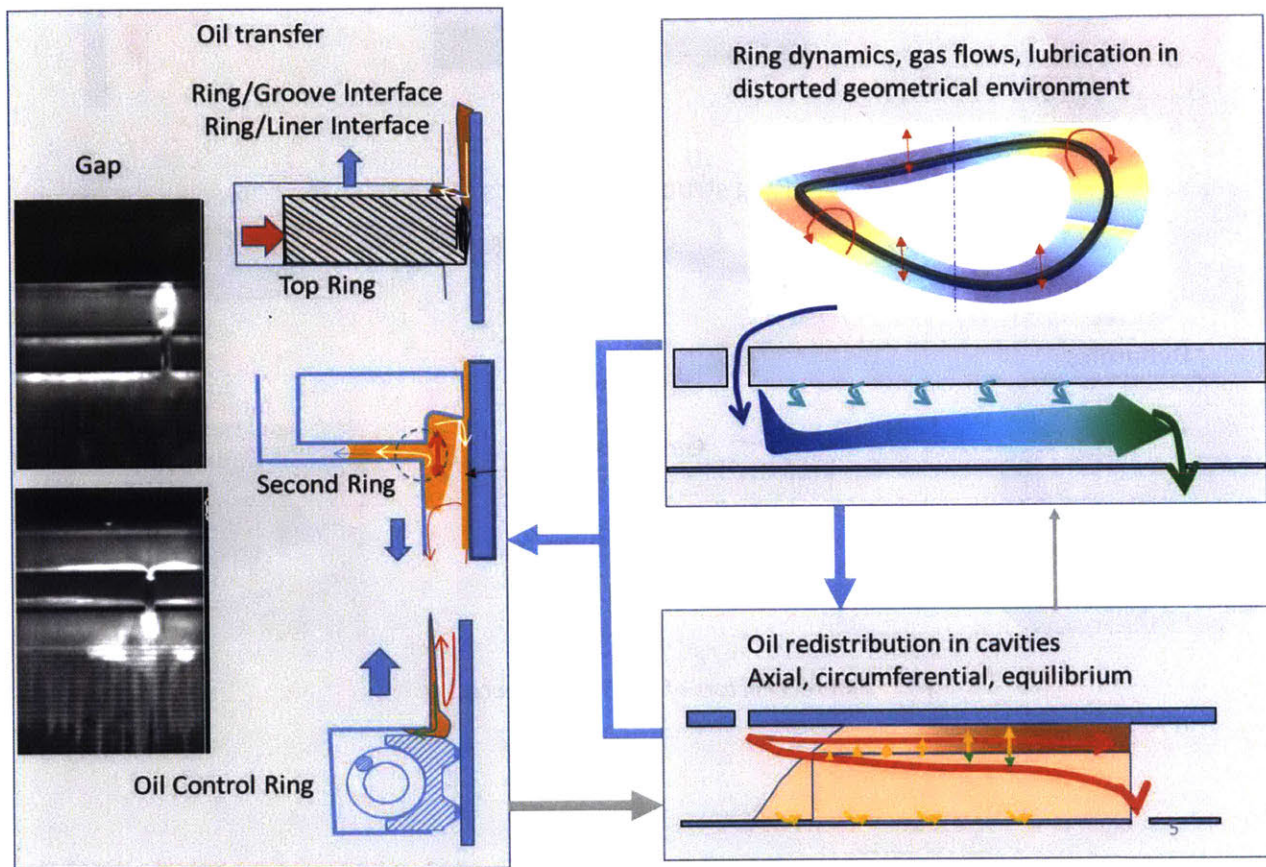
Figure 8 Oil Transport in Piston Ring Pack System

Oil transport and ring structure dynamics are the results of combined global and local processes with different length scales, as shown in Figure 9. The cylinder bore and the piston are distorted due to thermal and mechanical stresses. At structural level, the piston rings try to adapt to the distorted geometry with the help of gas pressure, inertial force and ring tension. Piston tilt or, more precisely, tilted grooves force the rings to twist to align with the angle of the groove flanks. All these above mentioned large-scale processes dictate how the force and structural deformation are distributed along the piston rings. Then, the exact local clearances are determined by the factors responsible for local

pressure generation such as ring-groove pumping, bridging, ring profile and surface roughness, resulting in variance of oil film thickness and flow rate in the circumferential direction. Figure 10 demonstrates the circumferential variance of gas flow and oil flow around piston ring pack system.
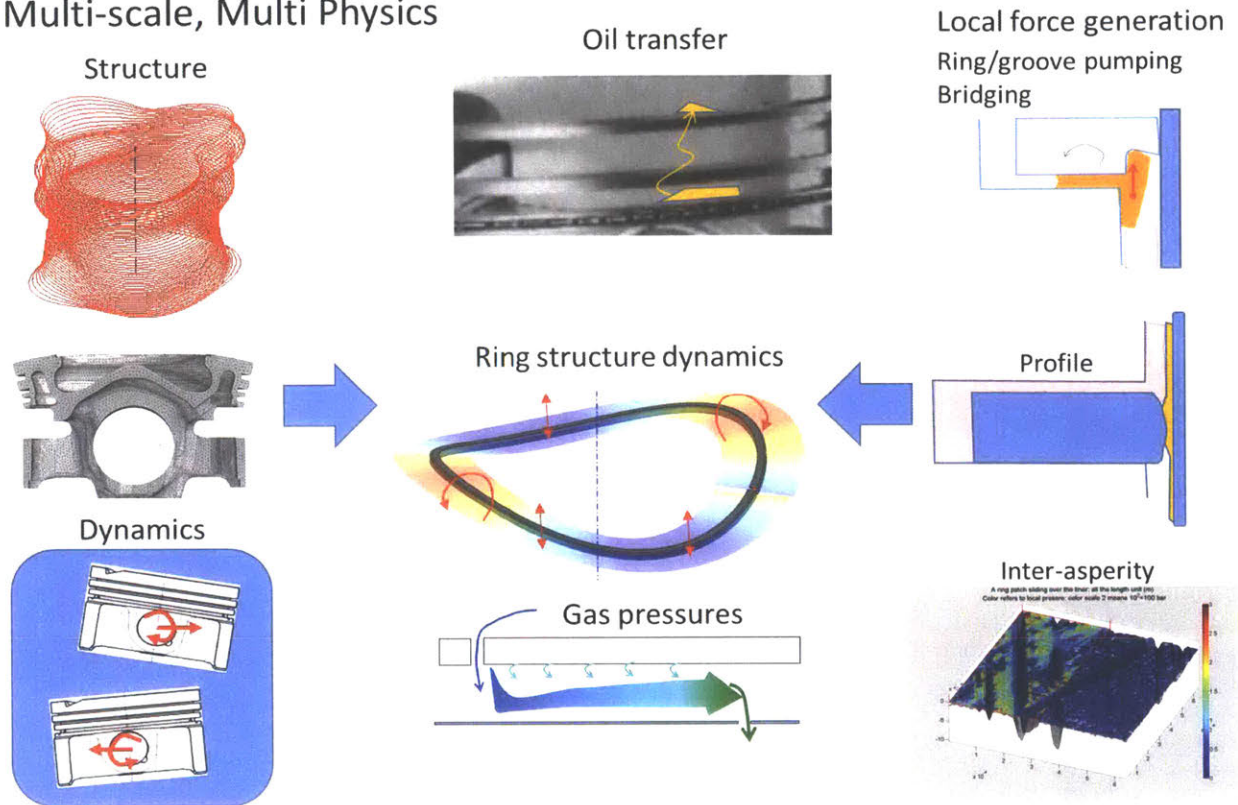
Figure 9 Factors of Oil Transfer Process

Experimental evidence of bridging

2nd land
2nd ring
3rd land
Oil Control Ring
Piston skirt
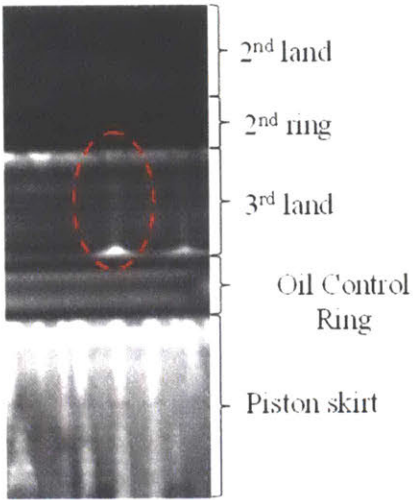
LIF image
(end of exhaust stroke)
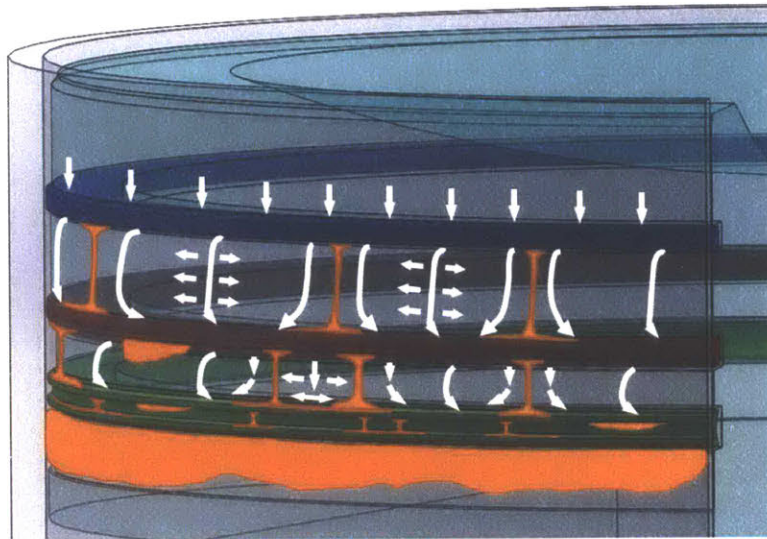
Figure 10 Variance of Gas Flow and Oil Flow around Piston Ring Pack System

1.2.1. Bore Distortion

The cylinder is distorted due to thermal and mechanical loads. The cylinder expands due to an increase of temperature which is called 0th order bore distortion with a magnitude around $100 \mu m$. Mechanical stress from the engine block assembly and temperature gradients under running conditions cause higher order bore distortion. The position of cooling chamber results in temperature difference of the liner in circumferential direction and contributes to 2nd order bore distortion on the order of $10 \mu m$. The mechanical stress from the bolts for block assembly causes 3rd order and 4th order bore distortion on the order of 1 to $5 \mu m$. Though the magnitude of the cylinder deformation is small compared to the cylinder radius (~80mm), it is sufficient to affect the contact between the ring and the liner (Figure 11).

Distorted bore (magnified x400)

Contact force distribution between ring and liner

Nominal bore contact

Ring

Distorted bore contact

Loss of contact
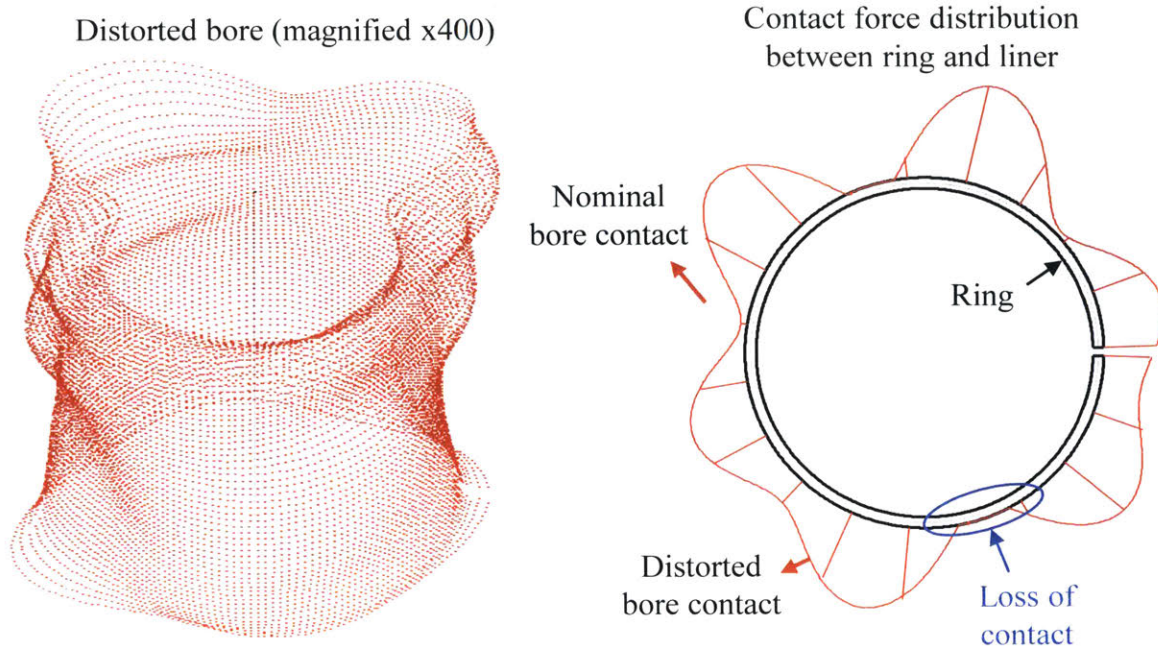
Figure 11 Bore Distortion and Ring-liner Contact Distribution

Normal load from gas pressure and ring tension deforms the ring to adapt to the cylinder geometry. If the ring is too stiff or the normal load is too small, then the ring may lose the contact with the liner. This affects the sealing performance of the ring since gas and lubricant can flow easily through the clearance where the ring is no longer touching the liner.

1.2.2. Piston Secondary Motion

The piston is able to rotate around the pin and move laterally due to the radial clearance between the piston skirt and the liner, as shown in Figure 12. The piston tilt is β_p and y_p is the lateral displacement of the piston. A positive piston tilt corresponds to an upward movement of the thrust side and a downward movement of the anti-thrust side. Positive lateral motion means that the piston is moving towards the thrust side. Tilt and lateral displacement constitute the piston secondary motion which were studied and calculated by Bai [17]. Piston secondary motion is important in modeling oil transport around the ring pack system. Lateral displacement changes the clearance between the piston lands and the liner, thus changing the corresponding volumes and affecting the gas pressure. Gas pressure and inertial force push the piston rings to conform to the geometry of the grooves. Therefore, piston tilt or more precisely tilted grooves force the rings to twist, as shown in Figure 13.

18
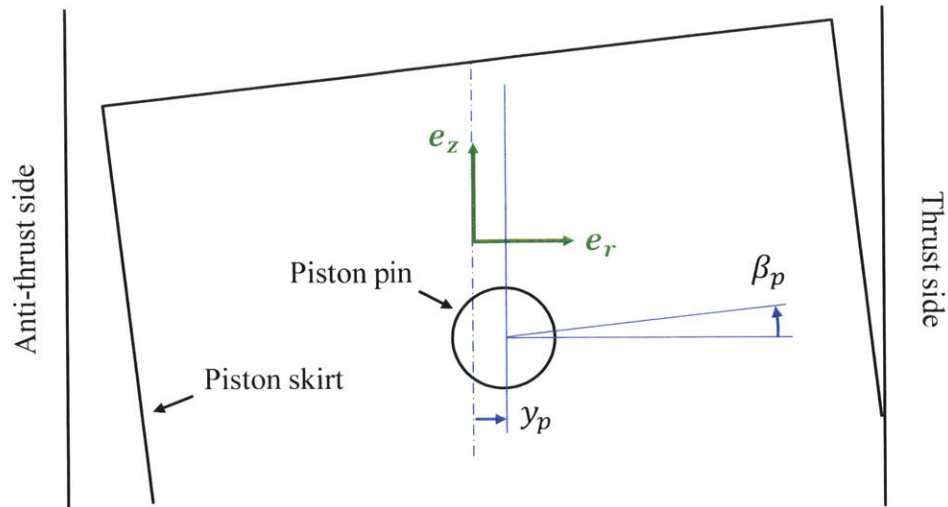
Figure 12 Piston Secondary Motion
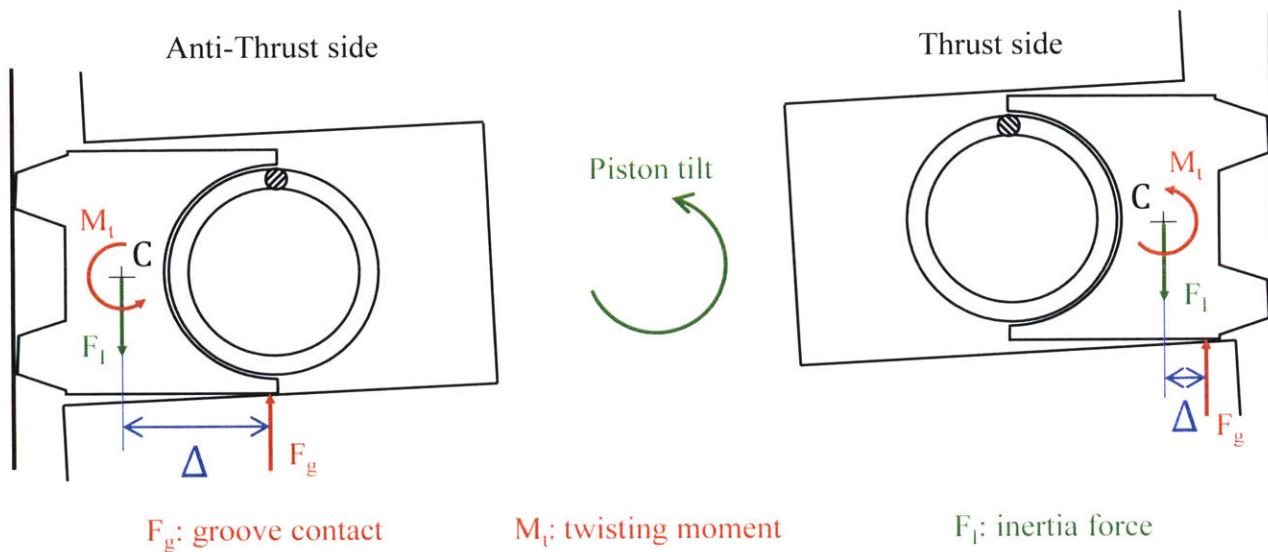
F_g: groove contact M_t: twisting moment F_I: inertia force

Figure 13 Ring in Tilted Piston

Ring twist is more important for the oil film thickness on the liner left by the OCR, since it can result in a loss of contact of one of the OCR lands. Piston tilt varies in the engine cycle. Initially, during the down-stroke, ring twist forces the OCR to twist negatively such that the lower land-liner clearance is larger than the upper land-liner clearance and oil is accumulated between the two lands. Then later in the down-stroke, the direction of the OCR twist is reversed and inertial force may drive the oil to the liner causing bridging (see Section 1.2.3) between the OCR two lands. Therefore the accumulated oil is released on the liner. When the OCR moves back to this position during the upstroke, ring twist changes its direction again and the oil is scraped from the liner and can flow to the piston (Up-scraping). The process is demonstrated in Figure 14.

19
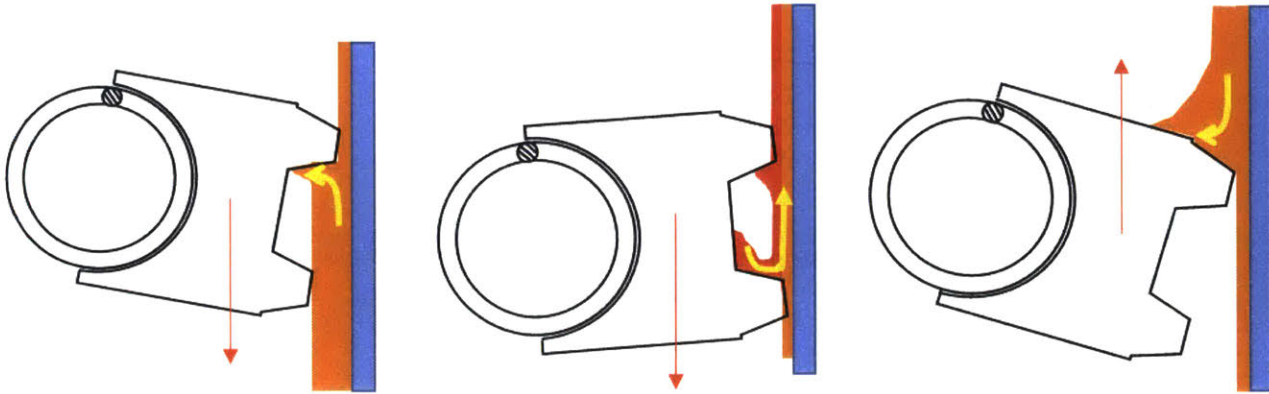
Figure 14 Oil transport Influenced by OCR twist

1.2.3. Bridging

As discussed earlier, scraping brings oil from the liner to the piston lands and OCR lands. When oil accumulation is large enough, oil can be returned to the liner driven by inertia force and viscose force. This mechanism is called bridging and has been studied by Fang [18]. Figure 15 describes a bridging event occurring on the second ring at the end of the exhaust stroke. Oil accumulated in the second ring hook flows to the liner due to inertial force and then is dragged down by the relative motion between the piston and the liner. The image on the right of Figure 15 is the experimental evidence supporting this description of bridging. It is an image taken from a single cylinder test engine set up for 2D Laser Induced Fluorescence (LIF) imaging (brightness is proportional to the amount of oil on the liner) [15] [16] [19] [20]. The circled bright strip corresponds to additional oil that was left on the liner due to bridging from the second ring. This oil is scraped and accumulated on top of the OCR. From this image, we can also observe that the distribution of oil in the piston ring pack is non-uniform and a 3D model is needed to describe the local behavior of oil transport around piston rings.
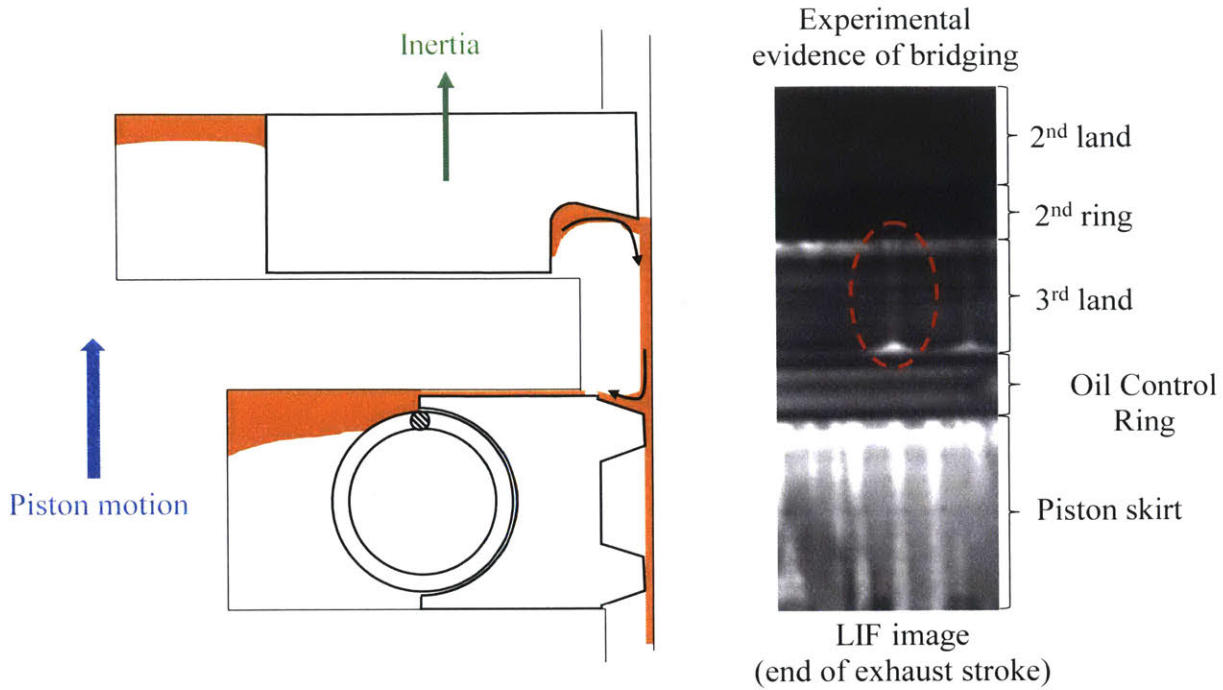
Figure 15 Bridging of Oil between Ring and Liner

1.2.4. Summary of Global and Local Processes of Oil Transport

As discussed before, oil transport in ring pack system is a result of the combination of global and local processes. In global scale, bore distortion and piston tilt determine the ring structural response. Gas pressure, ring tension and inertial force push the rings against the liner and the groove to adapt to their geometry. Conformabilities between the rings and the liner and between the rings and the groove seal oil and gas flow. The OCR has a good global conformability to the liner even when bore distortion is large. Its normal load is provided by the spring force uniformly and its cross section is thin. Therefore, the oil film thickness between the OCR and the liner is approximately uniform in an overall picture.

If global behavior is the only factor of oil transport, then there may not be many problems for oil consumption. The existence of local processes introduces various length scales and physics. Dynamic tilt of piston grooves varies along the circumferential direction due to the circular geometry (Figure 16), causing variance of ring twist. As discussed in Section 1.2.2, for the OCR, local ring twist may lead to a loss of contact of one of the two lands and finally thick oil film on the liner.
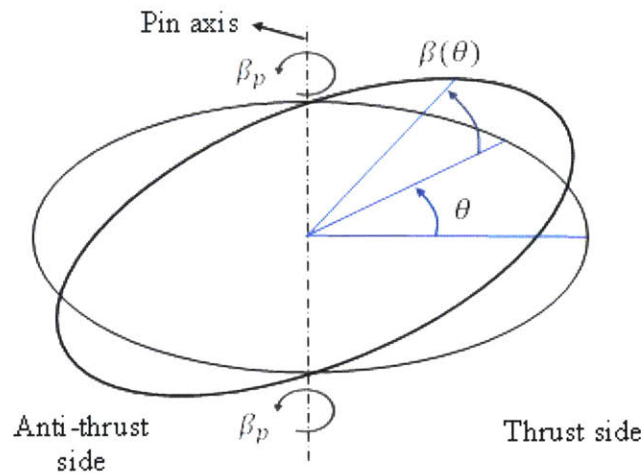
Figure 16 Tilted Plane of Ring Groove

Sometimes the liner has relatively large higher order distortion and stiffness of the rings and the normal load are not able to deform the rings completely to adapt to the bore geometry. Then the rings may lose their contact with the liner. During exhaust stroke, bridging may happen around the top dead center at the positions that happen to have relatively large local distortion. Then in the intake stroke, when the 2nd ring and top ring slide over these positions, they have great possibility to lose their contact with the liner and this thick oil film is allowed to pass, as shown in Figure 17. However during the compression stroke, gas pressure is rising in the top ring groove since it is connected to the combustion chamber, and helps the top ring to conform to the bore distortion as pictured in lower right graph of Figure 17. The thick oil film that was left on the liner during the intake stoke is scraped and can flow to the top land. Once on the top land, oil is very likely to be consumed either through evaporation or throw off in the combustion chamber. In this case it is not the poor conformability of the top two rings that has contributed to oil consumption but the bridging phenomenon and local difference of conformability between the intake and the compression strokes.
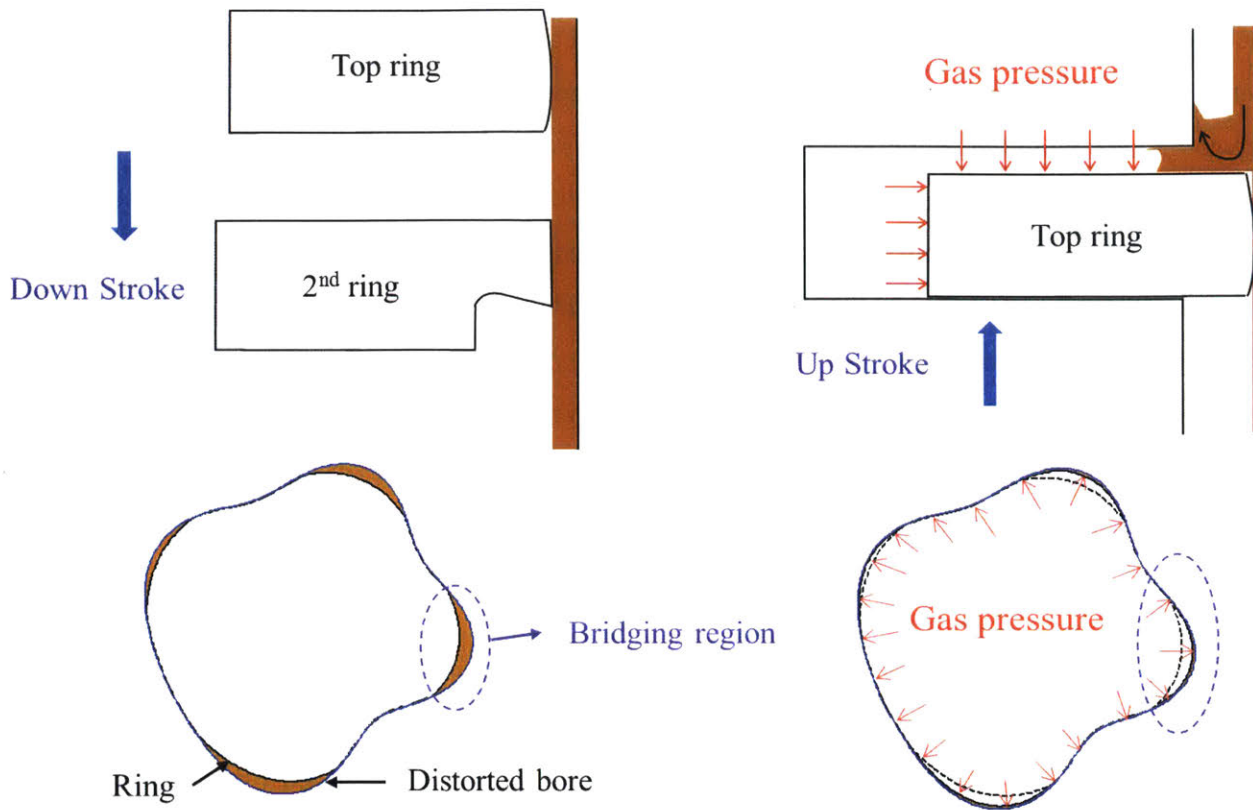
Figure 17 Conformability and Top Ring Up-Scraping

1.3. Existing Work

The relation between ring free shape and the contact pressure distribution in the cylinder was conducted both theoretically and experimentally by Prescott, Swift, Dragoni and Strozzi [21] [22] [23]. When bore distortion was identified as a potential cause of oil consumption, several studies of ring conformability were conducted. Mueller developed a theoretical criterion to calculate the maximum admissible bore distortion for a given ring configuration [24]. A similar analytical approach and a statistical treatment of bore distortion was used by Dunaevsky to suggest different bore distortion limits [25] [26] [27] [28] [29]. Tomanik later proposed a new conformability criterion based on experimental measurements of ring conformability limits [30] [31].

Later, more and more research work focused on ring dynamics and lubrication. Tian developed a 2D model based on an axisymmetric assumption to estimate ring dynamics and gas flow [32] [2] [33]. Most of the published 2D models combine the calculation of ring dynamics and gas flow and are found to be useful tools in understanding ring dynamics behavior [4] [34] [35] [36] [3]. To address non-axisymmetric characteristics of piston-ring system, Ejakov et al. simulated the dynamic twist angle of the piston ring

pack using finite element analysis [37]. Hu et al. and Ma et al. put a lot of effort on a 3D lubrication model coupling a detailed elastic analysis and a complementarity method to evaluate the conformability between the ring and the liner [38] [39] [40]. Liu et al. built a more complete 3D model with the combination of ring dynamics, gas flow and lubrication utilizing the straight beam finite element method [41] [42] [43]. Baelden et al. first introduced the curved beam finite element method to model oil transport around a twin-land oil control ring (TLOCR) which combined both OCR dynamics and lubrication [44] [45]. The curved beam finite element method has many advantages over the straight beam finite element method. It couples structural deformation to contact with different grid sizes, and also solves issues of the straight beam method by removing the discontinuities of quantities such as bending moment and curvature.

1.4. Thesis Scope

As discussed in previous sections, the optimization of modern power cylinder system is a complicated process with a consideration of multiple constraints and multiple components. A theoretical model is necessary for understanding the fundamentals of the system and improving product design. Though tremendous of modeling work about ring dynamics and ring-liner lubrication has been made, a model of framework is still missing that integrates both global and local processes into one package to simulate ring dynamics and oil transport for the entire ring pack system.

This thesis is to build a model to study oil transfer in piston ring pack system. An emphasis is put on oil transfer through the ring-liner interfaces since it is the most important path that allows oil flowing from the crank case to the combustion chamber [45]. The model developed here can be extended to study oil transfer through the ring-groove interfaces with an improvement of the ring-groove sub-model. Oil transfer is affected by different global and local processes which need to be included to give a better description of the system and to more realistically study the effects of different aspects of piston, ring, liner and lubricants. This model is the first one to study oil transport around the entire ring-pack system with the consideration of both global and local processes in different scales. The emphasis is to build a framework and all the sub-models used in this thesis were developed by Tian, Li, Chen and Liu [32] [46] [47] [48] [49] [50]. This model gives flexibility for the future developers to easily upgrade the existed sub-models or to add new ones to study other important factors. Besides modeling development, validation and application are also performed to assess the model and show capability of the model.

Ring Structural Model (Frame Work)
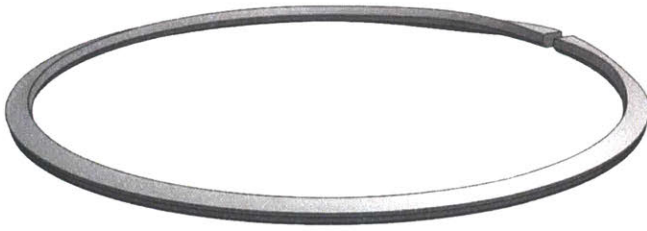
Ring Dynamics

Ring-Liner Lubrication Model
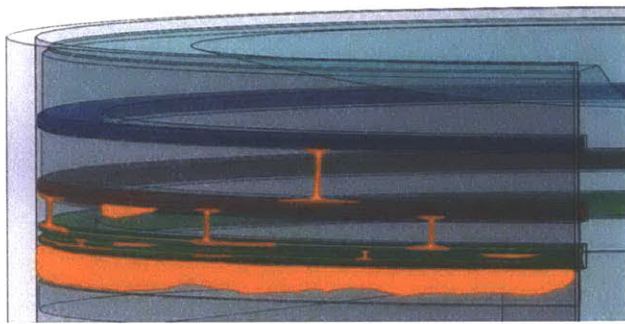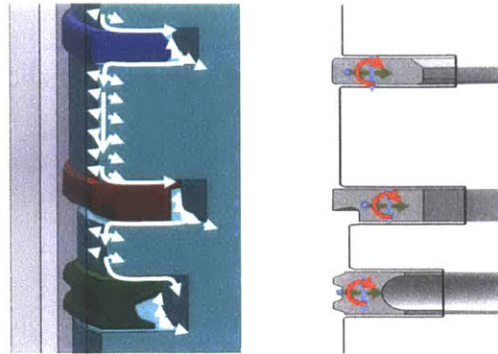
Figure 18 Thesis Scope

As shown in Figure 18, to address the contribution of global and local processes in different scales, a ring structural model based on the curved beam finite element method is developed in Chapter 2. This multi-scale model is able to solve structural deformation and dynamics of piston rings on a coarse mesh and consider the local interaction with the piston and the liner on a fine contact grid. In Chapter 3, ring static analysis is applied to study the effects of some global and local behaviors on ring-liner conformability.

A Ring dynamics model is developed to study the gas flow and ring dynamic behavior in real engine conditions. Gas pressure force, ring-groove interaction, ring-liner interaction, inertial force and ring tension are considered in this model. Bore distortion, piston deformation and piston tilt are also included to give a more realistic result. With the help of this model, we are able to study blow-by gas flow and gas pressure distribution of the ring-pack system. Inter-ring gas pressure and ring twist are obtained, which are necessary boundary conditions to study oil transport through the ring-liner interfaces.

A Ring-liner lubrication model is developed in Chapter 4 to study oil transfer through the ring-liner interfaces. Correlations are used to calculate hydrodynamic pressure and friction between piston rings

and liner. Phenomena that change local ring-liner lubrication behavior are also included such as bridging and lube-fuel dilution.

Finally, the last chapter summarizes and concludes the thesis work and suggests potential future work on the topic.

2. Curved Beam Finite Element Model of Piston Rings

When calculating piston structural response of piston rings, we usually treat them as metallic beams because the cross section dimensions of a ring are small compared to its radius. The radius of a piston ring of a passenger car engine is around 40mm. As a comparison, its height is around 1.5mm and its radius width is around 3mm. The ratio of ring cross section dimensions to its radius is lower than 1/10. Therefore, beam theory provides an accurate description for ring structural behavior. A complete treatment of the elementary beam theory is available in Timoshenko's strength of materials text [51].

A dual grid curved beam finite element method was developed by Baelden [44]. This method is used to couple ring deformation to contact interaction which are on different length scales. The magnitude of ring structural deformation is around $100\mu m$ similar to the magnitude of bore distortion, and its length scale is around 10mm which is determined by bore diameter, order of bore distortion and piston tilt. The contact interactions between ring and piston, ring and liner are within sub-micron level so any change of local clearance by several microns may totally change the behavior. The ring/liner and ring/groove interactions are also highly dependent on local boundary conditions such as bridging and fuel-lube interaction which typically have length scales from $10\mu m$ to $100\mu m$. The significant difference in length scales makes traditional straight beam finite element method difficult to respect the corresponding physics of structural deformation and local force generation. For example, in order to give an accurate prediction of ring-liner interaction, straight beam finite element method needs to reduce its element size below 1mm. However, if the grid size is too small, the beam element may lose its accuracy of structural response since the ratio of the cross section dimensions to the beam length is not small anymore.

The curved beam finite element method is able to address this problem by separating the structural mesh and contact grid using the element shape functions. Ring structural deformations are solved with sufficient accuracy on a coarse structural mesh and local interaction is handled on a much finer grid. Since this method is able to handle different length scales at the same time, it becomes a very powerful tool for our ring-pack oil transport model. As discussed before, oil transport is a combination of global and local processes with wide range of length scales. With this multi-grid method, we are able to simulate different processes on its proper length scale and provide more reasonable prediction of oil transport around the ring pack system.

Baelden [44] developed the curved beam finite element method and applied it to twin land oil control ring only. In this chapter, we apply this method to top two rings and derive the finite element equations for the entire ring pack.

2.1. Ring Differential Geometry

According to the beam theory, bending and twisting moments of a beam are proportional to changes of curvature and torsion of its neutral axis. To better understand the development of curved beam finite element method and relation between ring deformation and changes of curvature and torsion, a review of differential geometry and the calculation of curvature and torsion of a space curve is given in this section. A more complete treatment of differential geometry of space curves is available in Pressley's text [52].

Inside the engine, piston ring is expected to have both in-plane and out of plane deformation as well as ring twist. As a result, its neutral axis will bend and twist in three dimensions and should be treated as a space curve. First, three different reference frames that are used in this chapter are introduced here.
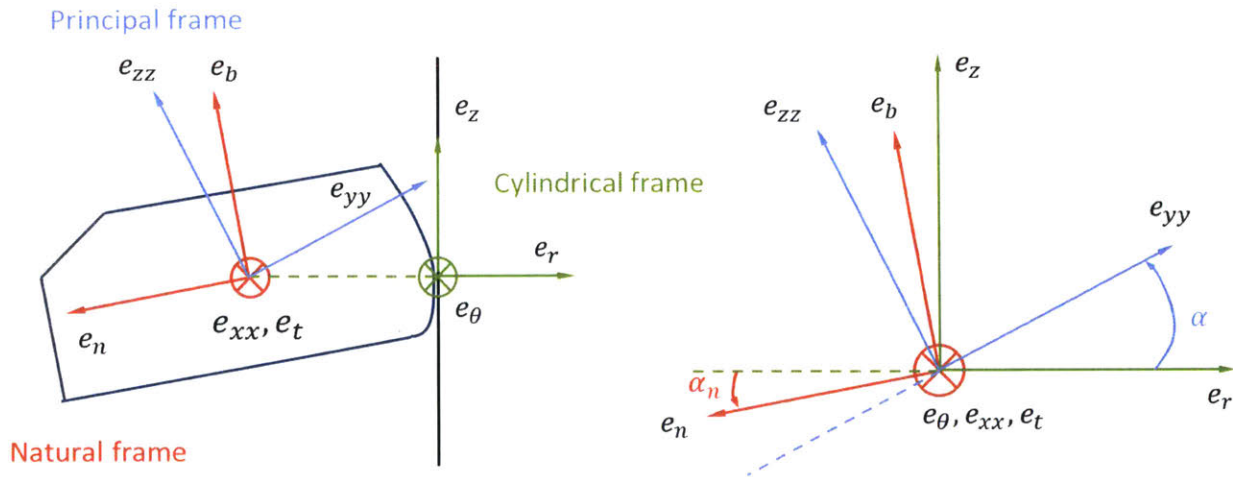
Figure 19 Ring Principal Frame, Natural Frame and Cylindrical Frame

As shown in Figure 19, the cylindrical frame is attached to the piston liner. e_r is in the bore radius direction and pointing outward, e_z is in the axial direction and pointing upwards and e_θ is in the bore circumferential direction. The natural frame is attached to the ring neutral axis and composed of the tangent unit vector e_t, normal unit vector e_n and binormal unit vector e_b. The definition and calculation of these three vectors are presented later. The orientation of the ring natural frame is α_n. The principal frame is composed of the two principal axes e_{zz} and e_{yy} that lie in the plane of ring cross section and of

the tangent unit vector e_{xx} that is perpendicular to the plane of ring cross section. Based on beam's theory, the principal frame is each of three mutually perpendicular axes in a body about which the moment of inertia is at a maximum and the product of inertia of each pair of the three axes is zero. This fact implies that bending moments that are perpendicular to a principal plane, result in deformation of the beam neutral axis in that principle plane.

An arbitrary spatial curve $\mathcal{C}$ can be expressed in cylindrical coordinate as:

$$\mathcal{C}(\theta)\colon \boldsymbol{r}(\theta) = \rho(\theta)\boldsymbol{e_r} + z(\theta)\boldsymbol{e_z} \ (\theta_1 \leq \theta \leq \theta_2)$$

Equation 2.1

$\boldsymbol{r}$ is the position vector to represent the curve. θ is the polar angle, ρ is the radius distance and z is the axial position, as shown in Figure 20. The natural frame of curve $\mathcal{C}$ is also shown in the same figure.
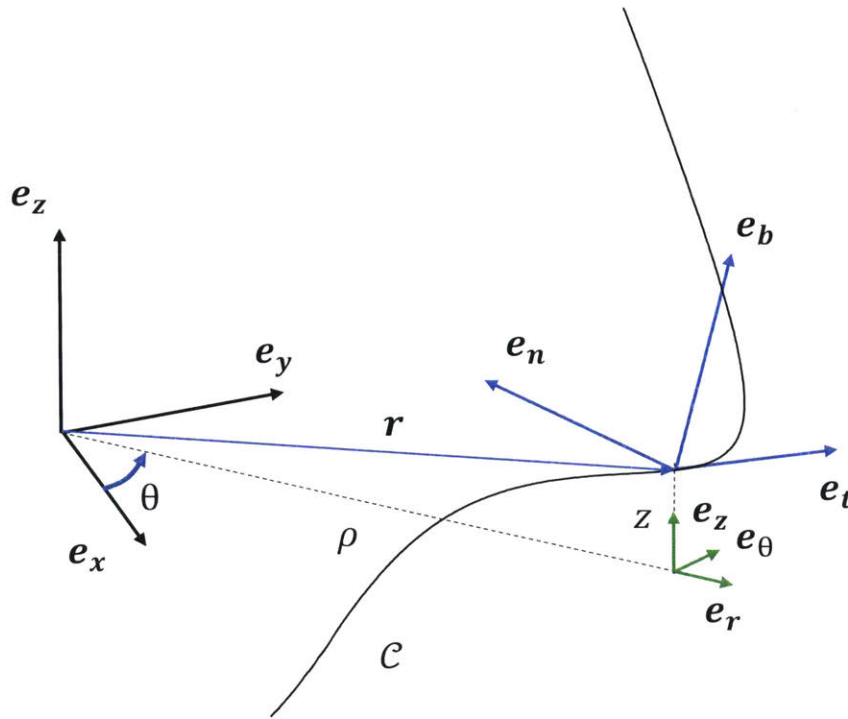
Figure 20 Space Curve in Cylindrical Coordinates

By definition, the curve unit tangent vector $\boldsymbol{e_t}$ is calculated by taking the derivative of the position vector $\boldsymbol{r(\theta)}$ with respect to θ.

$$\boldsymbol{e_t}(\theta) = \frac{\boldsymbol{r'}(\theta)}{\|\boldsymbol{r'}(\theta)\|} = \frac{\rho'\boldsymbol{e_r} + \rho\boldsymbol{e_\theta} + z'\boldsymbol{e_z}}{\sqrt{\rho^2 + \rho'^2 + z'^2}}$$

Equation 2.2

The prime sign here refers to a derivation with respect to the polar angle θ and this notation will be used for the remainder of this thesis.

The definition of the unit normal vector is the second derivative of the position vector $r(\theta)$ with respect to θ.

$$e_n(\theta) = \frac{r''(\theta)}{\|r''(\theta)\|} = \frac{(\rho'' - \rho)e_r + 2\rho'e_\theta + z''e_z}{\sqrt{(\rho'' - \rho)^2 + 2\rho'^2 + z''^2}}$$

Equation 2.3

The angle α_n is calculated by taking the ratio of axial component to radial component of the normal vector.

$$tan\alpha_n = \frac{z''}{\rho'' - \rho}$$

Equation 2.4

The binormal vector e_b is normal to both e_t and e_n and form a right hand coordinate system with them. It can be calculated by taking the cross product of e_t and e_n.

$$e_b(\theta) = e_t(\theta) \times e_n(\theta)$$

Equation 2.5

e_t and e_n form a plane called plane of curvature of curve $\mathcal{C}$ or the osculating plane. Locally $\mathcal{C}$ can be approximated by a planar curve in the osculating plane. The curvature of $\mathcal{C}$ is defined as the rate at which the tangent vector is rotated towards the normal vector as one moves along $\mathcal{C}$. It is actually the measure of how much the local planar curve is curved. The curvature can be calculated from the differential variation of the unit tangent vector e_t.

$$\frac{de_t}{ds} = \kappa e_n$$

Equation 2.6

ds is the arc length of differential element of $\mathcal{C}$ and its value can be calculated using the chain rule:

$$ds(\theta) = \|r'(\theta)\|d\theta = \sqrt{\rho^2 + \rho'^2 + z'^2}d\theta$$

Equation 2.7

By combining Equation 2.2, Equation 2.3, Equation 2.6 and Equation 2.7, the curvature can be written in the following expression:

$$\kappa = \frac{\|r'' \times r'\|}{\|r'\|^3} = \frac{\sqrt{(\rho z'' - 2\rho' z')^2 + ([\rho'' - \rho]z' - \rho' z'')^2 + (\rho[\rho - \rho''] + 2\rho'^2)^2}}{(\rho^2 + \rho'^2 + z'^2)^{3/2}}$$

Equation 2.8

For planar curve, the axial coordinate z can be removed and Equation 2.8 can be reduced to

$$\kappa = \frac{\left|\left(\rho^2 + 2\rho'^2 - \rho\rho''\right)^2\right|}{(\rho^2 + \rho'^2)^{3/2}}$$

Equation 2.9

Torsion represents the rate at which the binormal vector is rotated along the curve C. It is a measurement of how fast the osculating plane rotates and can be calculated from the differential variation of the unit normal vector e_b.

$$\frac{de_b}{ds} = -\tau e_n$$

Equation 2.10

By combining Equation 2.3, Equation 2.5, Equation 2.7 and Equation 2.10, the torsion can be written as

$$\tau = \frac{(r' \times r'') \cdot r'''}{\|r' \times r''\|^2} = \frac{\left(\rho z'' - 2\rho' z'\right)(\rho^{(3)} - 3\rho') + (3\rho'' - \rho)\left([\rho'' - \rho]z' - \rho' z''\right) + z^{(3)}\left(\rho[\rho - \rho''] + 2\rho'^2\right)}{(\rho z'' - 2\rho' z')^2 + ([\rho'' - \rho]z' - \rho' z'')^2 + \left(\rho[\rho - \rho''] + 2\rho'^2\right)^2}$$

The position vector r of the general ring neutral axis can be expressed as a function of the nominal ring radius R, the radial displacement y and the axial displacement z.

$$r = (R + y)e_r + ze_z$$

Equation 2.11

When assembled into engine, under the action of ring tension, gas pressure and inertia, piston rings deform to adapt to the groove and cylinder geometry. Therefore, the displacements of ring neutral axis in radial and axial direction should fall into the range of piston and cylinder deformation and piston displacement. For passenger car engines, the bore radius is close to 40mm and the cylinder deformation is on the order of $100\mu m$. The piston land and groove deformation in axial direction is on the order of $10\mu m$. The piston displacement due to secondary motion in axial direction is on the order of $100\mu m$. The piston land/groove deformation in radial direction and piston secondary motion in radial direction

are usually not the constraints to ring displacement. As a result, ring displacements in both radial and axial directions are expected to be much smaller than the nominal ring radius. The derivatives of the axial and radial displacements of the ring neutral axis are taken to be of the same order as the axial and radial displacements ($y \sim y' \sim y''$ and $z \sim z' \sim z''$). This assumption is valid because ring radial and axial displacement cannot change too rapidly due to the ring stiffness.

Finally, we can make an assumption called small displacement assumption: $\frac{y}{R} \sim \frac{y'}{R} \sim \frac{y''}{R} \ll 1$ and $\frac{z}{R} \sim \frac{z'}{R} \sim \frac{z''}{R} \ll 1$. Applying this assumption to the curvature and torsion calculation of ring neutral axis, we can obtain the following expressions:

$$\kappa \approx \frac{1}{R} - \frac{1}{R^2}(y + y'')$$

Equation 2.12

$$\tau \approx \frac{1}{R^2}(z' + z^{(3)})$$

Equation 2.13

A small displacement assumption can be applied to the calculation of the orientation of the Natural frame as well:

$$\alpha_n \approx -\frac{z''}{R}$$

Equation 2.14

The premise of small displacement assumption is that piston rings are assembled into engine. Otherwise, this assumption is not valid for top two rings because in their free state the displacement of top two rings' neutral axes from their nominal radius is on the order of several millimeters. In this case, radial displacement y cannot be assumed much smaller than nominal radius R.

2.2. Spline Interpolation of Ring Geometry with Hermite Polynomials

The ring neutral axis is a continuous curve which is free to take any shape under deformation. The curved beam finite element method discretizes the ring neutral axis into a number of elements and uses nodal displacements and their derivatives to interpolate its geometry. In interpolation, a careful selection of shape functions is very important to obtain enough accuracy of the ring neutral axis geometry. Figure 21 shows an example of spline interpolation of the ring radial displacement.
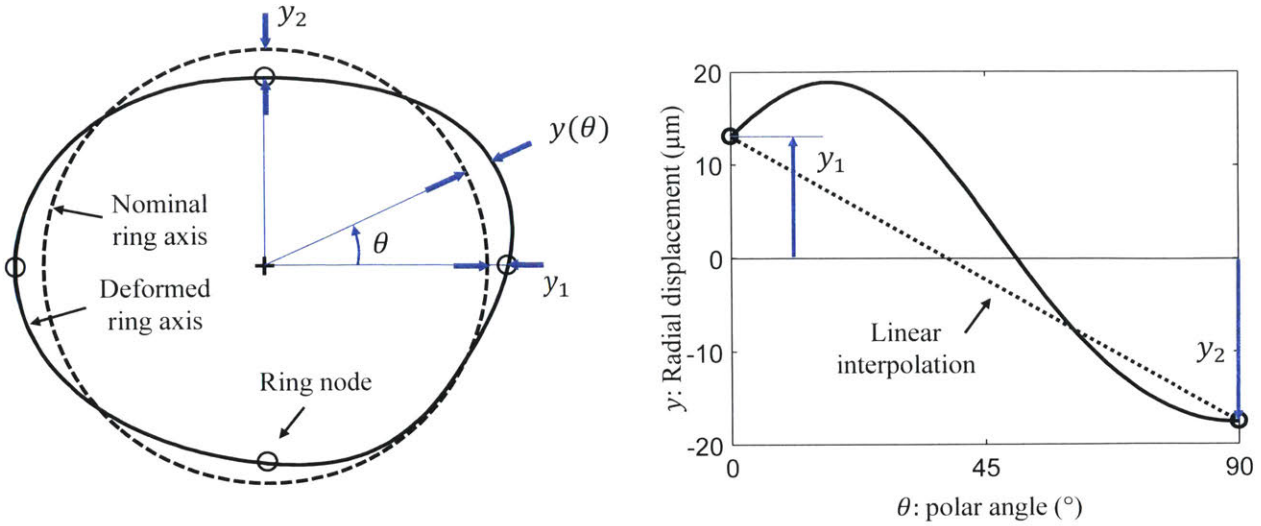
Figure 21 Spline Interpolation of Ring Displacement

In the right picture of Figure 21, the ring radial deformation (solid line) is approximated by a linear function (dotted line) which matches the actual deformation at node 1 and node 2.

$$y(\eta) = y_1 + \eta(y_2 - y_1)$$

Equation 2.15

Where η is the isoparametric variable and defined as

$$\eta = \frac{\theta}{\theta_e}$$

Equation 2.16

θ_e is the angular length of a ring element. The isoparametric variable is defined in such a way that it varies linearly from $\eta = 0$ at node 1 to $\eta = 1$ at node 2. The interpolation function can be rewritten as the sum of two first order polynomials with coefficients y_1 and y_2.

$$y(\eta) = (1 - \eta)y_1 + \eta y_2 = N_1 y_1 + N_2 y_2$$

Equation 2.17

where $N_1 = 1 - \eta$ and $N_2 = \eta$. N_1 and N_2 are the shape functions of the ring element associated with the nodal displacements y_1 and y_2. The above equation is a first order Hermitian interpolation of the ring radial displacement. The ring neutral axis can be divided into several elements and each element has its own interpolation function associated with the displacements and their derivatives at its two

nodes. The entire ring neutral axis displacement can be obtained by assembling the interpolation functions of each element.

The deformation of the ring to be interpolated can be broken down in three components: the radial and axial displacements of the neutral axis, and the orientation of the cross section, as shown in Figure 22.
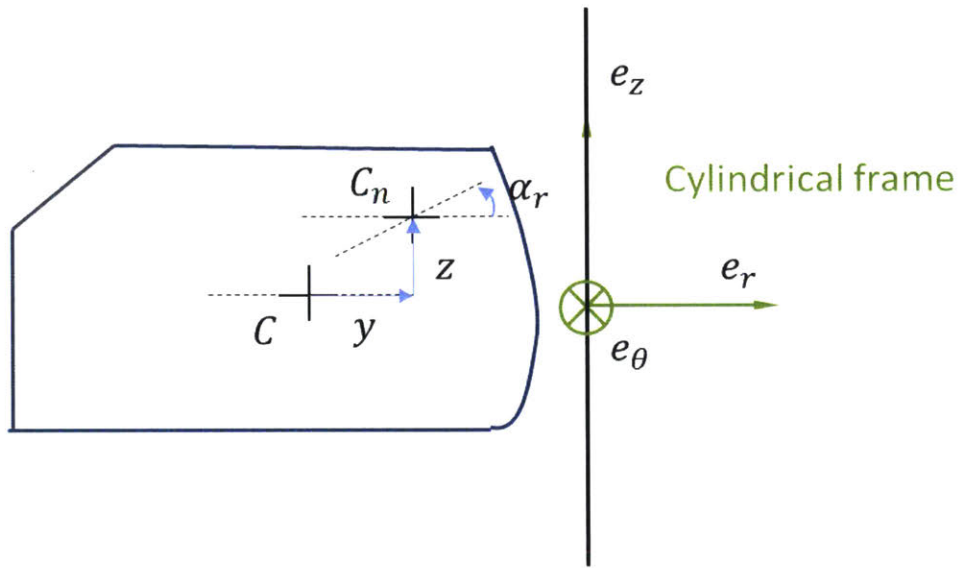
Figure 22 Ring Cross Section Displacements

The Hermite polynomial shape functions have been developed by Baelden [44] which are used in the curved beam finite element method to interpolate all the three components. The radial and axial displacement of the ring neutral axis are interpolated using 5th order Hermite polynomial spline. This is to guarantee continuity of the curvature of the ring which is the key variable for bending. 5th order interpolation requires nodal displacements to include the displacement, its first and second derivatives (Figure 23).
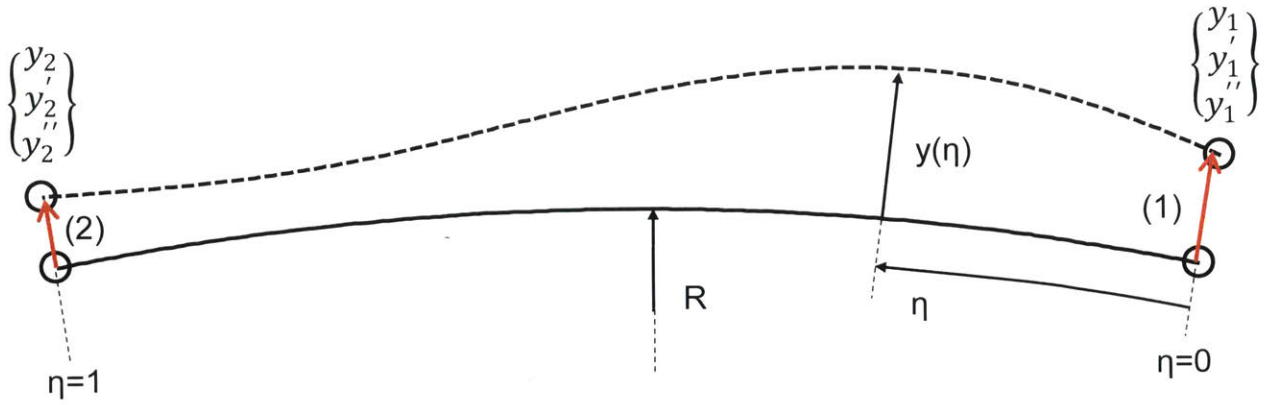
Figure 23 Spline Interpolation of Ring Radial Displacement

$$y(\eta) = \sum_{k=1}^{6} N_k(\eta) u_{yk} \ \text{where} \ \{u_y\} = \{u_{y1}, .., u_{y6}\}^T = \{y_1, y_1', y_1'', y_2, y_2', y_2''\}^T$$

Equation 2.18

$$z(\eta) = \sum_{k=1}^{6} N_k(\eta) u_{zk} \ \text{where} \ \{u_z\} = \{u_{z1}, .., u_{z6}\}^T = \{z_1, z_1', z_1'', z_2, z_2', z_2''\}^T$$

Equation 2.19

There are six shape functions: N_1, N_2, N_3, N_4, N_5, N_6. The details can be found in Baelden's thesis [44] [45] and their expression are listed below.

$$N_1 = 1 - 10\eta^3 + 15\eta^4 - 6\eta^5$$

Equation 2.20

$$N_2 = \theta_e(\eta - 6\eta^3 + 8\eta^4 - 3\eta^5)$$

Equation 2.21

$$N_3 = \theta_e^2 \left(\frac{\eta^2}{2} - 3\frac{\eta^3}{2} + 3\frac{\eta^4}{2} - \frac{\eta^5}{2} \right)$$

Equation 2.22

$$N_4 = 10\eta^3 - 15\eta^4 + 6\eta^5$$

Equation 2.23

$$N_5 = \theta_e(-4\eta^3 + 7\eta^4 - 3\eta^5)$$

Equation 2.24

$$N_6 = \theta_e^2 \left(\frac{\eta^3}{2} - \eta^4 + \frac{\eta^5}{2} \right)$$

Equation 2.25

The first order and second order derivatives of the displacement within one element can be calculated by taking derivatives to the shape functions.

$$y'(\eta) = \sum_{k=1}^{6} N'_k(\eta) u_{yk}$$

Equation 2.26

$$y''(\eta) = \sum_{k=1}^{6} N''_k(\eta) u_{yk}$$

Equation 2.27

$$z'(\eta) = \sum_{k=1}^{6} N'_k(\eta) u_{zk}$$

Equation 2.28

$$z''(\eta) = \sum_{k=1}^{6} N''_k(\eta) u_{zk}$$

Equation 2.29

The twist angle is interpolated using 3rd order Hermite polynomials. The twisting moment is proportional to the first order derivative of the twist angle. Thus, 3rd order polynomial interpolation is sufficient and requires ring twist and its first order derivative at two nodes.

$$\alpha_r(\eta) = \sum_{k=1}^{4} N_{\alpha k}(\eta) u_{\alpha k} \ where \ \{u_\alpha\} = \{u_{\alpha 1}, .., u_{\alpha 4}\}^T = \{\alpha_{r1}, \alpha'_{r1}, \alpha_{r2}, \alpha'_{r2}\}^T$$

Equation 2.30

The four shape functions are listed below.

$$N_{\alpha 1} = 1 - 3\eta^2 + 2\eta^3$$

Equation 2.31

$$N_{\alpha 2} = \theta_e(\eta - 2\eta^2 + \eta^3)$$

Equation 2.32

$$N_{\alpha 3} = 3\eta^2 - 2\eta^3$$

Equation 2.33

$$N_{\alpha 4} = \theta_e(-\eta^2 + \eta^3)$$

Equation 2.34

The first order derivative of the ring twist within one element can be calculated by taking derivative to the shape functions.

$$\alpha_r{}'(\eta) = \sum_{k=1}^{4} N'_{\alpha k}(\eta)u_{\alpha k}$$

Equation 2.35

The curved beam finite element method uses two 5th order and one 3rd order Hermite polynomials to discretize the ring deformation which leads to 8 degree of freedoms per node: 3 for radial displacements, 3 for axial displacements and 2 for twist. All nodal displacements can be assembled in one displacement vector.

$$\{u_k\} = \{y_k, y_k', y_k'', z_k, z_k', z_k'', \alpha_{r,k}, \alpha_{r,k}'\}^T$$

Equation 2.36

2.3. Euler-Lagrange Equations for Ring Structural Analysis

Baelden has used Hamilton's principle to derive the finite element equations of the piston ring model [45], which can be seen as an extension of the principle of virtual work that includes the dynamics of the system. The Lagrangian L of the system is defined as the combination of the kinetic energy T, the strain energy U and the work of external forces W:

$$L = T + W - U$$

Equation 2.37

Application of Hamilton's principle to the system leads to the Euler-Lagrange equations:

$$\frac{\partial}{\partial t}\left(\frac{\partial L}{\partial \dot{u}_i}\right) - \frac{\partial L}{\partial u_i} = 0 \; for = \{1, .., n\}$$

Equation 2.38

The variable u_i represents the ith nodal displacement of the discretized ring and $\dot{u}_i$ is the nodal speed. Hamilton's principle can be applied to one element of the piston ring as well. First kinetic energy, strain energy and work of external forces of the ring must be calculated.

The motion of the ring cross section can be split into three parts: the translation in the radial direction, the translation in the axial direction and the rotation around the ring neutral axis. The ring neutral axis displacements (y, z and α) are measured in the cylindrical frame. The zero displacement position corresponds to a ring centered in the piston groove and contacting a perfectly round cylinder. The kinetic energy of the ring element is calculated by integrating the kinetic energy of cross sections (Equation 2.39) along the ring neutral axis.

$$dT^{(e)} = \frac{1}{2}\rho[A(\dot{y}^2 + \dot{z}^2) + I_p\dot{\alpha}_r^{\,2}]ds$$

Equation 2.39

$$T^{(e)} = \frac{1}{2}\int_0^{L_e} \rho[A(\dot{y}^2 + \dot{z}^2) + I_p\dot{\alpha}_r^{\,2}]ds$$

Equation 2.40

The notation (e) refers to the ring element. In the equation, L_e is the length of the ring element, rho is the density of the ring material, I_p is the polar moment of inertia of the cross section and A is the cross section area.

Strain energy is potential energy stored in the ring due to structural deformation. According to beam theory, strain energy can be calculated from the ring's bending and twisting moments and the corresponding curvature change and twist angle.
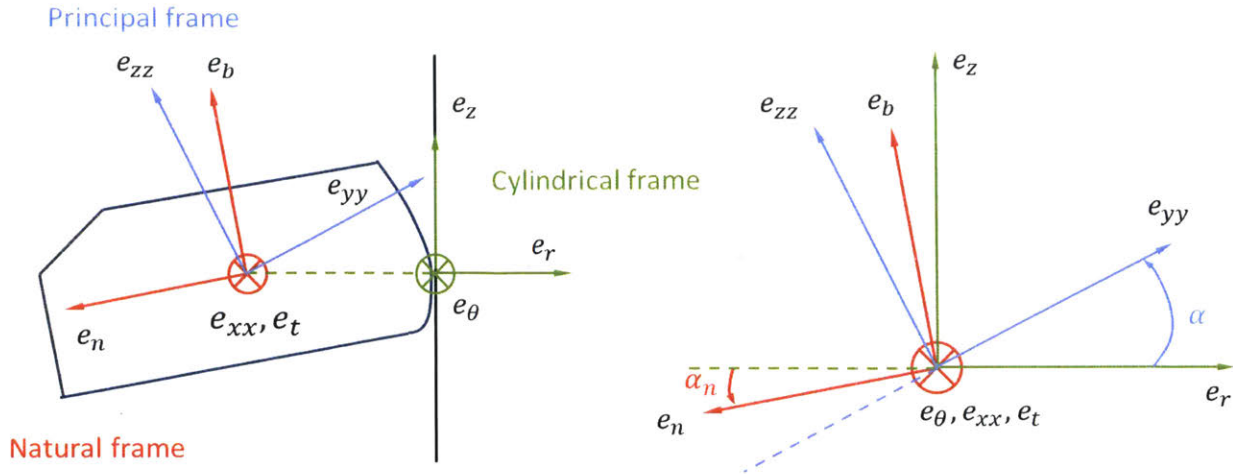
Figure 24 Ring Principal Frame, Natural Frame and Cylindrical Frame

As shown in Figure 24, the curvature of the ring neutral axis falls in the plane formed by the vectors e_b and e_n and aligns with the vector e_n. In Section 2.1, we demonstrated that $\alpha_n \approx -\frac{z''}{R}$. Then

$$\kappa_{yy} = \kappa \cos(\alpha - \alpha_n) = \kappa \cos(\alpha + \frac{z''}{R})$$

Equation 2.41

$$\kappa_{zz} = \kappa \sin(\alpha - \alpha_n) = \kappa \sin(\alpha + \frac{z''}{R})$$

Equation 2.42

Bending moment in e_{zz} direction is proportional to curvature change in e_{yy} direction and bending moment in e_{yy} direction is proportional to curvature change in e_{zz} direction. As shown in Baelden's thesis [45], there are two components in the ring twist angle: τ the torsion of the ring neutral axis, and the rotation of the ring section per unit length $\frac{d}{ds}(\alpha_r - \alpha)$.

$$M_{zz} = EI_{zz}\left(\kappa_{yy} - \kappa_{yy0}\right)$$

Equation 2.43

$$M_{yy} = EI_{yy}(\kappa_{zz} - \kappa_{zz0})$$

Equation 2.44

$$M_\theta = GJ_t\left[\tau + \frac{d}{ds}(\alpha_n - \alpha)\right]$$

Equation 2.45

The strain energy of the ring element is the integration of the strain energy of cross sections (Equation 2.46, Equation 2.48, Equation 2.50) along the ring neutral axis.

$$dU_{zz}^{(e)} = \frac{1}{2}M_{zz}(\kappa_{yy} - \kappa_{yy0})ds = \frac{1}{2}EI_{zz}(\kappa_{yy} - \kappa_{yy0})^2 ds$$

Equation 2.46

$$U_{zz}^{(e)} = \frac{1}{2}\int_0^{L_e} EI_{zz}(\kappa_{yy} - \kappa_{yy0})^2 ds$$

Equation 2.47

$$dU_{yy}^{(e)} = \frac{1}{2}M_{yy}(\kappa_{zz} - \kappa_{zz0})ds = \frac{1}{2}EI_{yy}(\kappa_{zz} - \kappa_{zz0})^2 ds$$

Equation 2.48

$$U_{yy}^{(e)} = \frac{1}{2}\int_0^{L_e} EI_{yy}(\kappa_{zz} - \kappa_{zz0})^2 ds$$

Equation 2.49

$$dU_{\theta}^{(e)} = \frac{1}{2}M_{\theta}\left[\tau + \frac{d}{ds}(\alpha_n - \alpha)\right]ds = \frac{1}{2}GJ_t\left[\tau + \frac{d}{ds}(\alpha_n - \alpha)\right]^2 ds$$

Equation 2.50

$$U_{\theta}^{(e)} = \frac{1}{2}\int_0^{L_e} GJ_t\left[\tau + \frac{d}{ds}(\alpha_n - \alpha)\right]^2 ds$$

Equation 2.51

And the total strain energy is the sum of the three components.

$$U^{(e)} = U_{zz}^{(e)} + U_{yy}^{(e)} + U_{\theta}^{(e)}$$

Equation 2.52

The resulting force of cross section can be composed into three parts: radial force f_r, axial force f_z and twisting moment m_θ (shown in Figure 25). The calculation of the resulting forces will be derived in next several chapters when we start to build the models. The quantities f_r, f_z and m_θ are forces and moment per unit length respectively.

Cross section resultants
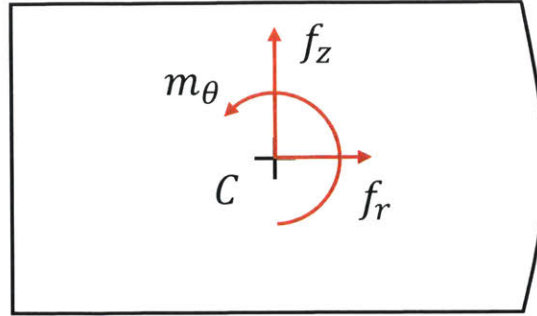
Figure 25 Resulting Forces on Ring Cross Section

$$W^{(e)} = \int_0^{L_e} [f_r y + f_z z + m_t \alpha] ds$$

Equation 2.53

The Lagrangian of the ring element is calculated as:

$$L^{(e)} = T^{(e)} + W^{(e)} - U^{(e)}$$

Equation 2.54

and applying Hamilton's principle, we can obtain the Euler-Lagrange equations for the ring element.

$$\frac{\partial}{\partial t}\left(\frac{\partial L^{(e)}}{\partial \dot{u}_i}\right) - \frac{\partial L^{(e)}}{\partial u_i} = 0 \; for = \{1,..,n\}$$

Equation 2.55

where u_i is the ith degree of freedom of the two nodes of the ring element.

$$u^{(e)} = \{y_1, y_1', y_1'', z_1, z_1', z_1'', \alpha_1, \alpha_1', y_2, y_2', y_2'', z_2, z_2', z_2'', \alpha_2, \alpha_2'\}$$

Equation 2.56

Subscript 1 refers to the first node of the element and subscript 2 refers to the second node of the element.

2.4. Ring Gap Closing with Large Displacement
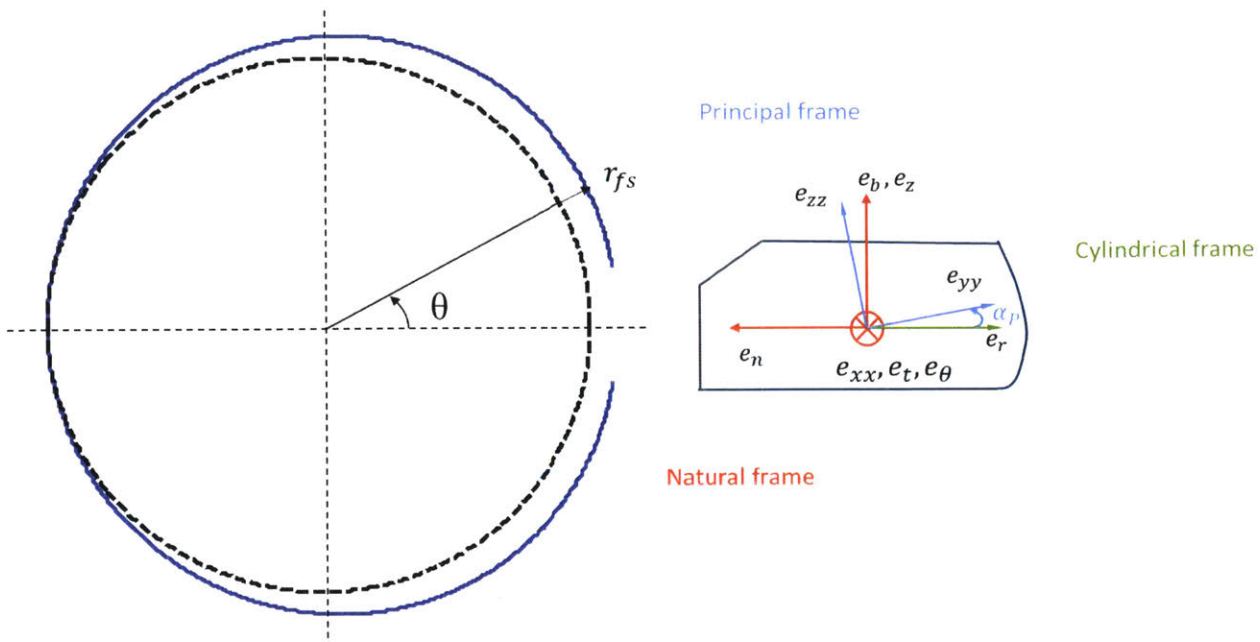
Figure 26 Single Piece Ring at Free State

In section 2.1, we use small displacement assumption to simplify the calculation of curvature and torsion of the ring neutral axis. However, as we stated at the end of that section, this assumption is not valid when top two rings are in their free shape (free state). In this case, the ring neutral axis is a planar curve and the axial displacement of the ring neutral axis is zero but the radial displacement with respect to the nominal bore radius (which is the reference point of ring neutral axis displacement in radial direction) is in the order of several millimeters and cannot be assumed small. Therefore, we have to use the general expression of curvature of a planar curve, Equation 2.9, to calculate the curvature.

$$\kappa_{fs} = \frac{\left(r_{fs}^2 + 2r_{fs}'^2 - r_{fs}r_{fs}''\right)^2}{\left(r_{fs}^2 + r_{fs}'^2\right)^{3/2}}$$

Equation 2.57

The calculation of the curvature change will become very complicated and non-linear if directly applying the above equation. In order to simplify the calculation, we add an intermediate state that the ring is closed at its nominal radius without twist. Once the ring is closed, the curvature change with respect to the intermediate state can be simplified using the small displacement assumption. In the left plot of Figure 27, the red curve is the ring free shape and the blue curve is the ring at its round shape.

The right plot of Figure 27 demonstrates the required preload to close the ring from its free shape to its round shape.
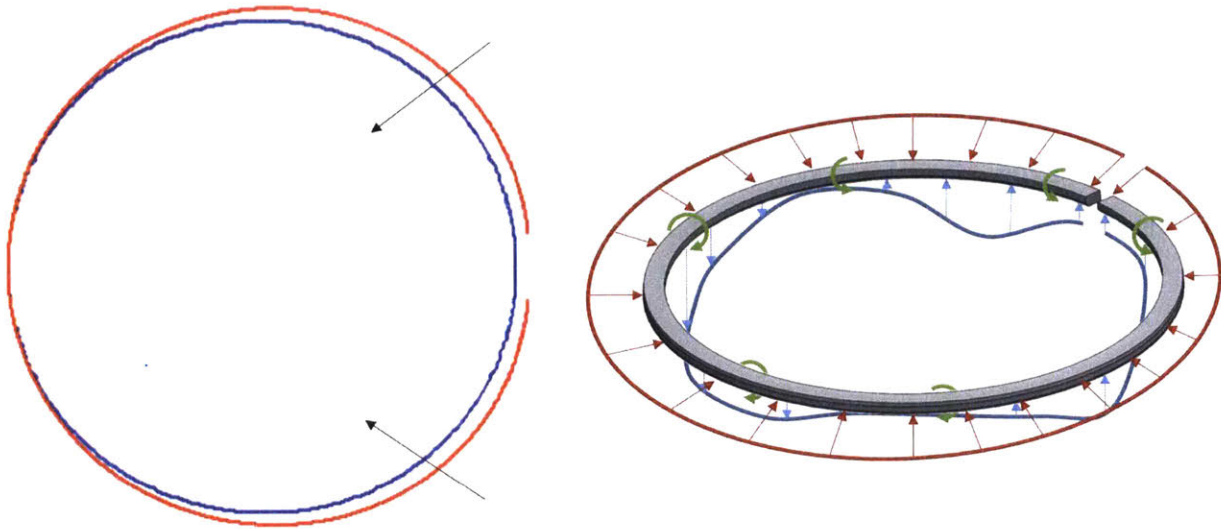
Figure 27 Intermediate State and the Required Preload

The required preload holding the ring at this intermediate state from its free shape is obtained by applying Euler-Lagrange Equations. As shown in Figure 26, due to asymmetric geometry of a single piece ring's cross section, the principal frame does not align with the cylindrical frame at their free state and the orientation angle is called principal angle, α_p. From Figure 24 and Figure 26, it is not difficult to derive the relation between the orientation angle of the principal frame and the ring cross section twist:

$$\alpha_r = \alpha - \alpha_p$$

Equation 2.58

The initial curvature and torsion are calculated as follow:

$$\kappa_{yy0} = \kappa_{fs}\cos\alpha_p$$

Equation 2.59

$$\kappa_{zz0} = \kappa_{fs}\sin\alpha_p$$

Equation 2.60

$$\tau_0 = 0$$

Equation 2.61

$$\alpha_0 = \alpha_p$$

Equation 2.62

$$\alpha_{n,0} = 0$$

Equation 2.63

At final state, the ring gap is closed at its nominal radius. Thus, the assumption of small displacement in both radial direction, y, and axial direction, z, becomes valid.

$$\alpha_n \approx -\frac{z''}{R}$$

Equation 2.64

$$\kappa \approx \frac{1}{R} - \frac{y + y''}{R^2}$$

Equation 2.65

$$\kappa_{yy} = \kappa \cos(\alpha - \alpha_n) = \left(\frac{1}{R} - \frac{y + y''}{R^2}\right) \cos\left(\alpha + \frac{z''}{R}\right)$$

Equation 2.66

$$\kappa_{zz} = \kappa \sin(\alpha - \alpha_n) = \left(\frac{1}{R} - \frac{y + y''}{R^2}\right) \sin\left(\alpha + \frac{z''}{R}\right)$$

Equation 2.67

$$\tau \approx \frac{1}{R^2}\left(z' + z^{(3)}\right)$$

Equation 2.68

Then at final state, the strain energy of one ring element can be written as follow:

$$U_{zz}^{(e)} = \frac{1}{2}\int_0^{L_e} EI_{zz}(\kappa_{yy} - \kappa_{yy0})^2 ds = \frac{L_e EI_{zz}}{2}\int_0^1 \left(\left(\frac{1}{R} - \frac{y + y''}{R^2}\right)\cos\left(\alpha + \frac{z''}{R}\right) - \kappa_{fs}\cos\alpha_p\right)^2 d\eta$$

Equation 2.69

$$U_{yy}^{(e)} = \frac{1}{2}\int_0^{L_e} EI_{yy}(\kappa_{zz} - \kappa_{zz0})^2 ds = \frac{L_e EI_{yy}}{2}\int_0^1 \left(\left(\frac{1}{R} - \frac{y + y''}{R^2}\right)\sin\left(\alpha + \frac{z''}{R}\right) - \kappa_{fs}\sin\alpha_p\right)^2 d\eta$$

Equation 2.70

$$U_\theta^{(e)} = \frac{1}{2} \int_0^{L_e} GJ_t \left(\tau + \frac{d}{ds}(\alpha_n - \alpha) \right)^2 ds = \frac{L_e GJ_t}{2} \int_0^1 \left(\frac{z' - R\alpha'}{R^2} \right)^2 d\eta$$

Equation 2.71

$$U^{(e)} = U_{zz}^{(e)} + U_{yy}^{(e)} + U_\theta^{(e)}$$

Equation 2.72

As demonstrated in Section 2.2, the ring element displacements in the radial and axial direction and cross section twist can be interpolated using the nodal displacements at the two nodes:

$$y(\eta) = \sum_{k=1}^6 N_k(\eta) u_{yk} \ \text{where} \ \{u_y\} = \{u_{y1}, .., u_{y6}\}^T = \{y_1, y_1', y_1'', y_2, y_2', y_2''\}^T \ [\textit{Equation 2.18}]$$

$$z(\eta) = \sum_{k=1}^6 N_k(\eta) u_{zk} \ \text{where} \ \{u_z\} = \{u_{z1}, .., u_{z6}\}^T = \{z_1, z_1', z_1'', z_2, z_2', z_2''\}^T \ [\textit{Equation 2.19}]$$

$$\alpha_r(\eta) = \sum_{k=1}^4 N_{\alpha k}(\eta) u_{\alpha k} \ \text{where} \ \{u_\alpha\} = \{u_{\alpha 1}, .., u_{\alpha 4}\}^T = \{\alpha_{r1}, \alpha_{r1}', \alpha_{r2}, \alpha_{r2}'\}^T \ [\textit{Equation 2.30}]$$

The ring element has two nodes and therefore 16 nodal displacements (Equation 2.56):

$$\{u\}^{(e)} = \{u_1, u_2, \dots, u_{16}\}^T = \{y_1, y_1', y_1'', z_1, z_1', z_1'', \alpha_1, \alpha_1', y_2, y_2', y_2'', z_2, z_2', z_2'', \alpha_2, \alpha_2', \}^T \ [\textit{Equation 2.56}]$$

The mapping function to select the shape function corresponding to a ring element k^{th} nodal displacement is shown below.

$$k_y = [1,2,3,9,10,11]$$

Equation 2.73

$$k_z = [4,5,6,12,13,14]$$

Equation 2.74

$$k_\alpha = [7,8,15,16]$$

Equation 2.75

$$k \rightarrow m(k)$$

$$[1,2,3,4,5,6,7,8,9,10,11,12,13,14,15,16] \rightarrow [1,2,3,1,2,3,1,2,4,5,6,4,5,6,3,4]$$

Equation 2.76

Equation 2.18, Equation 2.19 and Equation 2.30 can be re-written as:

$$y(\eta) = \sum_{k_y} N_{m(k_y)}(\eta) u_{k_y}$$

Equation 2.77

$$z(\eta) = \sum_{k_z} N_{m(k_z)}(\eta) u_{k_z}$$

Equation 2.78

$$\alpha_r(\eta) = \sum_{k_\alpha} N_{m(k_\alpha)}(\eta) u_{k_\alpha}$$

Equation 2.79

Then we can apply Hamilton's principle to Equation 2.69, Equation 2.70, Equation 2.71 and Equation 2.72 with new notations. The derivatives of the ring strain energy with respect to the nodal displacements are shown below.

$$\frac{\partial U^{(e)}}{\partial u_{k_y}} = \frac{\partial U_{zz}^{(e)}}{\partial u_{k_y}} + \frac{\partial U_{yy}^{(e)}}{\partial u_{k_y}} =$$

$$L_e E I_{zz} \int_0^1 (\kappa_{yy} - \kappa_{yy0}) \left[-\frac{\cos\left(\alpha + \frac{z''}{R}\right)}{R^2} \right] \left(N_{m(k_y)} + N''_{m(k_y)} \right) d\eta \;+$$

$$L_e E I_{yy} \int_0^1 (\kappa_{zz} - \kappa_{zz0}) \left[-\frac{\sin\left(\alpha + \frac{z''}{R}\right)}{R^2} \right] \left(N_{m(k_y)} + N''_{m(k_y)} \right) d\eta$$

Equation 2.80

$$\frac{\partial U^{(e)}}{\partial u_{k_z}} = \frac{\partial U_{zz}^{(e)}}{\partial u_{k_z}} + \frac{\partial U_{yy}^{(e)}}{\partial u_{k_z}} + \frac{\partial U_{\theta}^{(e)}}{\partial u_{k_z}} = L_e E I_{zz} \int_0^1 (\kappa_{yy} - \kappa_{yy0}) \left[-\frac{1}{R} + \frac{1}{R^2}(y + y'') \right] \sin\left(\alpha + \frac{z''}{R}\right) \frac{N''_{m(k_z)}}{R} d\eta \;+$$

$$L_e E I_{yy} \int_0^1 (\kappa_{zz} - \kappa_{zz0}) \left[\frac{1}{R} - \frac{1}{R^2}(y + y'') \right] \cos\left(\alpha + \frac{z''}{R}\right) \frac{N''_{m(k_z)}}{R} d\eta \;+$$

$$L_e G J_t \int_0^1 \left(\frac{z' - R\alpha'}{R^2}\right) \frac{N'_{m(k_z)}}{R^2} d\eta$$

Equation 2.81

$$\frac{\partial U^{(e)}}{\partial u_{k_\alpha}} = \frac{\partial U_{zz}^{(e)}}{\partial u_{k_\alpha}} + \frac{\partial U_{yy}^{(e)}}{\partial u_{k_\alpha}} + \frac{\partial U_\theta^{(e)}}{\partial u_{k_\alpha}} = L_e EI_{zz} \int_0^1 \left(\kappa_{yy} - \kappa_{yy0}\right)\left[-\frac{1}{R} + \frac{1}{R^2}(y + y'')\right]\sin\left(\alpha + \frac{z''}{R}\right)\frac{N'_{\alpha m(k_\alpha)}}{R}\,d\eta \; +$$

$$L_e EI_{yy} \int_0^1 (\kappa_{zz} - \kappa_{zz0})\left[\frac{1}{R} - \frac{1}{R^2}(y + y'')\right]\cos\left(\alpha + \frac{z''}{R}\right)\frac{N'_{\alpha m(k_\alpha)}}{R}\,d\eta \; +$$

$$L_e GJ_t \int_0^1 (\frac{z' - R\alpha'}{R^2})(-\frac{N'_{\alpha m(k_\alpha)}}{R})\,d\eta$$

Equation 2.82

Substitute of Equation 2.80, Equation 2.81 and Equation 2.82 into Euler-Lagrange equation leads to the load required to close the ring gap without any out of plane bending nor twist:

$$F_{initial,k_y}^{(e)} = \frac{\partial U^{(e)}}{\partial u_{k_y}}\Big|_{\substack{y=0,y'=0,y''=0 \\ z=0,z'=0,z''=0 \\ \alpha=\alpha_p,\alpha'=0}}$$

$$= L_e EI_{zz} \int_0^1 \left(\frac{1}{R} - \kappa_{fs}\right)\left[-\frac{\cos^2\alpha_p}{R^2}\right]\left(N_{m(k_y)} + N''_{m(k_y)}\right)d\eta$$

$$+ L_e EI_{yy} \int_0^1 \left(\frac{1}{R} - \kappa_{fs}\right)\left[-\frac{\sin^2\alpha_p}{R^2}\right]\left(N_{m(k_y)} + N''_{m(k_y)}\right)d\eta$$

Equation 2.83

$$F_{initial,k_z}^{(e)} = \frac{\partial U^{(e)}}{\partial u_{k_z}}\Big|_{\substack{y=0,y'=0,y''=0 \\ z=0,z'=0,z''=0 \\ \alpha=\alpha_p,\alpha'=0}}$$

$$= L_e EI_{zz} \int_0^1 \left(\frac{1}{R} - \kappa_{fs}\right)\left(-\frac{1}{R}\right)\cos\alpha_p \sin\alpha_p \frac{N''_{m(k_z)}}{R}\,d\eta$$

$$+ L_e EI_{yy} \int_0^1 \left(\frac{1}{R} - \kappa_{fs}\right)\frac{1}{R}\sin\alpha_p \cos\alpha_p \frac{N''_{m(k_z)}}{R}\,d\eta$$

Equation 2.84

$$F^{(e)}_{initial,k_\alpha} = \frac{\partial U^{(e)}}{\partial u_{k_\alpha}}\Big|_{\substack{y=0,y'=0,y''=0 \\ z=0,z'=0,z''=0 \\ \alpha=\alpha_p,\alpha'=0}}$$

$$= L_e E I_{zz} \int_0^1 \left(\frac{1}{R} - \kappa_{fs}\right)\left(-\frac{1}{R}\right) cos\alpha_p sin\alpha_p \frac{N'_{\alpha m(k_\alpha)}}{R} d\eta$$

$$+ L_e E I_{yy} \int_0^1 \left(\frac{1}{R} - \kappa_{fs}\right)\frac{1}{R} sin\alpha_p cos\alpha_p \frac{N'_{\alpha m(k_\alpha)}}{R} d\eta$$

Equation 2.85

After obtaining the required forces to close a single piece ring to its nominal radius, we can solve ring deformation from this intermediate state by applying these forces as preload or initial load, $\{F_{initial}\}$.

2.5. Derivation of Mass, Stiffness and Load Finite Element Matrices for Top Two Rings

Baelden has derived the mass, stiffness and load finite element matrices for twin land oil control ring [45]. Here we are going to show the derivation of these matrices for top two rings which is very similar to what Baelden did.

After applying the initial load, the ring gap is closed with only in-plane bending. The current state of the ring becomes round shape without any lift or twist. In reference to further ring static analysis and dynamics calculation, this state is defined as the initial state with preload $F_{initial}$. Once the ring gap is closed, small displacement assumption becomes applicable to calculate the curvature and torsion of the ring neutral axis.

$$\kappa_{yy0} = \frac{1}{R}cos\alpha_p \approx \frac{1}{R}$$

Equation 2.86

$$\kappa_{zz0} = \frac{1}{R}sin\alpha_p \approx \frac{\alpha_p}{R}$$

Equation 2.87

$$\tau_0 = 0$$

Equation 2.88

$$\alpha_0 = \alpha_p$$

Equation 2.89

$$\alpha_{n0} = 0$$

Equation 2.90

$$\kappa_{yy} \approx \left[\frac{1}{R} - \frac{1}{R^2}(y + y'')\right]\cos(\alpha + z''/R) \approx \frac{1}{R} - \frac{1}{R^2}(y + y'')$$

Equation 2.91

$$\kappa_{zz} \approx \left[\frac{1}{R} - \frac{1}{R^2}(y + y'')\right]\sin(\alpha + z''/R) \approx \frac{1}{R}(\alpha + z''/R)$$

Equation 2.92

$$\tau \approx \frac{1}{R^2}(z' + z^{(3)})$$

Equation 2.93

$$\alpha_n \approx -\frac{z''}{R}$$

Equation 2.94

We will see that when we calculate the curvature change in e_{zz} direction there will be a term $\alpha - \alpha_p$ and this term is exactly the ring twist α_r that we have defined before. Since α_r and α only shifts with a constant of α_p, their derivatives with respect to θ are the same.

$$U_{zz}^{(e)} = \frac{L_e}{2}\int_0^1 EI_{zz}\left(\kappa_{yy} - \kappa_{yy0}\right)^2 d\eta = \frac{L_e}{2}\int_0^1 EI_{zz}\left(\frac{1}{R} - \frac{1}{R^2}(y + y'') - \frac{1}{R}\right)^2 d\eta$$

$$= \frac{L_e}{2R^4}\int_0^1 EI_{zz}\left\{\sum_{k=k_y}\left(N_{m(k)} + N''_{m(k)}\right)u_k\right\}^2 d\eta$$

Equation 2.95

$$U_{yy}^{(e)} = \frac{L_e}{2}\int_0^1 EI_{yy}(\kappa_{zz} - \kappa_{zz0})^2 d\eta = \frac{L_e}{2}\int_0^1 EI_{yy}\left(\frac{\alpha - \alpha_p}{R} + \frac{z''}{R}\right)^2 d\eta$$

$$= \frac{L_e}{2R^4}\int_0^1 EI_{yy}\left\{\sum_{k=k_z} N''_{m(k)}u_k + R\sum_{k=k_\alpha} N_{\alpha m(k)}u_k\right\}^2 d\eta$$

Equation 2.96

49

$$U_\theta^{(e)} = \frac{L_e}{2} \int_0^1 GJ_t \left[\tau + \frac{d}{ds}(\alpha_n - \alpha) \right]^2 d\eta = \frac{L_e}{2} \int_0^1 GJ_t \left[\frac{1}{R^2}(z' + z^{(3)}) + \frac{\alpha_n'}{R} - \frac{\alpha'}{R} \right]^2 d\eta$$

$$= \frac{L_e}{2R^4} \int_0^1 GJ_t \left\{ \sum_{k=k_z} N'_{m(k)} u_k - R \sum_{k=k_\alpha} N'_{\alpha m(k)} u_k \right\}^2 d\eta$$

Equation 2.97

$$U^{(e)} = U_{zz}^{(e)} + U_{yy}^{(e)} + U_\theta^{(e)}$$

Equation 2.98

The strain energy of the ring element is a bilinear form of the nodal displacements and can be written in a matrix form.

$$U^{(e)} = \frac{1}{2}\{u\}^{(e)^T} [K]^{(e)} \{u\}^{(e)}$$

Equation 2.99

$[K]^{(e)}$ is the stiffness matrix and its terms are found by comparing the matrix form of the strain energy to the original expression (Equation 2.95, Equation 2.96, Equation 2.97 and Equation 2.98).

$$K_{ij}^{(e)} = \begin{cases} \frac{L_e}{R^4} \int_0^1 EI_{zz}(N_{m(i)} + N''_{m(i)})(N_{m(j)} + N''_{m(j)})d\eta & for\ \{i,j\} \in k_y \\[2mm] \frac{L_e}{R^2} \int_0^1 \left(EI_{yy}N_{\alpha m(i)}N_{\alpha m(j)} + GJ_t N'_{\alpha m(i)}N'_{\alpha m(j)} \right)d\eta & for\ \{i,j\} \in k_\alpha \\[2mm] \frac{L_e}{R^4} \int_0^1 \left(EI_{yy}N''_{m(i)}N''_{m(j)} + GJ_t N'_{m(i)}N'_{m(j)} \right)d\eta & for\ \{i,j\} \in k_z \\[2mm] \frac{L_e}{R^3} \int_0^1 \left(EI_{yy}N''_{m(i)}N_{\alpha m(j)} - GJ_t N'_{m(i)}N'_{\alpha(j)} \right)d\eta & for\ i \in k_z\ and\ j \in k_\alpha \\[2mm] 0 & for\ all\ other\ \{i,j\} \end{cases}$$

Equation 2.100

Equation 2.40 gives the expression of the kinetic energy of the ring element. By substituting Equation 2.73 to Equation 2.79, we can rewrite this expression as a function of the nodal velocities $\dot{u}_k$ and shape functions N_k.

$$T^{(e)} = \frac{1}{2}\int_0^{L_e} \rho[A(\dot{y}^2 + \dot{z}^2) + I_p\dot{\alpha}_r^2]ds$$

$$= \frac{L_e}{2}\int_0^1 \rho\left[A\left(\left\{\sum_{k=k_y} N_{m(k)}\dot{u}_k\right\}^2 + \left\{\sum_{k=k_z} N_{m(k)}\dot{u}_k\right\}^2\right) + I_p\left\{\sum_{k=k_\alpha} N_{\alpha m(k)}\dot{u}_k\right\}^2\right]d\eta$$

$$= \frac{L_e}{2}\int_0^1 \rho\left[A\left(\sum_{k_1=k_y}\sum_{k_2=k_y} N_{m(k1)}N_{m(k2)}\dot{u}_{k1}\dot{u}_{k2} + \sum_{k_1=k_z}\sum_{k_2=k_z} N_{m(k1)}N_{m(k2)}\dot{u}_{k1}\dot{u}_{k2}\right)\right.$$

$$\left. + I_p\sum_{k_1=k_\alpha}\sum_{k_2=k_\alpha} N_{m(k1)}N_{m(k2)}\dot{u}_{k1}\dot{u}_{k2}\right]d\eta$$

Equation 2.101

Like the strain energy, the kinetic energy is a bilinear form of the nodal velocities and can be rewritten as a matrix form:

$$T^{(e)} = \frac{1}{2}\{\dot{u}\}^{(e)^T}[M]^{(e)}\{\dot{u}\}^{(e)}$$

Equation 2.102

$[M]^{(e)}$ is the mass matrix. The terms of the mass matrix are found by comparing the bilinear form (Equation 2.101) to the matrix form of the kinetic energy.

$$M_{ij}^{(e)} = \begin{cases} L_e\int_0^1 \rho A N_{m(i)}N_{m(j)}d\eta & for\ \{i,j\} \in k_y\ or\ k_z \\ L_e\int_0^1 \rho I p N_{\alpha m(i)}N_{\alpha m(j)}d\eta & for\ \{i,j\} \in k_\alpha \\ 0\ for\ all\ other\ \{i,j\} \end{cases}$$

Equation 2.103

The work of external forces is now written as a function of the nodal displacements:

$$W^{(e)} = L_e\int_0^1 \left[f_r\sum_{k=k_y} N_{m(k)}u_k + f_z\sum_{k=k_z} N_{m(k)}u_k + m_t\sum_{k=k_\alpha} N_{\alpha m(k)}u_k\right]d\eta = \{u\}^{(e)^T}\{F\}^{(e)}$$

Equation 2.104

The terms of the load vector are the integration of the product between the cross section resulting forces and the shape functions

$$F_{ext,i}^{(e)} = \begin{cases} \displaystyle\int_0^{L_e} f_r N_{m(i)} \, ds & if \ i \in k_y \\[3mm] \displaystyle\int_0^{L_e} f_z N_{m(i)} \, ds & if \ i \in k_z \\[3mm] \displaystyle\int_0^{L_e} m_\theta N_{\alpha m(i)} \, ds & if \ i \in k_\alpha \end{cases}$$

Equation 2.105

The Euler-Lagrange equation yields the finite element equation of motion

$$[M]^{(e)}\{\ddot{u}\}^{(e)} + [K]^{(e)}\{u\}^{(e)} = \{F_{ext}\}^{(e)} - \{F_{initial}\}^{(e)}$$

Equation 2.106

2.6. Assembly of finite element matrices

To obtain the finite element equations for the complete ring, stiffness matrices and load vectors of ring elements are assembled. An example of matrix assembly for two ring elements is given.
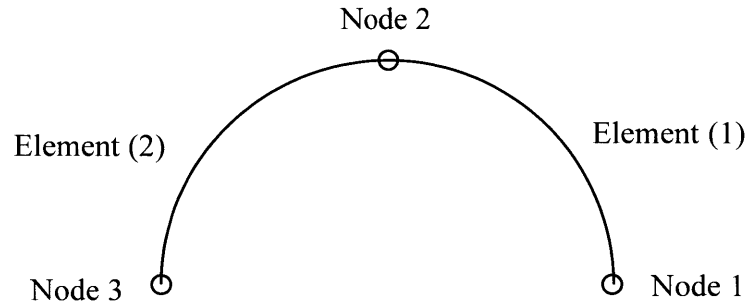
Figure 28 Ring Mesh with Two Elements

The ring mesh in this example has two elements and three nodes. Element (1) and element (2) share node 2. For element (1), we have a displacement vector:

$$\{u\}^{(1)} = \left\{u_1^{(1)}, u_2^{(1)}, \dots, u_{15}^{(1)}, u_{16}^{(1)}\right\} = \{y_1, y_1', y_1'', z_1, z_1', z_1'', \alpha_1, \alpha_1', y_2, y_2', y_2'', z_2, z_2', z_2'', \alpha_2, \alpha_2'\}^T$$

Equation 2.107

For element (2), we have the second displacement vector:

$$\{u\}^{(2)} = \left\{u_1^{(2)}, u_2^{(2)}, \dots, u_{15}^{(2)}, u_{16}^{(2)}\right\} = \{y_2, y_2', y_2'', z_2, z_2', z_2'', \alpha_2, \alpha_2', y_3, y_3', y_3'', z_3, z_3', z_3'', \alpha_3, \alpha_3'\}^T$$

Equation 2.108

The superscript (k) refers to the element k and the subscript i of y, z and α refers to node i. As shown in previous section, for each element we have a stiffness matrix and we write it into 4 sub-matrices form:

$$[K]^{(1)} = \begin{bmatrix} K_{11} & K_{12} \\ K_{12} & K_{22}^{(1)} \end{bmatrix}$$

Equation 2.109

$$[K]^{(2)} = \begin{bmatrix} K_{22}^{(2)} & K_{23} \\ K_{23} & K_{33} \end{bmatrix}$$

Equation 2.110

In the ring finite element model proposed in this thesis, there are 8 degrees of freedom per node (Equation 2.36), hence the element stiffness matrix is of dimension [16x16] and K_{11} is an [8x8] matrix. The half ring has 3 nodes and 24 nodal displacements, the global stiffness matrix $[K]$ is obtained by assembling $[K]^{(1)}$ and $[K]^{(2)}$

$$[K] = \begin{bmatrix} K_{11} & K_{12} & 0 \\ K_{12} & K_{22}^{(1)} + K_{22}^{(2)} & K_{23} \\ 0 & K_{23} & K_{33} \end{bmatrix}$$

Equation 2.111

When assembling the element matrices the contributions of both elements to the stiffness in node 2 are summed. The same process is used to assemble the global load vector. The finite element equations of motion can now be written with the global matrices

$$[M]\{\ddot{u}\} + [K]\{u\} = \{F_{ext}\} - \{F_{initial}\}$$

Equation 2.112

The global displacement vector $\{u\}$ is the assembly of the nodal displacement vectors.

$$\{u\} = \{u^{(1)}, u^{(2)}, \dots, u^{(i)}, \dots, u^{(n-1)}, u^{(n)}\}^T$$

Equation 2.113

2.7. Conclusion

Most of the formulation for the top two rings is the same as the TLOCR model developed by Baelden except an additional step closing the ring. Unlike TLOCR, top two rings have free shapes at their free state, which have several millimeters displacement with respect to the radius of the nominal bore. Thus, the small displacement assumption in Baelden's thesis is not applicable any more. In order to solve this

issue, an intermediate state is added that a single piece ring is closed at its nominal radius with a preload. This intermediate state is the initial state for the calculation of the single piece ring dynamics and static analysis. When the ring is at its nominal radius and deforms inside the cylinder, the displacement with respect to the reference point (a ring centered in the piston groove and contacting a perfectly round cylinder) is small compared to the bore radius. Therefore, the small displacement assumption becomes applicable again.

The curved beam finite element method and the momentum equation, Equation 2.112, provide a numerical framework for the study of ring performance. Ring statics, ring dynamics and ring-liner lubrication models were developed based on this equation with different boundary conditions and sub-models.

3. Ring Static Analysis

In the last chapter, we have extended the curved beam finite developed by Baelden for the TLOCR [44] [45]. To derive the finite element equations for top two rings, we developed a method to handle large displacement from the free shapes of top two rings to their nominal radius.

As shown in Liu [41] [43] [53], many useful analyses can be conducted without involvement of ring dynamics such as free-shape and contact force distribution relations, ring interaction with a distorted bore (commonly called conformability analysis), ring-liner and ring-groove interaction with elevated gas pressures. Similar approach was carried out with the current model. In this chapter, a comprehensive analytical tool based on the curved beam finite element method is presented, which calculates the ring free shape, evaluates the ring-liner and ring-groove conformability under different boundary conditions and studies the relation between local contact behavior and global structural deformation. The advantage of the current model enables different force generation mechanisms along the circumference handled with their own length scale and at the same time keeps accuracy of structural response of ring elements with enough flexibility.

3.1. Top Two Rings' Free shape Calculation

A single piece ring's free shape is an important parameter. In practice, ring designers need to determine the geometry of the ring free shape to reach a desired ring tension and force distribution when the ring is closed to the bore diameter. Currently this process largely relies on internal proprietary formula and experience. Here we developed a straightforward routine to determine the free-shape with known force distribution.
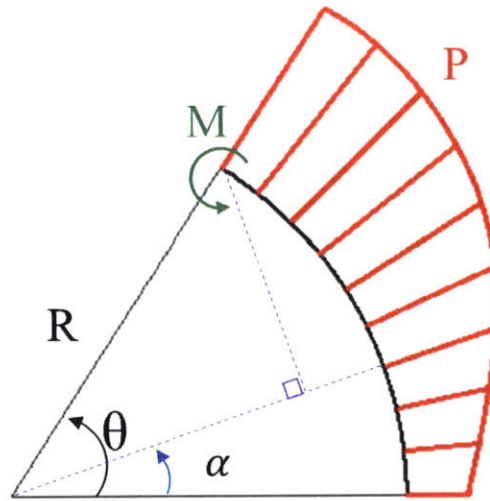
Figure 29 Relation between Bending Moment and Contact Pressure

The bending moment is calculated from the ring gap ($\theta = 0$) which is a free end without internal and external stress. The calculation of the bending moment at angular position θ is shown below:

$$M(\theta) = \int_{0}^{\theta} PR^2 sin(\theta - \alpha)d\alpha$$

Equation 3.1

As shown in Figure 29, P is the desired contact pressure distribution when ring is closed at its nominal round shape. R is the ring nominal radius and α is the angle swiping from 0 to θ.

Figure 30 Ring Differential Element Position Change

The curvature of the ring free shape can be calculated using Equation 2.9Equation 2.7, $\kappa_{fs}(\theta) =$

$\frac{r_{fs}^2 + 2r_{fs}'^2 - r_{fs}r_{fs}''}{\left(r_{fs}^2 + r_{fs}'^2\right)^{3/2}}$, where r_{fs} is the radius of the ring free shape. The ring is closed from its free shape to

the round shape under the given pressure distribution $P(\theta)$. The curvature change can be related to

bending moment using Equation 2.43. Another issue we need to address is that when the ring is closed

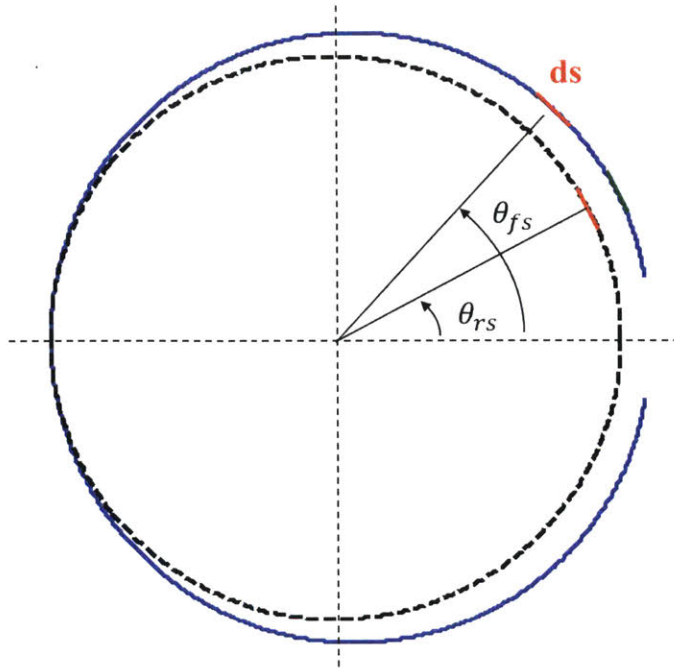from its free shape to the round shape, the element ds of the ring changes its angular position from θ_{fs}

to θ_{rs} (as shown in Figure 30). As a result, the calculation of the curvature change needs to be applied to

a specified ring differential element ds instead of a specified angular position θ.

$$\kappa_{fs}(s) = \frac{1}{R} - \frac{M(s/R)}{EI}$$

Equation 3.2

s is the arc length of the ring and ds is the ring differential element. The differential equation between

angular position θ and the arc length s can be found by simplifying Equation 2.7.

$$ds = \sqrt{r_{fs}^2 + r_{fs}'^2}\, d\theta$$

Equation 3.3

57

By combining Equation 2.9, Equation 3.1, Equation 3.2 and Equation 3.3, we should be able to solve the ring free shape numerically with three boundary conditions that $r_{fs}(\theta = 180°) = R$, $\frac{dr_{fs}}{ds}(\theta = 180°) = 0$ and $\frac{d\theta}{ds}(\theta = 180°) = \frac{1}{R}$.

Then let's look at an example. In this calculation, the bore diameter is set to be 82.51mm and the desired contact pressure distribution is uniform along the circumferential direction with a value of $242.4N/m$ (10N tangential force, F_t). The ring is divided into 32 elements. The ring cross section and its parameters are shown below. The centroid of the cross section is at the center. The nominal radius of the ring neutral axis equals the bore radius minus half of the ring width. The calculated value is 39.755mm.
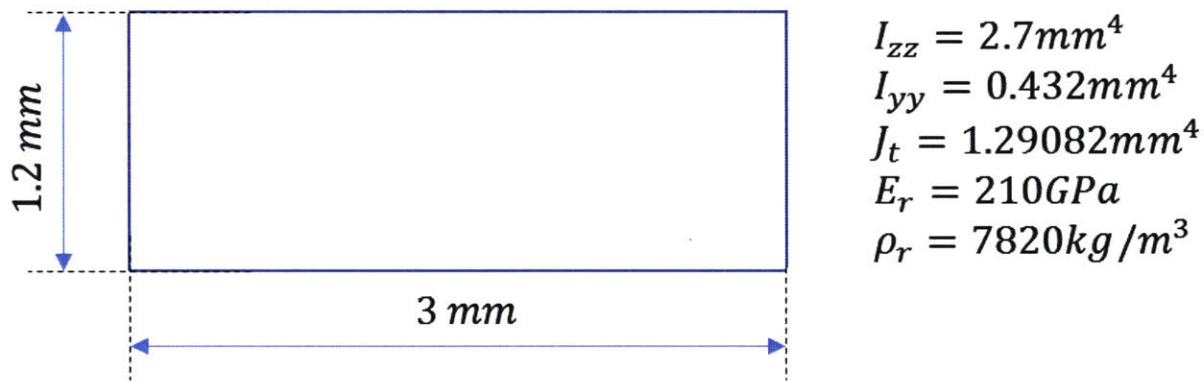

$$I_{zz} = 2.7mm^4$$
$$I_{yy} = 0.432mm^4$$
$$J_t = 1.29082mm^4$$
$$E_r = 210GPa$$
$$\rho_r = 7820kg/m^3$$

Figure 31 Ring Cross Section and Its Parameters

Figure 32 shows the results of this example. The first plot is the radius of the free shape along the circumferential direction, the second plot is the curvature and the third plot shows the comparison between the ring neutral axis (red curve) and the nominal round shape (black dashed line). At free shape, the ring leaves a gap such that it can be closed and assembled into piston. In this example, the ring free gap is 10.1mm. The gap can be seen as the source of the ring expansion force. The larger the gap is, the higher expansion force the ring will have when closed to its round shape. The ring is symmetric around the angular position of 180°. Therefore, this point can be seen as a fixed end and at this position the ring internal moment is at its highest value and the curvature reaches its minimum. Conversely, the ring gap is a free end because it does not have any constraint from the other side. Thus, the internal stress is zero and the local curvature should be the same as the curvature of the nominal round shape. In this case, this value equals $\frac{1}{R} = \frac{1}{39.755mm} = 0.02515 \ /mm$.

The last plot is the actual contact pressure distribution when the ring is assembled into a round bore. This distribution is expected to be uniform because the free shape is calculated from a uniform contact pressure distribution. The result shows that most part of the ring has uniform contact pressure, but around the ring gap the pressure is concentrated. The explanation is that unlike other part of the ring, the ring gap does not have constraint from the other side, and under the action of expansion force, the ring gap tends to expand more which leads to higher contact pressure from the cylinder.
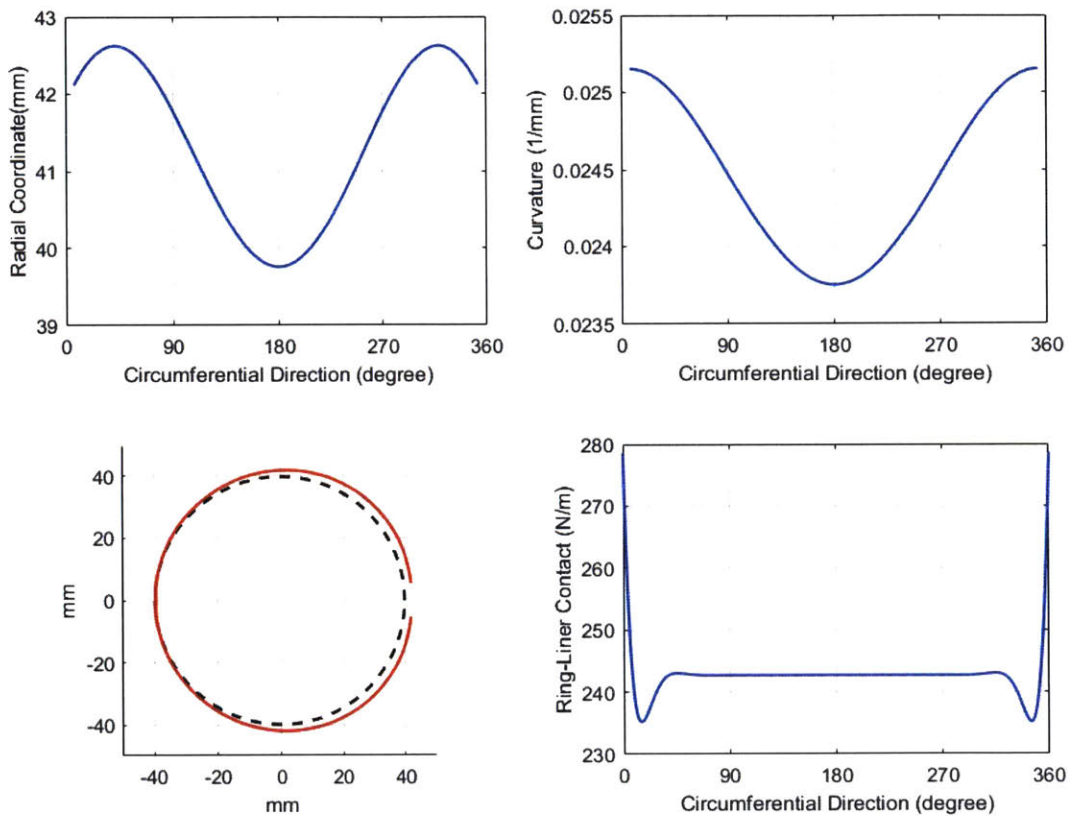

Figure 32 Results of Ring Free Shape Calculation

3.2. Model Development

We can derive the governing equation for ring static analysis from Equation 2.112. Ring static analysis, as its name suggests, neglects dynamic terms and focuses on static structural response. By omitting the time derivative term, we have:

$$[K]\{u\} = \{F_{ext}\} - \{F_{initial}\}$$

Equation 3.4

Stiffness matrix $[K]$ and initial load vector $\{F_{initial}\}$ can be calculated and assembled from Equation 2.100 and Equation 2.83 to Equation 2.85 respectively. Now we need to calculate the external load vector $\{F_{ext}\}$ from Equation 2.105. Figure 33 demonstrates the forces that are included in the ring statics model. Some of them are not static force but are generated due to piston or ring relative motion. The purpose of including the dynamic forces is to provide more insights into ring performance. Gas pressure of piston upper land, groove and piston lower land can be set as boundary conditions, which makes it possible to study the effect of gas pressure on ring-liner and ring-groove conformability. Groove interaction provides the constraint in axial direction such that ring cannot deform freely but to adapt to groove geometry. Groove interaction is composed of two parts. The first one is asperity contact and the second one is the hydrostatic pressure force which is caused by the gas pressure difference at two ends. Ring-liner interaction provides another constraint in radial direction such that ring's deformation adapts to cylinder geometry. Ring-liner interaction includes contact force in normal direction and friction force in axial direction. Liner contact is the sum of asperity contact and hydrodynamic pressure. Hydrodynamic pressure is from the relative motion between ring and liner on a thin lubricant film. This force is actually a dynamic one but it can help study the local contact behavior more thoroughly. The friction force is composed of asperity contact friction and hydrodynamic shear stress. Inertia force could be also applied in this model. Inertial force is caused due to piston acceleration and deceleration.
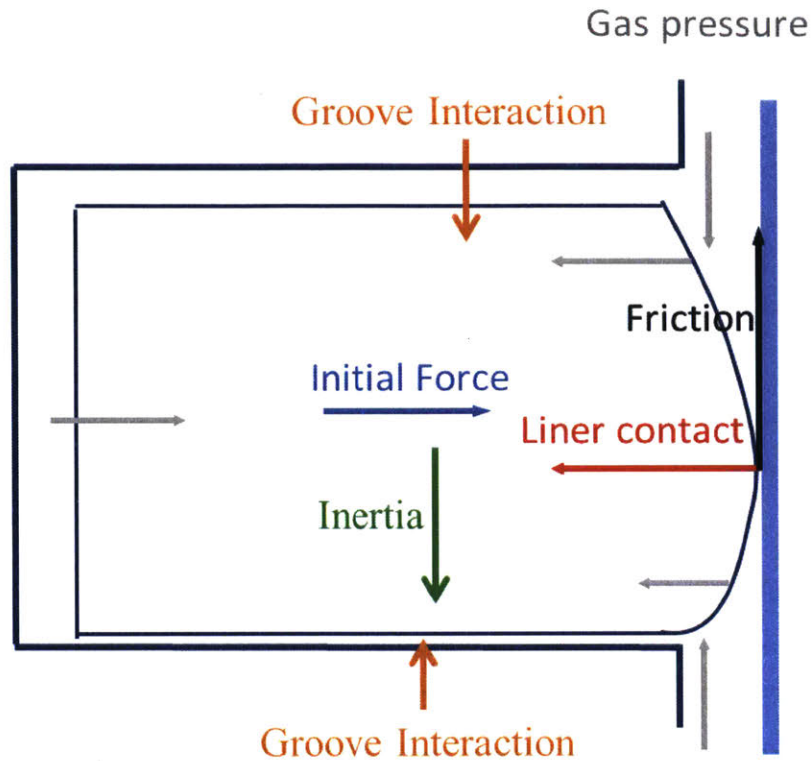
Figure 33 Force Analysis of Ring Cross Section

The calculation of these forces will not be included in this section. Instead, readers can find the details in Chapter 4 and Chapter 5.

3.3. Conformability Calculation

In this section, we are going to show calculation results of the ring statics model and a comparison to the straight beam finite element model. In the calculation, the bore diameter is set to be $133mm$, the ring tension is 32N and the desired contact pressure distribution is uniform along the circumferential direction. The ring cross section geometry and its parameters are shown in Figure 34. In some of the calculation, the bore is distorted with

0th order: $185.6\mu m$;

2nd order: $18.4\mu m$;

3rd order: $12.4\mu m$;

4th order: $5.5\mu m$.
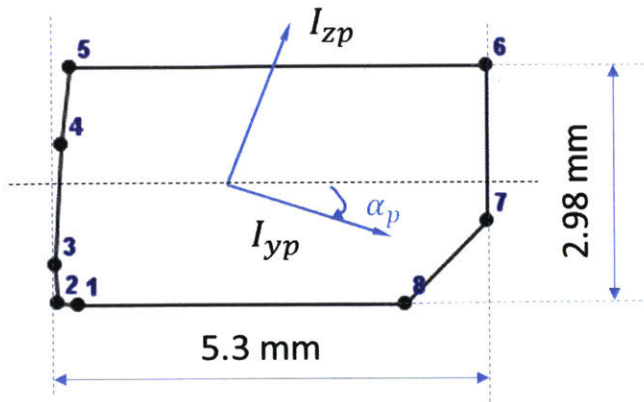
$$E_r = 152.3 \, GPa$$

$$Bore = 133 \, mm$$

$$I_{zp} = 32.5639 \, mm^4$$

$$I_{yp} = 10.5973 \, mm^4$$

$$Principal \; Angle = -4.66961°$$

$$Ft = 32.18 \, N$$

Figure 34 Ring Cross Section and Bore Distorsion

Figure 35 shows the results. The left hand side plots show the results for round bore and the right hand side plots show the results for distorted bore. The blue lines represent the results calculated from the curved beam finite element ring statics model (CBM) and the green dash lines represent the results from the straight beam finite element ring statics model (SBM) that was developed by Liu [43]. Since the desired contact pressure distribution is uniform, we are expecting a roughly uniform ring-liner contact force distribution from the model results. For round bore, the top left plot shows that both models provide very uniform pressure distribution from ring-liner interaction except for the gap area, which matches our expectation. At the angular position of 180°, the pressure calculated by CBM is still uniform but the result of SBM has a sudden drop. It is difficult to find a physical explanation. However when comparing the difference between the curved beam finite element method and the straight beam finite element method, we realize that the shape function that CBM uses guarantees the continuity of second derivative of displacement and the separation of structural mesh and contact grid, which help it reach sufficient calculation accuracy with only few long ring elements (16 elements), but SBM needs more ring elements (377 elements) with much smaller element length. The element size of SBM reaches a level that the dimension of the cross section of the beam element is comparable to the length of the beam element. The structural deformation of the ring elements is solved based on the beam theory with an assumption that the length of the beam should be much larger than the dimension of its cross section. Thus, SBM starts to lose its accuracy of structural response as the length of its beam elements reduces.

For distorted bore, the bore is not round, so the contact pressure is no longer uniform. Both models give very close results and they all follow the geometry change of the cylinder.

The ring twist results from both models are very similar. The negative ring twist means that ring ID is higher than ring OD. CBM also shows that the ring neutral axis lifts around gap area and then falls down. It actually matches the industry experience with this kind of tapper faced ring that has negative principal angle.
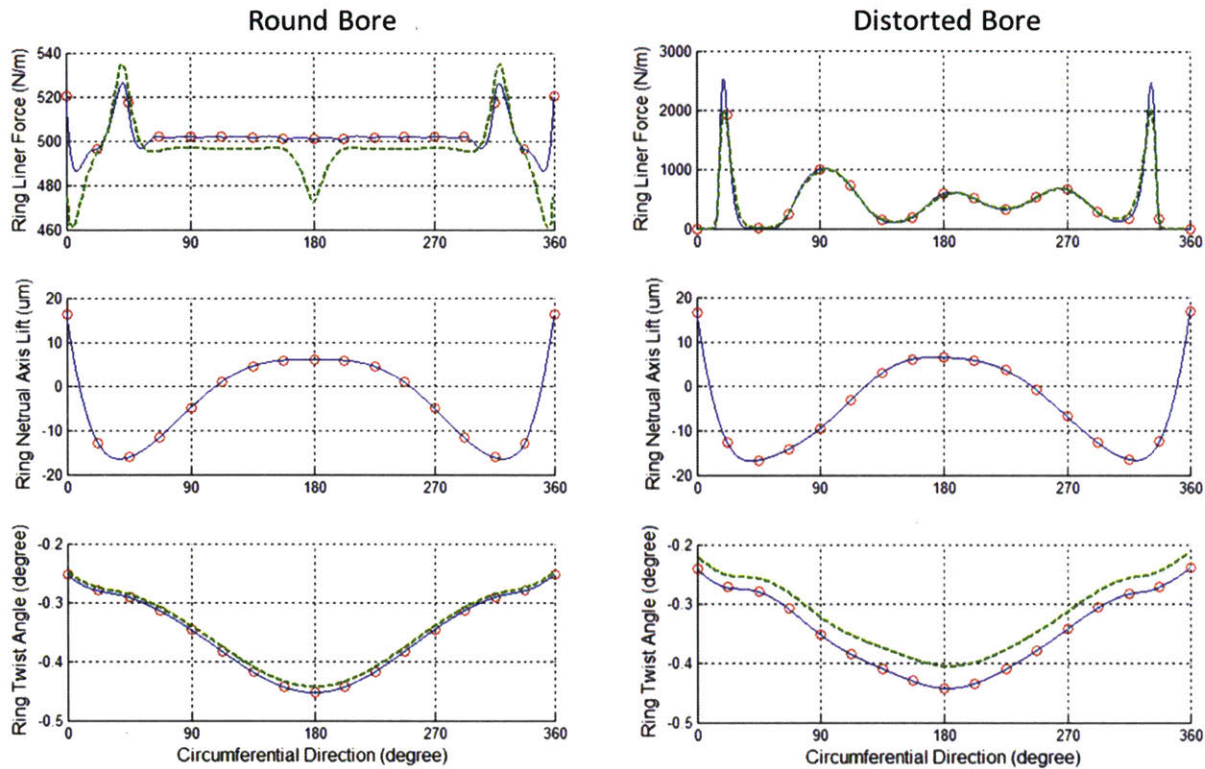

Figure 35 Comparison between Curved Beam Model (Blue Curves) and Straight Beam Model (Green Dashed Curves)

3.4. Ring In-Plane Structural Conformability with Different Normal Load

The ring statics model is a powerful tool to study ring-liner conformability. In a typical passenger car engine, thermal and mechanical stress causes bore distortion on the order of $100\mu m$. The stiffness prevents the ring from changing its shape rapidly, so sometimes the ring has difficulty conforming to higher order bore deformation. From ring design point of view, the conformability can be changed by changing the stiffness of the ring (cross section, Young's modulus) as well as the free shape. During engine operation, the top two rings are surrounded by changing gas pressures and these pressures can greatly influence the ring conformability. In this section, we are going to use our curved beam finite element statics model to study the effects of bore distortion, normal load and stiffness on ring-liner conformability.

Several studies of ring conformability were conducted. Mueller [24] developed an analytical criterion (Equation 3.5) to calculate the maximum admissible bore distortion for a given gapless ring configuration without losing contact with the liner. A_n^{max} is the maximum acceptable amplitude of bore distortion for order n, F_t is the ring tension, R is the bore radius, E is the Young's modulus of the ring and I is the area moment of inertia of the ring cross section along the cylinder axis

$$A_n^{max} = \frac{F_t R^3}{EI(n^2 - 1)^2}$$

Equation 3.5

Tomanik proposed another conformability criterion (Equation 3.6) based on experimental measurements of ring conformability limits [31]. This limit mainly reflects the conformability between the ring and the liner at the ring end gap.

$$A_n^{max} = \frac{F_t R^3}{20EI(n^2 - 1)}$$

Equation 3.6

Both criteria try to answer the question that given a ring configuration, what the maximum admissible bore distortion is. However, in automotive industry the reduction of bore distortion may be more expensive. Thus, engineers sometimes prefer asking the question that given a bore distortion, what the best combination of ring tension and stiffness is.

To answer this question, we are going to show the relation between relative maximum ring-liner clearance ($\frac{h_{max}}{y_b}$) and a dimensionless number, conformability score ($\frac{f_n (R/n)^4}{EI y_b}$). h_{max} is the maximum ring-liner clearance along the circumferential direction (excluding the gap area, as shown in Figure 35), y_b is the magnitude of bore radial distortion at nth Fourier order, f_n is the normal force (including ring tangential force and gas pressure force) per unit length. R, E and I were defined above.
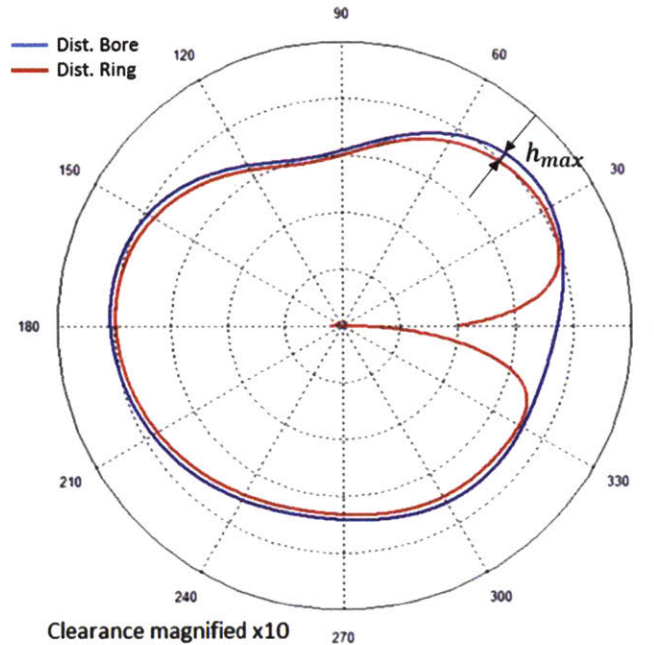
Figure 36 Maximum Clearance between Ring and Distorted Bore

In the calculation, since we are only interested in in-plane structural conformability, a rectangular single piece ring and a twin-land oil control are used (as shown in Figure 37). The single piece ring has a free shape designed to have uniform pressure distribution at a round shape with a ring tension of 10N and the twin-land oil control ring has several ring tensions of 5N, 7.5N, 10N, 15N, 20N and 30N. Gas pressure is also applied to provide extra normal force to the single piece ring. The pressure set-up is shown in following Table 3.1. P_u is the upper land pressure, P_i is the ring groove pressure and P_d is the lower land pressure (as shown in Figure 38).
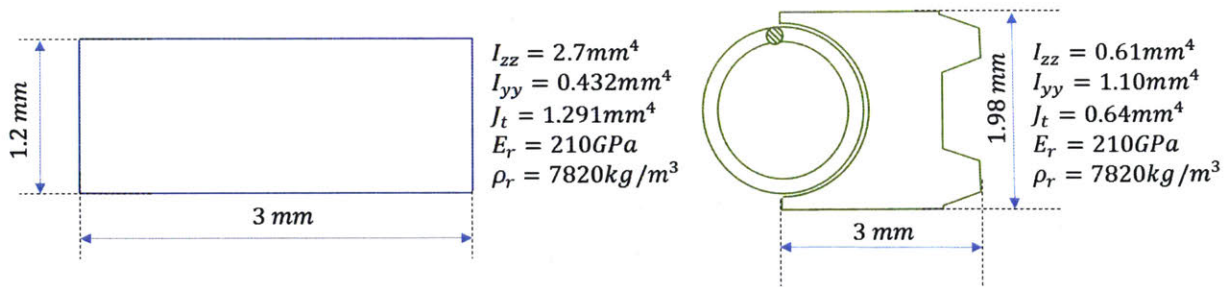

$I_{zz} = 2.7mm^4$
$I_{yy} = 0.432mm^4$
$J_t = 1.291mm^4$
$E_r = 210GPa$
$\rho_r = 7820kg/m^3$

$I_{zz} = 0.61mm^4$
$I_{yy} = 1.10mm^4$
$J_t = 0.64mm^4$
$E_r = 210GPa$
$\rho_r = 7820kg/m^3$

Figure 37 Ring Geometry

Table 3.1 Pressure Set-up

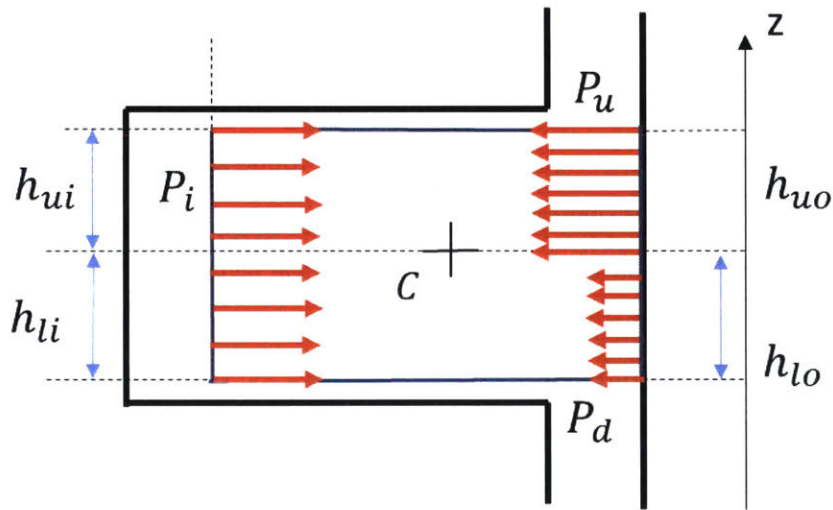| Pu(bar)	Pi(bar)	Pd(bar)
1	1	1
5	5	1
10	10	2
20	20	5
40	40	10
70	70	12

Figure 38 Gas Pressure around a Single Piece Ring

Figure 39 shows the calculation results. The grey, orange, green, red and blue markers represent the results with bore distortions of $2\mu m$, $5\mu m$, $10\mu m$, $15\mu m$ and $20\mu m$ correspondingly. The round, rectangular, cross, triangle, square and diamond shape markers represent the results with bore distortion of 3rd order, 4th order, 5th order, 6th order, 7th order and 8th order. Thus, in this figure red rectangular markers tell how ring-liner maximum relative clearance ($\frac{h_{max}}{y_b}$) changes with different normal loads (included in the dimensionless number, conformability score, $\frac{f_n(R/n)^4}{EIy_b}$) at 4th order bore distortion with a magnitude of $15\mu m$. As we can see, when using these two dimensionless numbers, the

66

results with different orders and magnitudes of bore distortion can almost collapse to a single curve. This implies that the conformability score can be treated as a measurement of the conformability between the ring and the distorted bore, which can be improved by increasing normal load and bore diameter, as well as by reducing bore distortion order, bore distortion magnitude and ring stiffness. From the figure, we can see that when the relative ring-liner clearance is large, the relative clearance is proportional to the conformability score. It is because in this region the ring does not conform to the bore at the structural level and the maximum ring-liner clearance is determined by ring structural deformation that is reflected by this dimensionless number $\frac{f_n(R/n)^4}{EIy_b}$. However, when the maximum relative clearance is small, the relative clearance is almost flat with the conformability score. It is because in this region the ring conforms to the liner almost everywhere and the maximum ring-liner clearance is determined by their contact behavior that is mostly determined by ring profile and the contact model we choose. Neither of them is included in this dimensionless number.

◆ 8th ■ 7th ▲ 6th ✖ 5th ━ 4th ● 3rd

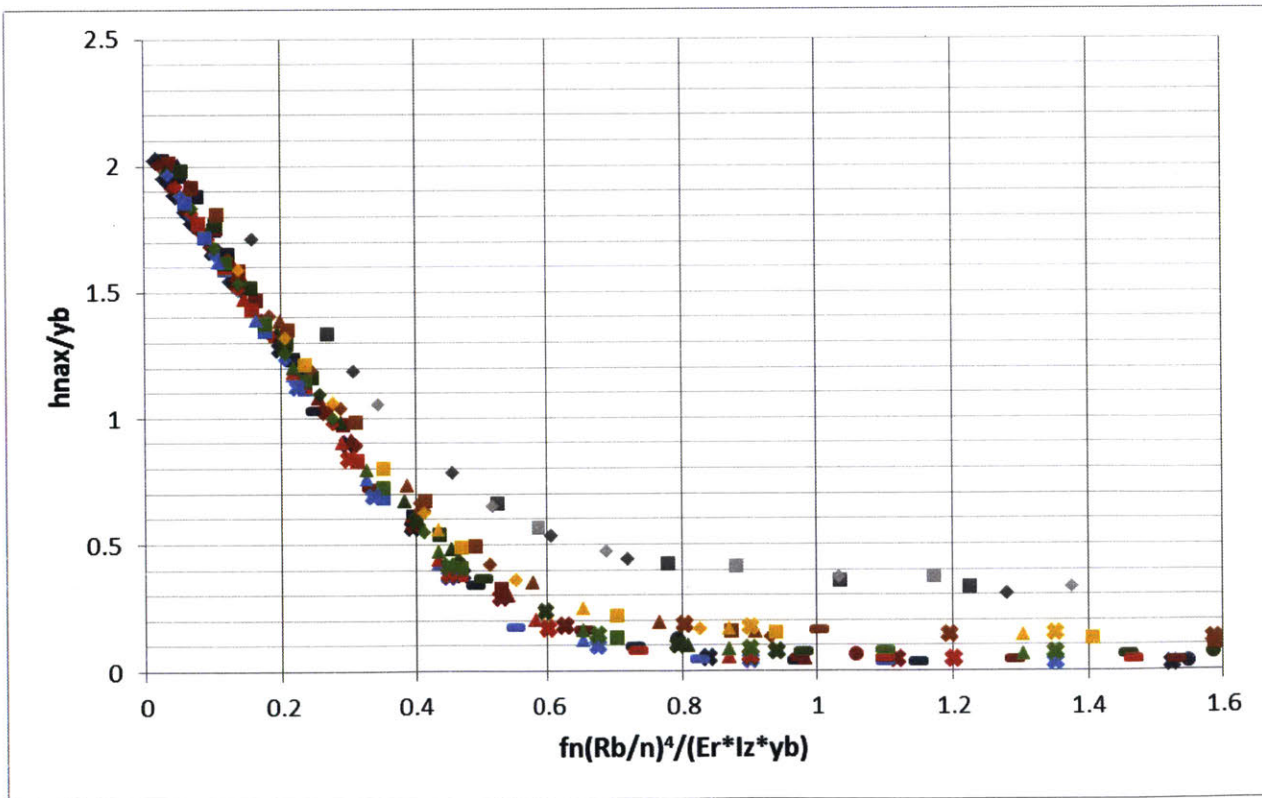━ $20\mu m$ ━ $15\mu m$ ━ $10\mu m$ ━ $5\mu m$ ━ $2\mu m$

Figure 39 Ring-Liner Conformability Results

Since the stiffness of the OCR is smaller than the top ring, the OCR tends to have better conformability to the bore. However, when the surrounded pressure is lifted in the compression and expansion strokes, the conformability of the top ring to the bore may exceed that of the OCR, as shown in Figure 40. Y-axis is the liner axis with positive direction pointing downwards and 0 is the TDC of the top ring. X-axis is the ratio of the conformability score of the top ring to the OCR. The blue line marks the TDC of the OCR. The result is from a SI-engine running condition with full-load and peak cylinder pressure of 90bar. The dark blue, green, red and light blue curves represent the results of the intake, compression, expansion and exhaust strokes correspondingly. In the early expansion stroke, the top ring has higher conformability score than the OCR which means that in this region the top ring has better structural conformability to the bore than the OCR. This implies that the OCR must conform to the bore in this area; otherwise the top ring will scrape the oil from the liner to either 2nd land or crown land, which may easily contribute to oil consumption.
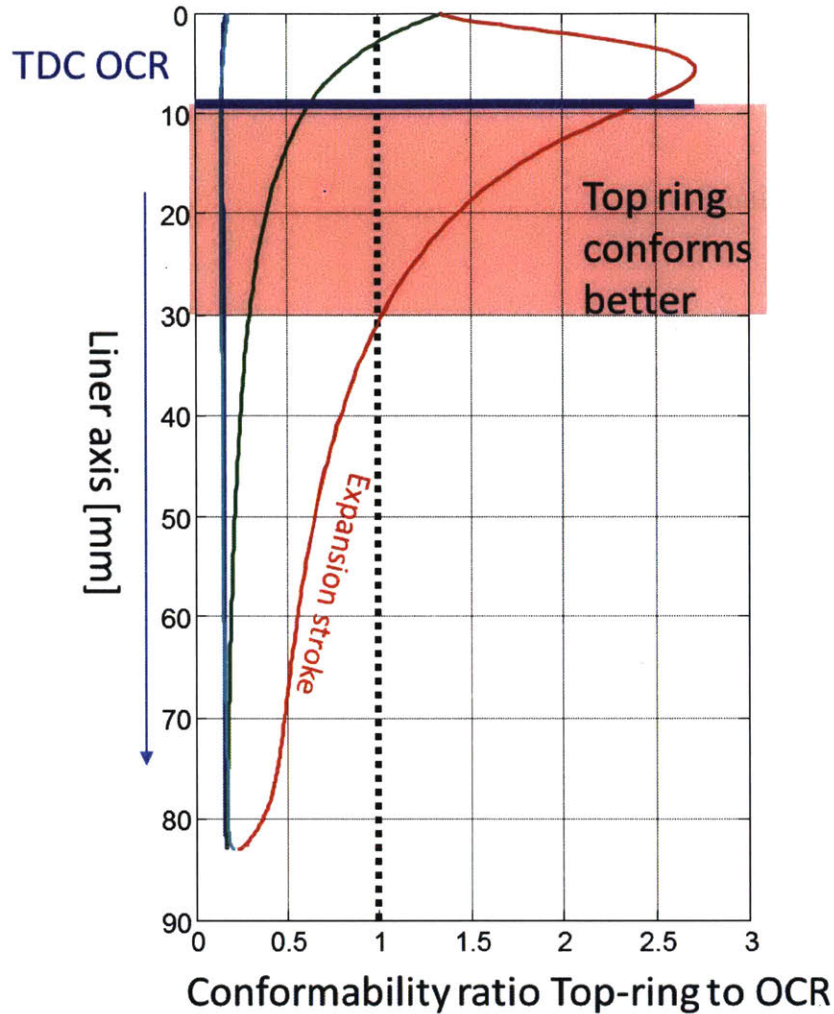
Figure 40 Conformability Ratio of Top Ring to OCR

3.5. Relation between Local Contact Behavior and Global Structural Behavior

Global and local behavior can be coupled at their corresponding length scales using the curved beam finite element method by separating structural mesh and contact grid. In this section, we will examine their relationship and demonstrate the necessity of this approach.

Global behavior is referred as ring structural response under the effects of bore distortion, piston tilt and gas pressure. Local behavior mainly represents the local contact change with different boundary conditions such as bridging and lube-fuel interaction. In this section, bore distortion and bridging are used to represent global and local processes correspondingly.

The ring used in the calculation is a typical top ring configuration with its geometry and parameters shown in Figure 41. The ring gap is located at the thrust side. The bore has a diameter of 82.51mm and is distorted with:

0th order distortion $\sim 100 \mu m$;
2nd order $\sim 10 \mu m$;
4th order $\sim 5 \mu m$.

The bore distortion is also shown in Figure 41. Bridging may happen around the bottom dead center during the intake and the expansion strokes and around the top dead center during the compression and the exhaust strokes. It brings oil from the piston to the liner by inertial force and viscous force, causing local oil supply to the top two rings fully-flooded. Bridging is a result of local oil accumulation on the piston lands and its range varies from sub-millimeters to tens of millimeters [15] [16] [18] [20].
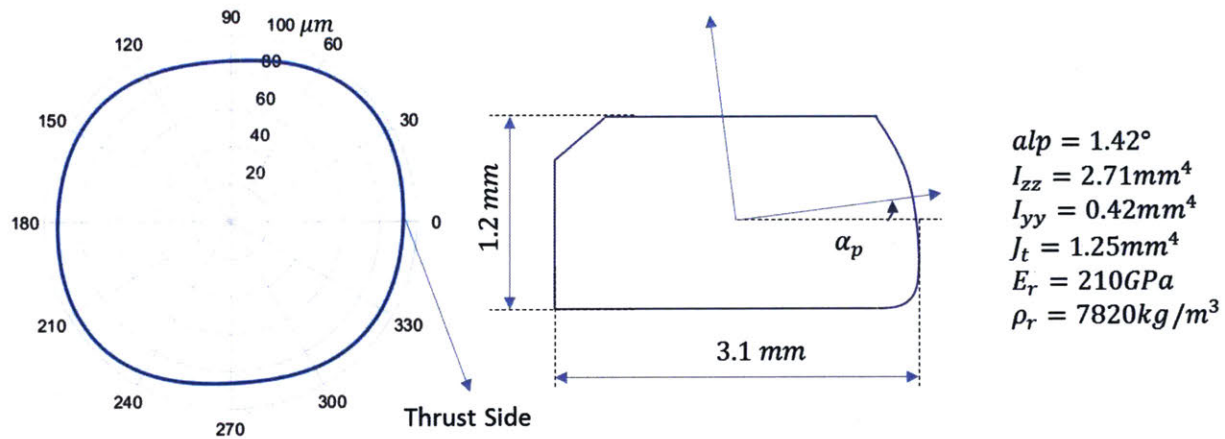

$$alp = 1.42°$$
$$I_{zz} = 2.71mm^4$$
$$I_{yy} = 0.42mm^4$$
$$J_t = 1.25mm^4$$
$$E_r = 210GPa$$
$$\rho_r = 7820kg/m^3$$

Figure 41 Bore Distortion and Ring Geometry

Figure 42 shows the ring static analysis results with different boundary conditions of oil supply. The blue curves (No Bridging) represent the results that the oil supply to the ring is well controlled to sub-micron level and is partially flooded. The red curves (Bridging with 20 degree) represent the results that have bridging centered at 90 degree away from the thrust side with the widths of $20°$ in the circumferential direction. The oil supply to the ring is fully flooded within the bridged area and is controlled to sub-microns outside of the bridged area. The yellow curves represent the results that the oil supply is fully-flooded everywhere along the circumferential direction. From the top to bottom, from the left to right, the plots show the results of the ring neutral axis displacement in the radial direction (relative to the nominal bore radius) y_r, the ring neutral axis displacement in the axial direction (relative to the center position in the ring groove) z_r, the ring cross section twist, α_r, the ring-liner minimum clearance, h_{min}, and the ring-liner force distribution f_l correspondingly. The first three plots reflect the

ring structural response and the last two reflect the ring-liner local contact behavior. The definition of the ring-liner clearance h_{min} is shown in Figure 43.

The ring neutral axis displacement in the radial direction has two global maximum points around 45° and 225°, corresponding to the 2nd order bore distortion and 2 local maximum points around 140° and 320°, corresponding to the 4th order bore distortion. Since there is no piston tilt and groove distortion, the ring neutral axis deformation in axial direction and the ring cross section twist are mainly caused by ring internal stress. In the plot of ring-liner minimum clearance, one can clearly see how the ring structural response affects its local contact behavior. 4 peaks of ring-liner minimum clearance can be found corresponding to the 4th order bore distortion. The reason why the 2nd order bore distortion is not reflected here is that compared to the 4th order bore distortion, it is much easier for the ring to conform to the 2nd order bore distortion. When the ring boundary condition becomes fully-flooded, its hydrodynamic pressure generation ability increases, leading to higher ring-liner minimum clearance. Therefore, we can find a spike in the plot of ring-liner minimum clearance at the position where bridging happens. Since the ring conforms to the bore, the oil film thickness on the liner is still controlled to the roughness level though the oil supply is fully flooded. The contact force distribution seems to follow more closely to the trend of ring structural response but local process still makes a difference on the contact behavior. The force distribution without bridging and the force distribution with fully-flooded boundary condition almost fall to the same line corresponding to the ring structure deformation, though they have different ring-liner hydrodynamic behavior due to different oil supply. There exists a discontinuity of the force distribution due to the discontinuity of the oil supply and change of hydrodynamic model. The dry contact pressure model and hydrodynamic pressure model are very sensitive to the minimum ring-liner clearance at small oil film thickness. Thus big spikes are inevitable around the boundary of the bridging area. Because of stiffness, the ring neutral axis cannot change rapidly. At the boundary of the bridging area there is a narrow range that the ring loses contact with the liner, as shown in Figure 42. Once outside of the bridging area, the force distributions are very close to the results without bridging. The ring neutral axis radial deformation is affected by the existence of bridging as well but insignificantly. The effect of bridging stays locally. Once outside of the range of bridging, its effect decays very fast.
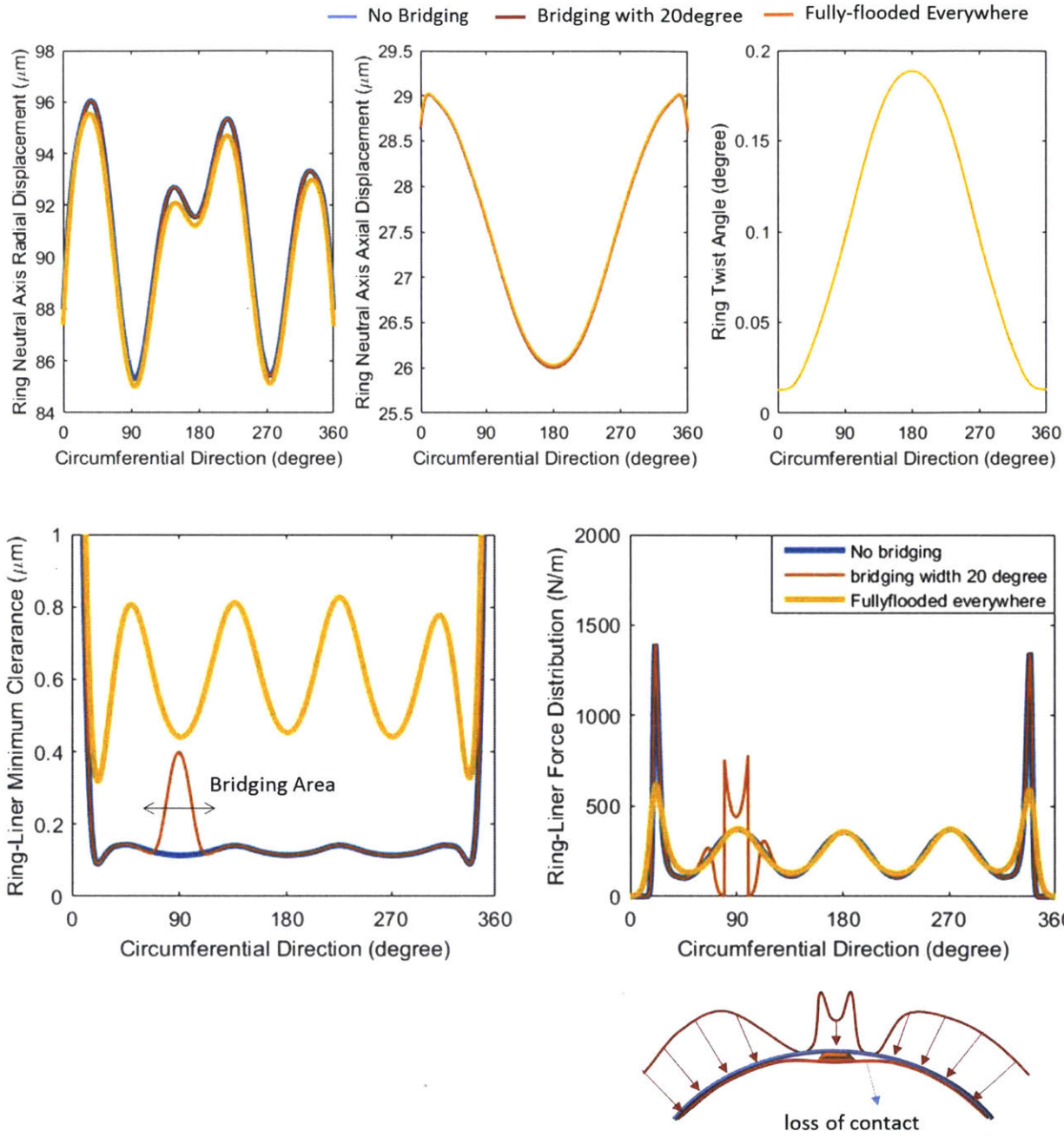
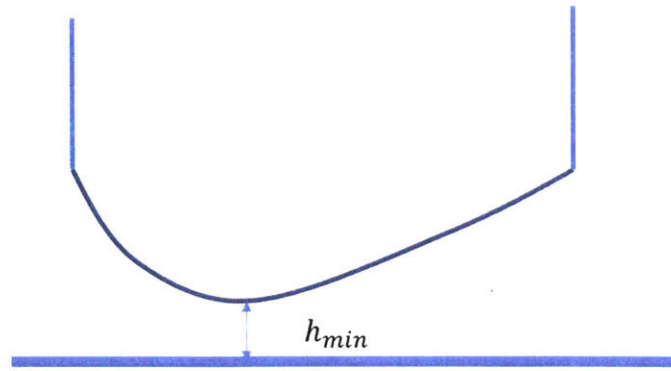*Figure 42 Ring Static Analysis Results with Different Oil Supply*

Figure 43 The Minimum Clearance between the Profiled Ring and the Liner

As we can see from the results that with uniform boundary conditions the local force and ring-liner clearance are largely determined by the ring structural response to the distorted environment. The reason is shown in Figure 44. The green curves represent the required force to deform a ring to a certain displacement and with the increase of the Fourier order of bore distortion the force that is required to deform the ring to the same magnitude increases. The blue and red curves represent the relation between the local pressure and the clearance. It is clear that the local pressure is more sensitive to the displacement of the ring neutral axis because when the ring neural axis changes by 1μm, the local clearance changes roughly by 1μm and the picture of the local pressure changes completely, but the required force to deform the ring almost stays the same. Thus, the ring-liner clearance and pressure distribution has to follow the trend of the structural response of the ring, and with given force distribution, the ring-liner clearance can be solved by a 1D model.
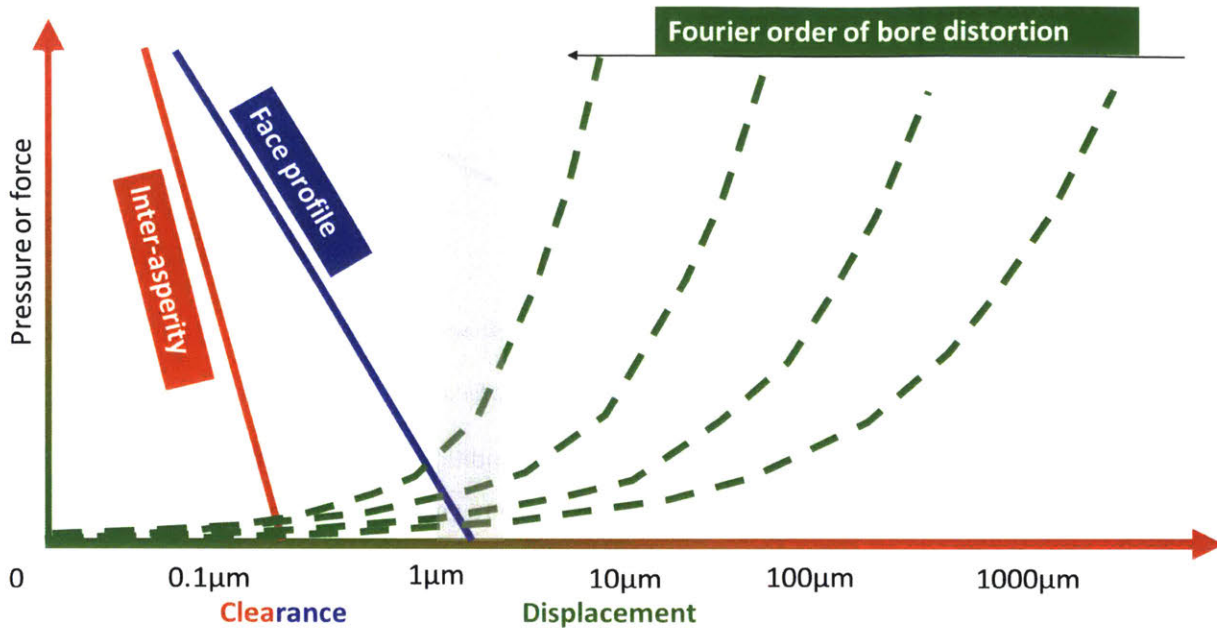
Figure 44 Relationship among Different Length Scales and Local Clearance

However, when the boundary condition is not uniform, the ring-liner clearance is determined by the combination of structure and local force generation. These different responses also reflect the stiffness of the ring. For instance, if the ring is completely flexible, the film thickness will respond as a 1D solution.

This static model can also help study the oil transfer caused by different conformability in the intake and compression strokes. Given a distorted bore shown in Figure 45, the top ring will have problem conforming to the bore in the intake stroke. However, in the compression stroke when the pressure is raised in the combustion chamber, the top ring is able to conform to the bore with the help of the pressure, as shown in Figure 46. In this case, if bridging happens around the angular position of 300° with a large ring-liner clearance, most of the bridged oil is allowed to pass the ring and a thick oil film is left on the liner during the intake stroke. Then, in the ensuing compression stroke the ring conforms to the liner and the ring-liner clearance decreases to sub-micron level though at this time the oil supply is fully-flooded. As a result, the thick oil film left on the liner in the intake stroke is scraped by the top ring to the crown land and is very likely to contribute to oil consumption.
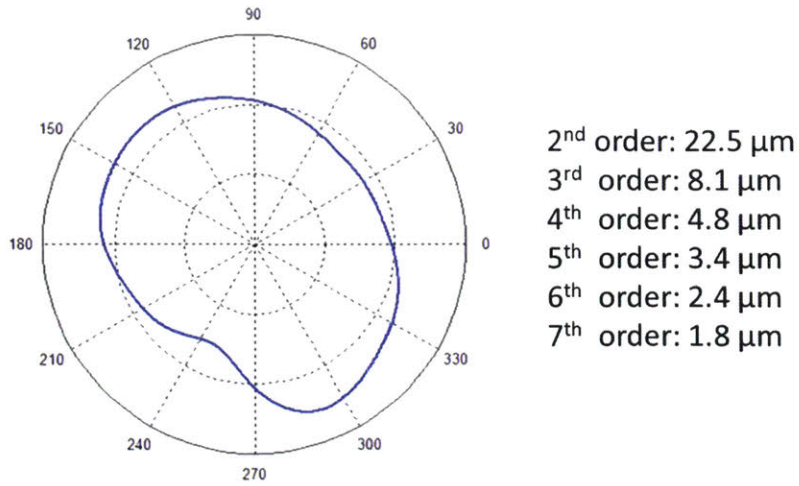
2nd order: 22.5 μm
3rd order: 8.1 μm
4th order: 4.8 μm
5th order: 3.4 μm
6th order: 2.4 μm
7th order: 1.8 μm

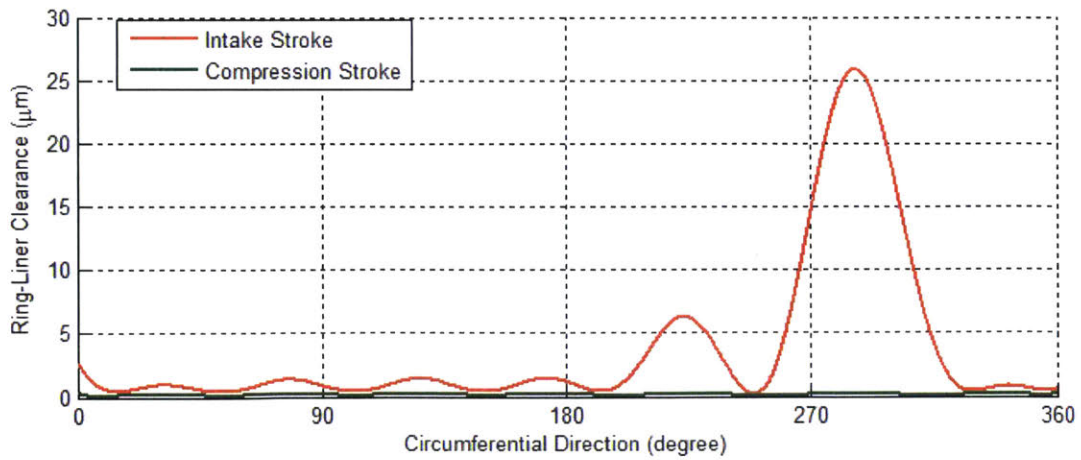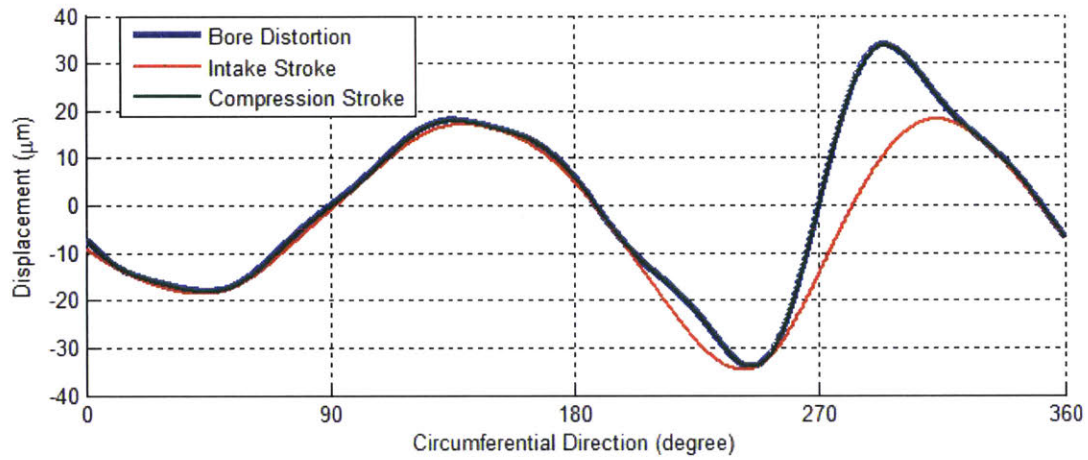*Figure 45 Bore Distortion up to 7th Order*

Figure 46 Difference of Conformability in the Intake and Compression Strokes

3.6. Conclusion

In this chapter, a ring statics model based on the curved beam finite element method was demonstrated. This is a comprehensive tool to analyze ring structural response and to study ring-liner and ring-groove conformability. By changing boundary conditions, this model is also able to help understand some local processes and its effect on ring-liner and ring-groove contact.

The results illustrate that the curved beam finite element method is able to give a reasonable prediction of ring structural response. The study of in-plane conformability shows that compared to top two rings, generally OCR is easier to conform to the distorted bore due to smaller stiffness and a more uniform normal load. The top ring may have better conformability to the liner around the top dead center during the compression and expansion strokes with the help of gas pressure. As a result, OCR should conform to the liner. Otherwise, the top ring, with the help of the cylinder pressure, can directly scrape the excessive oil left by the OCR to either crown or second land.

The curved beam finite element method also enables the ring statics model to study the global and local behaviors and the interaction between each other. The global structural response has a significant effect on the trend of the ring/liner and ring/groove contact behavior while the local process makes a difference to the oil supply and contact behavior locally. Oil transport varies along the circumferential direction and local oil accumulation is observed in the experiments [15] [16]. As a result, both of them need to be included to study oil transport around the ring pack system.

4. Modeling Ring Dynamics and Gas Pressure for the Whole Ring Pack System

The new ring dynamics model based on the curved beam finite element method has been developed and is demonstrated in this chapter. It is to simulate the piston ring pack dynamic behavior and inter-ring gas pressure in engine cycles. Its results could be used to analyze the performance of the ring pack system such as blow-by control and wear conditions between the ring and the groove and it also simulates the environmental conditions to model ring-liner lubrication which predicts oil transport around the ring pack system through the ring-liner interfaces.

In engine cycles, a variety of forces is applied to piston rings. (a) Initial force is caused by top two rings' strain energy change or OCR spring force, when they are closed and assembled into piston. (b) Gas pressure changes dramatically around the ring pack system and it applies pressure force on the piston rings. (c) Piston experiences acceleration and deceleration. As a result, when the piston is chosen as a reference frame, inertial force needs to be applied. (d) Ring-liner interfaces provide normal force and friction force on the piston rings. Since the purpose of this model is to calculate the ring dynamic behavior instead of lubrication, a simplified dry-contact model is used to calculate contact force between top two rings and the liner which is accurate enough for dynamics calculation. (e) Ring-groove interaction provides axial forces on the piston rings, which includes asperity contact, gas pressure from ring-groove gas flow, hydrostatic pressure and oil pressure due to squeezing. In the ring-groove interfaces, the oil film thickness is set to be constant to simplify the calculation.

Gas pressure plays an important role in the ring pack dynamic behavior but its value at the same time is dependent on the ring deformation as well. Thus, we need to couple the ring dynamics and gas pressure calculation in order to obtain reasonable results. In this model, we consider gas flow in the axial direction, the radial direction and the circumferential direction, through ring-groove interfaces, ring gaps, drain-holes of the OCR groove and ring-liner interfaces when the rings lose contact with the liner.

The ring dynamics model is built based on the curved beam finite element method. The advantage of this method is to separate grid sizes from structural analysis, contact force analysis and gas pressure analysis, which enables the model to capture both global and local phenomena at their proper length scales and differentiates it from straight beam finite element method.

4.1. Force Analysis in Ring Dynamics Model

In engine cycles, the piston rings have different forces applied. The first is initial force. When assembled into piston, the top two rings are closed from their free shape and the change of curvature and torsion of their neutral axes causes internal stress which are described as preload or initial force in Chapter 2. The OCR is assembled together with a spring that provides the expansion force pushing it towards the liner. Pressured gas flows around the ring pack system, which contributes to pressure force in both radial and axial directions. The ring-groove interaction is composed of dry contact force, oil pressure force due to squeezing and gas pressure force if there exists gas flow through the ring-groove clearance. The liner provides contact force in the radial direction and friction force in the axial direction. The reference frame is fixed to the piston. Thus, inertial force also needs to be included due to the piston acceleration and deceleration relative to the engine block. The following figure demonstrates all the forces acting on the ring.
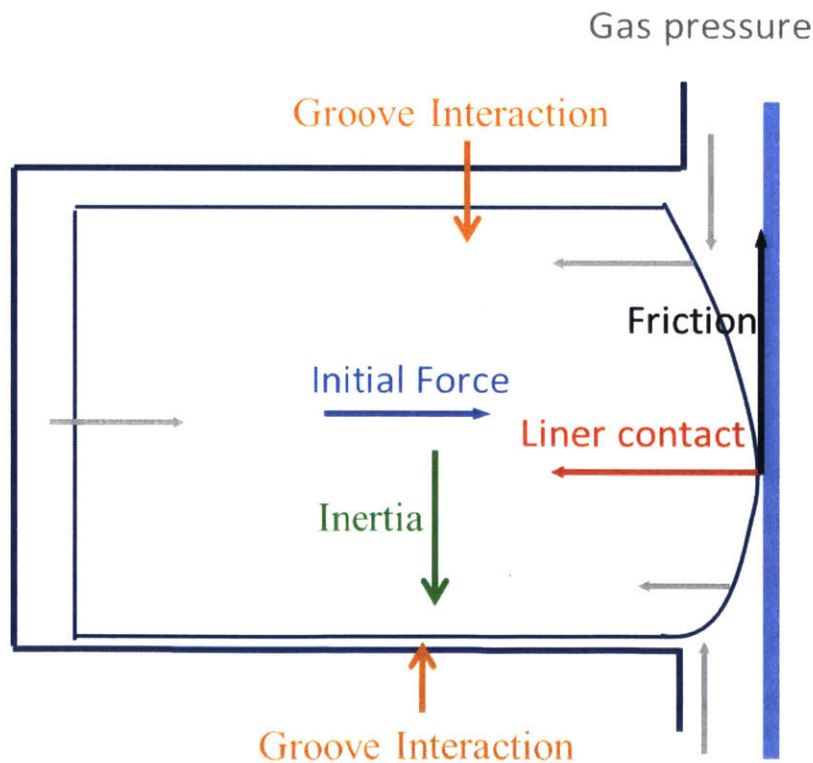

Figure 47 Force Analysis of Piston Ring

The resultant force can be split into 3 components: the radial force, the axial force and the twisting moment. These three components will be used later to calculate the external load vector in the governing equations.
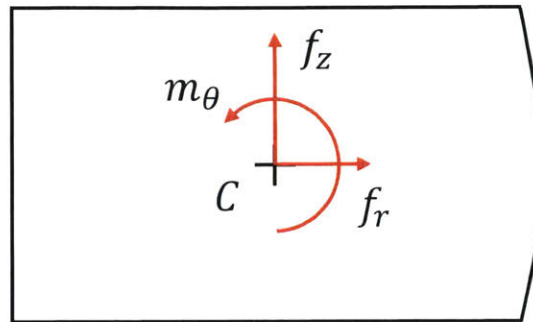
Cross section resultants

Figure 48 Resultant Forces on Piston Ring

4.2. Gas Flow Analysis in Ring Dynamics Model

Around the ring pack system, the gas flow can be categorized into channel flow and orifice flow. The potential channel flow pathways include the ring-groove interfaces in the radial direction, the ring-liner interfaces in the axial direction, the clearance between the ring back and the groove in the circumferential direction and the clearance between the piston land and the liner in the circumferential direction. The gas flow through the ring gaps and the drain holes in the OCR groove can be approximated by orifice flow. Figure 49 illustrates the mesh and the gas flow map. From top to bottom are the 1srt ring groove, the piston 2nd land, the 2nd ring groove, the piston 3rd land and the OCR groove. The boundary condition above the 1st ring groove is the crown land pressure that is assumed to be equal to the pressure in the combustion chamber and the boundary condition below the OCR groove is the crank case pressure which is an input. The blue, red and green lines in the flow map represent the structural mesh of the top ring, the second ring and the oil control ring correspondingly, which are used to calculate the ring-liner and ring-groove clearances. When the ring has good conformability to the groove and the liner, the gas flow may be blocked by the oil film. The calculation of gas flow mass rate is presented in Section 4.5 and 4.7.
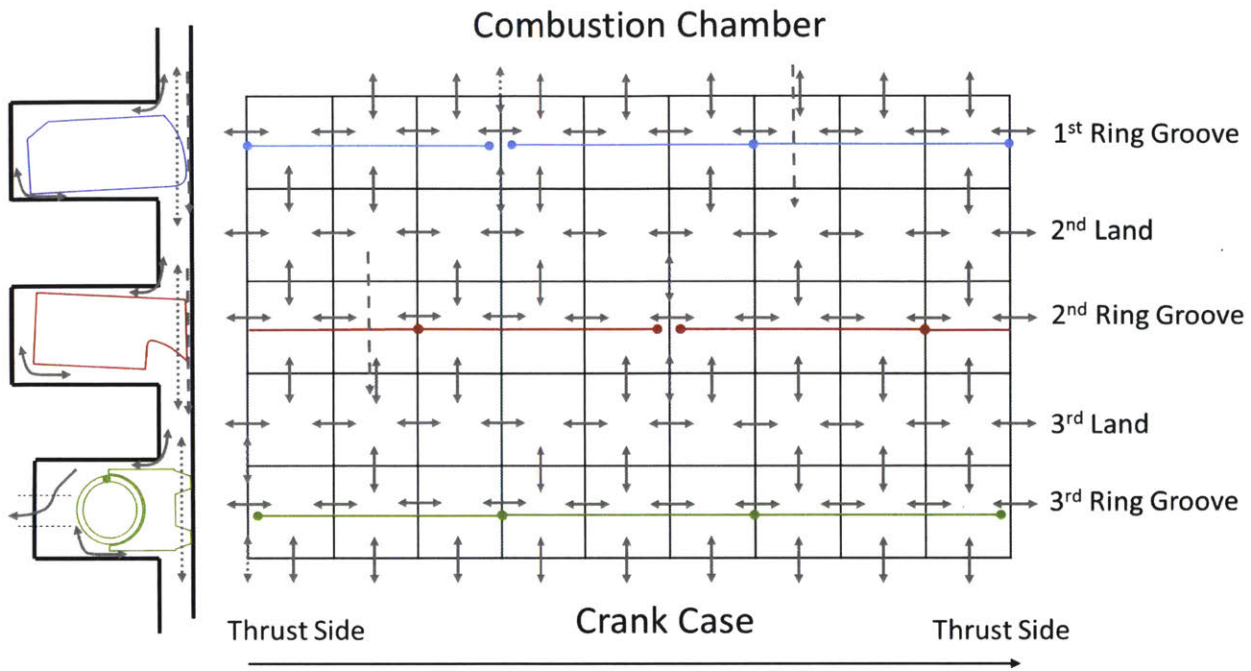
Figure 49 Gas Flow Map

4.3. Governing Equations

Since the calculation of the ring dynamic behavior and gas pressure are coupled, the governing equations have two parts: the first part are the dynamic equations and the second part are the equations of mass conservation of gas.
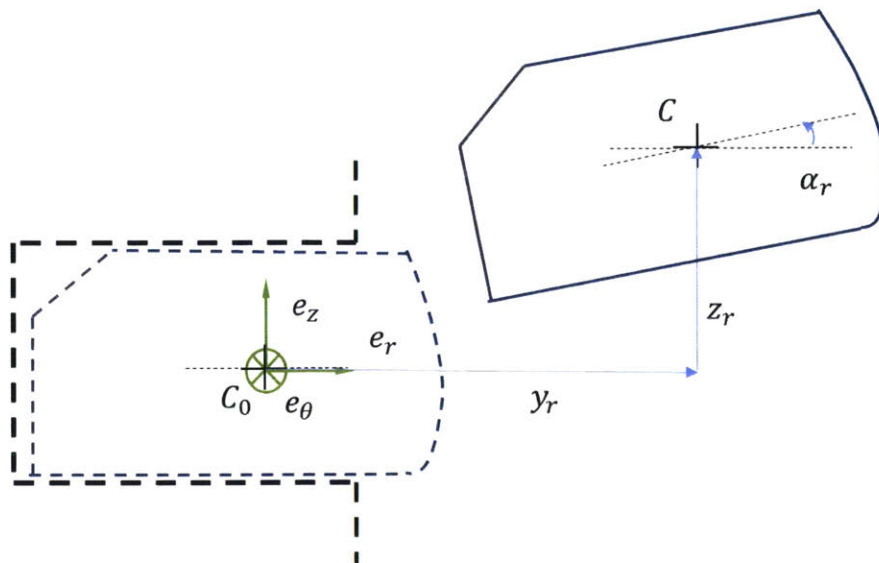

Figure 50 Ring Displacement in Three Directions

In the reference position, the ring is centered axially in the piston groove and its radial position is such that it is in contact with the non-deformed cylinder. The displacement of the cross section has three components: the radial displacement y_r, the axial displacement z_r and the rotation of the section α_r, as shown in Figure 50. Dynamic equations are used to calculate the ring dynamic response to the external loads. As discussed in Section 2.5, the equations can be obtained after the assembly of the mass, stiffness matrices and load vector of each element:

$$[M]\{\ddot{u}\} + [K]\{u\} = \{F_{ext}\} - \{F_{initial}\} \quad \text{[Equation 2.112]}$$

The load vector $\{F_{ext}\}$ is calculated from the resultant force on the cross section and the details can be found in Section 4.5, 4.6 and 4.8. The preload $\{F_{initial}\}$ is calculated from Equation 2.83 to Equation 2.85.

Mass Conservation Equations of Gas for each cell can be obtained by applying mass conservation and ideal gas law:

$$\frac{d}{dt}\left(\frac{P_k V_k}{RT_k}\right) = \sum \dot{m}_{k,i}(P, u)$$

Equation 4.1

where subscript k refers to the kth gas cell, P is the gas pressure, V is the gas volume which changes with the piston secondary motion and bore distortion, R is the specific gas constant of the air, T is the temperature and $\dot{m}_i$ is the rate of gas flow into the kth gas cell from i^{th} path which is a function of the pressure in adjacent cells and the ring displacement (which determines the ring-groove clearance and ring-liner clearance).

4.4. Greenwood-Tripp Contact Model

The asperity contact model used in this thesis is derived from Greenwood and Tripp theory [54]. The simplified formulation derived by Hu is adopted [38].

$$P_c = \begin{cases} 0 & \dfrac{h}{\sigma} \geq 4 \\ P_k\left(4 - \dfrac{h}{\sigma}\right)^z & \dfrac{h}{\sigma} < 4 \end{cases}$$

Equation 4.2

P_c is the asperity contact pressure, h is the local clearance and σ is the standard deviation of the surface roughness. The correlation constant P_K is a function of the properties of the ring and the liner material.

$$P_K = \frac{2KA}{\frac{1 - v_l^2}{E_l} + \frac{1 - v_r^2}{E_r}}$$

Equation 4.3

E_l, E_r, v_l and v_r are the Young's modulus and Poisson ratio of the liner and the ring respectively. K, A and z are constants calculated by Hu [38].

$$K = 1.198 \times 10^{-4}, A = 4.4068 \times 10^{-5} \text{ and } z = 6.804$$

4.5. Ring-Groove Sub-model

Ring-groove interaction is important in the ring dynamics model. This ring-groove sub-model is to solve the acting force and the gas flow rate through the ring-groove interfaces. The acting force comes from the asperity contact force, oil pressure force due to squeezing, hydrostatic force and gas pressure force. Since oil transport through the ring-groove interfaces is not included in this thesis, it is assumed that there is a uniform oil layer on the upper and lower flanks of the grooves. This oil layer is used to provide qualitatively accurate acting force on the ring from oil squeezing effect, which makes the ring-groove sub-model more complete.

4.5.1. Ring-Groove Geometry

As illustrated in Figure 51, the piston groove moves axially and is tilted due to piston dynamic tilting. Since the magnitude of piston tilt β_p is small (~0.1°), the tilted angle of the groove and its axial displacement can be approximated into linear form of β_p using small displacement assumption.
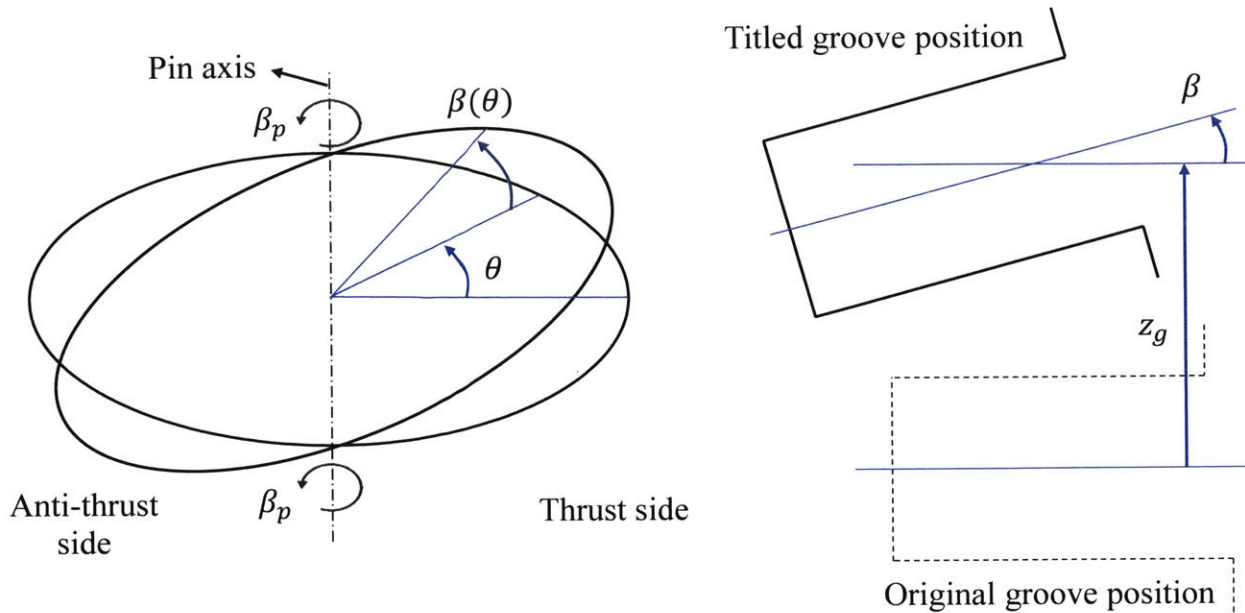
Figure 51 Displacement of the Groove of a Tilted Piston

The rotation of the groove located at angular position θ can be calculated by the following expression where $\theta = 0$ is set to be at the thrust side:

$$\beta = \beta_p cos\theta$$

Equation 4.4

The axial displacement of the groove is calculated as:

$$z_g = (Rcos(\theta) - off)\beta_p$$

Equation 4.5

where off corresponds to the piston offset (positive when the pin axis is moved towards the thrust side) and R is the ring radius. In addition to piston tilt, the thermal deformation of the piston groove is considered in this model.
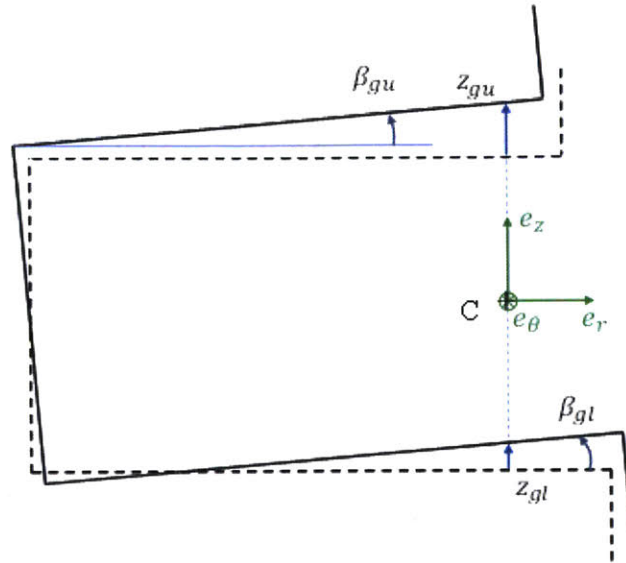
Figure 52 Thermal Deformation of Piston Groove

The axial displacements of the upper and lower flanks of the groove due to thermal distortion are z_{gu} and z_{gl}. They are measured at the radial location of the ring cross section centroid C. β_{gu} and β_{gl} are the groove tilt angles due to thermal distortion.
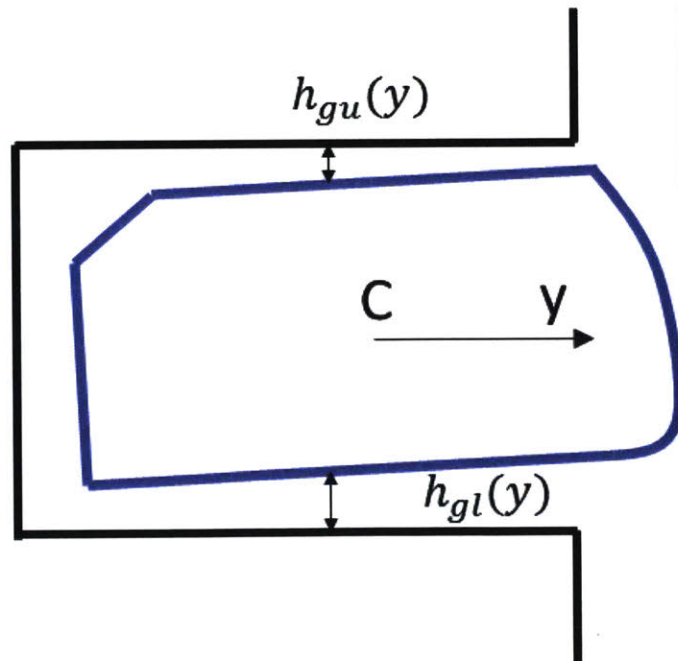

Figure 53 Ring-Groove Clearance

The ring-groove clearance can be calculated at the radial location y and the reference point is the radial location of the cross section centroid C. h_g is the axial clearance between the ring and its groove. The clearance between the ring upper flank and the groove h_{gu} is calculated as:

$$h_{gu}(y) = \frac{h_g}{2} + z_g + z_{gu} - z_r + y(\beta + \beta_{gu} - \alpha_r)$$

Equation 4.6

The clearance between the ring lower flank and the groove h_{gl} is calculated as:

$$h_{gl}(y) = \frac{h_g}{2} - z_g - z_{gl} + z_r + y(\alpha_r - \beta - \beta_{gl})$$

Equation 4.7

4.5.2. Ring-Groove Dry Contact

The ring-groove dry contact force can be calculated by integrating the asperity contact pressure (Equation 4.2) over the contact area (as shown in Figure 54).
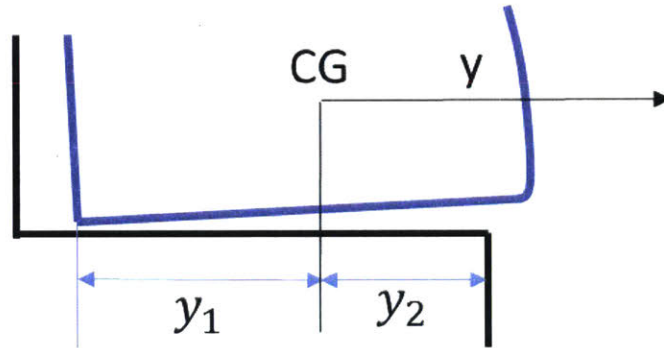

Figure 54 Contact Area between Ring and Groove

Based on Equation 4.6, the ring-groove clearance at centroid of the ring cross section h_{guo} is defined as:

$$h_{guo} = \frac{h_g}{2} + z_{gu} + z_g - z_r$$

Equation 4.8

Then the clearance between the ring upper flank and the groove can be rewritten as:

$$h_{gu}(y) = h_{guo} + y(\beta + \beta_{gu} - \alpha_r)$$

Equation 4.9

Put this equation into Equation 4.2 and integrate over the ring-groove contact area:

$$f_{c,gu} = \int_{y_1}^{y_2} -P_k \left[\Omega - \frac{h_{gu0} + y(\beta + \beta_{gu} - \alpha_r)}{\sigma_g} \right]^z dy$$

$$= -\frac{P_k \sigma_g}{(z+1)(\alpha_r - \beta - \beta_{gu})} \left[\left(\Omega - \frac{h_2}{\sigma_g} \right)^{z+1} - \left(\Omega - \frac{h_1}{\sigma_g} \right)^{z+1} \right]$$

Equation 4.10

$$m_{c,gu} = \int_{y_1}^{y_2} -P_k \left[\Omega - \frac{h_{gu0} + y(\beta + \beta_{gu} - \alpha_r)}{\sigma_g} \right]^z y\,dy$$

$$= \frac{P_k \sigma_g}{(z+1)(z+2)(\alpha_r - \beta - \beta_{gu})^2} \left\{ \left(\Omega - \frac{h_1}{\sigma_g} \right)^{z+1} [(h_{gu0} - h_1)(z+1) + h_{gu0} - \Omega\sigma_g] \right.$$

$$\left. - \left(\Omega - \frac{h_2}{\sigma_g} \right)^{z+1} [(h_{gu0} - h_2)(z+1) + h_{gu0} - \Omega\sigma_g] \right\}$$

Equation 4.11

where y_1 is the left end of the contact area (the sign may be negative if y_1 is at the left side of the centroid C) and y_2 (the value may be negative if y_2 is at the left side of the centroid C) is the right end of the contact area and h_1 and h_2 are the local clearances at the corresponding points. The negative sign inside the integrals implies that the direction of the force is downward.

Similarly, we can also get the force and moment acting on the ring from the lower groove flank.

$$h_{gl0} = \frac{h_g}{2} - z_{gl} - z_g + z_r$$

Equation 4.12

$$h_{gl}(y) = h_{gl0} + y(\alpha_r - \beta - \beta_{gl})$$

Equation 4.13

$$f_{c,gl} = \int_{y_2}^{y_1} P_k \left[\Omega - \frac{h_{gl0} + y(\alpha_r - \beta - \beta_{gl})}{\sigma_g} \right]^z dy$$

$$= -\frac{P_k \sigma_g}{(z+1)(\alpha_r - \beta - \beta_{gl})} \left[\left(\Omega - \frac{h_2}{\sigma_g} \right)^{z+1} - \left(\Omega - \frac{h_1}{\sigma_g} \right)^{z+1} \right]$$

Equation 4.14

$$m_{c,gl} = \int_{y_1}^{y_2} P_k \left[\Omega - \frac{h_{gl0} + y(\alpha_r - \beta - \beta_{gl})}{\sigma_g} \right]^z y\,dy$$

$$= \frac{P_k \sigma_g}{(z+1)(z+2)(\alpha_r - \beta - \beta_{gl})^2} \left\{ \left(\Omega - \frac{h_2}{\sigma_g} \right)^{z+1} [(h_{gl0} - h_2)(z+1) + h_{gl0} - \Omega\sigma_g] \right.$$

$$\left. - \left(\Omega - \frac{h_1}{\sigma_g} \right)^{z+1} [(h_{gl0} - h_1)(z+1) + h_{gu0} - \Omega\sigma_g] \right\}$$

Equation 4.15

4.5.3.   Oil Squeezing Force and Hydrostatic Force between a Ring and Its Groove

There is no experimental data about the oil film thickness on the groove flanks. As suggested by Tian [32], if it is assumed that the oil film thickness is on the order of a few microns, the oil flow between the ring and the groove flank has Reynolds number on the order of one and the angle between the ring and the groove is on the order of 0.01rad. Thus, the applicability of the Reynolds equation is justified. Tian also pointed out that the ring's moving away from the groove starts from certain point and then gradually extends to the entire part of the ring. Base on this picture, the possibility of 'suction' or occurrence of 'negative pressure' is neglected.
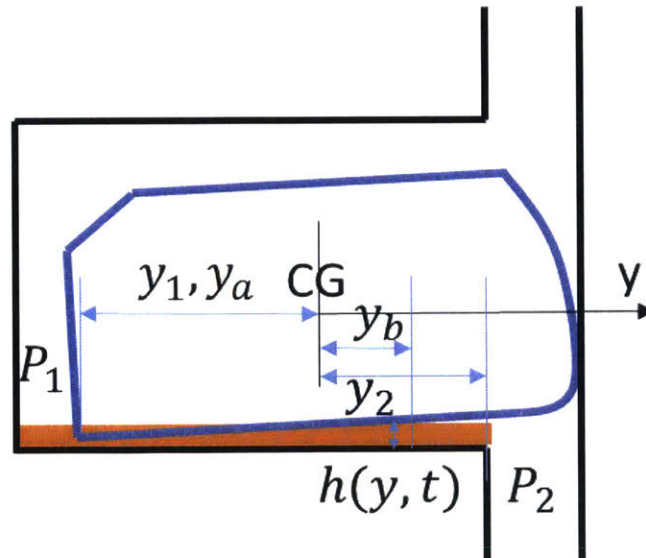

Figure 55 Illustration of Ring/Oil/Groove Contact

As illustrated in Figure 55, y_1 and y_2 are the two end points of the ring-groove interacting area and y_a and y_b are the two end points where ring touches the oil film on the groove flank. From Reynolds

Equation, we can calculate the squeezing pressure in the oil film. In Equation 4.16, P_{oil} is the pressure in the oil film due to squeezing and μ_{oil} is the oil dynamic viscosity. Since the possibility of 'suction' or occurrence of 'negative pressure' is neglected, the term of $\frac{\partial h}{\partial t}$ is set to be zero when its value is greater than zero.

$$\frac{1}{12\mu_{oil}}\frac{\partial}{\partial y}\left(h^3\frac{\partial P_{oil}}{\partial y}\right) = \frac{\partial h}{\partial t}$$

Equation 4.16

$$\frac{\partial P_{oil}}{\partial y} = \frac{1}{h^3}\left(12\mu_{oil}J(y) + c_1\right)$$

Equation 4.17

where

$$J(y) = \int_a^y \frac{\partial h}{\partial t}dy'$$

Equation 4.18

and

$$c_1 = \frac{P_u - P_i - 12\mu_{oil}\int_a^b \frac{J(y)}{h^3}dy}{\int_a^b \frac{dy}{h^3}}$$

Equation 4.19

Integrating Equation 4.17 by parts, we can obtain the squeezing force and the corresponding moment from the ring groove.

$$f_{oil} = \int_a^b P_{oil}dy = P_2(y_b - y_a) - \int_a^b (y - y_a)\frac{\partial P_{oil}}{\partial y}dy$$

$$= P_2(y_b - y_a) - 12\mu_{oil}\int_a^b \frac{(y - y_a)J(y)}{h^3}dy - c_1\int_a^b \frac{y - y_a}{h^3}dy$$

Equation 4.20

88

$$m_{\theta,oil} = \int_a^b P_{oil} y \, dy = \frac{P_2(y_b^2 - y_a^2)}{2} - \frac{1}{2}\int_a^b (y - y_a)^2 \frac{\partial P_{oil}}{\partial y} \, dy$$

$$= \frac{P_2(y_b^2 - y_a^2)}{2} - 6\mu_{oil}\int_a^b \frac{(y^2 - y_a^2)J(y)}{h^3} \, dy - \frac{c_1}{2}\int_a^b \frac{y^2 - y_a^2}{h^3} \, dy$$

Equation 4.21

The ring-groove interacting area is not necessarily the same as the ring/oil contact area. Therefore, gas will fill into the space between the ring and the oil film and generate hydrostatic pressure force. The force and moment can be calculated using the following expression:

$$f_{hydro-static} = (y_a - y_1)P_1 + (y_2 - y_b)P_2$$

Equation 4.22

$$m_{\theta,hydro-static} = \frac{1}{2}\left[(y_a^2 - y_1^2)P_1 + (y_2^2 - y_b^2)P_2\right]$$

Equation 4.23

4.5.4. Ring-Groove Gas Flow and Gas Pressure Force

When the ring-groove clearance is larger than the given oil film thickness, gas is allowed to flow driven by pressure difference. As discussed by Tian [32], the gas flow through the ring-groove interfaces can be treated as laminar flow. However, convection and unsteady effects could be significant when the ring is in transition, especially when it flutters and the analytical solution does not exist. Since detailed study of the gas flow through the ring-groove interfaces during ring transition is beyond the scope of this thesis, the description of the gas flow is only limited to be qualitatively accurate and an analytical solution is needed to form a fast engineering model.
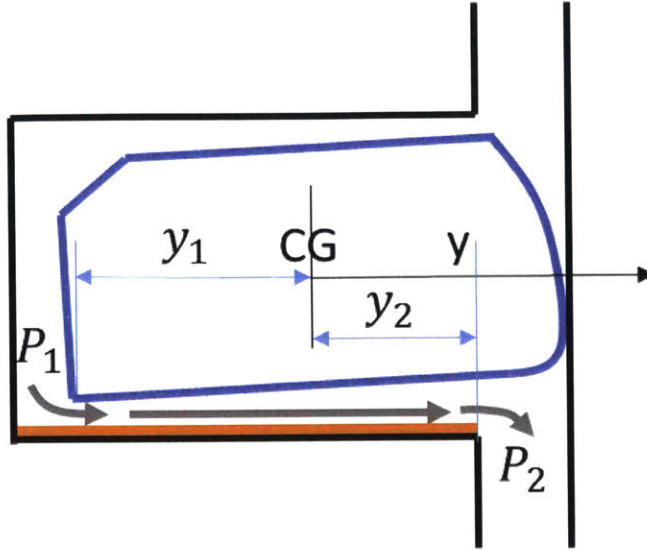
Figure 56 Schematic for Gas Flow through the Channel between Ring and Groove

The geometry of the channel between the ring and the groove is shown in Figure 56. The ring-groove gas flow is approximated as a fully-developed, quasi-steady and locally-parallel flow. Meanwhile, the pumping and squeezing effect due to the ring-groove relative motion is neglected because of very small viscosity of gas.

For Poiseuille Flow, local velocity profile is represented as:

$$u(z) = \frac{1}{2\mu} \frac{dP_{gas}}{dy} z(z - h_c)$$

Equation 4.24

where

$$h_c(y) = h(y) - h_{oil}$$

Equation 4.25

Pressure gradient satisfies:

$$\frac{d}{dy}\left(h_c^3 \frac{dP_{gas}}{dy}\right) = 0$$

Equation 4.26

Integrating the above equation with two boundary conditions, $P(y_1) = P_1$ and $P(y_2) = P_2$, we can obtain:

$$\frac{dP_{gas}}{dy} = \frac{P_2 - P_1}{h_c^3 \int_{y_1}^{y_2} \frac{dy}{h_c^3}}$$

The volume flow rate through the ring-groove channel per unit length at each cross section is calculated by integrating Equation 4.24 over the channel:

$$\dot{V}_{gas} = \frac{P_1 - P_2}{12\mu_{gas} \int_{y_1}^{y_2} \frac{dy}{h_c^3}}$$

The gas could be treated as ideal gas and the gas density is approximated as:

$$\rho_{gas} = \frac{P_1 + P_2}{2RT}$$

Then we obtain the mass flow rate of the gas per unit length by multiplying the gas density with the volume flow rate per unit length:

$$\dot{m}_{gas} = \frac{P_1^2 - P_2^2}{24\mu_{gas}RT \int_{y_1}^{y_2} \frac{dy}{h_c^3}}$$

The axial force and the moment per unit length at each cross section can be expressed as:

$$f_{gas} = \int_{y_1}^{y_2} P_{gas}dy = P_b(y_b - y_a) - \int_{y_1}^{y_2} (y - y_a)\frac{dP_{gas}}{dy}$$

$$m_{gas} = \int_{y_1}^{y_2} P_{gas}ydy = \frac{P_b(y_b^2 - y_a^2)}{2} - \frac{1}{2}\int_{y_1}^{y_2} (y^2 - y_a^2)\frac{dP_{gas}}{dy}$$

Substituting Equation 4.27 into Equation 4.31 and Equation 4.32, we can further develop the equations to the following form:

$$f_{gas} = P_a \frac{\int_{y_1}^{y_2} \frac{y - y_1}{h_c^3} dy}{\int_{y_1}^{y_2} \frac{dy}{h_c^3}} + P_b \frac{\int_{y_1}^{y_2} \frac{y_2 - y}{h_c^3} dy}{\int_{y_1}^{y_2} \frac{dy}{h_c^3}}$$

Equation 4.33

$$m_{gas} = \frac{1}{2} P_a \frac{\int_{y_1}^{y_2} \frac{y^2 - y_1^2}{h_c^3} dy}{\int_{y_1}^{y_2} \frac{dy}{h_c^3}} + \frac{1}{2} P_b \frac{\int_{y_1}^{y_2} \frac{y_2^2 - y^2}{h_c^3} dy}{\int_{y_1}^{y_2} \frac{dy}{h_c^3}}$$

Equation 4.34

The gas flow through the ring-liner clearance in the axial direction when the ring loses contact with the liner, the clearance between the ring back and the groove in the circumferential direction and the clearance between the piston land and the liner in the circumferential direction can be treated as channel flow as well and the same equation to calculate the flow rate is applied.

4.6. Ring-Liner Sub-Model

The forces acting on the ring from liner include dry-contact force, hydrodynamic force from the oil film between ring and liner and gas pressure force. In the ring dynamics model, the hydrodynamic force is neglected for top two rings in order to achieve better calculation speed. Hydrodynamic force is considered in the ring-liner lubrication model whose objective is to calculate the accurate ring-liner clearance. Neglecting the hydrodynamic force may cause significant bias of ring-liner clearance estimation but in the following section, we are going to demonstrate that it will have negligible effect on other results such as the radial and axial deformation of the ring neutral axis and ring twist. These results are what we really need from this ring dynamics model.

4.6.1. Validation of Neglecting Hydrodynamic Force for Top Two Rings in Ring Dynamics Model

Neglecting hydrodynamic force is equivalent to changing the local ring-liner contact behavior. As discussed in Section 3.5, a change of local ring-liner lubrication condition does not affect the overall structure response of the ring. It is because compared to ring neutral axis deformation which has the same magnitude order as bore distortion ($\sim 100 \mu m$), ring liner clearance is much smaller with a magnitude order close to surface roughness ($\sim 0.1 \mu m$), as shown in Figure 57.
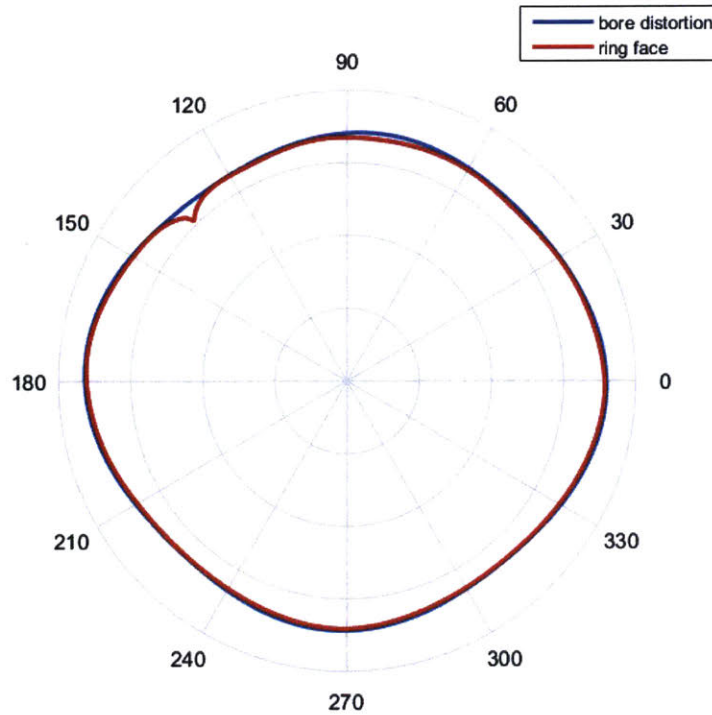
Figure 57 Ring and Bore Distortion

Ring-liner friction force may affect ring neutral axis deformation in axial direction and ring twist but when there exist pressure force and inertial force, friction force is too small compared to these two and its effect becomes negligible. For a typical passenger car engine running with a partial load and a speed of 2000RPM, the initial force is on the order of 50N/m, the pressure force is within the range of 100N/m to 3000N/m while the friction force is within the range of 10N/m to 100N/m. The friction force reaches its maximum value approximately at the same time as the pressure force.

Figure 58 shows an example of different ring-liner contact models. The blue lines represent the results with only dry-contact force considered in ring-liner contact model. The red and green lines represent the results that take both dry-contact force and hydrodynamic force into consideration while the oil supply of the red lines is partially flooded and green lines fully flooded. The other boundary conditions are set to match the environment of the real engine in the intake stroke when pressure force is relatively small. In the last plot of ring-liner contact force distribution, the blue curve is almost identical to the red one so it is not clearly shown in the plot. We see that even when the pressure force is relatively small, different ring-liner contact models still do not have significant impact on the ring structural response although the exact ring-liner clearances are affected, as expected. Thus, to resolve accurately the ring-liner interaction, one needs to employ proper lubrication model, as to be discussed in the next chapter.

However, the ring structural dynamics modeled here is not affected significantly by the exact ring-liner lubrication conditions.
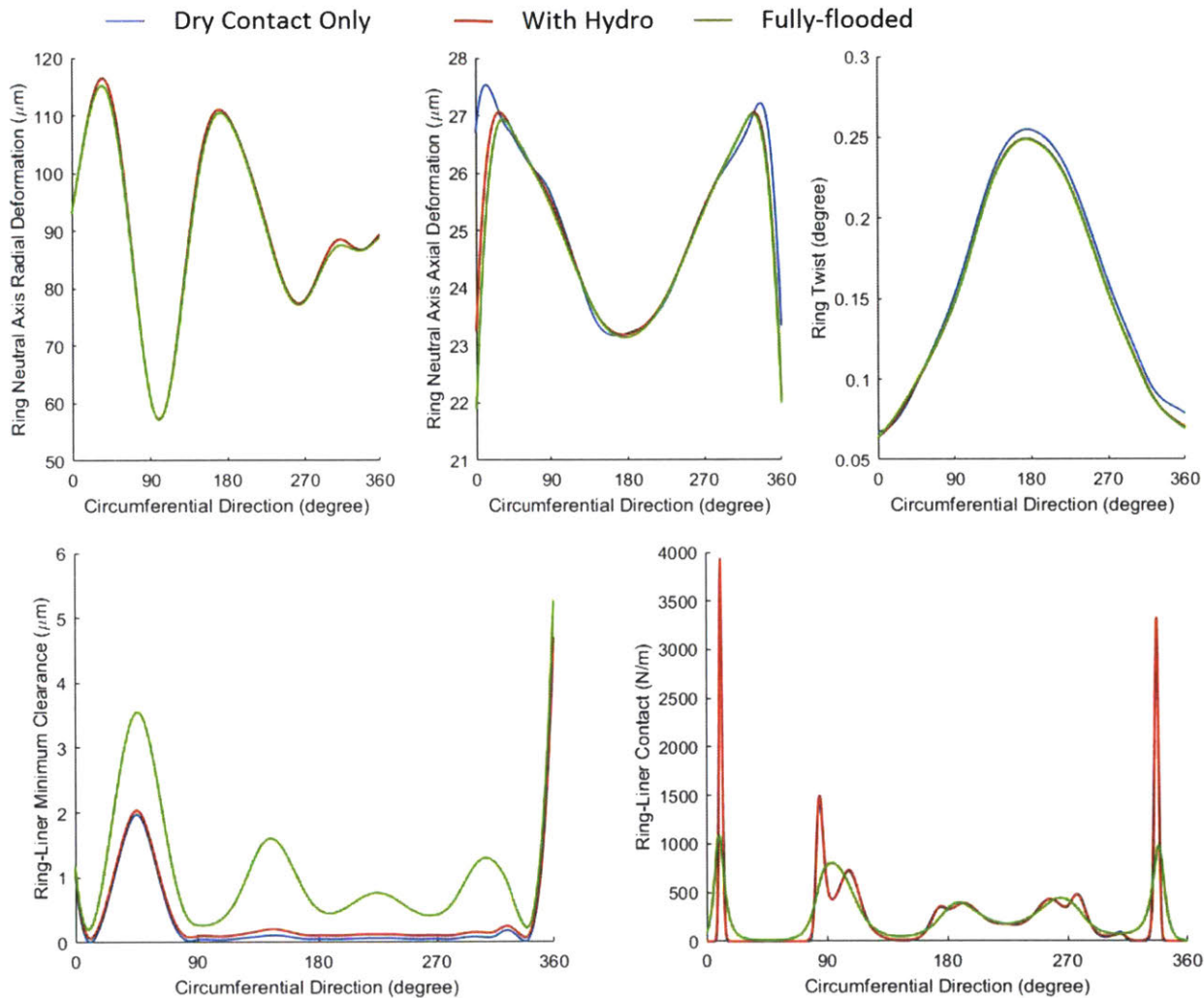

Figure 58 The Comparison of Different Ring-Liner Contact Models

4.6.2. Ring-Liner Dry Contact

At the reference postion, the ring is in contact with the non-deformed cylinder. The distance between the centroid of the ring cross section and the norminal bore is y_c. The running surface of ring is approximated as barrel shape with the expression (as shown in Figure 59):

$$y_{barrel} = a_0 + a_1(z - rbn) + a_2(z - rbn)^2$$

Equation 4.35

The ring-liner minimum point is defined as the point on the ring running surface that is closest to the liner. rbn is the minimum point when ring is in free state (no twist). The barrel drop of the ring profile is typically around the magnitude of 100 μm. The radial position of ring's running surface at the reference point is $y = y_c - y_{barrel}$.
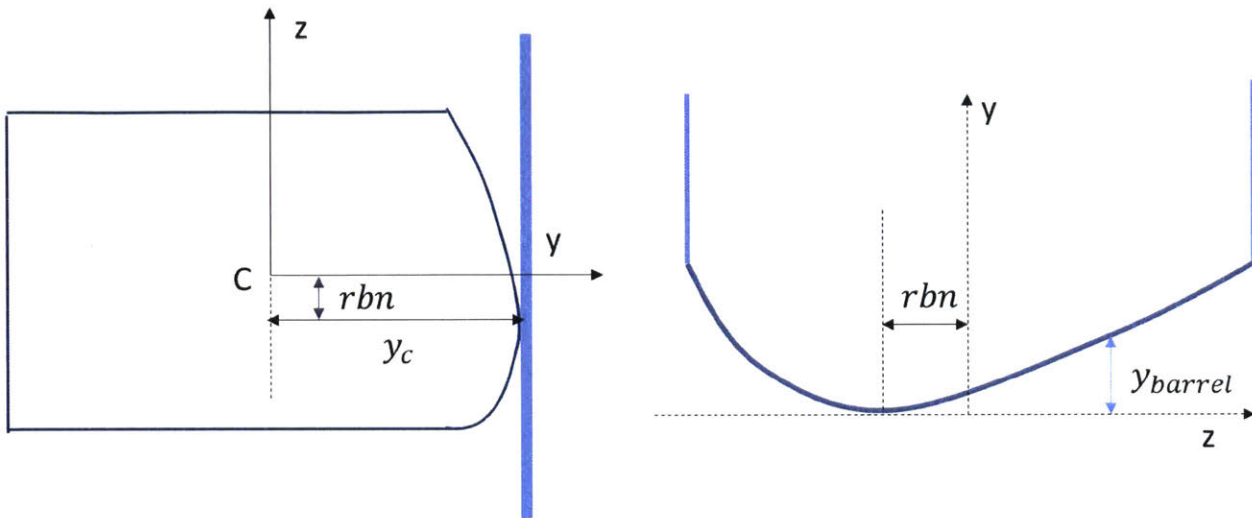
Figure 59 Ring Profile

When ring has a twist around its centroid with value of α_r, its running surface will move to a new position that can be calculated by the following equation:

$$\begin{bmatrix} y' \\ z' \end{bmatrix} = \begin{bmatrix} cos\alpha_r & -sin\alpha_r \\ sin\alpha_r & cos\alpha_r \end{bmatrix} \begin{bmatrix} y \\ z \end{bmatrix}$$

Equation 4.36

As shown in Figure 60, the radial displacement of the cylinder from its nominal position due to bore distortion is y_b and ring's radial deformation relative to its reference position is y_r. Therefore, the local clearance between ring and liner is:

$$h(z) = y_b - y_r + y_c - y' = y_b - y_r + y_{barrel} + \alpha_r z$$
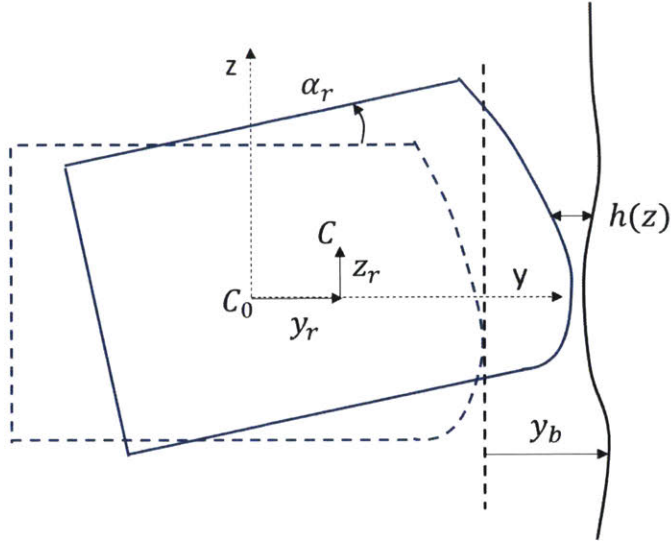
Equation 4.37

95

Figure 60 Schematic of Ring-Liner Contact

As described before, dry contact pressure is calculated by simplified Greenwoods-Tripp model:

$$P_c = P_k \left(\Omega - \frac{h}{\sigma_p} \right)^z \quad \text{[Equation 4.2]}$$

Substituting the ring-liner clearance and taking the integral, we can obtain the force and moment per unit length from the liner at each cross section as:

$$f_{cL} = \int_{rw} -P_k \left(\Omega - \frac{y_b - y_r + y_{barrel} + \alpha_r z'}{\sigma_p} \right)^z dz'$$

Equation 4.38

$$m_{cL} = \int_{rw} P_k \left(\Omega - \frac{y_b - y_r + y_{barrel} + \alpha_r z'}{\sigma_p} \right)^z [\alpha_r(y_c - y_{barrel}) + z'] dz'$$

Equation 4.39

Where rw represents the ring-liner contact area and the negative sign in f_{cL} corresponds to the fact that the contact force acting on the ring is pointing inwards.

4.7. Gas Flow through Ring Gaps and Drain Holes

Gas flow through ring gaps is a major contribution to the total gas flow in axial direction. Especially when top two rings are stable sitting at the lower flank of the ring groove, gas flow through the two ring gaps

is almost the only way that 2nd land and 3rd land pressure can be release to the crank case. An isentropic orifice flow model is used to calculate its flow rate [32]:

$$\dot{m}_{gap} = \frac{C_D A_{gap} P_U}{\sqrt{RT_U}} f_m$$

Equation 4.40

Where A_{gap} is the gap area that allows gas to flow through, P_U is the pressure of which land gas flows from (upstream) and correspondingly P_D is the pressure of which land gas flows to (downstream), f_m can be expressed as:

$$f_m = \begin{cases} \gamma^{\frac{1}{2}} \left(\frac{2}{\gamma+1}\right)^{\frac{\gamma+1}{2(\gamma-1)}} & \frac{P_D}{P_U} \leq \left(\frac{2}{\gamma+1}\right)^{\frac{\gamma}{\gamma-1}} \\ \left(\frac{P_D}{P_U}\right)^{\frac{1}{\gamma}} \left\{\frac{2\gamma}{\gamma-1}\left[1-\left(\frac{P_D}{P_U}\right)^{\frac{\gamma-1}{\gamma}}\right]\right\}^{\frac{1}{2}} & \frac{P_D}{P_U} > \left(\frac{2}{\gamma+1}\right)^{\frac{\gamma}{\gamma-1}} \end{cases}$$

Equation 4.41

And

$$C_D = 0.85 - 0.25\left(\frac{P_D}{P_U}\right)^2$$

Equation 4.42

4.8. Gas Pressure Force and Moment acting on the Ring Running Surface, Ring flank and Back of the Ring

Gas pressure also exists in land-liner clearance and clearance between ring back and groove and generates force and moment on the ring. Gas pressure inside the ring groove pushes the ring towards the liner. Some types of top ring and second ring have cut on the back of the ring and the ring may have axial force acting on it due to the cut. Gas pressure in the land-liner clearance provides both axial force and radial force on the ring. In this model, the pressure acting in the regions above the minimum point (which is defined before as the point on the ring running surface that is closest to the liner) is assumed to be the piston upper land pressure P_u and the pressure below the minimum point is assumed to the piston lower land pressure P_d, as shown in Figure 61. The location of the minimum point shifts with ring dynamics twist and is called dynamic minimum point, z_0. The minimum point when ring is in free state is called original minimum point, rbn.
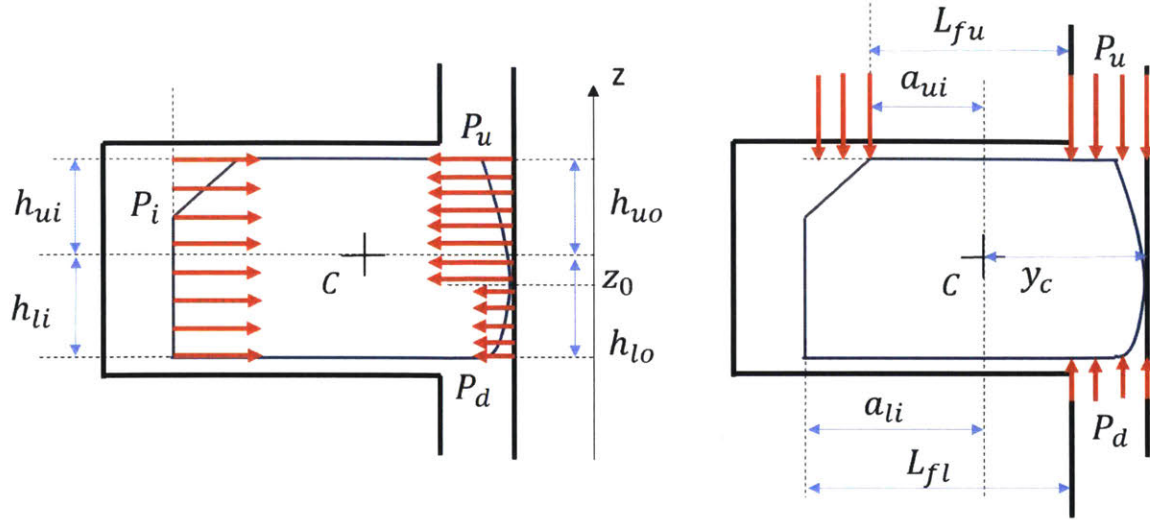
97

Figure 61 Pressure Force Acting on the Ring

As shown in Figure 61, the radial force, axial force and moment generated by gas pressure in land-liner clearance and the clearance between the ring back and groove can be calculated as:

$$f_{radial} = P_i(h_{li} + h_{ui}) - P_u(h_{uo} - z_0) - P_d(h_{lo} + z_0)$$

Equation 4.43

$$f_{axial} = -P_u(y_c + a_{ui} - L_{fu}) + P_d(y_c + a_{li} - L_{fl}) - P_i(a_{li} - a_{ui})$$

Equation 4.44

$$m_{gas,e} = \frac{1}{2}P_i(h_{li}^2 - h_{ui}^2) + \frac{1}{2}P_u(h_{uo}^2 - z_0^2) - \frac{1}{2}P_d(h_{lo}^2 - z_0^2) - \frac{1}{2}P_u(y_c + L_{fu} - a_{ui})(y_c + a_{ui} - L_{fu})$$

$$+ \frac{1}{2}P_d(y_c + L_{fl} - a_{li})(y_c + a_{li} - L_{fl}) + \frac{1}{2}P_i(a_{li} + a_{ui})(a_{li} - a_{ui})$$

Equation 4.45

4.9. Sample Results

The model was applied to a production gasoline engine to demonstrate the capabilities of the model and a number of important mechanisms for ring dynamics, ring/groove interaction, and gas flows as well as the influence of key parameters..

4.9.1. Calculation Set-up

The engine has a bore diameter of 77mm and a stroke of 85.8mm. A cross-sectional view of the ring pack and their parameters are shown in Figure 62. The cut in the upper ID of the top ring and the hook

in the lower OD of the second ring give a positive static twist. In the figure, a_r represents the ring width in the radial direction, h_r is the ring thickness in the axial direction, alp is the principal angle when the ring is at its free state and F_t is the tangential force. The top ring, second ring and TLOCR gap positions are set to be 135°, 225° and 45° away from the thrust side respectively.

Top Ring
$ar = 2.9mm$
$hr = 1.2mm$
$alp = 1.48°$
$Ft = 8.5N$
$T_g = 135°$ (Thrust side: 0°)

Second Ring
$ar = 3.1mm$
$hr = 1.5mm$
$alp = 5.78°$
$Ft = 6.5N$
$T_g = 225°$ (Thrust side: 0°)
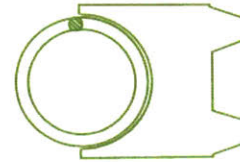
Twin-land Oil Control Ring
$ar = 2.05mm$
$hr = 1.98mm$
$Ft = 15N$
$T_g = 45°$ (Thrust side: 0°)

Figure 62 Cross-sections of the Ring Pack and Ring Parameters

The engine is running at full load with peak pressure of 103bar and speed of 2000RPM. The bore is distorted due to thermal and mechanical stress. It has radial deformation with 0th order up to $100\mu m$, 2nd order up to $10\mu m$ and 4th order up to $5\mu m$. The piston secondary motion is considered as well with tilt angle magnitude up to 0.25° and lateral motion on the order of 50 μm. The piston secondary motion is calculated by Bai [55] [56]. It is an output of his piston lubrication model. The plots of the combustion chamber pressure, the piston tilt, the piston secondary motion and the bore distortion are shown in Figure 63.
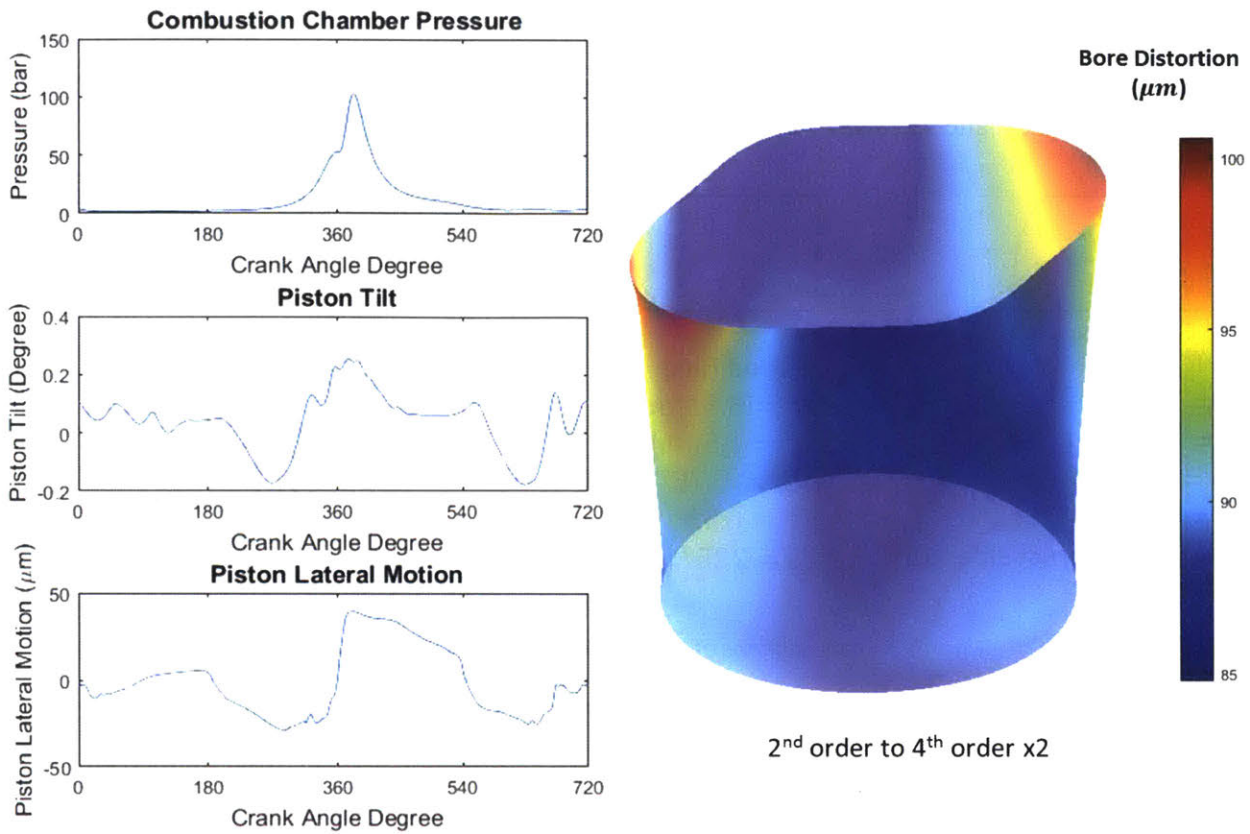
Figure 63 Plots of Combustion Chamber Pressure, Piston Tilt and Bore Distortion

Piston is distorted due to temperature difference. Figure 64 is a section view of a piston finite element model simulating thermal distortion of the piston. Piston thermal distortion can cause the grooves to rotate or move vertically, which is considered into the model as well. In this example, the magnitude of piston thermal tilt is on the order of -0.1° and piston groove distortion has a shape of 2nd order with a magnitude up to $6\mu m$.

Axial deformation
and tilt of piston
grooves
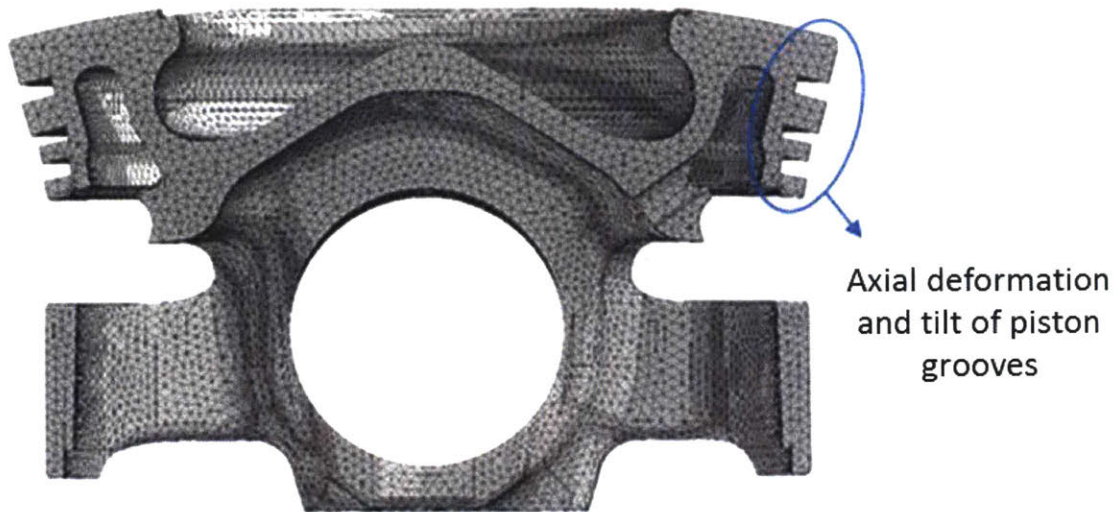
Figure 64 Thermal Distortion of the Piston

4.9.2. Results for a Gasoline Engine at 2000RPM and Full-Load

Figure 65 shows the results of pressure in different piston regions at the thrust side and a comparison of the results from the curved beam model and Tian's 2D model [32]. Tian's 2D ring dynamics model is used to compare because it has been used in the industry for many years and has been proved to be an accurate tool to predict blow-by gas flow and inter-ring pressures. Based on the results, it is clear to see how the top ring behaves as a gas seal. Under the pressure of the combustion chamber, the top ring is pushed down against the ring groove lower flank, thus closing the path of gas flow. After the top ring, the gas pressure drops dramatically from cylinder pressure (up to $100bar$) to a value around $5bar$. The second ring helps reduce the pressure from around 5bars to almost atmospheric pressure. The lower plot in Figure 65 shows that the ring dynamics model based on the curved beam finite element method (CBM) and Tian's 2D ring dynamics model predict very close gas pressure behavior. The small difference is from the fact that the CBM results are for one set of ring gap locations while the results of 2D model represent the average of all the gap locations. With similar pressure estimation, it is not surprising that both models also give very close prediction of blow-by gas flow. The 2D model predicts the average blow-by gas flow in one cycle as 6.359L/min (0.123g/s) which is very close to 8.117L/min (0.157g/s) predicted by the 3D model. The difference is due to the different positions of the second ring gap. In the 2D model, the position of the second ring gap is fixed at the thrust side while in the 3D model the position of the second ring gap is set at 225° off the thrust side (close to the anti-thrust side). In the

expansion stroke, the piston moves towards the thrust side. As a result, the second ring gap area in the 2D model is smaller than that in the 3D model during the expansion stroke, causing a decrease of the piston 2nd land pressure and an increase of the blow-by flow rate in the 3D model.
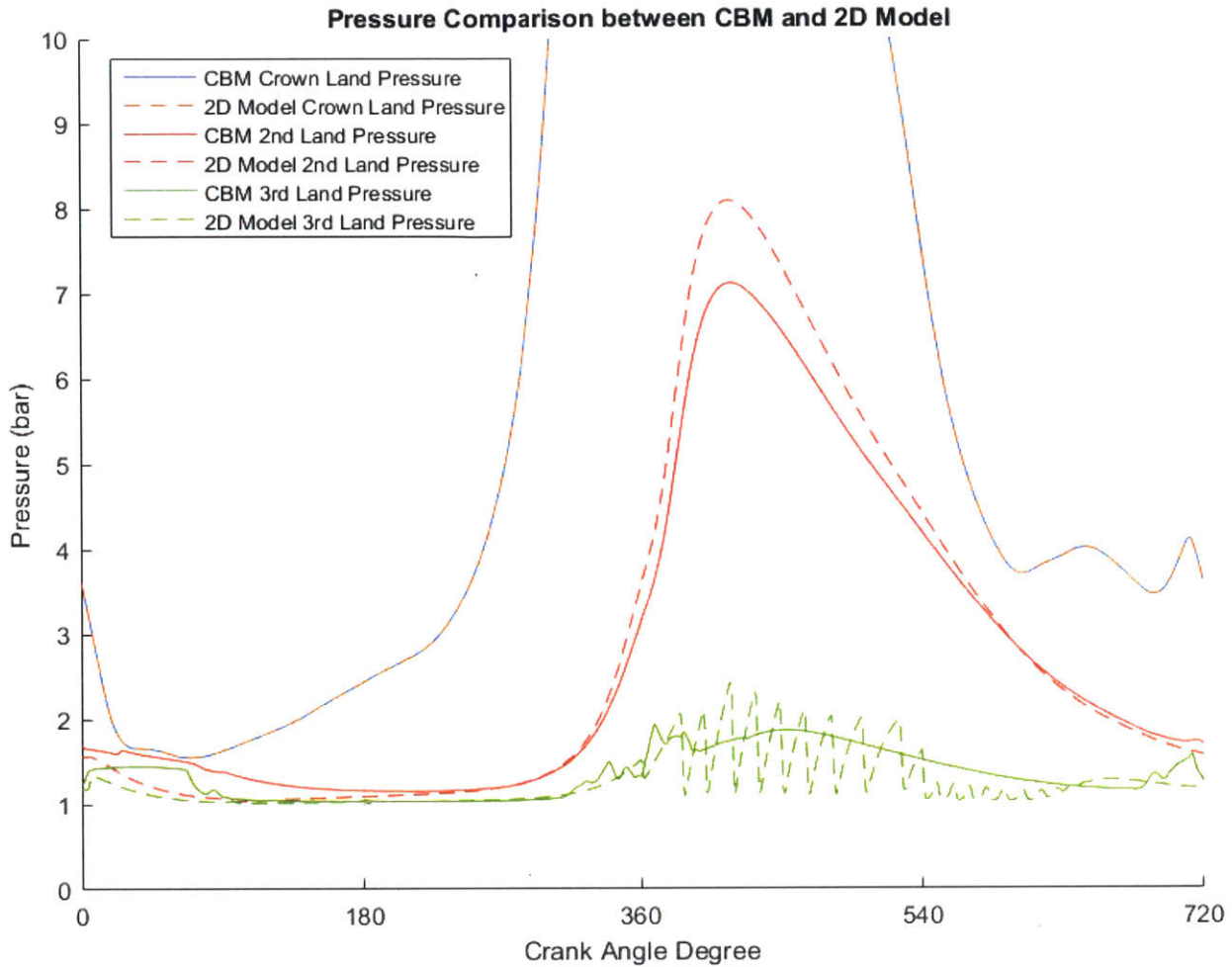

Engine Pressure(Thrust Side)
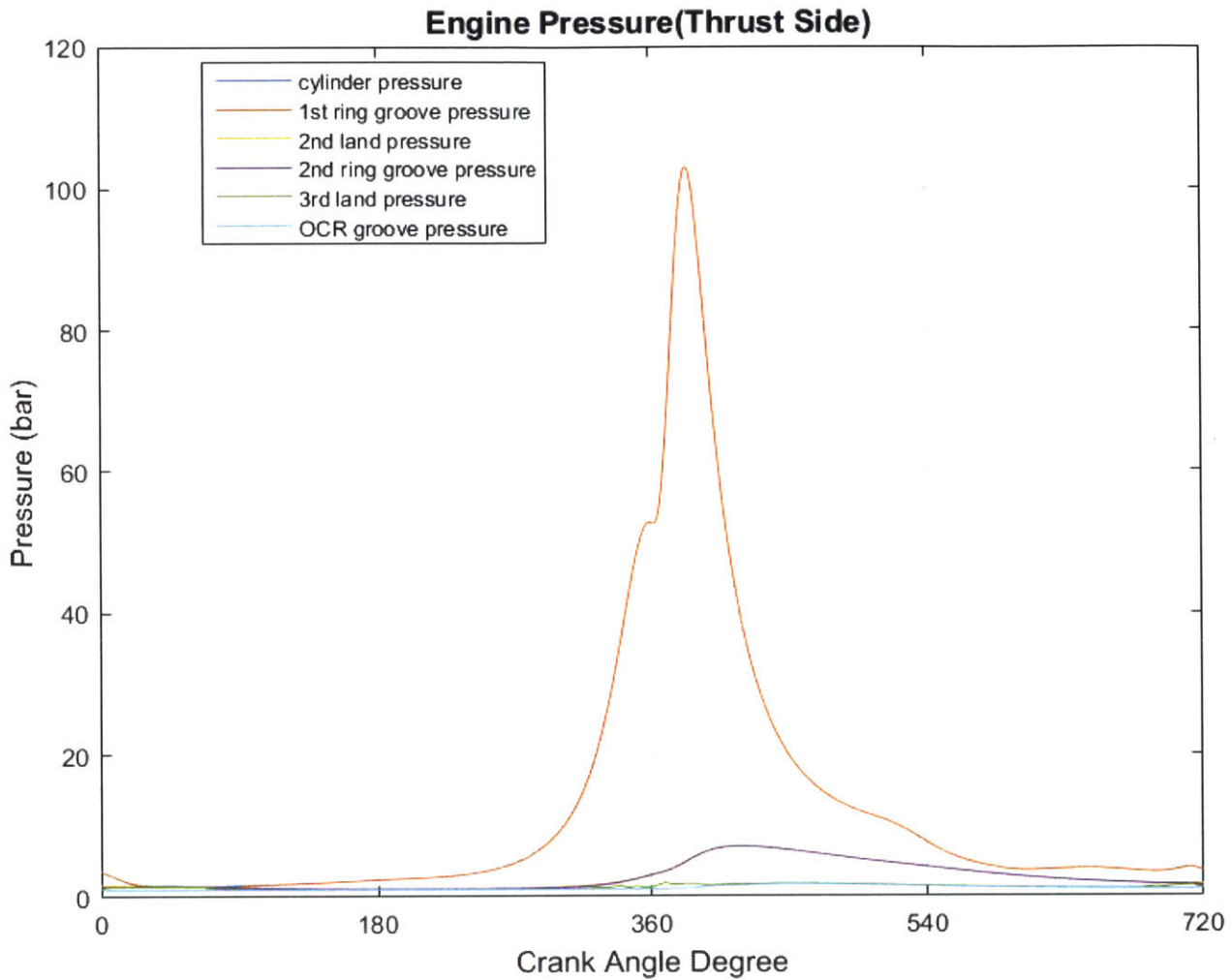
Figure 65 Inter-Ring Gas Pressure and Comparison between CBM and 2D Model

Figure 66 shows the results of gas pressure at different piston positions. In the figure, the blue, red and green curves represent the results of the pressure at the thrust side, the anti-thrust side and the pin side (90° away from the thrust side). Based on the results, we can figure it out that the variance of the gas pressure in the circumferential direction is small because of the relatively large clearances between the piston lands and the bore and between the ring backs and the piston grooves. The gas pressure in the 3rd ring groove should be close to the crank case pressure all the time because it is connected to the crank case through the drain holes which is shown in Figure 66.
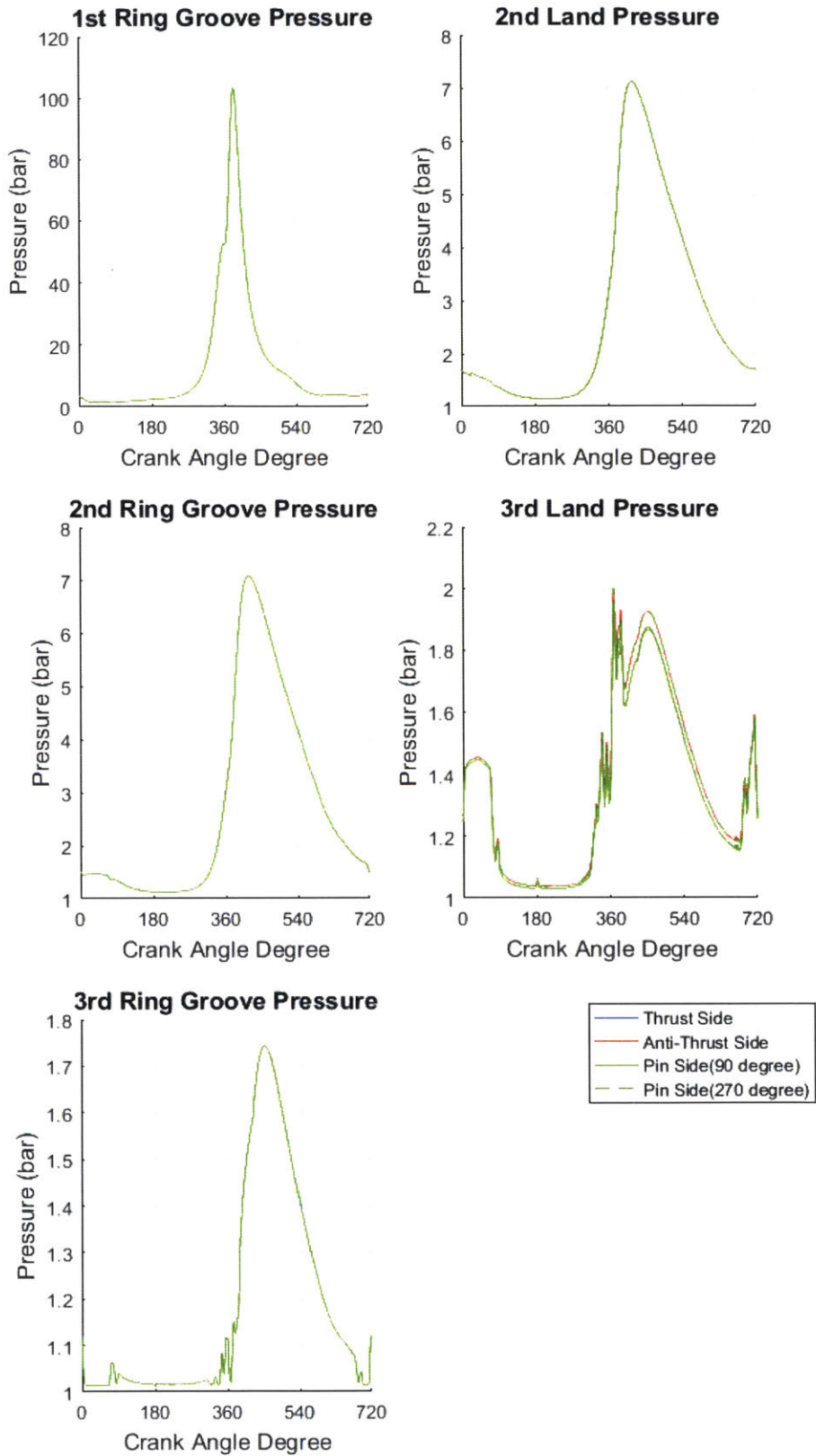
Figure 66 Inter-Ring Gas Pressure at Different Circumferential Positions

Figure 67 demonstrates the dynamic behavior of the top ring. Axial lift is defined as the ring axial lift or axial distance between the lower flanks of the ring and groove at the centroid position of the ring cross section. Ring twist relative to the piston is defined as the angle between the lower flanks of the ring and groove, as shown in Figure 68. At the beginning of the intake stroke, the inertial force is pointing upwards but the downward gas pressure force overcomes the inertial force, pushing the ring to the lower flank of the groove. Later in the intake stroke, the pressure in the combustion chamber drops quickly (Figure 65) and the inertial force becomes dominant and starts to lift the ring. The inertia switches direction at the middle of the intake stroke, and the gas pressure in the combustion chamber starts to rise. The ring is pushed back to the groove lower flank again. Then during the rest of the cycle, the gas pressure in the combustion chamber remains high and pushes the ring tightly against the groove lower flank.
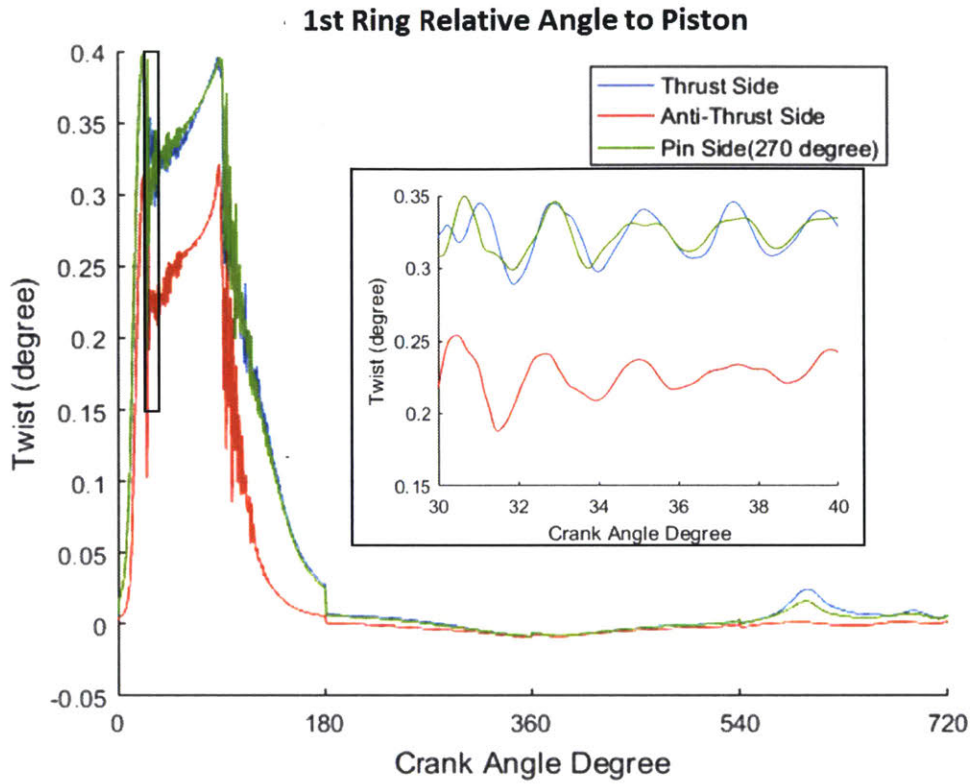
1st Ring Relative Angle to Piston
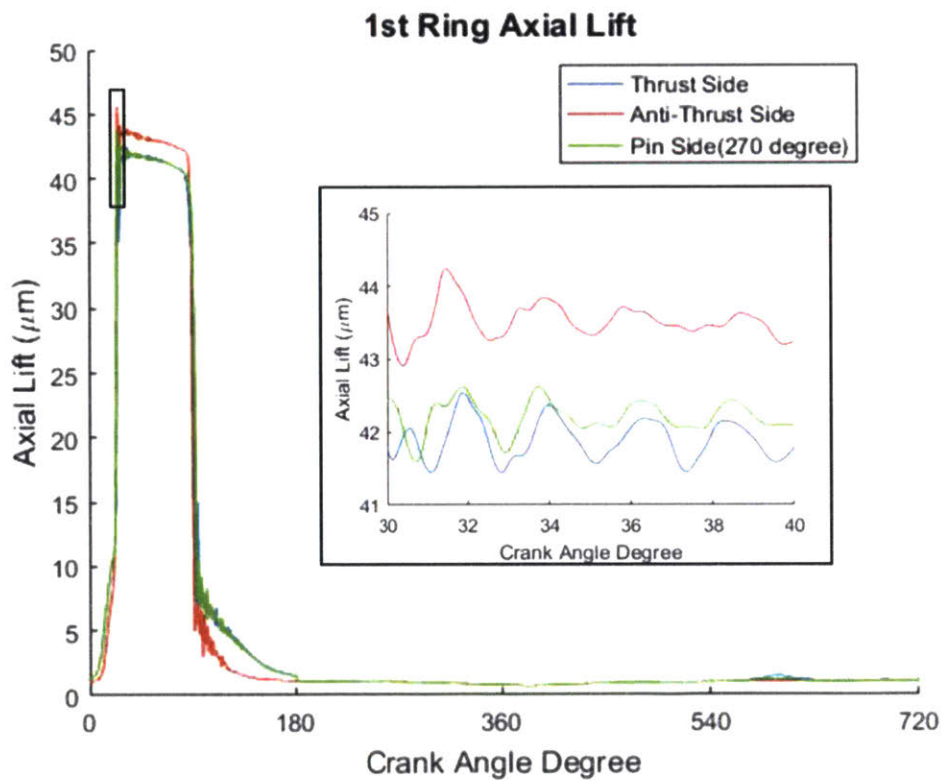
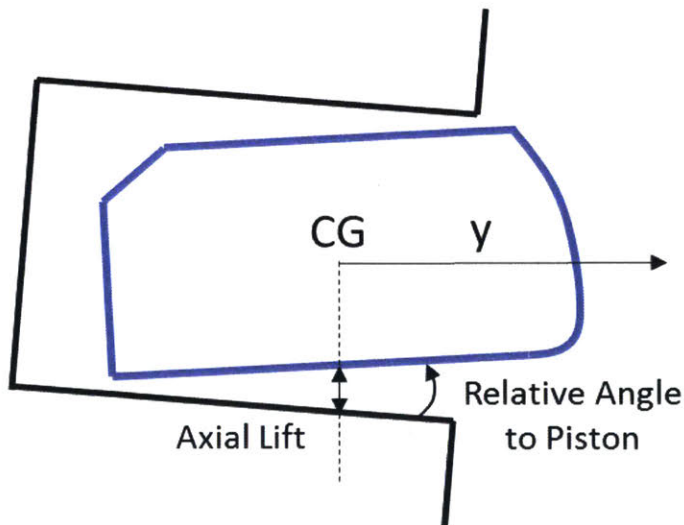*Figure 67 Results of the Top Ring Dynamics*

Figure 68 Definition of Axial Lift and Relative Ange to Piston

When the top ring is assembled inside the engine, it has a positive static twist due to the internal stress change from the free state. When the gas pressure in the combustion chamber still remains low during the first half of the intake stroke, the inertial force pushes the ring to the groove upper flank and

the contact force from the groove upper flank generates a negative twisting moment to the ring (as shown in Figure 69). When the ring is approaching mid-stroke, the negative twisting moment decreases with a decrease of the inertial force. As a result, around 90 crank angle degree there is a rise of ring twist relative to the piston. Then when the gas pressure in the combustion chamber quickly increases, pressure force pushes the ring downwards and generates a large negative twisting moment. The pressure force is so large that it is able to push the ring almost parallel to the groove flank and at its maximum value the ring even has a negative twist relative to the piston (Figure 69). In the exhaust stroke, the combustion chamber pressure drops faster than the pressure in the piston 2nd land and the negative twisting moment decreases. Correspondingly, around 600 crank angle degree the ring twist has a small rise.
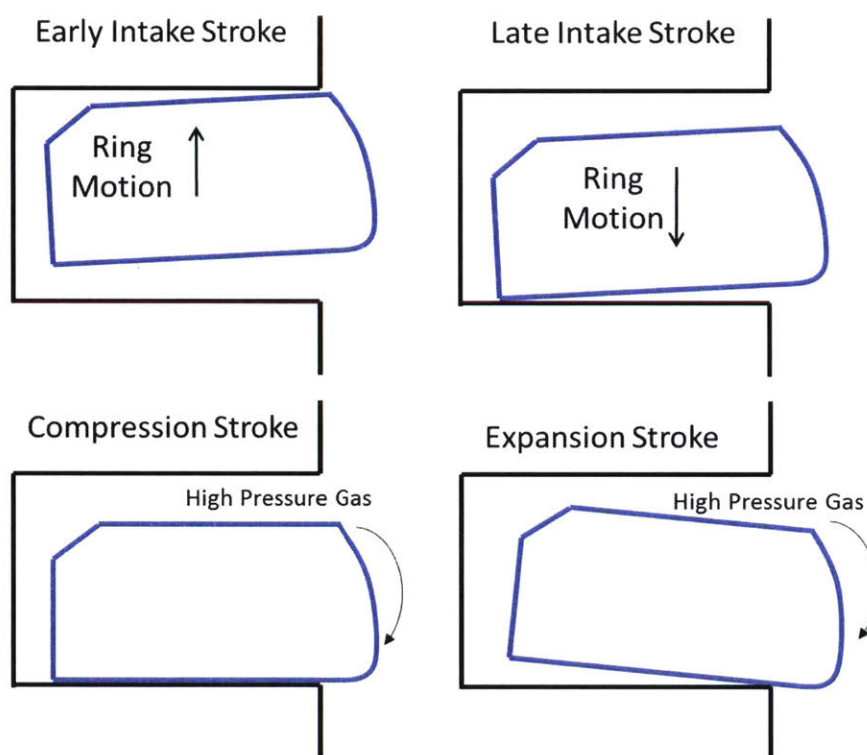

Figure 69 Typical Positions of the Top Ring with a Positive Static Twist

There are some high frequency oscillations in the ring dynamic behavior. It is often a question whether these oscillations reflect the real physics or are caused by numerical instability since the external forces such as pressure force or inertial force changes much slower with time. When we zoom in around where oscillation happens, we can find that the ring movement is fairly smooth for the small time step used (the time step used in this example is 0.01 crank angle degree). The frequency is roughly

on an order of $10^4 Hz$. There are two relevant frequencies in the system that we may relate this frequency to. The first is the natural frequency of the ring beam, which is approximately $\sqrt{\frac{EI}{\rho AR}} \sim 50Hz$, and is much less than what we observe. The second is the frequency related to the contact between the ring and the groove. When the ring has interaction with the groove, the contact pressure is a function of clearance as well as ring neutral axial displacement. Then it can be treated as a non-linear spring force. The ring-groove interaction can be simplified as a rigid-body-spring system, as shown in Figure 70. The spring force is non-linear and its simplified stiffness has a form of $\frac{P_k z a_r}{\sigma}\left(\Omega - \frac{h}{\sigma}\right)^{z-1}$, where P_k, z and Ω are constants from Greenwood-Tripp model, σ represents the combined roughness of the ring and groove flanks and a_r is the ring width in radial direction. This stiffness varies from 0 to $3.1542 \times 10^{12} N/m^2$. The natural frequency of this system can be approximated as $\sqrt{\frac{\frac{P_k z a_r}{\sigma}\left(\Omega - \frac{h}{\sigma}\right)^{z-1}}{\rho A}}$, varying from 0Hz to 1e7Hz. The observed frequency is within this range. Thus the oscillation of the ring position, which occurs mainly after the ring makes initial contact with the groove, is the true dynamics that can only be resolved with sufficiently small time step as used in this example.
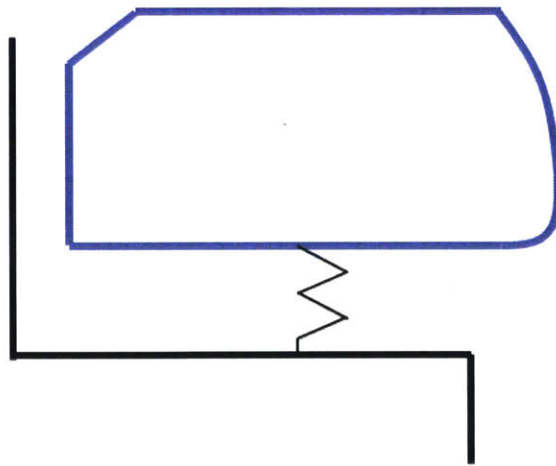

Figure 70 Simplified Ring-Groove Interaction

Figure 72 shows the ID and OD clearances between the lower flanks of the top ring and the top ring groove (as defined in Figure 71, the green arrow shows the ID clearance between the lower flanks of the ring and the ring groove and the red arrow shows the corresponding OD clearance.). In the first half of the intake stroke, the ring has a positive twist relative to the piston (shown in Figure 73), so the OD clearance is larger than the ID clearance. There is an insignificant variance along the circumferential direction introduced by the piston secondary motion, the asymmetric ring static twist (Figure 42) and

the gap position. However, their effects becomes negligible compared to the gas pressure in the rest of the cycle and the top ring is pushed against the ring lower flank tightly with very small clearance.
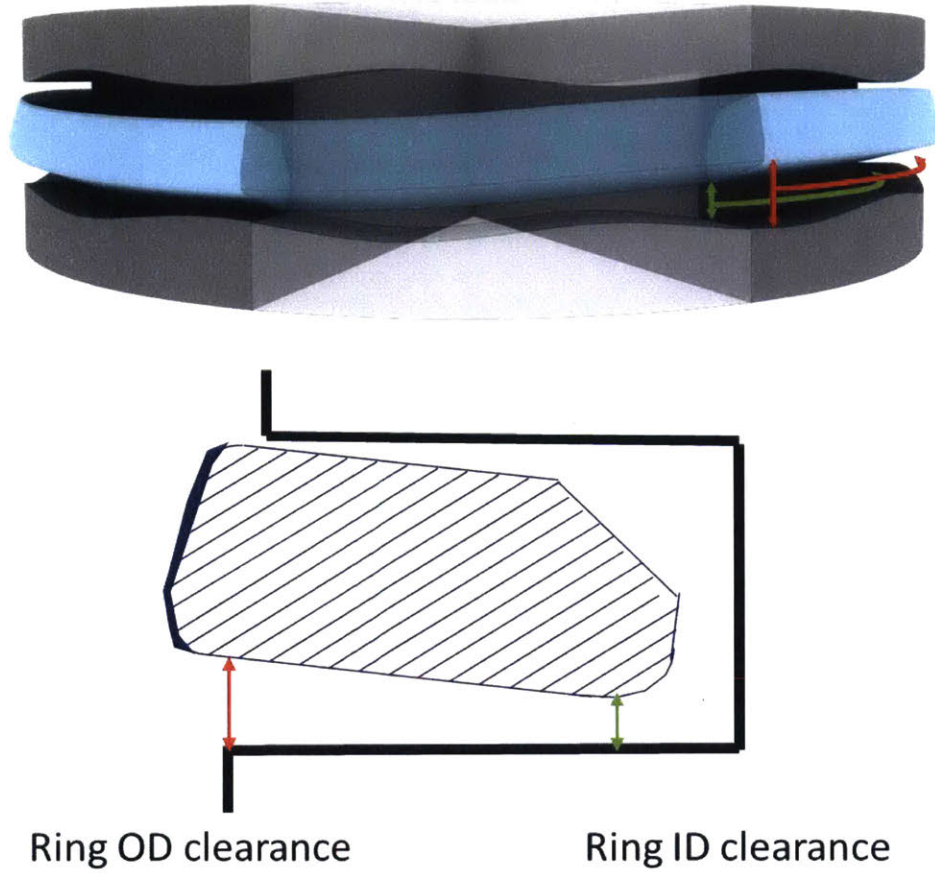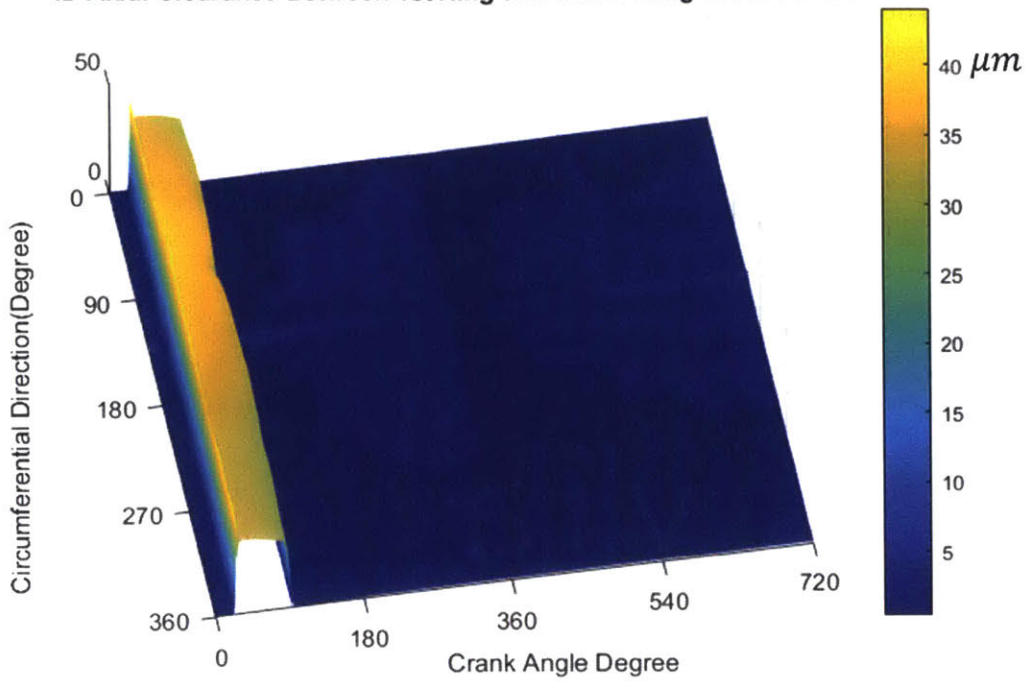

Ring OD clearance   **Ring ID clearance**

Figure 71 the Ring ID and OD Axial Clearance

ID Axial Clearance Between 1st Ring and Lower Ring Groove Flank

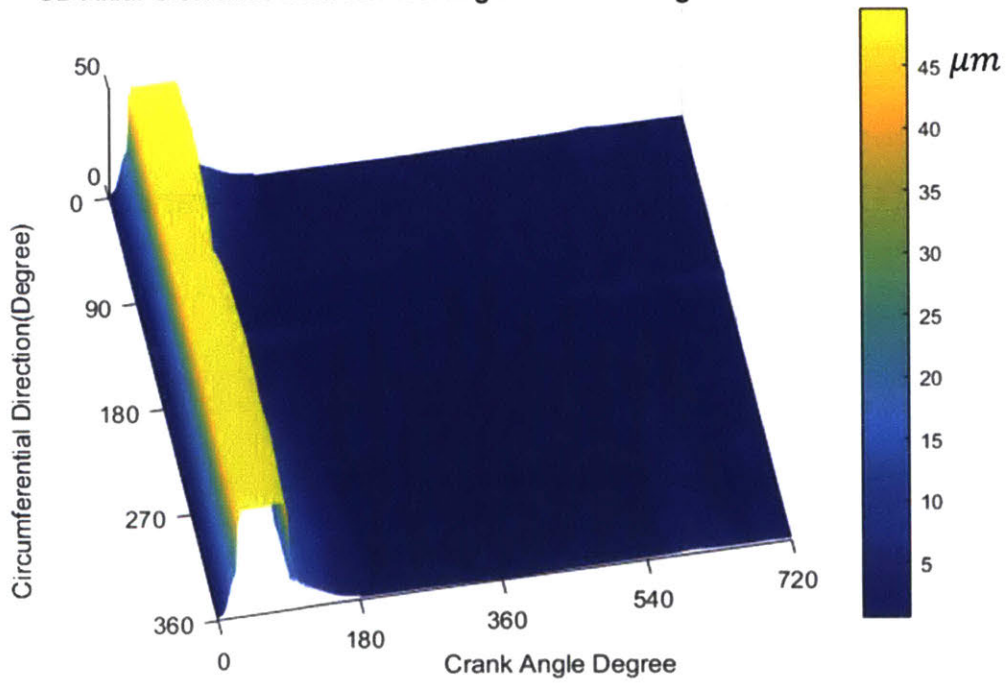
OD Axial Clearance Between 1st Ring and Lower Ring Groove Flank

Figure 72 Clearance between the Lower Flanks of the Top Ring and Top Ring Groove
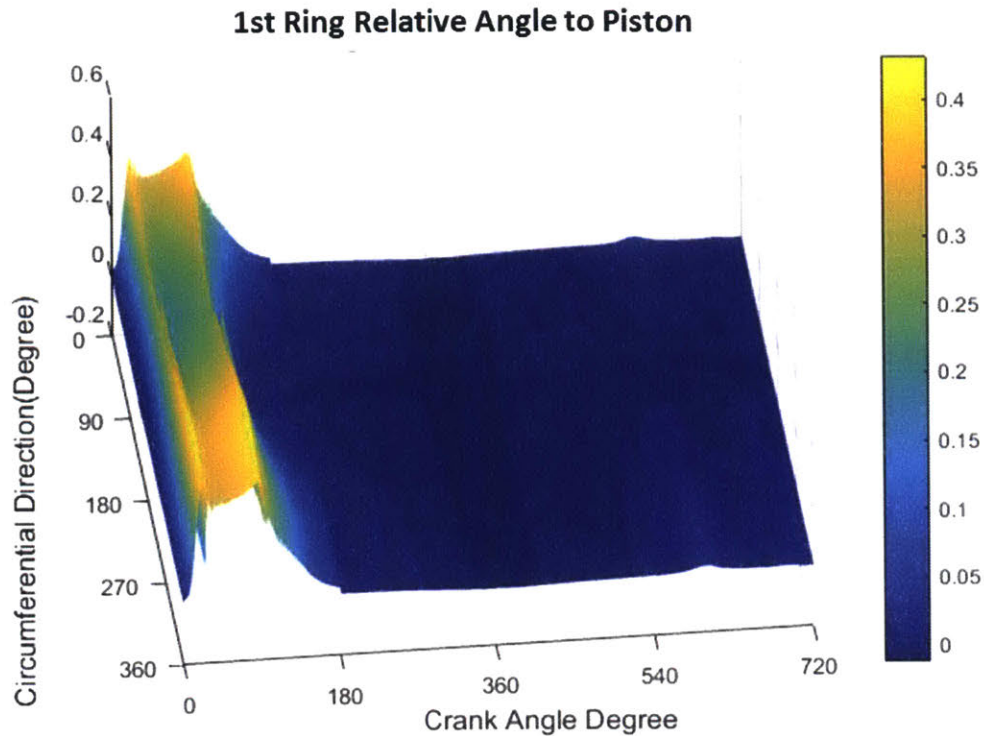
Figure 73 The Top Ring Relative Angle to the Piston

Figure 74 shows the results of gas flow rate through the clearances between the top ring both flanks and the groove. Negative value implies that gas flows out of the ring groove and positive value implies that gas flows into the ring groove. After the top dead center in the expansion stroke, the pressure in the combustion chamber drops faster than the pressure inside the top ring groove and reverse flow (gas flow from the lower part of the piston to the upper part of the piston; gas flows from the top ring groove to the combustion chamber) happens between the upper flanks of the ring and the groove. In most of the time, the top ring is pushed to the groove lower flank by the high pressure gas and closes the clearance that allows gas to flow. Therefore, the gas flow rate between the lower flanks of the ring and the groove remains zero for most of the time. Exception happens when the top ring is lifted by the inertial force in the first half of the intake stroke and the channel is open and allows gas flow from the top ring groove to the piston 2nd land.

Gas Flow Rate between 1st Ring and Upper Ring Groove Flank (g/mm s)

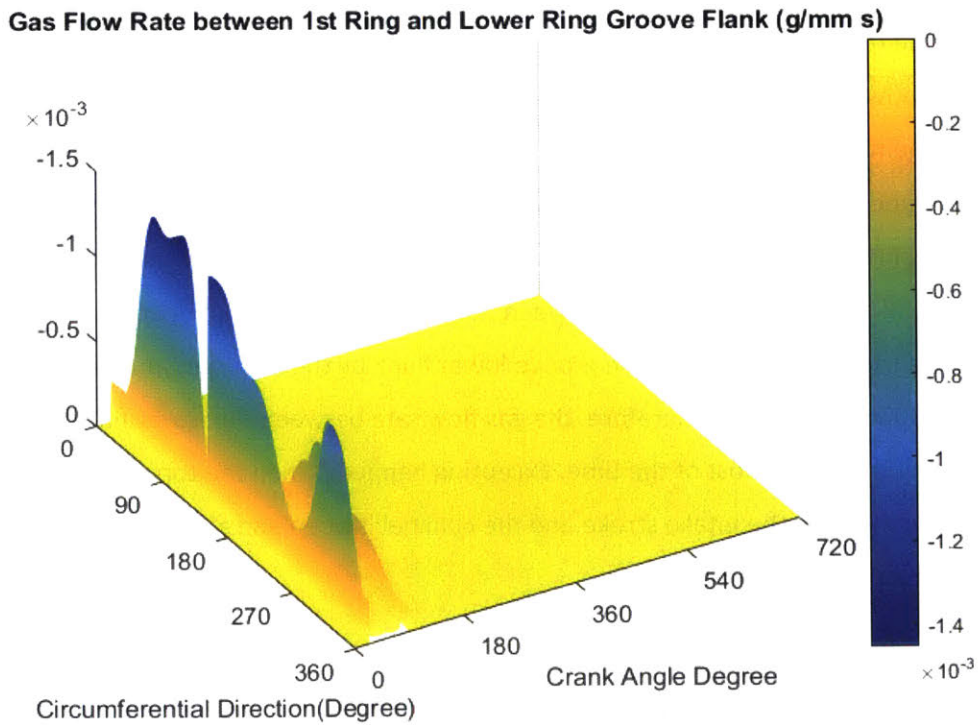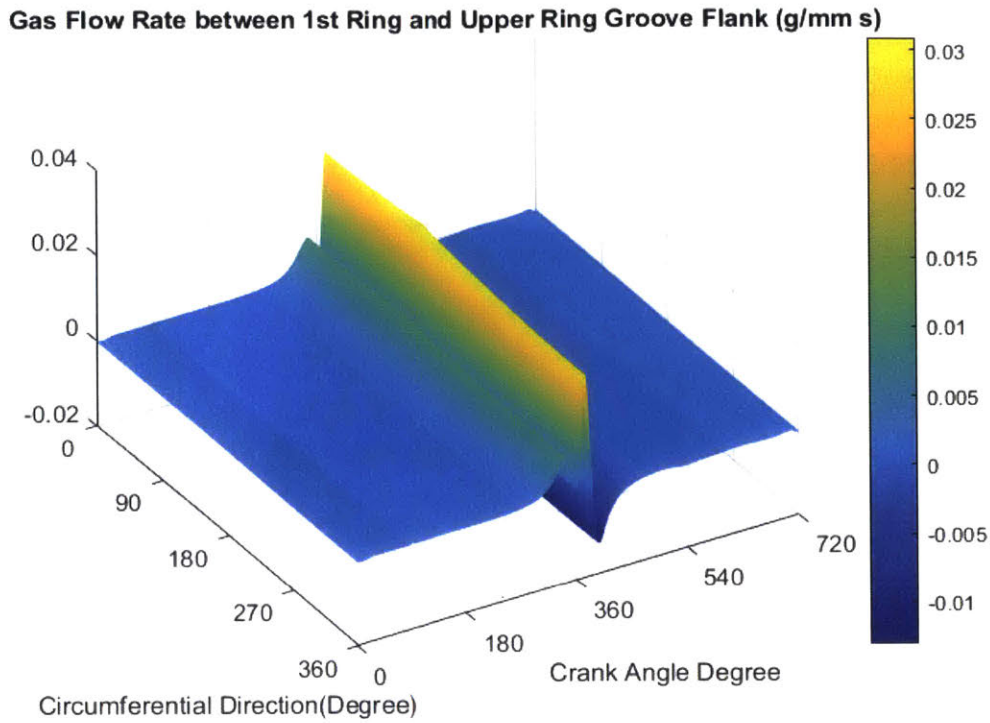**Gas Flow Rate between 1st Ring and Lower Ring Groove Flank (g/mm s)**

Figure 74 Gas Flow Rate between the Top Ring Both Flanks and the Ring groove

Figure 75 demonstrates the results of the second ring dynamic behavior. Unlike the top ring, gas pressure above the second ring is much lower and in most of the time the inertial force is at least

comparable to the gas pressure force. At the first half of the intake stroke, the ring is lifted due to the upward inertial force. Because of the positive twist, the second ring and the upper groove have the minimum clearance at the outside edge and the contact force from the groove flank gives a negative twisting moment. At the middle of the intake stroke, the inertial force switches direction. The second ring moves downwards and contacts with the lower flank of the groove. Due to the positive twist, the inside edge has the smallest clearance with the groove and the contact force gives a negative twisting moment. The moments acting on the ring are not sufficient to twist the ring significantly during the intake stroke. Then in the later part of the compression stroke, the pressure in the 2nd land starts to build up and gas pressure effect becomes dominant and pushes the second ring to the lower flank of the groove. The gas pressure generates a negative twisting moment and twists the second ring almost in parallel to the ring groove, which is close to the situation shown in Figure 69. At the beginning of the expansion stroke, there is a rise in both the axial lift and relative twist to the piston, which is caused by the rise of pressure in the piston 3rd land (Figure 65). Around the top dead center of the expansion stroke, the OCR is lifted by the inertial force and the friction force. The gap between the upper flanks of the OCR and its groove is closed, which stops gas flow from the 3rd land to the OCR groove and raises the pressure in the 3rd land. When the pressure increases to some certain value, the pressure force overcomes the inertial force and the friction force and pushes the OCR downwards. Then the pressure in the 3rd land is released and the pressure in the 2nd land keeps increasing, so the second ring is pushed downwards and twisted negatively again after a short period of rising. In the exhaust stroke, the pressure in the 2nd land drops, as well as the associated negative twisting moment, and the inertial force becomes important again. A lift of the second ring and rise of the relative twist to the piston are observed around the end of the exhaust stroke.
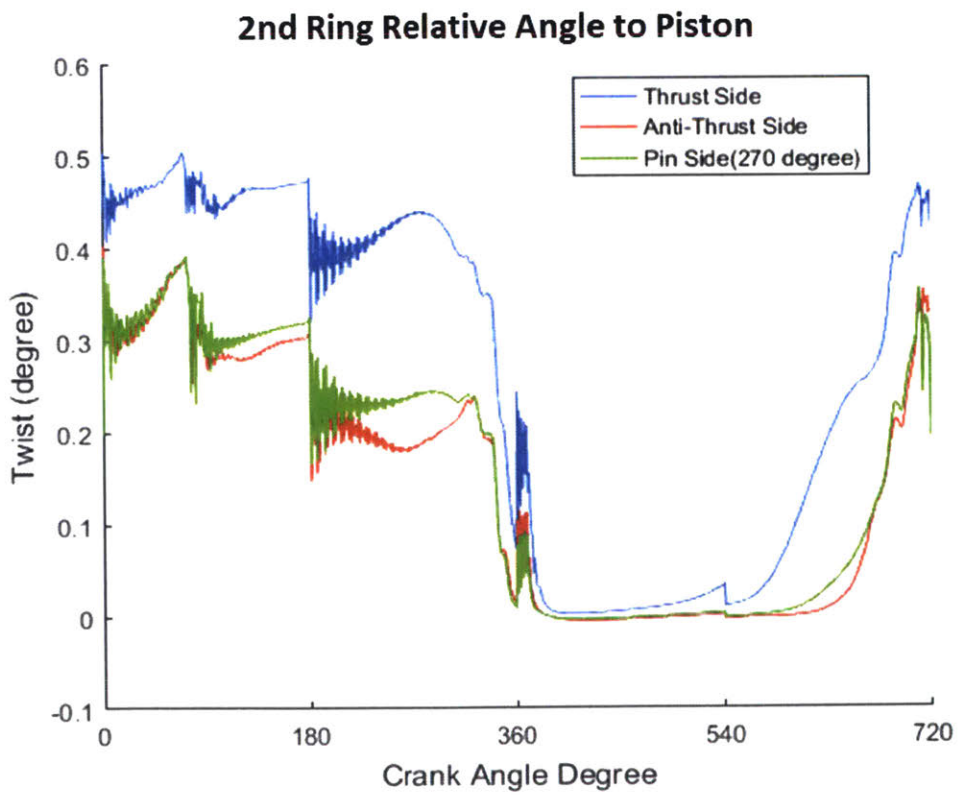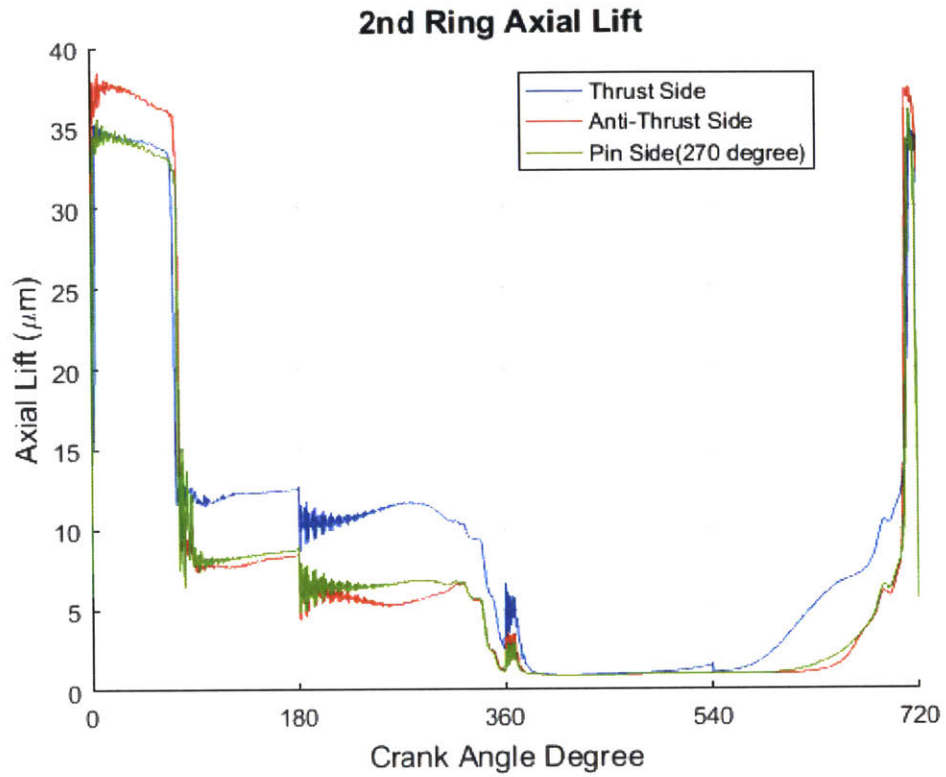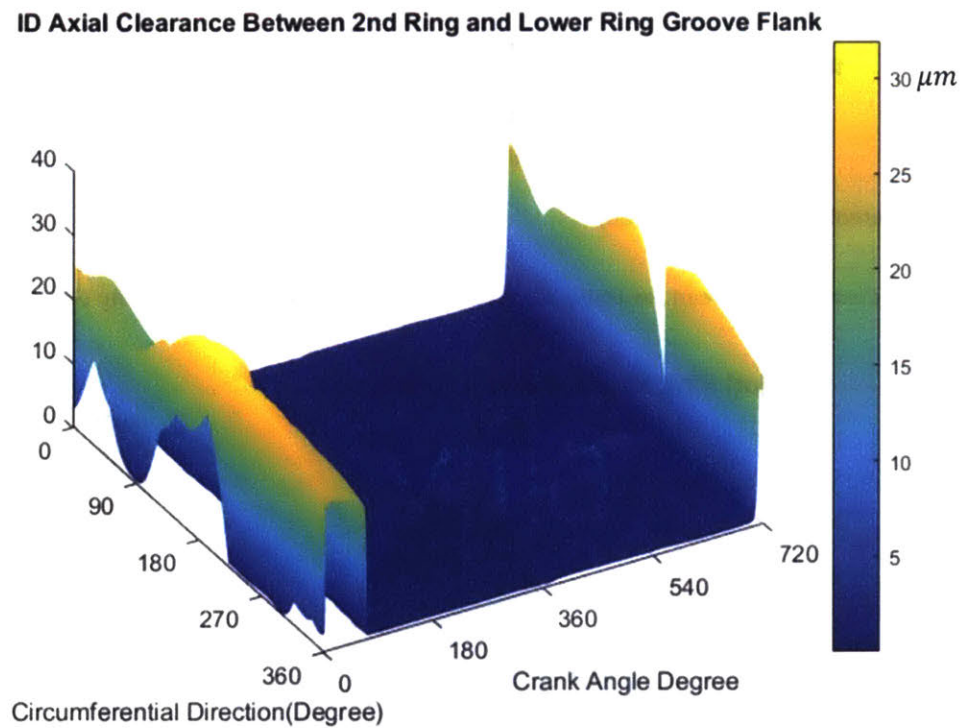
2nd Ring Axial Lift

2nd Ring Relative Angle to Piston

Figure 75 Results of the Second Ring Dynamics

Figure 76 shows the ID and OD clearances between the lower flanks of the second ring and the second ring groove. Because of the positive twist relative to the piston (shown in Figure 77), the OD clearance between the lower flanks of the ring and the groove is larger than the ID clearance. The variation along the circumference is caused by three asymmetrical factors, namely, piston secondary motion, ring twist variation (Figure 42), and the existence of the ring gap. Compared to the top ring, the gas pressure around the second ring is mild and these asymmetric factors are significant enough to make a difference. However, in the expansion stroke when the pressure in the 2nd land increases, these factors tend to become less significant compared to the pressure force and the variation along the circumferential direction reduces.

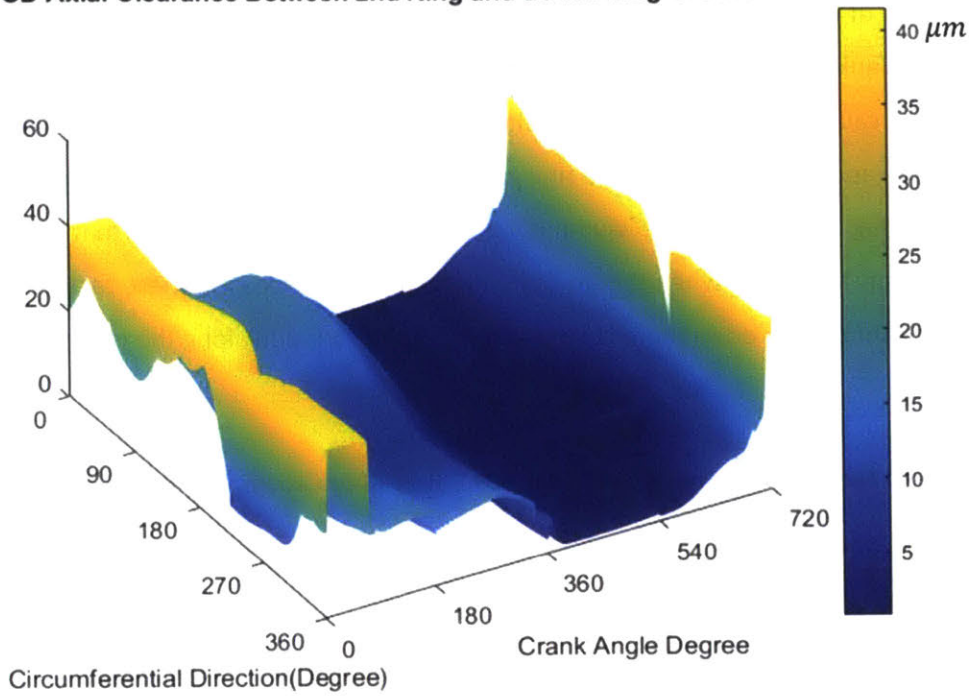**ID Axial Clearance Between 2nd Ring and Lower Ring Groove Flank**

115

OD Axial Clearance Between 2nd Ring and Lower Ring Groove Flank

Figure 76 Clearance between the Lower Flanks of the Second Ring and Second Ring Groove
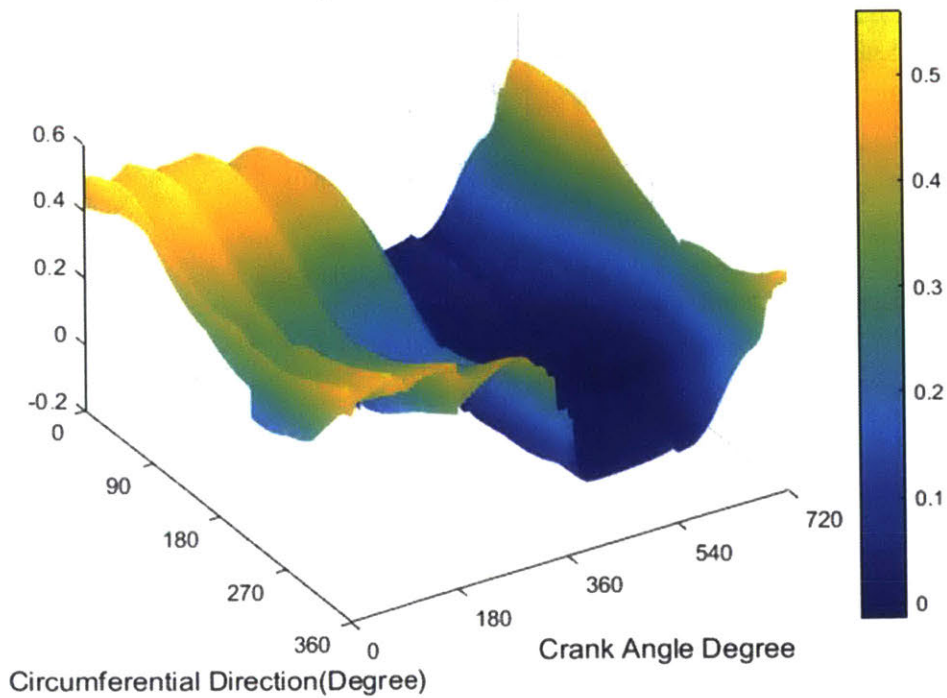
2nd Ring Relative Angle to Piston

Figure 77 The Second Ring Relative Angle to the Piston

Figure 78 shows the results of gas flow rate through the clearances between the second ring flanks and the groove. The sign convention for the gas flow rate is that the flow into the groove is positive and out negative. For most part of the cycle, the second ring stays in contact with the groove lower flank and the gas flows into the ring groove from the 2nd land with a flow rate increasing with the 2nd land pressure. Only at the end of the exhaust stroke and the beginning of the intake stroke, inertial force is able to lift the ring and open the clearance between the ring and the groove lower flanks while closing the clearance between the ring and the groove upper flank. In this case, gas is able to flow from the 2nd ring groove to the 3rd land but is blocked from the other side.
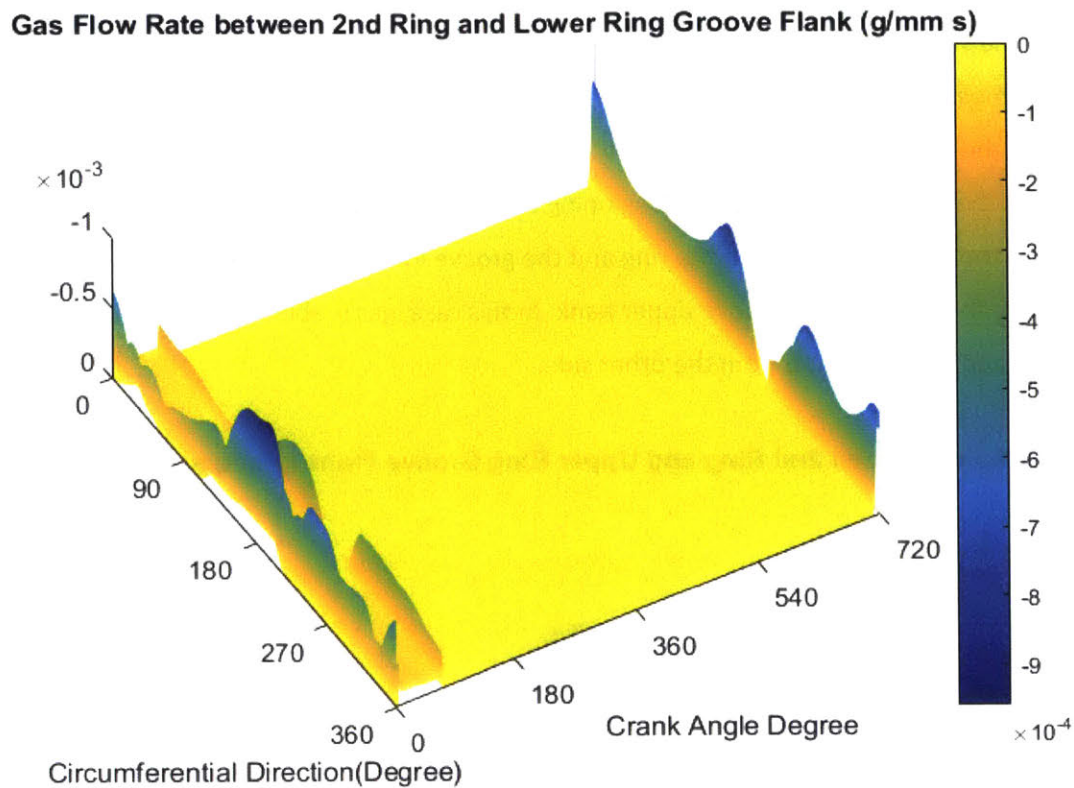

Gas Flow Rate between 2nd Ring and Upper Ring Groove Flank (g/mm s)
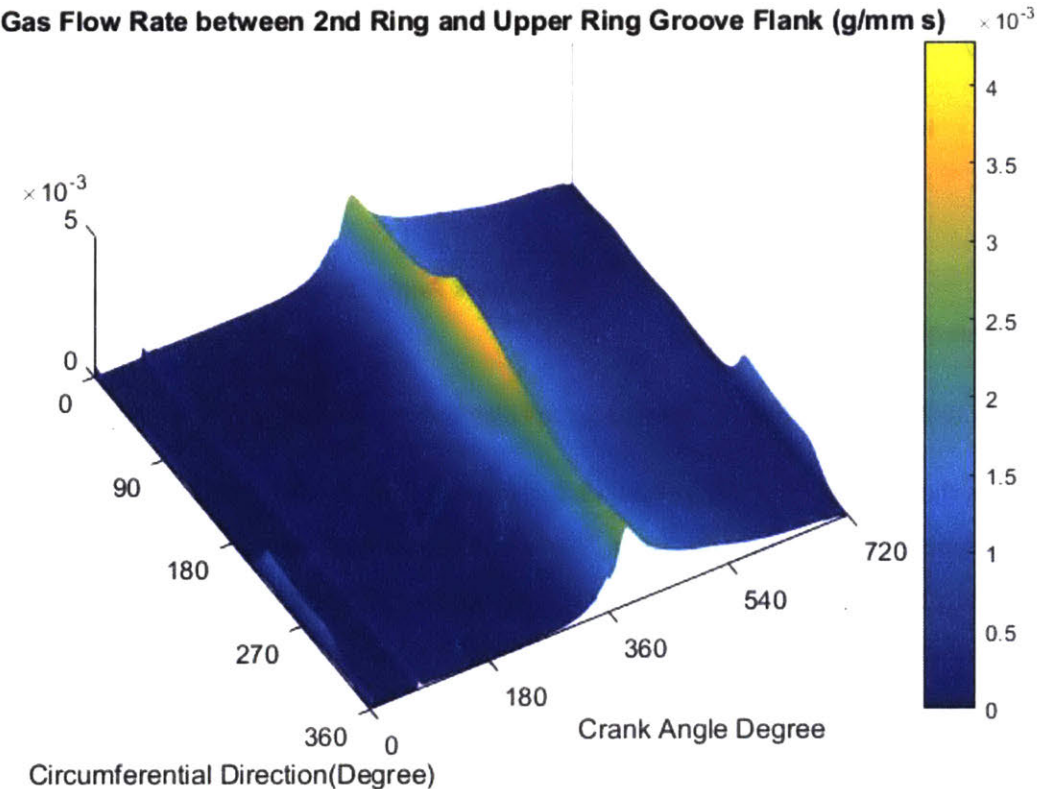
Figure 78 Gas Flow Rate between the Second Ring Both Flanks and the Ring groove

Figure 81 shows the results of the OCR dynamics. It is obvious from the results of the OCR axial lift that the OCR has severe flutter in axial direction. The reasons come from several aspects. First, compared to the top two rings, the OCR is thinner and has less resistance to deformation. Second, the ring flutters when there is a right match between the inertial force and the gas pressure. In this case, the gas pressure force acting on the OCR is on the order of 100N/m which is comparable to that of the inertial force (~50N/m). Thirdly, there are drain holes in the OCR groove. When the OCR is pushed down due to an increase in the 3rd land pressure, gas at the 3rd land is able to be quickly released through the drain holes and the pressure decreases. Then the inertial force may be able to lift the ring again and the process is repeated. Finally, the OCR has no static twist when it is assembled into the piston. Though the piston groove has a negative tilt ($\sim -0.1°$) due to thermal distortion which provides the OCR a positive twist relative to the piston, the magnitude is not sufficient to stabilize the ring. Piston secondary motion may tilt the groove largely enough ($\sim 0.3°$) causing the OCR a negative twist relative to the piston especially at the thrust side and anti-thrust side. As shown in Figure 79, a positive piston tilt causes a negative twist between the ring and the groove at the thrust side and a positive twist at the anti-thrust side. Contrarily, a negative piston tilt causes a positive twist between the ring and the groove at the

118

thrust side and a negative twist at the anti-thrust side. A negative twist introduces instability when the upper land gas pressure is high, as shown in Figure 80.
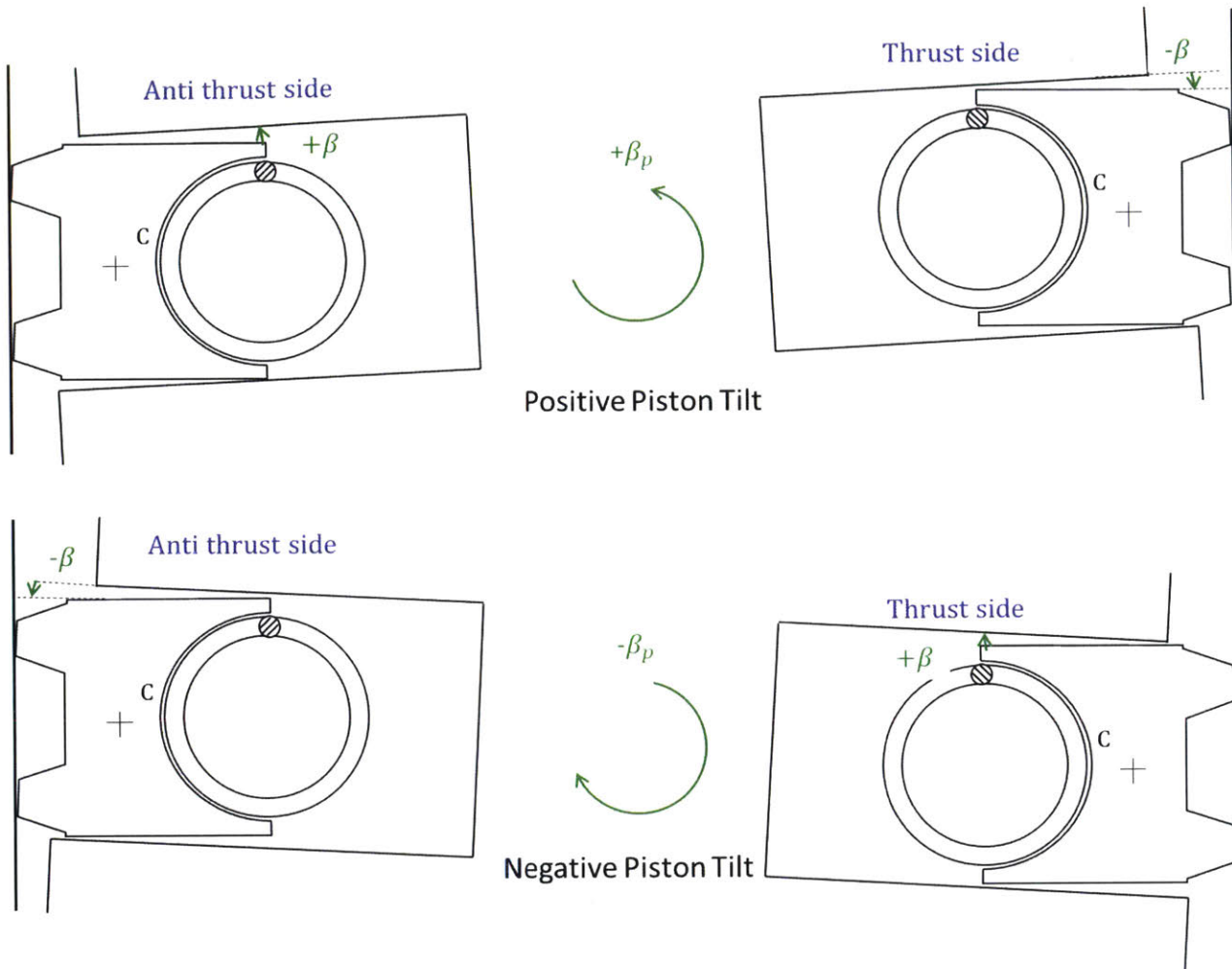

Figure 79 Piston Tilt and Relative Ring Twist to the Piston

Net downward force from gas pressure is low

Inertial force

Net downward force from gas pressure is high

Inertial force

Net downward force from gas pressure is high

Inertial force

Net downward force from gas pressure is low
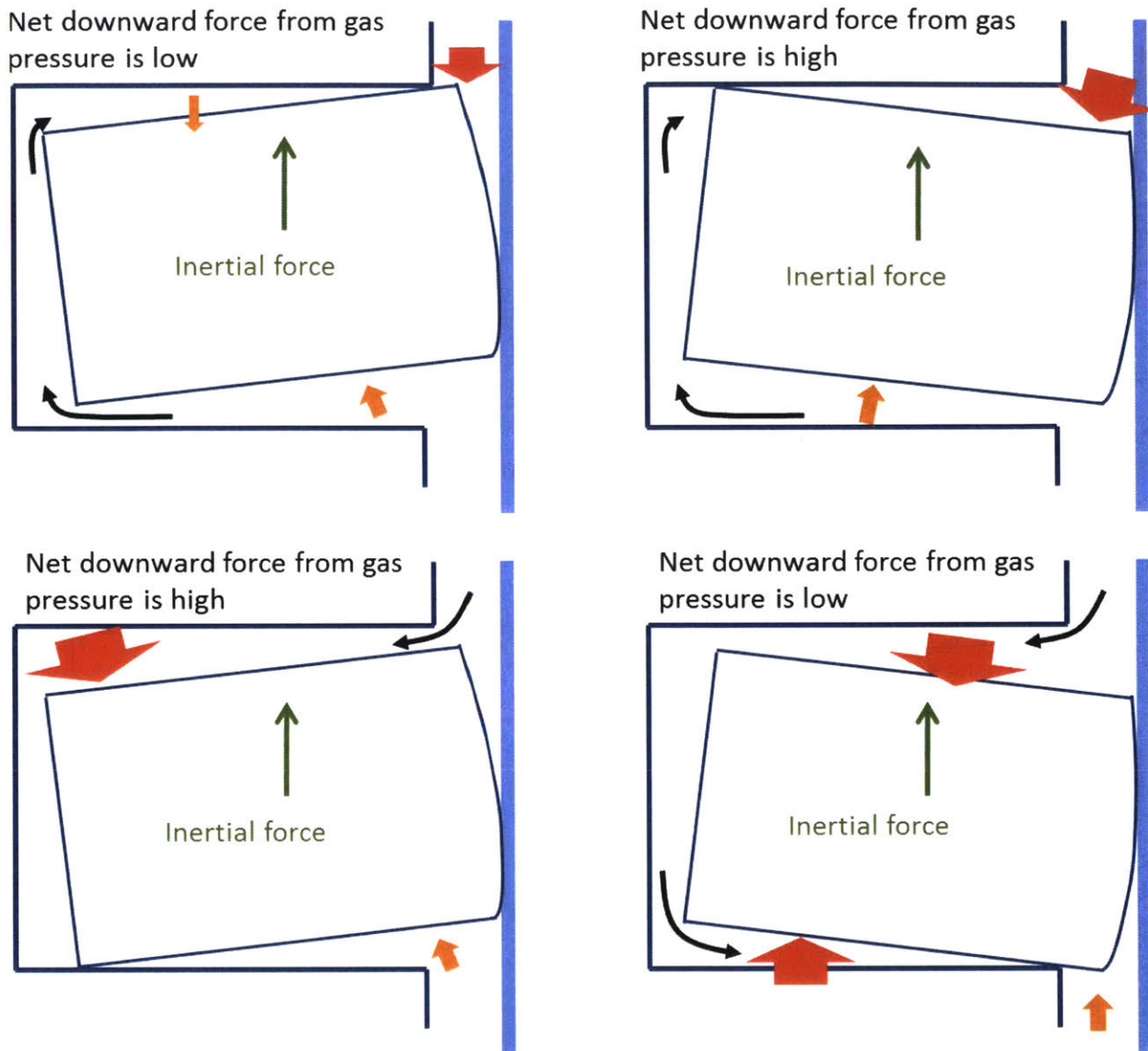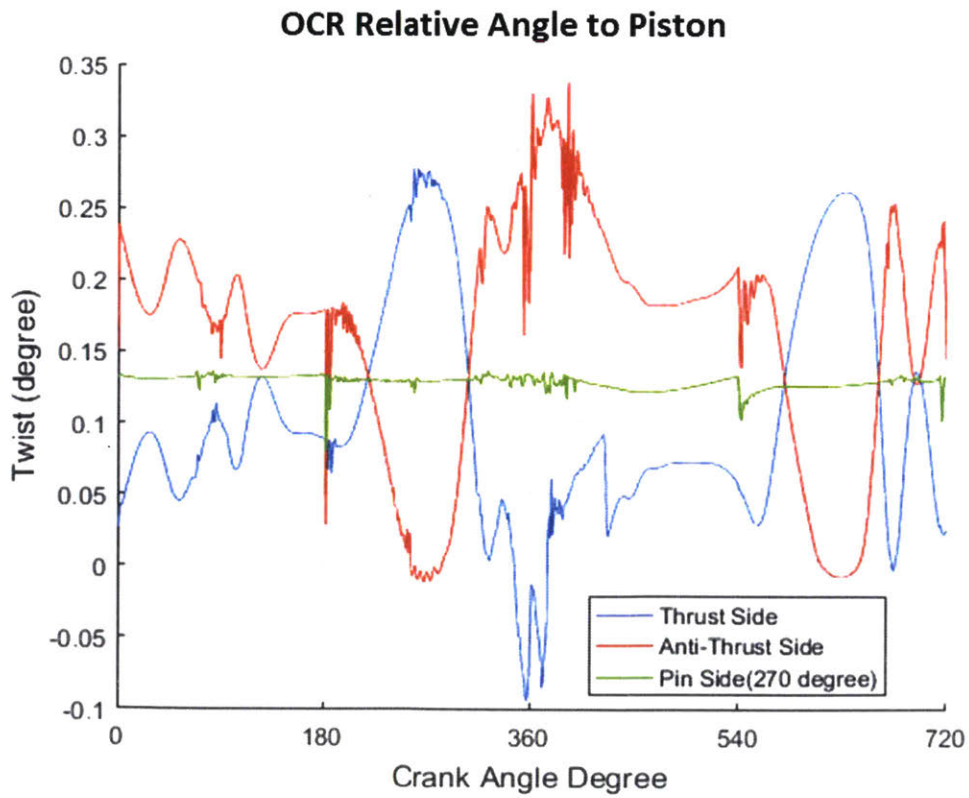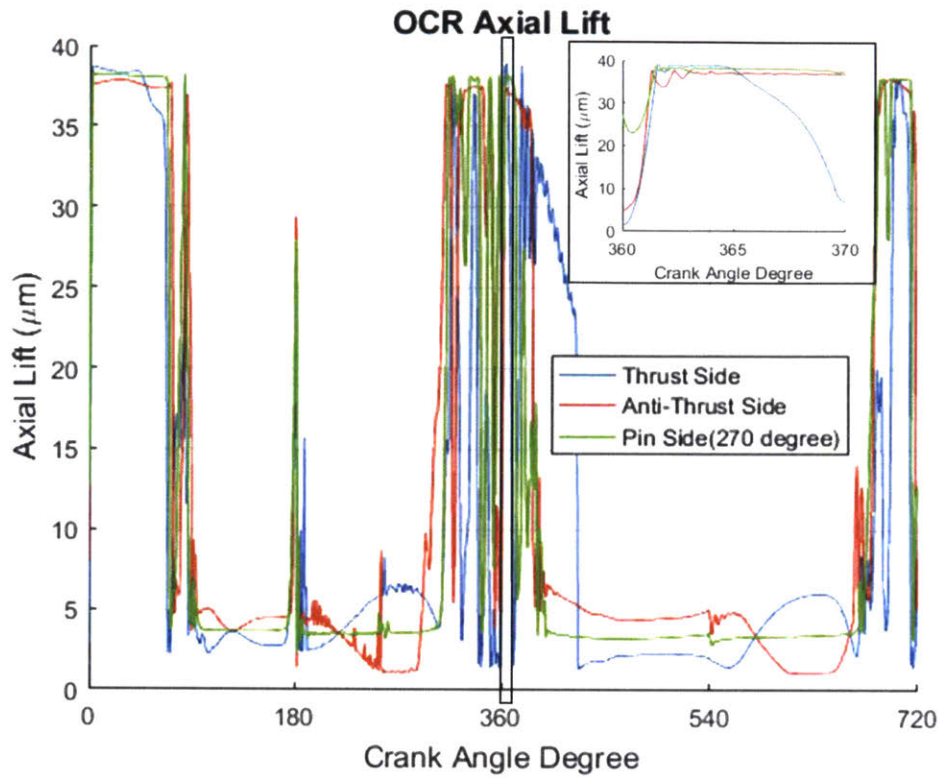
Inertial force

Figure 80 Difference between Positive and Negative Ring Angle Relative to the Piston with Higher Upper Land Gas Pressure

OCR Axial Lift

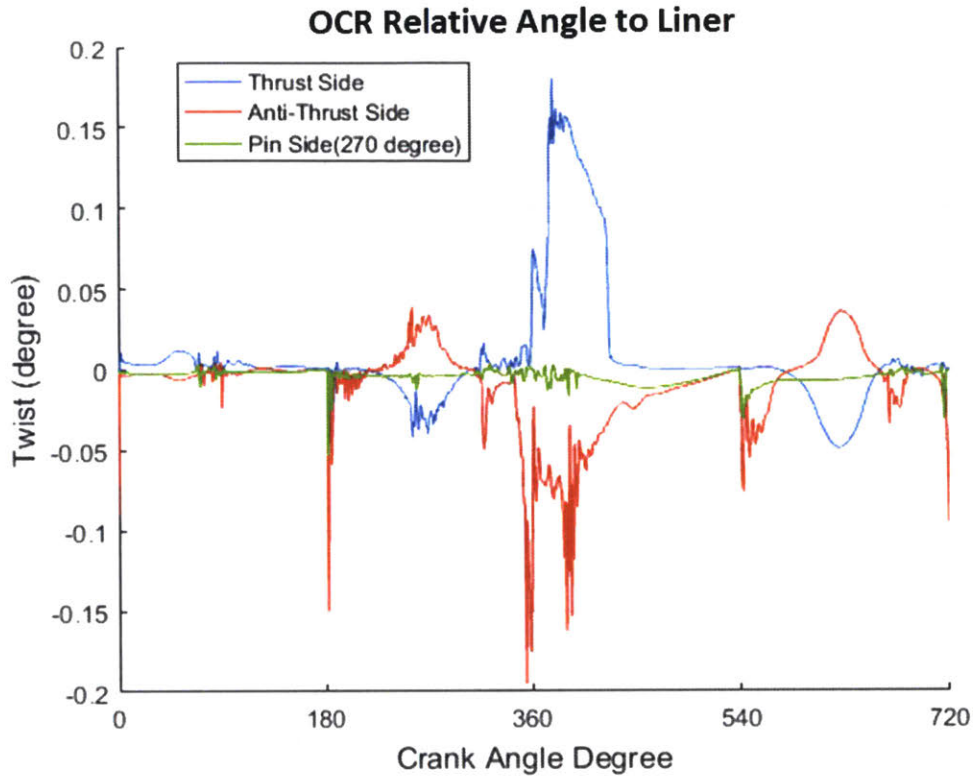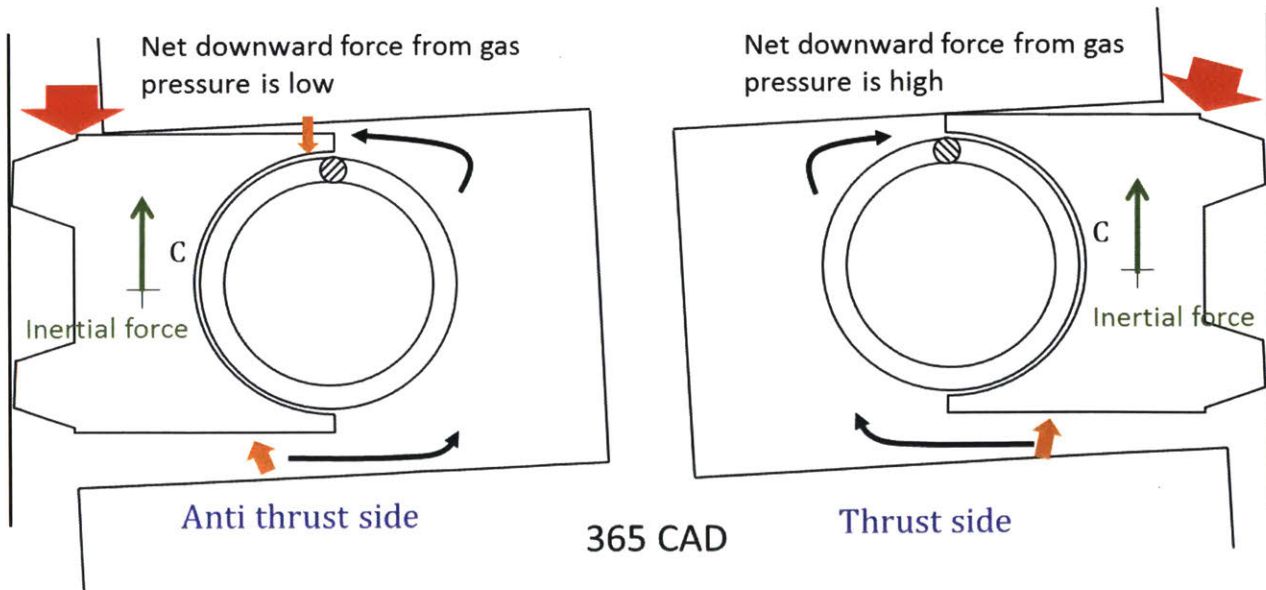**OCR Relative Angle to Piston**

Figure 81 Results of the OCR Dynamics

Net downward force from gas pressure is low

Net downward force from gas pressure is high

C

Inertial force

C

Inertial force

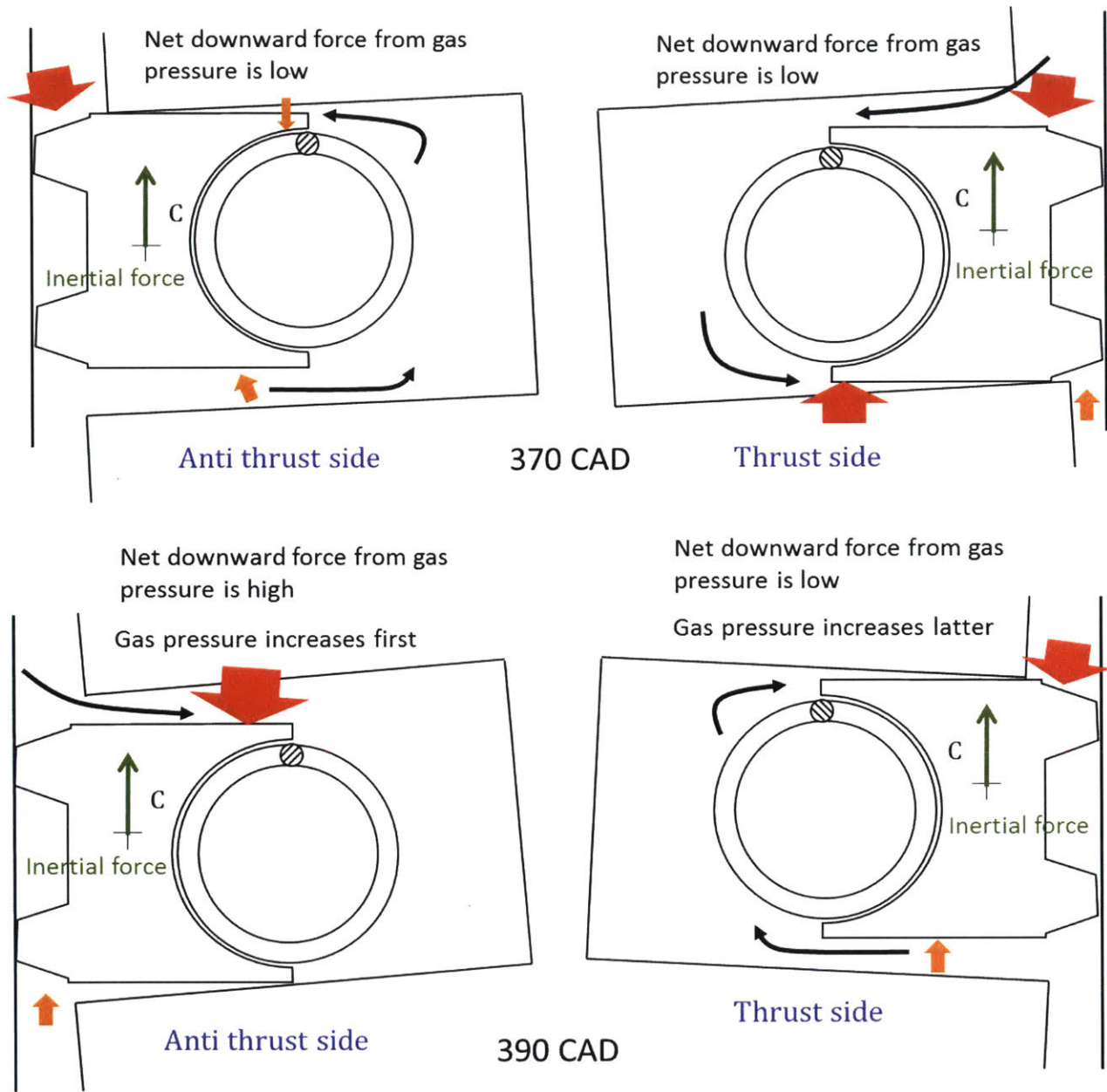Anti thrust side

365 CAD

Thrust side

Figure 82 the OCR Flutter from 365CAD to 390 CAD

The ring flutter looks complex but it is not completely chaotic. Around the top dead center of the expansion stroke, the thrust side of the OCR moves downwards first (Figure 81), because at this position the OCR has a negative twist relative to the piston and the net downward force from gas pressure is higher than other parts of the OCR with a positive twist relative to the piston (as shown in Figure 81 and Figure 82). When the OCR stays in contact with the lower groove flank at the thrust side, the OCR groove connects to the piston 3rd land and the net downward force decreases. Therefore, the thrust side of the OCR is raised by the inertial force again (at 370 CAD). When approaching the middle of the expansion

stroke (390 CAD), the thrust side of the OCR twist relative to the piston becomes positive. The thrust side of the OCR moves downwards later than the anti-thrust side and the pin side (270° away from the thrust side). This is because the second ring gap is set at the angular position of 225° away from the thrust side. Thus, the 3rd land pressure is higher around the anti-thrust side and the pin side (270° away from the thrust side), as shown in Figure 83.
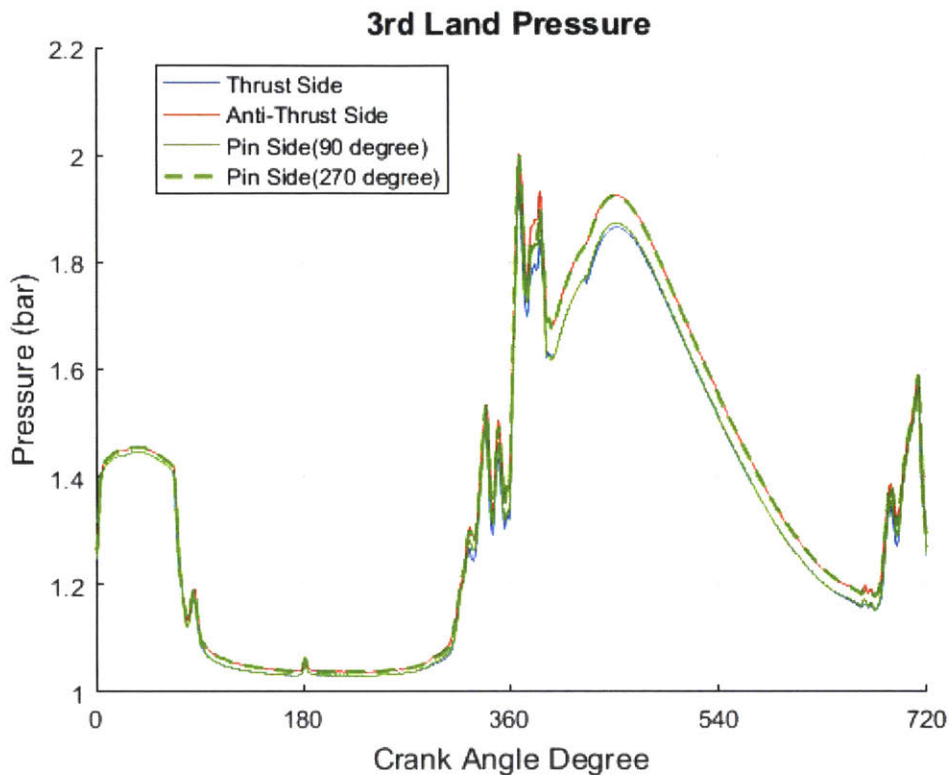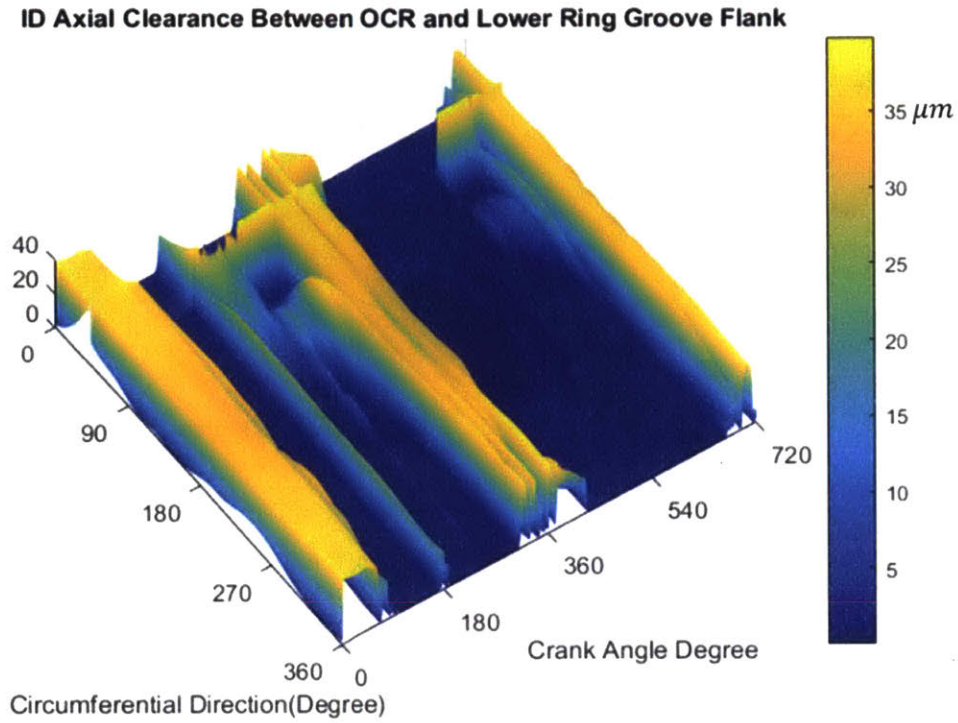
3rd Land Pressure

Figure 83 Results of Third Land Pressure

The TLOCR has two lands and a relatively large ring tension, which can help the OCR conform to the liner at both lands. As a result, the TLOCR has smaller relative angle to the liner compared to the twist relative to the piston. The OCR relative angle to the liner is dominated by the piston secondary motion. At the pin sides, the piston dynamic tilt has no impact due to the orthogonality. Thus, the OCR relative angle to the liner is close to zero at the pin sides. The thrust side and the anti-thrust side have approximately symmetric behavior because they are at the two ends of the piston which are symmetric about the piston pin.

Figure 84 demonstrates the results of the ID and OD clearances between the lower flanks of the OCR and the OCR groove. Because of the negative thermal tilt of the piston OCR groove, the OCR has positive ring twist relative to the piston in most of the time (shown in Figure 85). Therefore, its OD clearance

124

between the lower flanks of the ring and the groove is larger than the ID clearance in most of the time. Since the effects of the ring gap and the piston secondary motion are comparable to the effect of the gas pressure, it has a more obvious variance along the circumferential direction even in the compression and the expansion strokes.
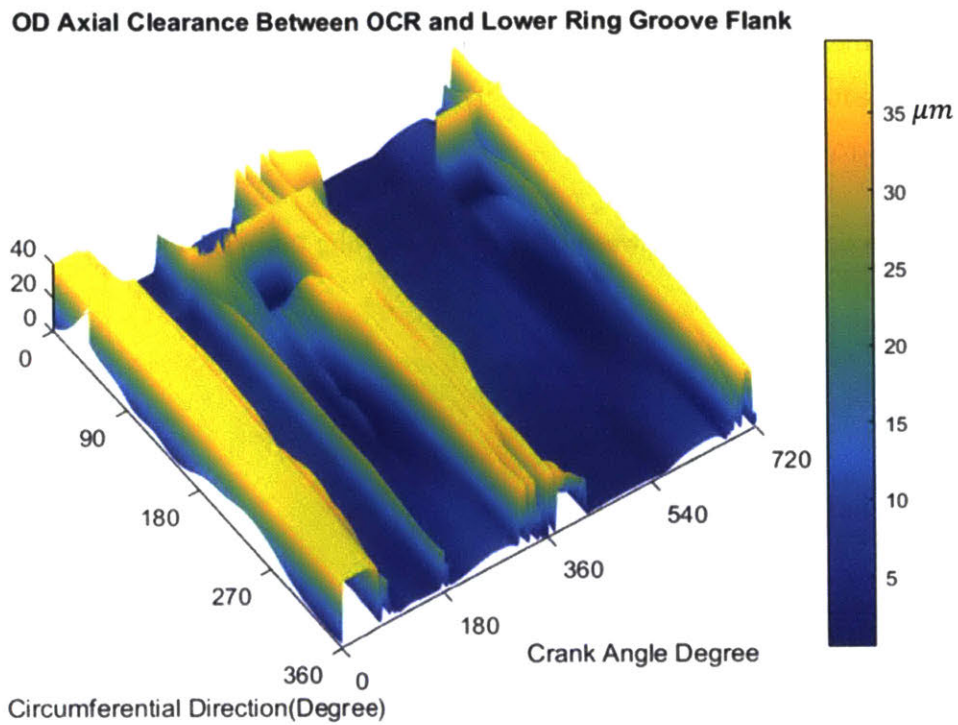
ID Axial Clearance Between OCR and Lower Ring Groove Flank

OD Axial Clearance Between OCR and Lower Ring Groove Flank

Figure 84 Clearance between the Lower Flanks of the OCR and OCR Groove
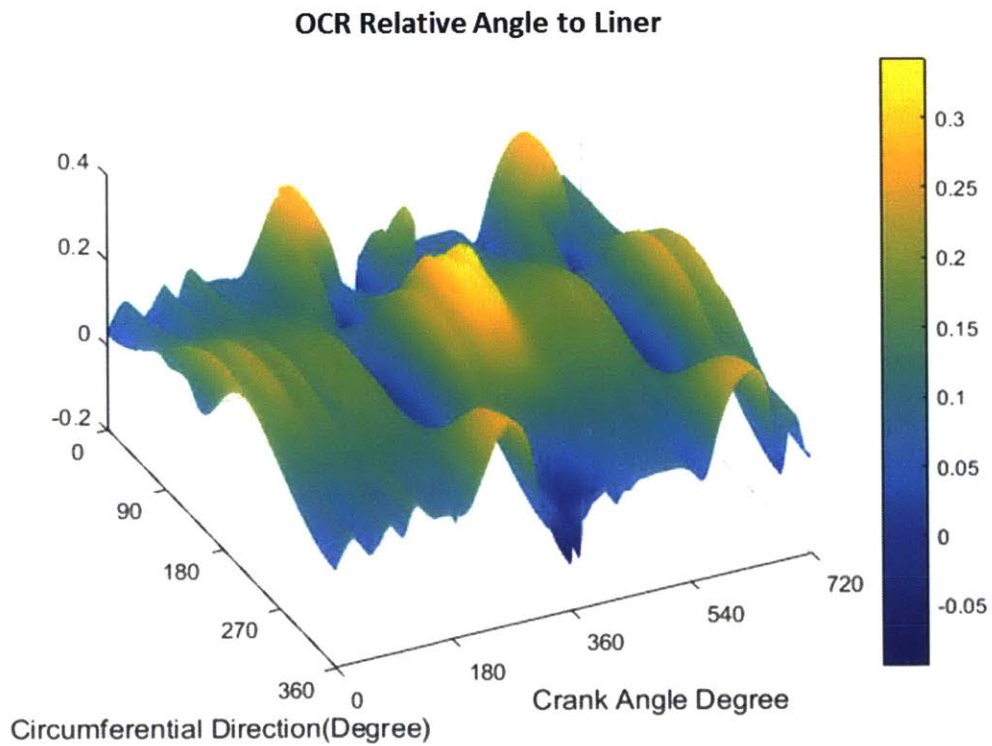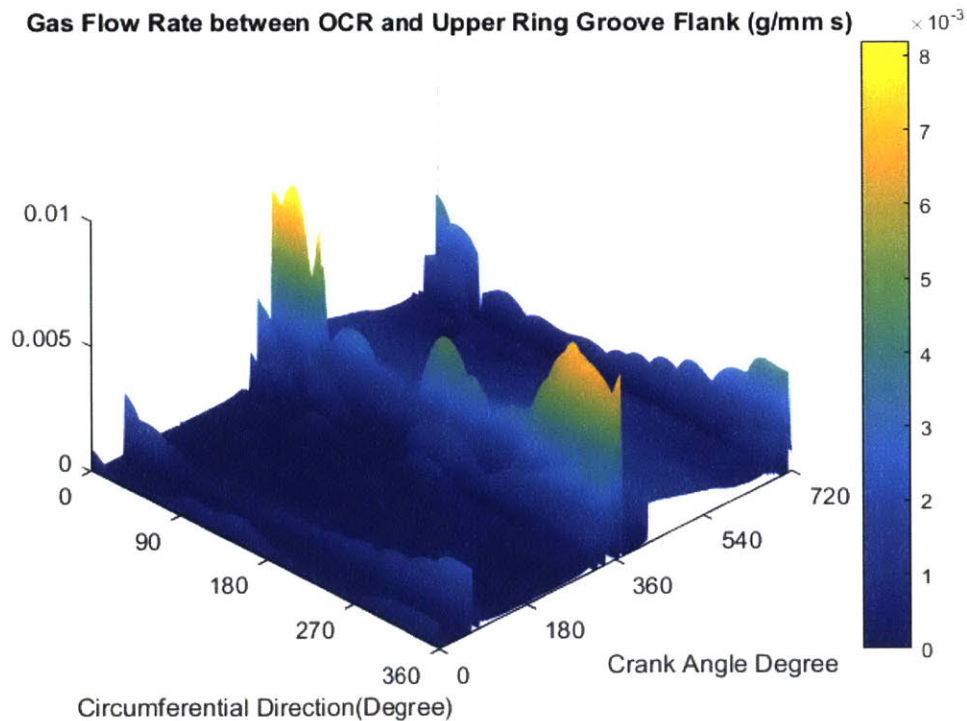
OCR Relative Angle to Liner

Figure 85 The OCR Relative Angle to the Piston

Figure 86 demonstrates the results of gas flow rate through the clearances between the OCR both flanks and the groove. Negative value implies that gas flows out of the ring groove and positive value implies that gas flows into the ring groove. The variance of the ring-groove clearance along the circumferential direction leads to a variance of the gas flow rate. The gas flow from the OCR groove to the piston 4th land contributes to part of the blow-by. The Blow-by gas also comes from the gas flow from the OCR groove to the crank case through the drain holes and from the piston 3rd land to the 4th land through the OCR gap.

Figure 87 shows the gas flow rate around the OCR. As defined earlier, for the mass flow rates through the drain holes and the clearances between the OCR and the groove, the negative value implies that gas flows out of the ring groove and positive value into the ring groove. For the mass flow rates into the ring gap area, the positive value implies that gas flow into the ring gap and negative value out of the ring gap. The results clearly show that most of the gas into the ring groove leaks through the drain holes. The only period with a bit flow through the lower flanks is when the OCR is bent around the thrust side in early part of the expansion stroke (Figure 81, Figure 84 and Figure 86).
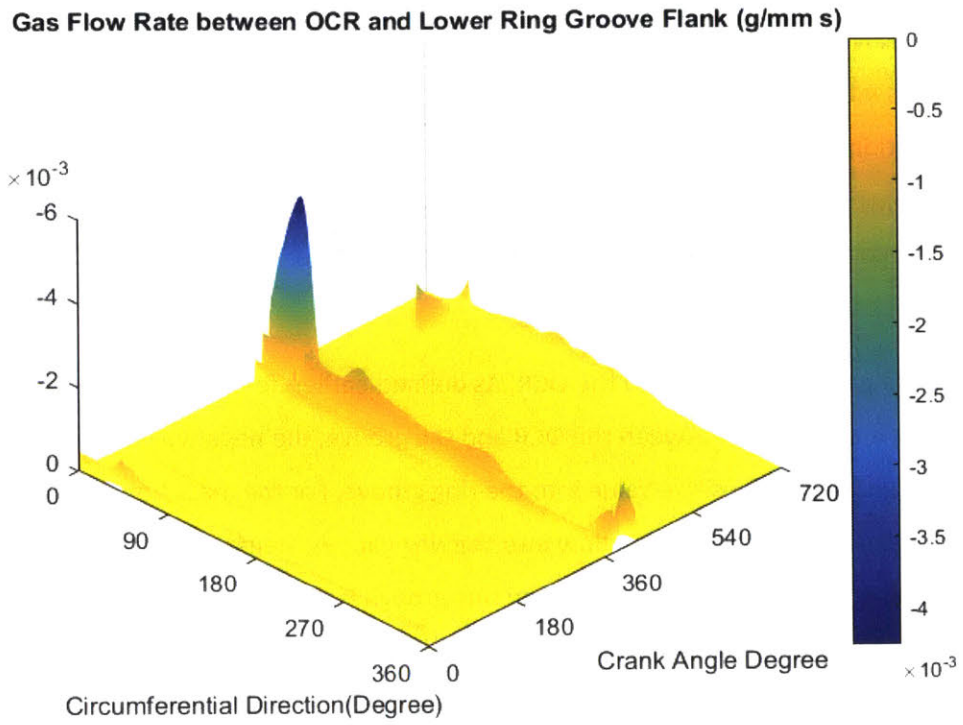

Gas Flow Rate between OCR and Upper Ring Groove Flank (g/mm s)

Figure 86 Gas Flow Rate between the OCR Both Flanks and the Ring groove
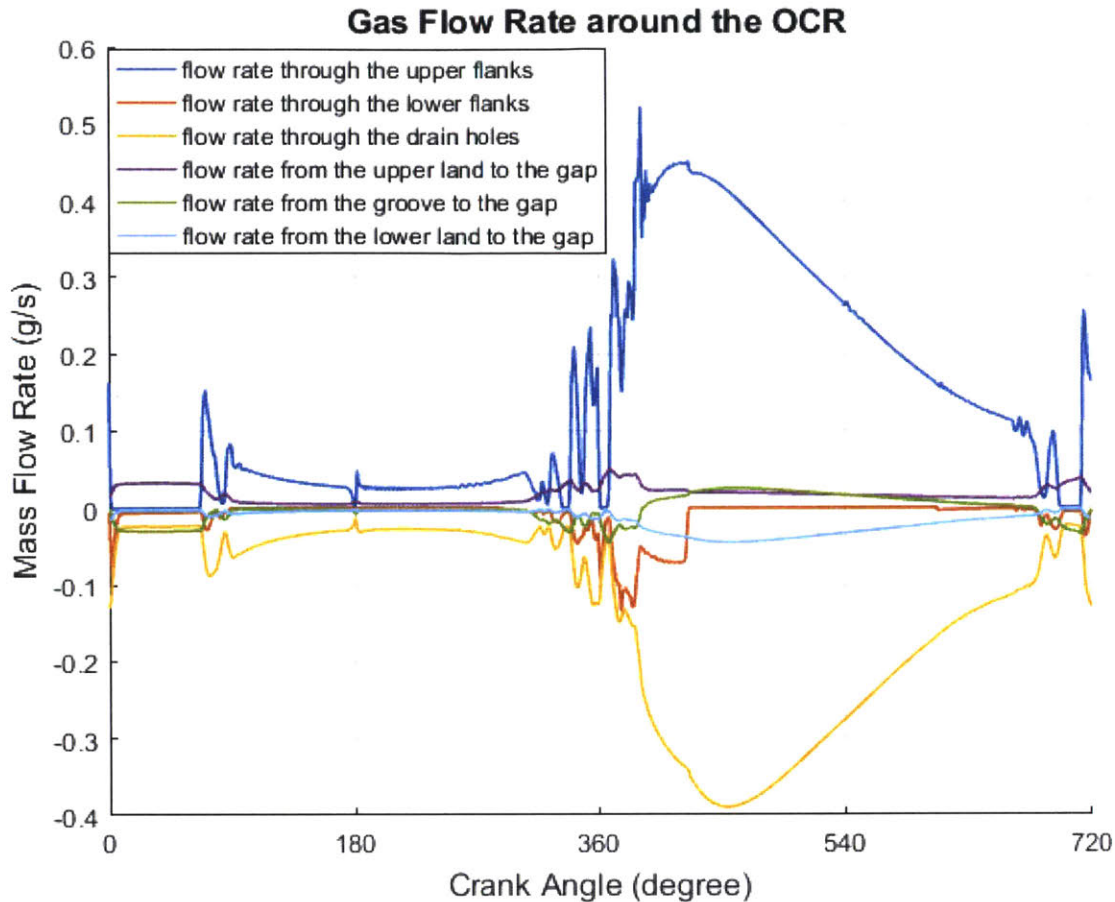
Gas Flow Rate around the OCR

Figure 87 Gas Flow Rate around the OCR

4.9.3. Effect of Groove Distortion on Gas and Oil Sealing

The previous section shows that the ring dynamics model based on the curved beam finite element method can provide a reasonable prediction of the inter-ring gas pressure and the ring pack dynamic behavior. Compared to the 2D model, this 3D model is able to capture the variance in the circumferential direction. This section demonstrates the capability of the model in reflecting both global and local behavior at the same time.

One of the good examples is the non-conformability between the ring and the groove with a high order groove distortion. Geometrical variations and distortion along the circumference on ring and groove flanks can exist due to manufacturing, excessive wear, and thermal and mechanical stresses. The last one usually gives low order distortion (2nd order mostly) while the other two may bring high order distortions. Without loss of generality, we assign all the distortion to the groove flanks. To show the ability of the model we choose 10th order distortion as it can give a large varieties of phenomena. The

profiles of both flanks of the top ring groove shown in Figure 88 was set in the second calculation. The top ring groove has a 10th order distortion and around 90 degree in the circumferential direction (the pin side) thick oil film was put on both flanks of the 1st ring groove, so that the gas flow path through the upper and lower flanks of the 1st ring and 1st ring groove was totally blocked in this area. The engine was running in the same condition and the same ring pack was used as well.
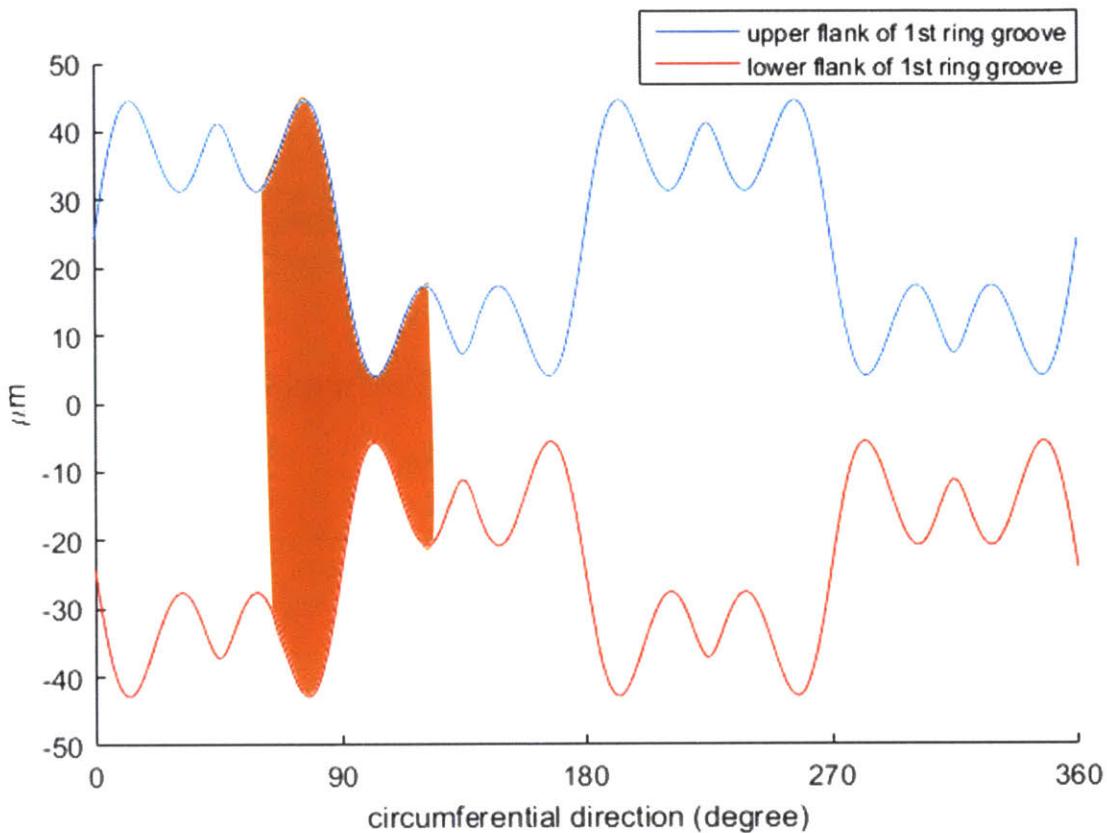

Figure 88 Profiles of Both Flanks of the Top Ring Groove

Figure 89 demonstrates land pressure results and a comparison to the results of the previous calculation. Since there is a 10th order distortion on both flanks of the top ring groove, a non-conformability between the top ring and its groove is expected and it has a negative effect on its sealing performance. It is obvious that the pressure in the piston 2nd land increases due to a leakage of gas from the top ring groove through the non-conformable area. However, the second ring is able to help control the pressure further increase. Then, the pressure in the piston 3rd land almost remains the same. The blow-by gas rate is 10.133L/min (0.196g/s) which is higher than 8.117L/min (0.157g/s) due to the non-conformability between the top ring and the top ring groove.
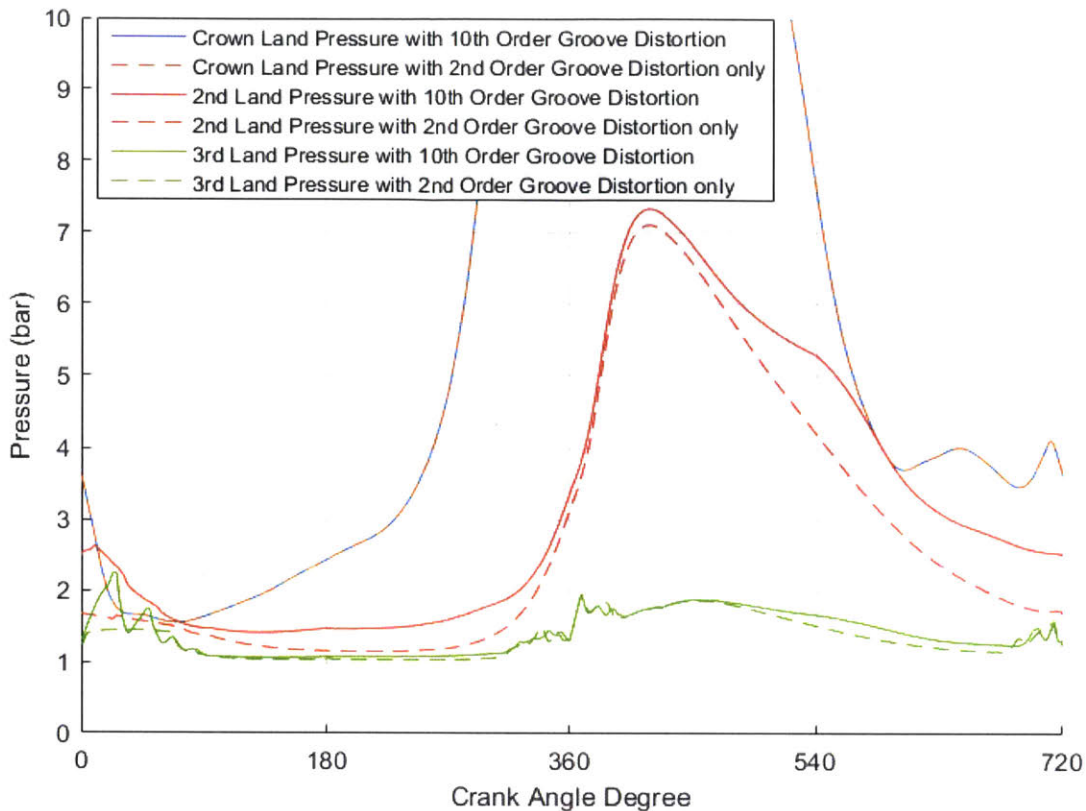
Figure 89 A Comparison of the Inter-Ring Pressure between a Piston with 10th Order Distortion and a Piston with 2nd Order Distortion

In Figure 90, it is obvious that the top ring has a 10th order non-conformability with the lower flank of the ring groove in most of the time, except for the expansion stroke. Around the top dead center of the expansion stroke, the gas pressure in the combustion chamber is so large that it is able to deform the ring to adapt to the 10th order groove distortion. Figure 91 shows the gas flow rate through the clearance between the lower flanks of the top ring and the top ring groove. Due to the non-conformability, the top ring cannot completely stop the gas flow from the top ring groove to the piston 2nd land and this can explain why the pressure in the piston 2nd land is higher compared to the one whose top ring groove does not have 10th order distortion. Around 90 degree in the circumferential direction, the gas flow rate from the 1st ring groove to the piston 2nd land is zero because of the thick oil film on the flanks of the 1st ring groove which blocks the path of gas flow.

ID Axial Clearance Between 1st Ring and Lower Ring Groove Flank
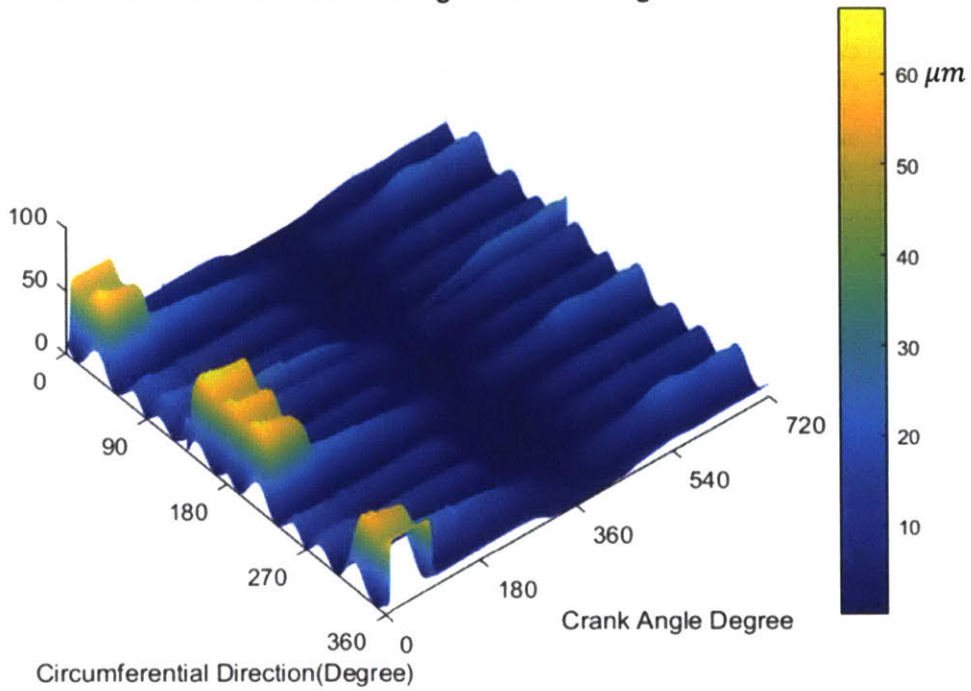
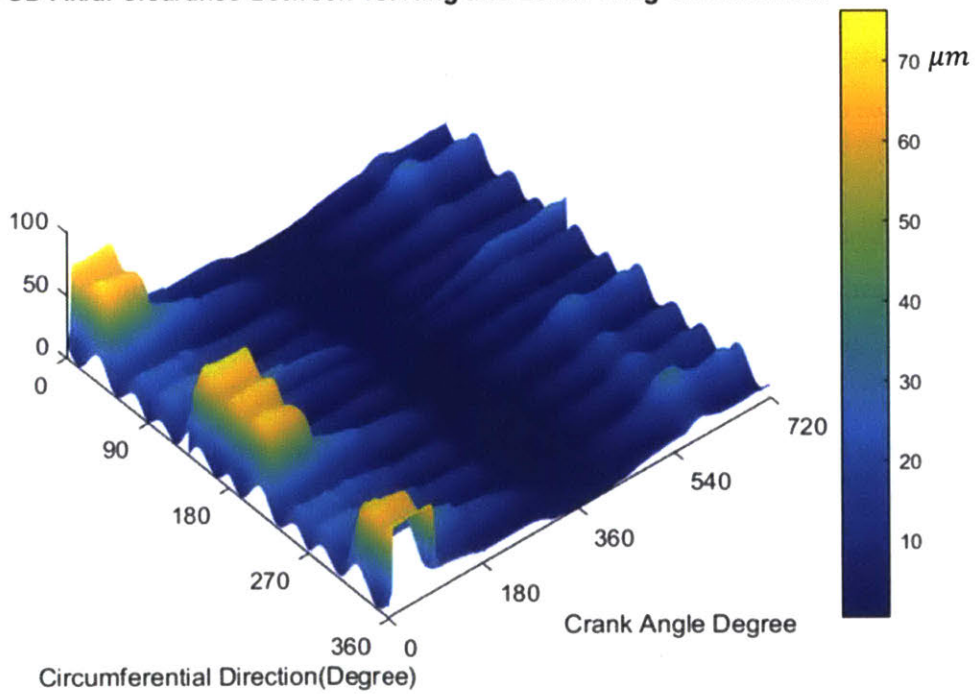**OD Axial Clearance Between 1st Ring and Lower Ring Groove Flank**

Figure 90 Clearance between the Lower Flanks of the Top Ring and Top Ring Groove
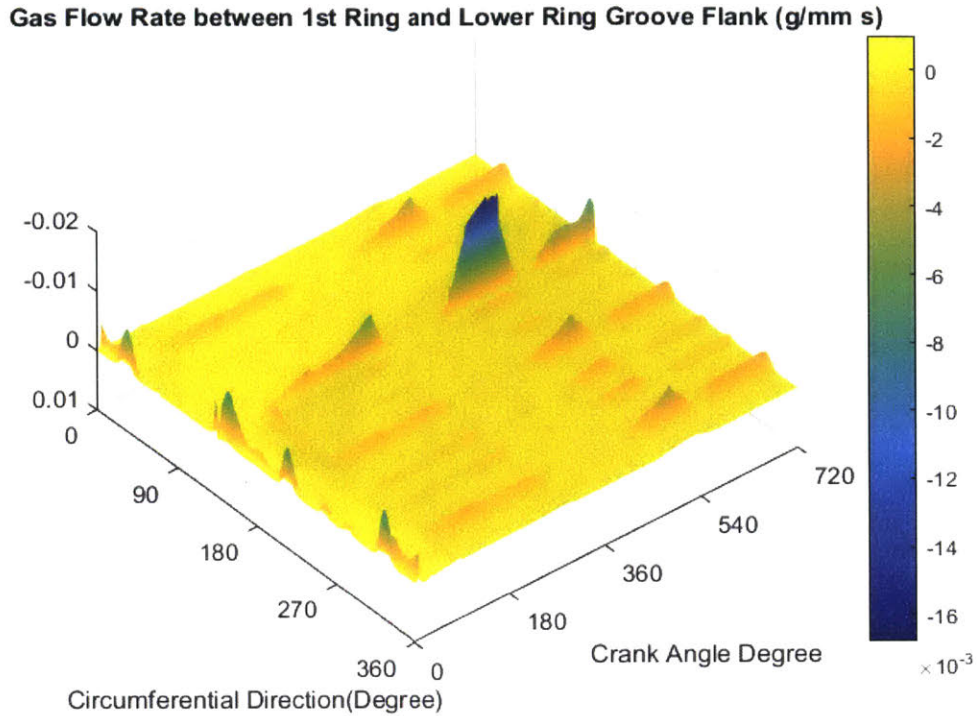
Figure 91 Gas Flow Rate between the Top Ring Lower Flank and the Ring groove

Even though the 10th order distortion of the top ring groove causes trouble of sealing gas leakage from the top ring groove to the piston 2nd land, the second ring is able to help control the blow-by gas, preventing further gas leakage into the piston 3rd land. In Figure 92 and Figure 93, the gap between the lower flanks of the second ring and the second ring groove is closed with the help of the pressure force from the piston 2nd land even at the end of the exhaust stroke and the corresponding gas flow rate reduces to zero. This example implies the necessary of second ring in internal combustion engines as part of a gas seal.

ID Axial Clearance Between 2nd Ring and Lower Ring Groove Flank

OD Axial Clearance Between 2nd Ring and Lower Ring Groove Flank

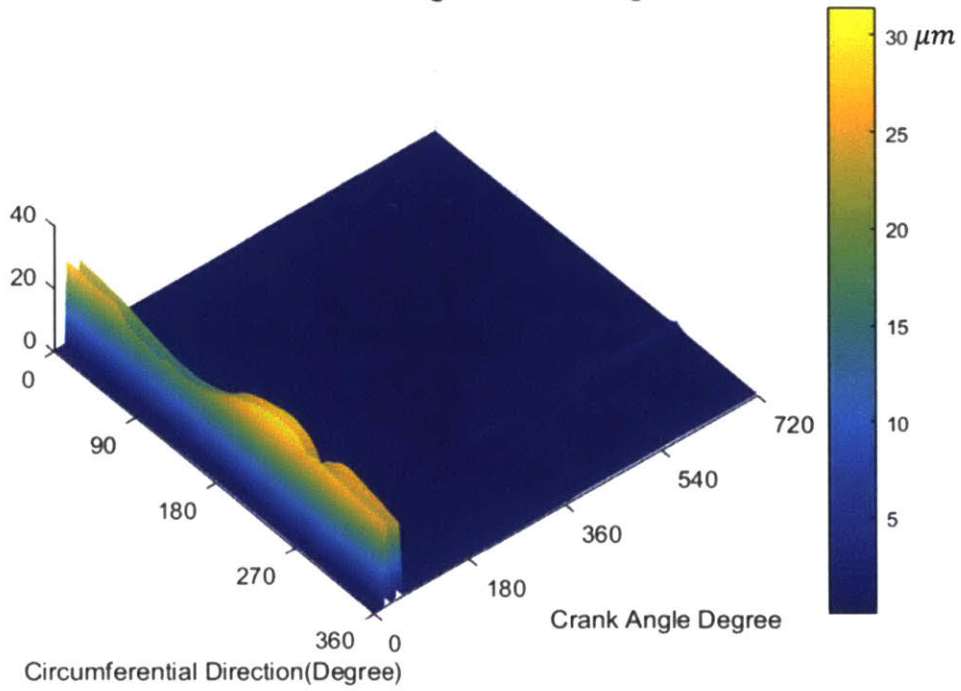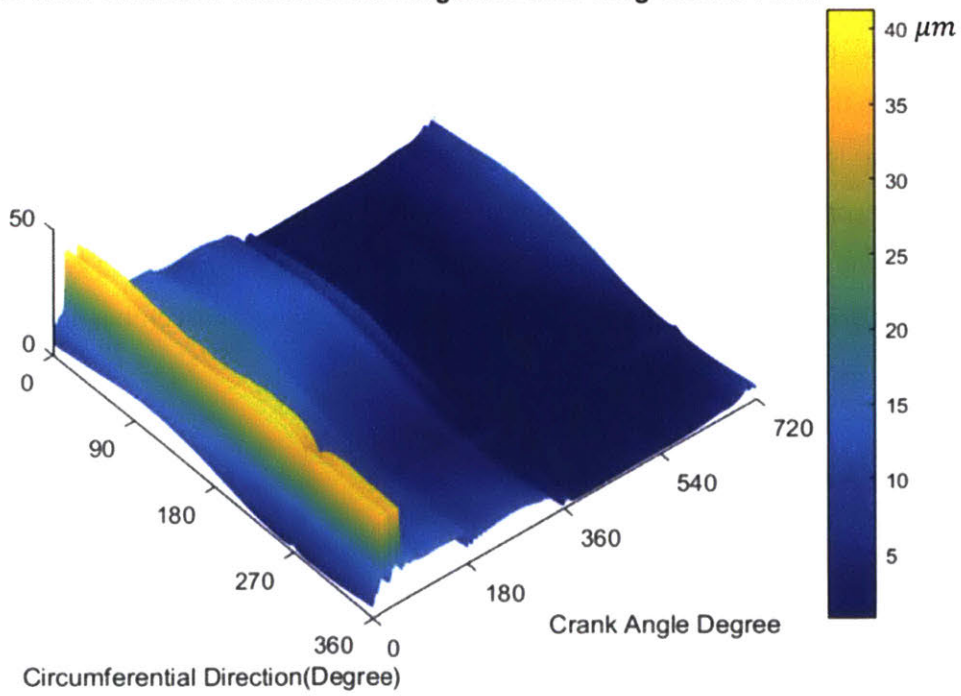*Figure 92 Clearance between the Lower Flanks of the Second Ring and Second Ring Groove*
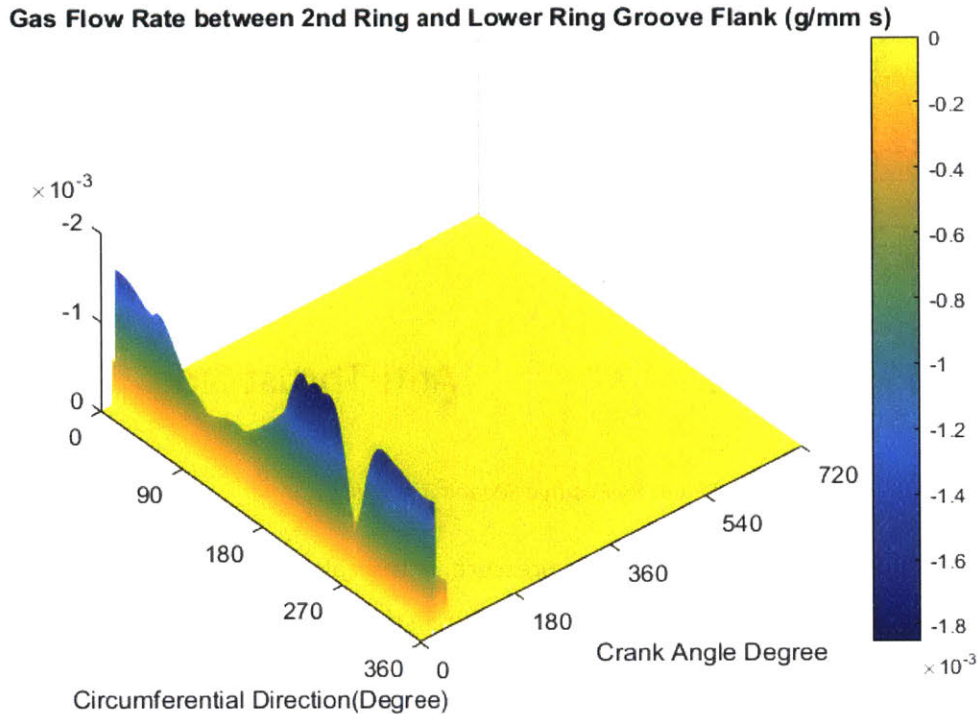
Gas Flow Rate between 2nd Ring and Lower Ring Groove Flank (g/mm s)

Figure 93 Gas Flow Rate between the Second Ring Lower Flank and the Ring groove

4.9.4. Results for a Piston with Positive 2nd Ring Groove Tilt

The 3D model is able to capture the variance along the circumference which is an advantage over the 2D model. Usually in a typical gasoline engine, the second ring groove has a negative thermal tilt which tends to give the second ring positive angle to the piston. In this section, we will artificially assign a positive tilt angle to the second ring groove with a magnitude of 0.16° (as shown in Figure 94), such that combined with a positive second ring static twist (with its lowest value at the ring gap and the highest value at 180° off the ring gap; in this example the second ring gap is set at 225° away from the thrust side), the relative angle between the second ring and the groove will change its sign along the circumference and a variation of its dynamic behavior will be expected. In this calculation, the engine is running at 4000rpm while other parameters are kept the same as the set-up shown in Section 4.9.1.
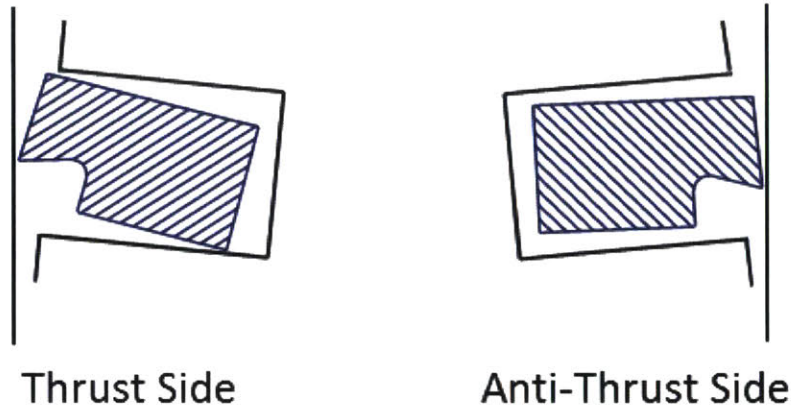
Thrust Side   Anti-Thrust Side

Figure 94 Positive Second Ring Tilt

Figure 95 shows the results of the inter-ring gas pressure. In this calculation set-up, the engine is running at 4000rpm which leads to larger inertial force. During the first half of the intake stroke when the pressure force is relatively small compared to the inertial force, all the three rings are lift due to the upward inertial force. As a result, the top ring groove is connected to the piston 2nd land and consequently these two spaces have the same gas pressure. Similarly, the second ring groove pressure is the same as that of the piston 3rd land. After the mid stroke, the inertial force changes its direction and the three rings are pushed to the groove lower flanks. In this situation, the top ring groove pressure drops to the combustion chamber pressure and the second ring groove pressure becomes the same as that of the piston 2nd land. At this time, the piston 3rd land is connected to the OCR groove which has drain holes to the crank case. Therefore, gas in the piston 3rd land is able to be quickly released through the clearance between the upper flanks of the OCR and the OCR groove. Then the piston 3rd land pressure drops to the same level as the OCR groove pressure. Around the TDC of the compression stroke and the expansion stroke, there are some fluctuations in the pressure of the second land, the second ring groove and the third land, which is caused by the second ring dynamics.
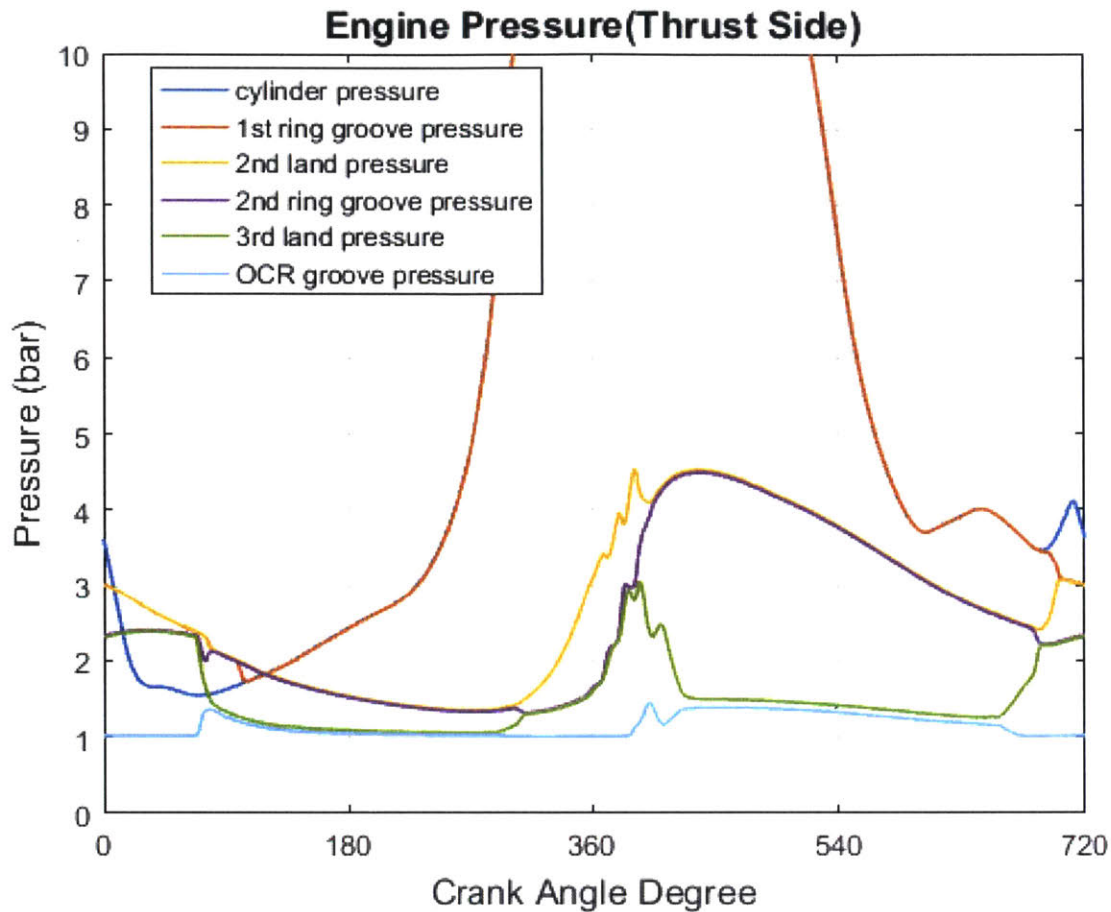
Figure 95 Inter-Ring Gas Pressure with a Positive Second Ring Groove Tilt

Figure 96 shows the results of the second ring dynamics. During the intake and the compression strokes, the pressure around the second ring is still small compared to the inertial force. As a result, the ring dynamics is determined by the inertial force. However, when the second ring has passed the TDC in the expansion stroke, the pressure in the second land increases and the pressure force on the second ring becomes comparable to the inertial force. Since the second ring gap is set at the angular position of 225°, its positive static twist has larger values at the thrust side and the 90° pin side and smaller values at the anti-thrust side and the 270° pin side. As a result, with a positive second ring groove tilt, the second ring has a positive twist relative to the piston at the thrust side and the 90° pin side and a negative twist at the anti-thrust side and the 270° pin side as shown in Figure 96. As discussed in Figure 80, when the pressure in the piston upper land is high, a negative twist introduces instability. Flutter happens when there is a right match between the pressure force and the inertial force. Therefore, after 360CAD, the second ring starts to flutter at the anti-thrust side and 270° pin side while the thrust side

and the 90° pin side is still stable with a positive twist to the piston. Clearly, the second ring has a variance of dynamics along the circumference when there is asymmetric geometry which in this case is caused by the piston 2nd ring groove tilt and the second ring static twist. After the mid-stroke of the expansion stroke, the pressure keeps increasing but the inertial force reduces to zero. Then the entire second ring is pushed downwards against the lower flank of the 2nd ring groove.

Around 360CAD before the second ring flutters, the second ring is lift due to the inertial force so that the pressure in the second ring groove is the same as the pressure in the piston 3rd land. When the second ring flutters, the second ring groove is connected to both piston 2nd land and 3rd land during the transition and the 2nd ring groove pressure is in between the 2nd land pressure and the 3rd land pressure. Then after the mid-stroke of the expansion stroke, the second ring is pushed downwards by the gas pressure force and the 2nd ring groove is connected the 2nd land, so the 2nd ring groove pressure becomes almost identical to the 2nd land pressure.

2nd Ring Relative Angle to Piston
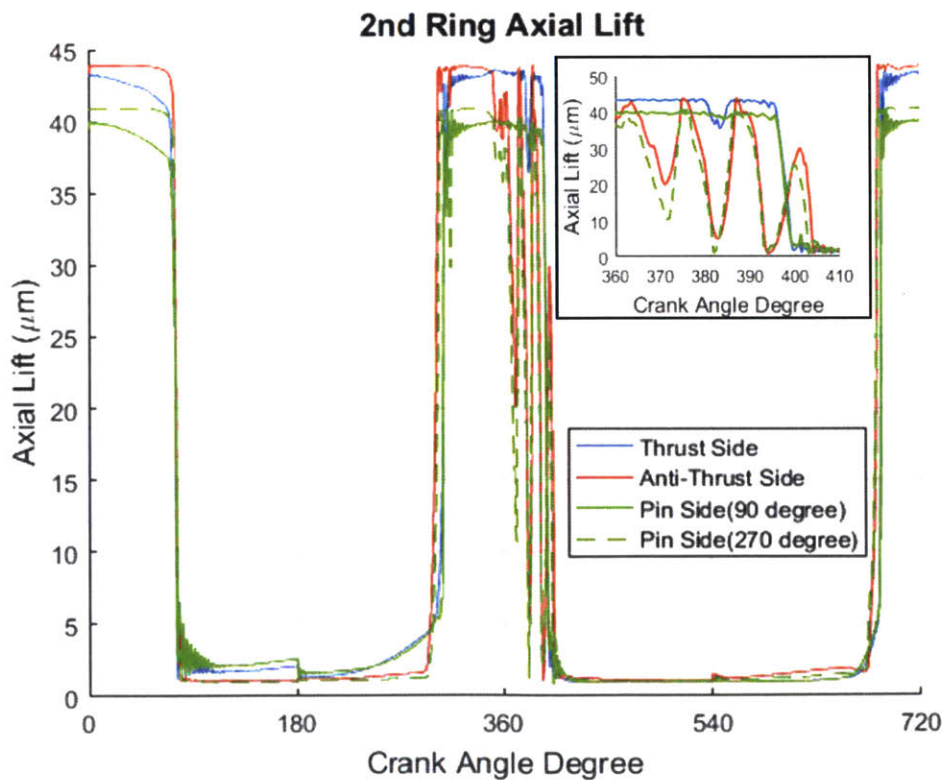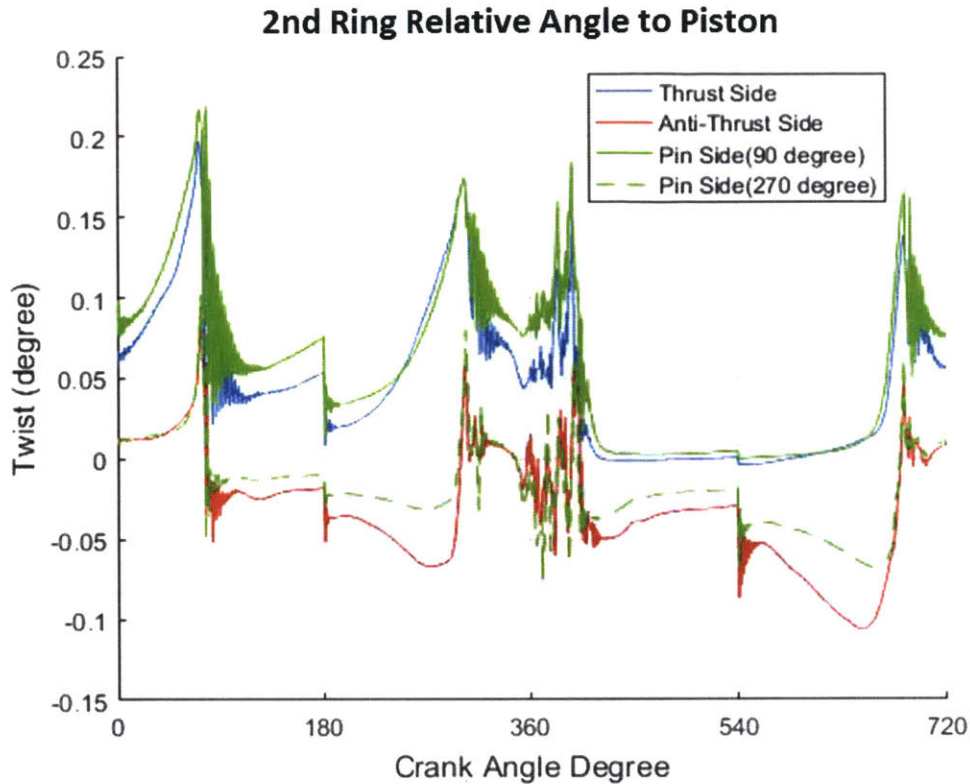
Figure 96 Results of the Second Ring Dynamics

As shown in Figure 95, around 360CAD the gas pressure in the piston 2nd land is larger than the pressure in the 2nd ring groove, and therefore the pressure force has a great opportunity to provide a net force pushing the 2nd ring inwards, which causes the 2nd ring collapse. As shown in Figure 97, the clearance between the second ring and the liner around 360CAD reaches a level of several microns, indicating the collapse of the 2nd ring. When the second ring collapses, it opens a channel between the ring and the liner and thus the gas can leak from the piston 2nd land to the piston 3rd land directly.

2nd Ring Ring-Liner Clearance (μm)

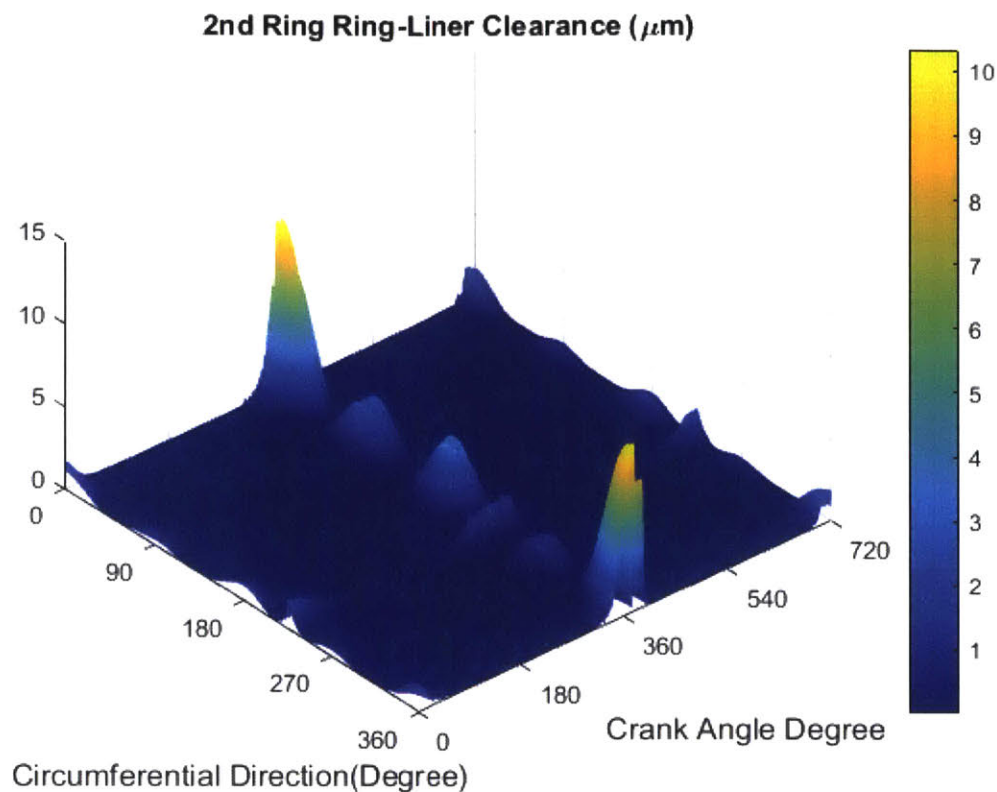*Figure 97 Second Ring Collapse around 360 CAD*

4.10.   Conclusion

In this chapter, we successfully implement the multi-scale curve beam element based model which bears its fundamental values to truly reflect the integral results of all the relevant mechanisms with their proper length scales from structural balance to local oil flows and asperity contact details.

The highest level balance is the structural dynamics of the rings inside the grooves, which is governed by inertial force and gas pressure while local force generation and gas leakage depends on oil availability. In reality, oil pumping through the ring-groove clearance can occur locally while the dynamics and gas pressure are dictated by the ring-groove interaction in the rest area. This process is critical to the oil leakage through ring grooves. Although the current model for oil flow is not mass conserved and thus is not able to predict the oil pumping rate, it can be easily done with an upgraded oil pumping sub-model.

The geometrical relationship between ring and groove changes along the circumference. Especially, due to the piston tilt from piston secondary motion, the relative angles between the ring and the groove can change signs. These are the situations that the current model has more fidelity than the 2D models in predicting ring stability and gas flows.

Although it is a 3-D numerical model, the selected physics sub-models and numerical approaches enable a good efficient numerical system. On author's PC (CORE i7 CPU, 16GB RAM), it takes 3 to 4 hours for one cycle when running with 0.01 crank angle degree as the time step, and each ring is divided into 8 elements within which there are 90 grids for contact force calculation and 10 grids for gas flow calculation.

One of the major objectives of this model is to provide the necessary boundary condition such as ring dynamics twists and land pressure for the ring-liner interaction to be described in the next chapter.

5. Modeling Ring-Liner Lubrication with Correlations

Oil control and lubrication in the ring-liner interface are the most critical elements for oil consumption and friction and they are the results of many global and local processes. These processes are

1. Interaction of rings with existence of gaps and distorted bore
2. Effects of gas pressures, ring twist, and piston secondary motion
3. Lubrication at Ring-face-profile level
4. Lubrication at the level of the roughness of the liner finish

Additionally, the oil supply condition to the top two rings can be localized with addition of oil from piston lands via bridging.

So far we have obtained our ring statics and dynamics model based on the curved beam finite element method. In this chapter, we will present the ring-liner lubrication model based on the same curved beam finite element method and its application in studying the oil transport through the ring-liner interfaces.

The ring-liner lubrication model is separated from the ring dynamics to allow faster computation for most of parametric studies on ring-liner interaction such as bore distortion and oil supply variations. In these studies, the ring dynamics and gas flows are not affected substantially by change of friction and radial force distribution, and thus does not have to be computed every time. This separation is based on the assumption that ring-liner interaction has negligible effect on ring structural dynamics. We have shown in previous section that this assumption is valid most of the time since the clearance between the ring and the liner is much smaller than the ring neutral axis deformation and so is the friction force compared to gas pressure force and inertial force.

This ring-liner lubrication model simulates oil transport through the ring-liner interface based on the boundary conditions from the ring dynamics model such as inter-ring gas pressure and ring dynamic twist. Unlike the ring dynamics model, a precise estimation of the ring-liner clearance is required to predict the oil film thickness on the liner. Thus, both hydrodynamic pressure and contact pressure are included in the ring-liner interaction.

Since the new ring-liner lubrication model is based on the same curved beam finite element method, it is able to integrate both global and local processes. The reason why we need to look into global process is straightforward. Piston rings conform to the distorted environment by gas pressure and

tangential load which determines the trend of the contact pressure distribution. Once the ring is in contact with the liner, local force generation depends on oil supply. In reality, circumferential gas flow causes local oil accumulation on the piston lands, leading to local oil supply to the top two rings by bridging. In the direct injection engine, fuel may be sprayed to the liner sporadically, disturbing ring-liner interaction by changing local oil film viscosity. These local processes are actually more important in high load, high speed engine conditions when oil consumption starts to become a problem.

5.1. Stiffness, Mass and Load Finite Element Matrices for Ring-Liner Lubrication Model

Since the ring-liner lubrication model only solves in-plane conformability, only terms related to the radial deformation are left in the mass, stiffness and load matrices.

$$M_{ij}^{(e)} = L_e \int_0^1 \rho A N_i N_j d\eta \quad for\ i,j \in \{1,2,3,4,5,6\}$$

Equation 5.1

$$K_{ij}^{(e)} = \frac{L_e}{R^4} \int_0^1 E I_z (N_i + N_i'')(N_j + N_j'') d\eta \quad for\ i,j \in \{1,2,3,4,5,6\}$$

Equation 5.2

$$F_{ext,i}^{(e)} = L_e \int_0^1 f_r N_i\, d\eta \quad for\ i \in \{1,2,3,4,5,6\}$$

Equation 5.3

The ring neutral axis displacement vector also reduces to the terms in the radial direction only:

$$\{u\}^{(e)} = \{y_1, y_1', y_1'', y_2, y_2', y_2''\}$$

Equation 5.4

As demonstrated in Chapter 2, the mass, stiffness and load matrices of each element are assembled to obtain the global ones and the global displacement vector $\{u\}$ is the assembly of the nodal displacement vectors. Then the governing equations become:

$$[M]\{\ddot{u}\} + [K]\{u\} = \{F_{ext}\} - \{F_{initial}\}$$

Equation 5.5

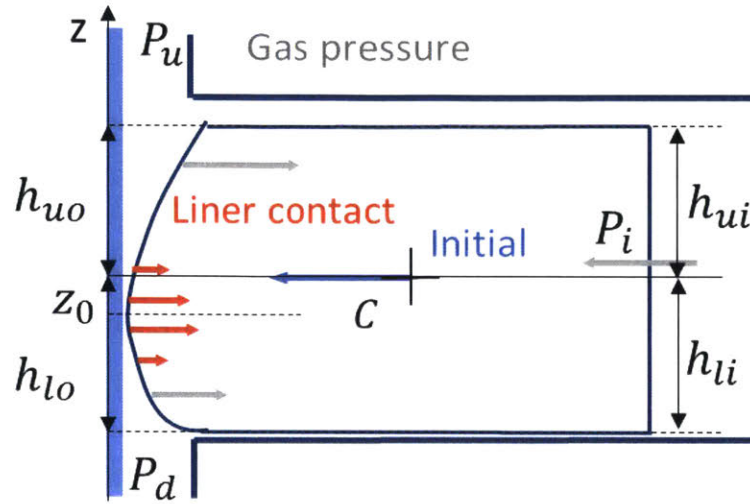## 5.2. Force Analysis of Ring-Liner Lubrication

Figure 98 Force Analysis in the Radial Direction

Figure 98 shows the forces in the radial direction to be used in the load vector. The first is gas pressure force. Gas pressure changes with time around the piston rings, especially for the top two rings. Gas from the piston upper land and the lower land pushes the ring inwards at the ring-liner clearance. Gas inside the ring groove acts on the ring as normal load and pushes the ring to the liner.

$$f_{r,gas} = P_i(h_{ui} + h_{li}) - P_u(h_{uo} - z_0) - P_d(h_{lo} + z_0)$$

Equation 5.6

The second is the ring initial force. For the top two rings, the initial force comes from the rings' strain energy when they are closed from their free shape. After the top two rings are closed and assembled into the cylinder, they tend to expand and push themselves to the liner. Chapter 3 provided the equations to calculate the initial force and we only need the ones in the radial direction.

$$F^{(e)}_{initial,y} = L_e E I_{zz} \int_0^1 \left(\frac{1}{R} - \kappa_{fs}\right) \left[-\frac{\cos^2 \alpha_p}{R^2}\right] \left(N_{m(k_y)} + N''_{m(k_y)}\right) d\eta$$

$$+ L_e E I_{yy} \int_0^1 \left(\frac{1}{R} - \kappa_{fs}\right) \left[-\frac{\sin^2 \alpha_p}{R^2}\right] \left(N_{m(k_y)} + N''_{m(k_y)}\right) d\eta \quad \text{[Equation 2.83]}$$

For the oil control ring, the initial force refers to the spring force from the oil control ring spring, F_t, which is an input from the ring design. This spring force is designed to be uniform along the circumferential direction in order to guarantee good conformability between the oil control ring and the

liner. Lastly, the contact force from the liner is composed of two parts. The first one is dry contact force which is calculated using the simplified Greenwoods-Tripp model and the second one is hydrodynamic pressure which can be calculated by the correlations derived by Chen, Liu and Li etc. [48] [50]. We are going to have more discussion on the hydrodynamic correlations in the next section.

5.3. Hydrodynamic Pressure Correlations

When the piston rings slide over the liner covered with lubricant, hydrodynamic pressure is generated in the oil film which can be estimated by Reynolds equation. Conventional lubrication models calculate the hydrodynamic pressure without consideration of surface roughness. However, this assumption may cause problem when predicting hydrodynamic pressure between the piston rings and the liner. The first reason is that the twin land oil control ring running surface is parallel to the liner surface and if without consideration of roughness, solving Reynolds equation would predict no generation of hydrodynamic pressure. Thus, roughness geometry cannot be neglected and is the only contributor to hydrodynamic pressure in this case. The twin land oil control ring is designed in this way to control oil film thickness on the liner down to a level of surface roughness. Then when we look at the top two rings, even though they have ring profile which could help generate hydrodynamic pressure, their oil supply is mostly determined by the oil control ring. When the supplied oil film thickness is limited to the level of surface roughness, it is not surprising that the oil film thickness between the top two rings and the liner is also at the level of surface roughness. Therefore, the roughness geometry is still an important factor to the hydrodynamic pressure between the top two rings and the liner.

5.3.1. Oil Supply to the Piston Ring Pack

The most important boundary condition to calculate the hydrodynamic behavior between the piston rings and the liner is oil supply. The oil is either splashed to the liner from the crank case or sprayed by the injector. During the down-stroke, the piston skirt redistributes the oil and part of it is accumulated in the piston chamfer below the OCR whose film thickness is much larger than what is allowed to pass the two lands of the TLOCR. Therefore, by convention, the oil supply to the TLOCR lower land during the down-stroke is always assumed to be fully flooded. The oil passing the lower land of the TLOCR will come to lubricate the upper land. If the upper land has higher clearance to the liner, its oil supply is partially flooded and it will not change the oil film thickness passing the lower land. If the upper land has smaller clearance, then its oil supply will become fully flooded and it will scrape the oil on the liner left by the lower land and further control the oil film thickness that is allowed to pass the TLOCR. However, bridging may occur between the TLOCR two lands and bring thick oil film thickness to the upper land

(usually much thicker than the clearance between the upper land and the liner; this will be discussed in Section 5.5.1). In this situation, the oil supply to the upper land will become fully flooded no matter how much oil is allowed to pass the lower land. In the model, the deterministic correlations are used to calculate the hydrodynamic pressure and shear stress between the TLOCR two lands and the liner with the assumption that the oil supply is always fully flooded, while in the calculation of the oil film thickness allowed to pass the TLOCR, the different boundary conditions of the oil supply to the upper land is considered.

The oil supply to the top two rings can come from different sources. In most part of the areas the top two rings travel, the oil film thickness on the liner is controlled by the oil control ring. In this situation, the oil supply is partially flooded and the deterministic correlations of top two rings are used to calculate the hydrodynamic pressure and shear stress (Section 5.3.3). However, bridging can bring additional oil from the piston lands to the liner. Depending on the timing and location of the bridging, the bridged oil may first interact with the top two rings and cause the top two rings fully flooded. The correlations developed in Section 5.3.4 are used to calculate the hydrodynamic pressure and shear stress between the top two rings and the liner under fully flooded boundary condition.

During the up-stroke, the oil supply to the piston ring pack is determined by the oil film thickness on the liner left during the down-stroke and the local addition of oil brought by bridging (from the piston lands or between the TLOCR two lands). However, as mentioned above, the hydrodynamic pressure and shear stress between the TLOCR two lands and the liner is calculated with the assumption of fully flooded boundary condition. The hydrodynamic behavior between the top two rings and the liner is calculated based on the local oil supply boundary conditions, so is the oil film thickness on the liner passing the three rings.

5.3.2. Deterministic Correlations of Twin Land Oil Control Ring

A deterministic model solving Reynolds equation of the sliding contact between the OCR and the cylinder liner at the scale of liner surface asperities has been develop by Li and Chen [47]. It considers the effect of the liner roughness on hydrodynamic pressure generation in the oil film and cavitation behind surface asperity. The oil supply is assumed to be fully-flooded and the ambient pressure is assumed to be atmospheric pressure. In this model OCR surface is assumed to be perfectly smooth, as shown in Figure 99.
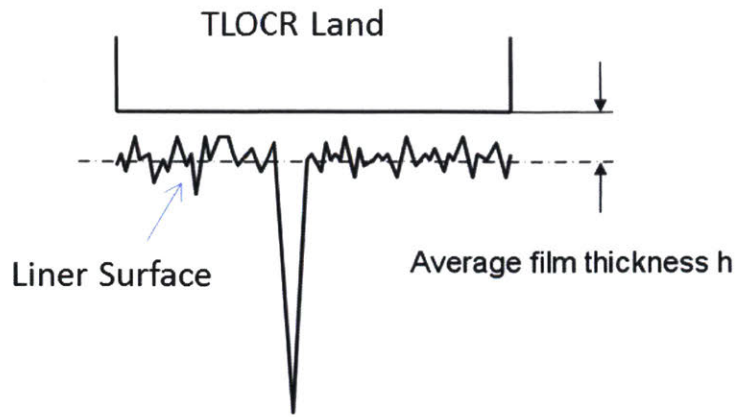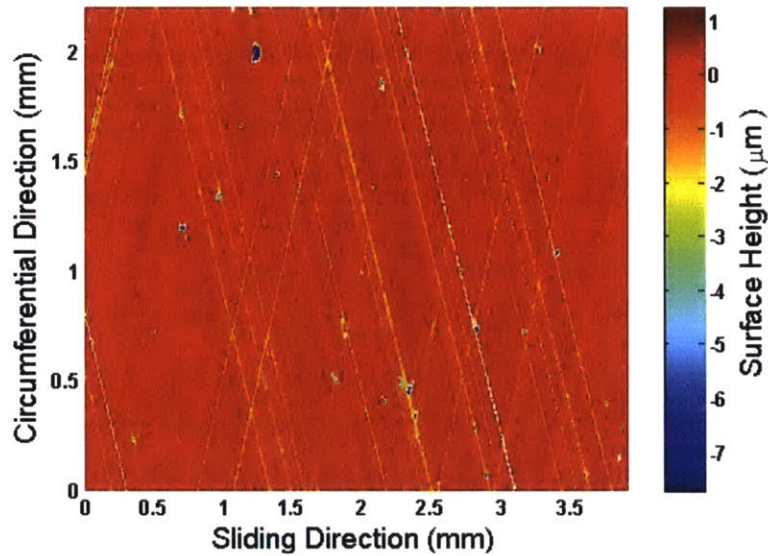
Figure 99 A Flat Ring on a Rough Surface

Figure 100 Liner Finish Measurement

Figure 100 shows the 3D measurement of roughness height matrix. A surface measurement patch usually has a size of 3mmx3mm and the land width of OCR varies from 0.06mm to 0.3mm. The simulation results using the deterministic model for a range of OCR-liner clearances are used to build a correlation between the ring-liner clearance h and the average hydrodynamic pressure P_h.
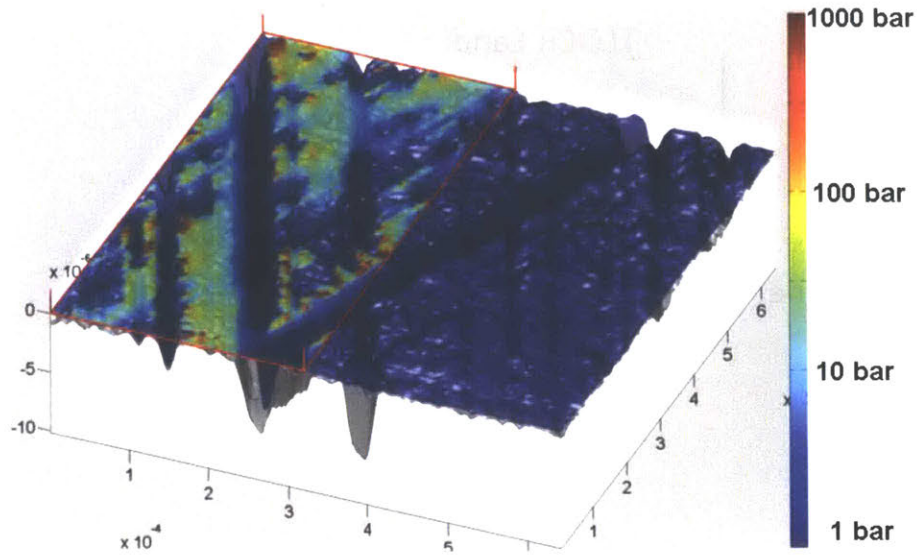
Figure 101 Hydrodynamic Pressure between the Ring Face and Liner Finish
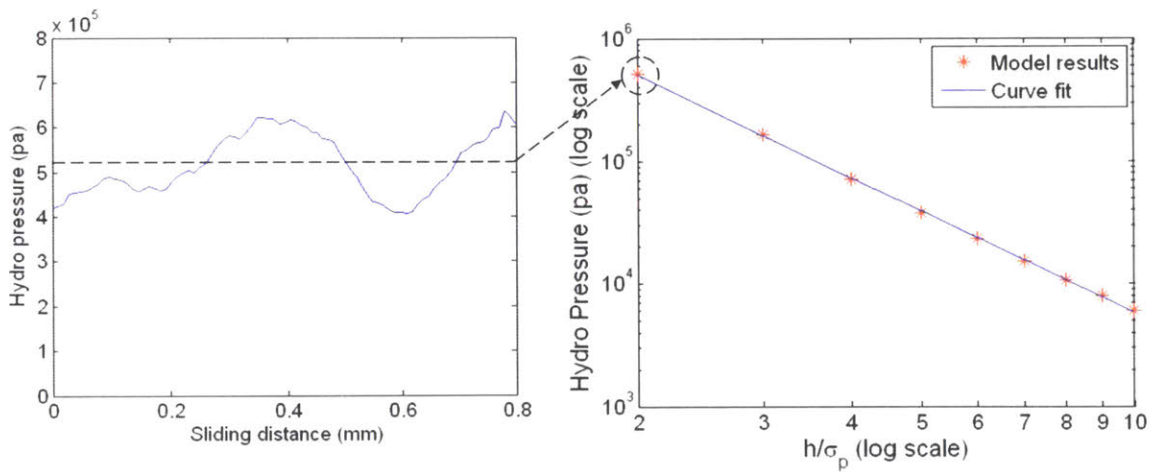

Figure 102 Hydrodynamic Pressure Generation of a Ring Face Sliding at a Constant Clearance

The inter-asperity hydrodynamic pressure is deterministic at given positions of the liner surface patch (Figure 101). The hydrodynamic behavior varies due to the change of surface micro geometry. Then, after we take the average over the entire ring sliding distance (or time steps), we can obtain an average hydrodynamic pressure with the given surface measurement, ring land width, ring-liner clearance, sliding speed and oil dynamic viscosity. Repeating this process over a range of ring-liner clearances (Figure 102), we should be able to find the dependency of the average hydrodynamic pressure P_h on the oil film thickness h.

$$P_h = P_0 \frac{\mu V}{(\mu V)_0} \left(\frac{h}{\sigma_p}\right)^{-a}$$

Equation 5.7

where P_0 and a are correlation coefficients and μ is oil viscosity, V is the sliding speed and $(\mu V)_0$ is the reference value of μV used in the simulation, h is the ring-liner clearance and σ_p is the plateau roughness. This correlation is going to be used in the ring-liner lubrication model to calculate the hydrodynamic pressure between the oil control ring and the liner.

5.3.3. Deterministic Correlations of Top Two Rings

A deterministic model solving hydrodynamic pressure between the top two rings and the liner has been developed by Chen [48]. This model takes into consideration of surface roughness and ring profile. However, unlike the OCR model, the top two ring deterministic model does not assume sufficient oil supply. Instead, it needs to use the oil film thickness result from the OCR model as an input to determine how much oil is fed into the top two rings. Chen has also developed a correlation including hydrodynamic pressure of the top two rings, the minimum clearance between the top two rings and the liner and the OCR ring-liner clearance (the definitions are shown in Figure 103).
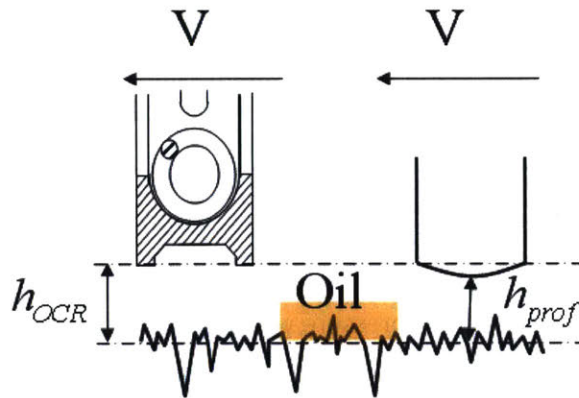

Figure 103 OCR Ring-Liner Clearance and Top Two Ring Minimum Ring-Liner Clearance

$$P_{hydro} = \left(\frac{h_{OCR}}{h_{prof}}\right)^{K_p} \frac{\mu V}{(\mu V)_0} (a_p P_{0,OCR}) \left(\frac{h_{prof}}{\sigma_p}\right)^{-K_{OCR}}$$

Equation 5.8

where $P_{0,OCR}$ and K_{OCR} are coefficients from the OCR deterministic correlation, μ and V represent oil dynamic viscosity and ring sliding speed. $(\mu V)_0$ is the reference value of μV in the simulation. h_{OCR} is the OCR ring-liner clearance and h_{prof} is the minimum clearance between the top two rings and the liner. The term $\left(\frac{h_{OCR}}{h_{prof}}\right)^{K_p}$ represents the filling effect. Since the rate of filling effect changes with oil supply, K_p is not a constant and correlated as a linear function of $\frac{h_{OCR}}{\sigma_p}$ (first order approximation). The term a_p captures the ring profile effect and given a liner finish and a ring profile, a_p will be a constant.

In Chen's thesis, this correlation is also called single phase correlation since it considers oil vapor and cavitation effect but does not include the gas pressure effect. However, inside internal combustion engines, especially in compression and expansion strokes, gas pressure is an important boundary condition to determine hydrodynamic pressure in the oil film. Liu has developed a multiphase correlation (Equation 5.9) which depends on Li's multiphase deterministic model with the consideration of gas pressure effect [50] [49].

$$P_{multiphase} = P_{single\ phase} + P_{static}$$

Equation 5.9

$P_{single\ phase}$ is the single phase correlation shown above and P_{static} is the gas hydrostatic pressure which captures the effect of boundary gas pressure. P_{static} is calculated by solving Reynolds equation on gas phase with the consideration of density dependency of pressure.

$$\frac{\partial}{\partial x}\left(\frac{h^3}{12\mu_g}\frac{\partial P_{static}^2}{\partial x}\right) + \frac{\partial}{\partial y}\left(\frac{h^3}{12\mu_g}\frac{\partial P_{static}^2}{\partial y}\right) = 0$$

Equation 5.10

Figure 104 shows results of gas hydrostatic pressure with different ring-liner clearances. The boundary pressure is set to be 5atm and 30atm. h is the minimum clearance between the profiled ring and the liner. σ_p refers to the plateau roughness. Looking at the result, one may argue that gas hydrostatic pressure is similar to a step function especially when the minimum clearance is small. As a result, in the ring liner lubrication model, we simplify the calculation of P_{static}. Instead of using P_{static}, we use $P_{multiphase} = P_{single\ phase} + \frac{P_u(h_{uo}-z_0)+P_d(h_{lo}+z_0)}{h_{uo}+h_{lo}}$ where P_u, P_d, h_{uo}, h_{lo} and z_0 are shown in Figure 105. The term of $P_u(h_{uo} - z_0) + P_d(h_{lo} + z_0)$ is actually the gas pressure force shown in Section 5.2.
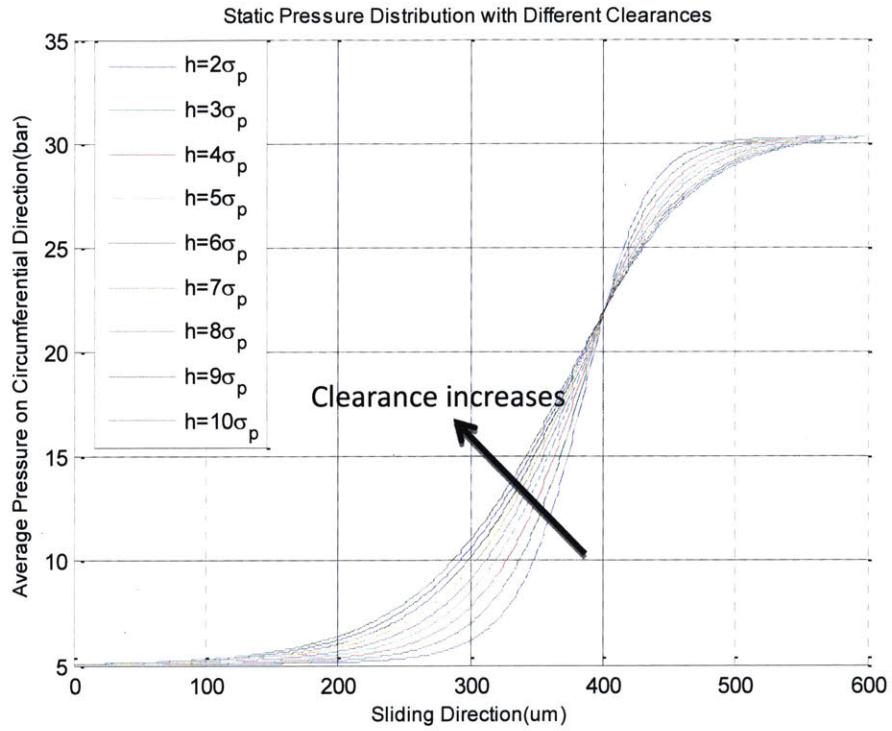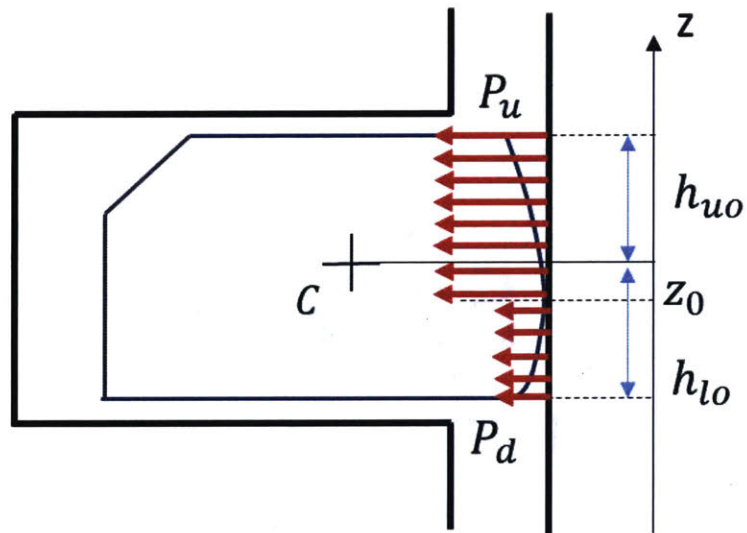
Figure 104 Gas Hydrostatic Pressure

Figure 105 Gas Pressure Acting on Ring Running Surface

5.3.4. Correlations of Top Two Rings under Fully-flooded Boundary Condition

The oil supply to the top two rings does not always come from the oil film left by the OCR. Sometimes around the top dead center or the bottom dead center of the liner, bridging may happen and it will bring additional oil from the piston to the liner. This extra amount of oil bypasses the OCR and is directly fed into the top two rings. Thus, the boundary condition of the top two rings will become fully flooded. The magnitude order of the oil film thickness that flows to the liner due to bridging is around $10\mu m$, which exceeds the correlating range of the single piece ring deterministic correlation. The large oil film thickness also implies that the change of surface roughness geometry is not important anymore. Then we can apply Reynolds Equation on a given ring profile and a smooth liner. The geometry is shown in Figure 106.
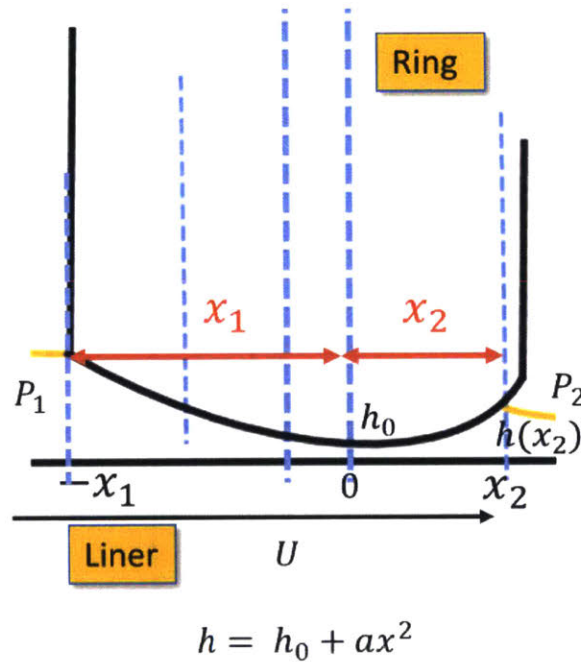

$$h = h_0 + ax^2$$

Figure 106 Schematic for Ring Profile and Liner

The oil supply is sufficient at the leading edge (x_1, which is an input to the model). x_2 refers to the end of the wetting area and at this point, a boundary condition of $\frac{\partial P}{\partial x}|_{x_2} = 0$ is applied. x_2 is dependent on the leading edge length x_1 and the minimum ring-liner clearance h_0. The ambient pressure is the atmospheric pressure and similar to how we addressed the top two ring deterministic correlation, we use $P_u(h_{uo} - z_0) + P_d(h_{lo} + z_0)$ to calculate the boundary gas pressure force on the ring and it is not included in the hydrodynamic pressure calculation. Another assumption is applied here that compared

to Couette flow, oil squeezing effect is small and neglected. Thus, the steady state Reynolds Equation is going to be used. Since $\frac{\partial P}{\partial x}\big|_{x_2} = 0$, the steady state Reynolds Equation can be written as:

$$\frac{dP}{dx} = \frac{6\mu U}{h^3}\left(h - h(x_2)\right)$$

Equation 5.11

Applying ambient pressure boundary condition, we have

$$0 = \int_{-x_1}^{x_2} \frac{dP}{dx}dx = \int_{-x_1}^{x_2} \frac{6\mu U}{h^3}\left(h - h(x_2)\right)dx$$

Equation 5.12

And we can get the dependency of x_2 on x_1

$$h(x_2) = \frac{\int_{-x_1}^{x_2} \frac{dx}{h^2}}{\int_{-x_1}^{x_2} \frac{dx}{h^3}}$$

Equation 5.13

The hydrodynamic force per unit length ($f_{hydrodynamic}$) equals $f_{hydrodynamic} = \int_{-x_1}^{x_2} P dx$. Integrating by part, this equation can be written as

$$f_{hydrodynamic} = \int_{-x_1}^{x_2} x \frac{dP}{dx}dx = \int_{-x_1}^{x_2} x \frac{6\mu U}{h^3}\left(h - h(x_2)\right)dx$$

Equation 5.14

By solving Equation 5.13 and Equation 5.14 numerically, we can obtain the results shown below in Figure 107. The normalized hydrodynamic pressure force per unit length is $\overline{f_{hydrodynamic}}'$. $f_{hydrodynamic}$ equals to the multiplication of this term by $\frac{6\mu U}{ah_0}$:

$$f_{hydrodynamic} = \overline{f_{hydrodynamic}}' * \frac{6\mu U}{ah_0}$$

Equation 5.15

$$\overline{f_{hydrodynamic}} = \overline{f_{hydrodynamic}'} * \frac{6\mu U}{ah_0}$$

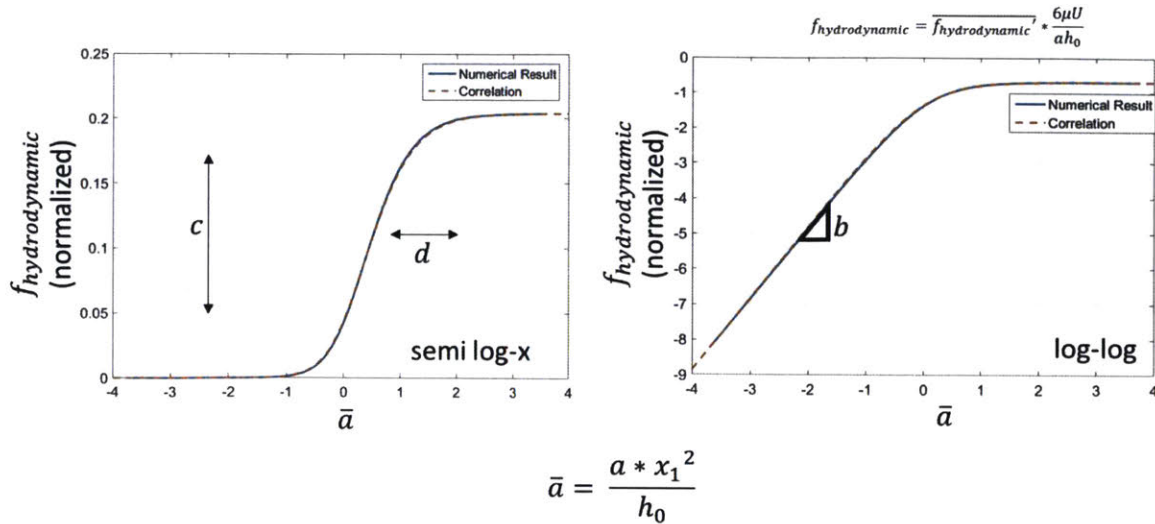$$\bar{a} = \frac{a * x_1^2}{h_0}$$

Figure 107 Results of Hydrodynamic Pressure with Fully-flooded Boundary Condition

Based on this numerical results, Li has developed a correlation between the hydrodynamic force per unit length and the minimum clearance between the top two rings and the liner.

$$f_{hydrodynamic} = \frac{12\mu V}{ah_0} c \left(\frac{1 + \tanh\left(\frac{\log_{10}(ax_1^2/h_0) + d}{e}\right)}{2} \right)^b$$

Equation 5.16

where h_0 is the minimum clearance between the rings and the liner and x_1 is the length of ring converging area, as shown in Figure 106. The term of a is the ring profile shape factor shown in Figure 106 and b, c, d, e are universal constants.

5.3.5. Unsteady Effect

In previous sections, we have discussed the correlations we are going to use to calculate the hydrodynamic pressure. However, we need to notice that all the correlations are based on either quasi-steady state results or steady state results. This implies that when using the correlations, we are not able to capture the unsteady effect on ring-liner lubrication. In most of the time, unsteady effect is negligible because the oil squeezing rate is much smaller than the one from sliding.

There are two unsteady effects in ring-liner lubrication. One is usually called squeezing effect caused by the change of clearance. Under the condition of sufficient oil supply to the top two rings, squeezing effect can become important a few degrees around the TDC and BDC when the sliding speed is close to

zero. Therefore, considering the squeezing effect or not does not make difference in friction power loss. The other unsteady effect is the redistribution of the oil film on the liner, which is caused by the change of oil volume in the wetted area. This effect mainly occurs for the top ring in the expansion stroke in high load conditions that the top ring tends to develop larger wetting area and leaves less oil on the liner during the early part of expansion stroke and do the opposite in later part of the stroke. Neither of the unsteady effects can be reflected using the deterministic correlations. This part needs further improvements of the sub-model of the ring-liner hydrodynamic behavior.

5.4. Oil Film Thickness Estimation

As shown above, the correlations only reveal the relationship between the hydrodynamic pressure and the ring-liner clearance. Therefore, applying the correlations to the ring-liner lubrication model will only provide the ring-liner clearance instead of the oil film thickness on the liner. However, to analyze oil transport through the ring-liner interfaces, the oil film thickness on the liner is needed. Then, in order to obtain the oil film thickness, we have made an assumption that if the ring is fully flooded, the oil film thickness left on the liner is equal to half of the ring-liner clearance (the minimum ring-liner clearance for the top two rings).

Based on this assumption, we can calculate the oil film thickness under two different cases (shown in Figure 108). First, when oil supply to the ring is fully flooded, the oil film thickness on the liner is equal to half of the ring-liner clearance. Second, when oil supply to the ring is not fully flooded, the deterministic correlations are applied. Since the correlations are based on the quasi-steady state simulation results, the average oil flux into the ring is equal to the average oil flux out of the ring. As a result, the oil film thickness on the liner left by the ring is equal to the oil film thickness fed into the ring. After all, the expression of the oil film thickness left on the liner h_{oft} can be written as:

$$h_{oft} = \begin{cases} \dfrac{h_{min}}{2} & for\ fully\ flooded\ boundary\ condition \\ h_{os} & for\ partially\ flooded\ boundary\ condition \end{cases}$$

Equation 5.17

Where h_{min} is the minimum clearance between the ring and the liner (the ring-liner clearance for twin land oil control ring) and h_{os} is the supplied oil film thickness to the ring.

Fully Flooded

$$h_{oft} = \frac{1}{2} h_{min}$$

Fully-flooded Correlation

h_{os}

h_{oft}

h_{min}
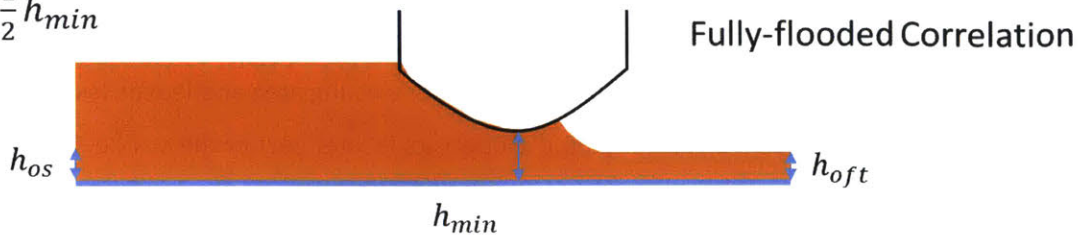
Partially Flooded

$$h_{oft} = h_{os}$$

Full attachment
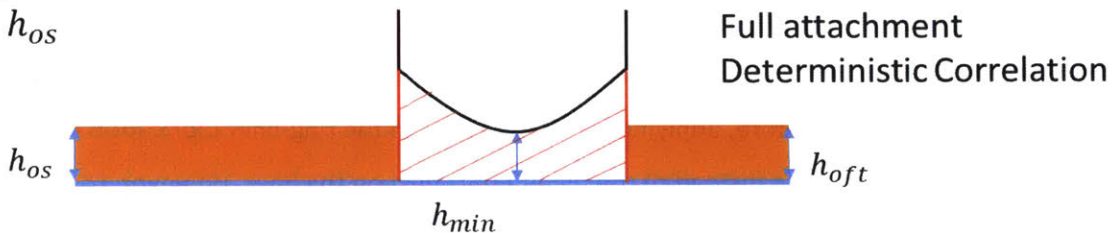Deterministic Correlation

h_{os}

h_{oft}

h_{min}

Figure 108 Oil Film Thickness and Ring-Liner Clearance

One may argue whether this assumption is valid or not. For the twin land oil control ring, this assumption is a very good approximation because its land profile is parallel to the liner surface and surface roughness determines hydrodynamic pressure behavior. As a result, hydrodynamic pressure is almost evenly distributed within the ring-liner interacted area, as shown in Figure 109. Therefore, the oil flux is mainly from the Couette flow and the oil film thickness left on the liner is approximately half of the ring-liner clearance.

Hydro Pressure ($10^{\text{Color scale}}$ bar)

Circumferential (mm)

Axial (mm)

h_{oft}

Average film thickness h

$$flux = \frac{hV}{2} = h_{oft}V$$
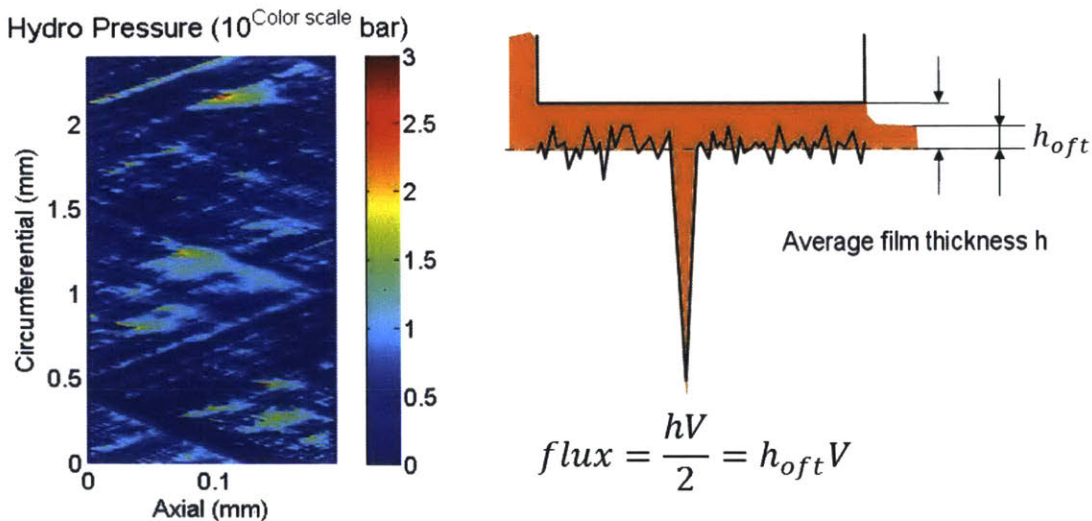
Figure 109 Hydrodynamic Pressure Distribution and Oil Film Thickness on the Liner for TLOCR

156

For the top two rings, we need to be more careful about this assumption. Because of the ring profile, the pressure gradient at the minimum clearance between the ring and the liner is not negligible anymore and actually it is at its maximum magnitude. The oil flux then should be calculated using the following equation:

$$flux = \frac{1}{2}Vh_{min} - \frac{h_{min}^3}{12\mu}\frac{\partial P}{\partial x}$$

Equation 5.18

At the minimum clearance, $\frac{\partial P}{\partial x}$ is a negative value and the flux thus is greater than $\frac{1}{2}Vh_{min}$, as shown in Figure 110. When we look into detail and scale each term, one can notice that V is the sliding speed which is on the order of $10m/s$, and h_{min} is on the order of $1\mu m$, P should be scaled as the pressure difference across the ring which has the same order as the combustion pressure ($\sim100bar$), x is scaled as the wetting width of the ring on the order of $0.1mm$ and μ is the oil dynamic viscosity on the order of $5mPa \cdot s$. The flux of the Couette flow has a magnitude order of $10^{-5}m^2/s$ and the flux of the Poiseuille flow is on the order of $10^{-6}m^2/s$. Since the flux of the Couette flow is much larger than that of the Poiseuille flow, we can still use the Couette flow to approximate the oil film thickness left on the liner which implies that $h_{oft} = \frac{1}{2}h_{min}$.
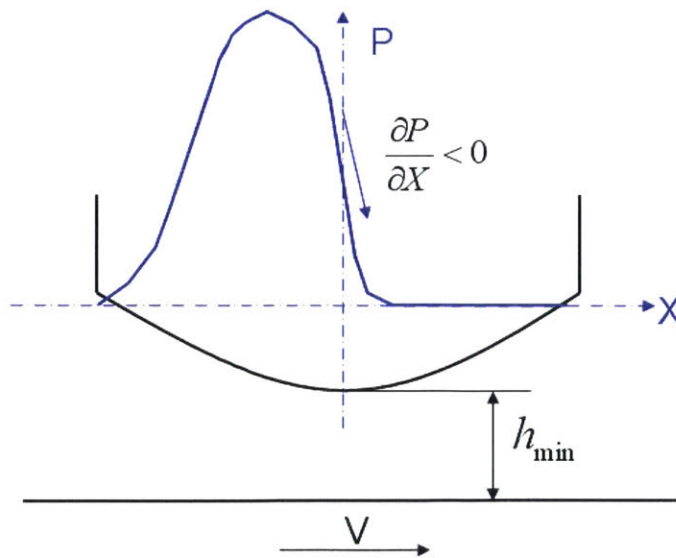
$$Flux = \frac{1}{2}Vh_{min} - \frac{h_{min}^3}{12\mu}\frac{\partial P}{\partial X} > \frac{1}{2}Vh_{min}$$

Figure 110 Oil Flux of a Profiled Ring

5.5. Oil Control by Twin-Land Oil Control Ring (TLOCR)

Baelden developed an oil transfer model for twin-land oil control ring based on the curved beam finite element method [45]. In his thesis, he studied the effects of bore distortion and piston tilt on ring-liner conformability and scraping of oil due to ring twist. When he calculated the oil film thickness on the liner, he assumed that the oil film thickness on the liner is determined by the smaller clearance between the two lands and the liner, as shown in Figure 111. However, this assumption is not always true since it does not consider the bridging between the TLOCR two lands, in which case excessive oil flows to the liner and wets the trailing land. At the same time, if ring twist causes a loss of contact of the TLOCR trailing land, thick oil film is left on the liner as shown in Figure 112. The image on the right in Figure 112 was taken from 2D LIF imaging which shows the existence of the bridging between the OCR two lands [16] [57]. As a result, in order to model oil transfer around TLOCR, a more careful study of the TLOCR trailing land boundary condition is necessary.
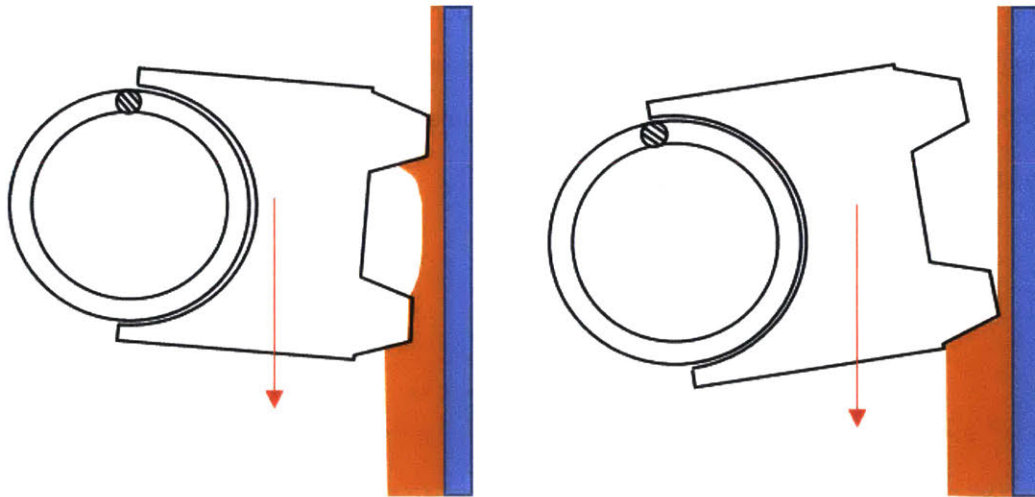
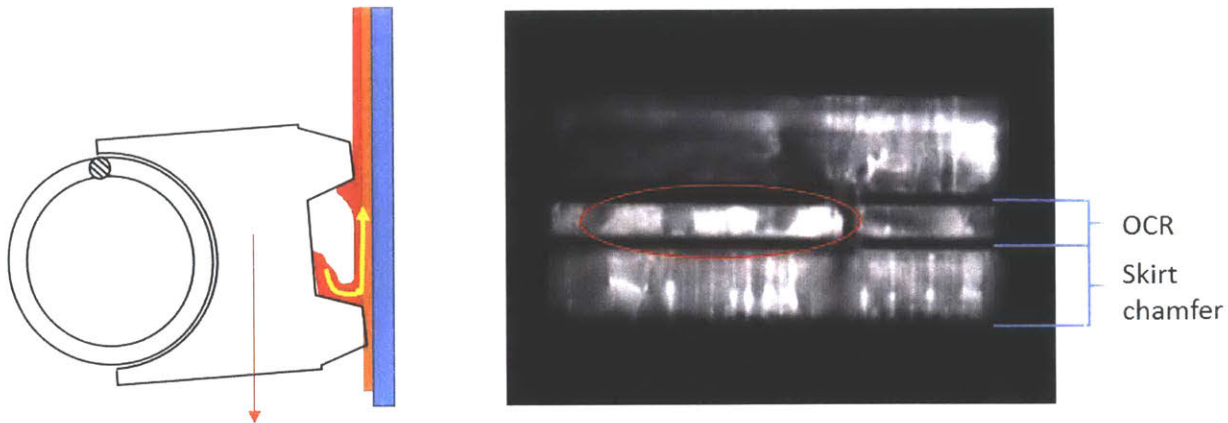*Figure 111 Starved Boundary Condition of OCR*

Figure 112 Bridging between the Two Lands of TLOCR

5.5.1. Bridging between the Two Lands of TLOCR

Bridging brings excessive oil from the TLOCR lands to the liner and affects the boundary condition of the trailing land as well as the oil film allowed to pass the TLOCR. Therefore, we need to know when bridging happens in order to study oil transfer around the OCR. Bridging timing and its factors was studied by Fang [18]. According to his work [58], the start timing of bridging depends on the amount of oil accumulated between the lands and the engine speed, as shown in Figure 113. The solid lines represent the results of the piston sliding speed when bridging starts around the bottom dead center (BDC) and the dashed lines represent the results of the piston sliding speed when bridging starts around the top dead center (TDC). Different colors are used to differentiate different engine speeds. U_{max} is the maximum piston sliding speed and U is the instantaneous piston speed when bridging occurs. The figure shows that as the accumulated oil volume between the TLOCR two lands decreases, $U_{max} - U$ increases which implies that bridging happens later and later. This figure also implies that in the same cycle, the piston speed when bridging starts to happen around the BDC is equal to the piston speed when bridging starts to happen around the TDC. Thus, given a start timing of bridging around the BDC, we should be able to calculate the corresponding start timing of bridging around the TDC.
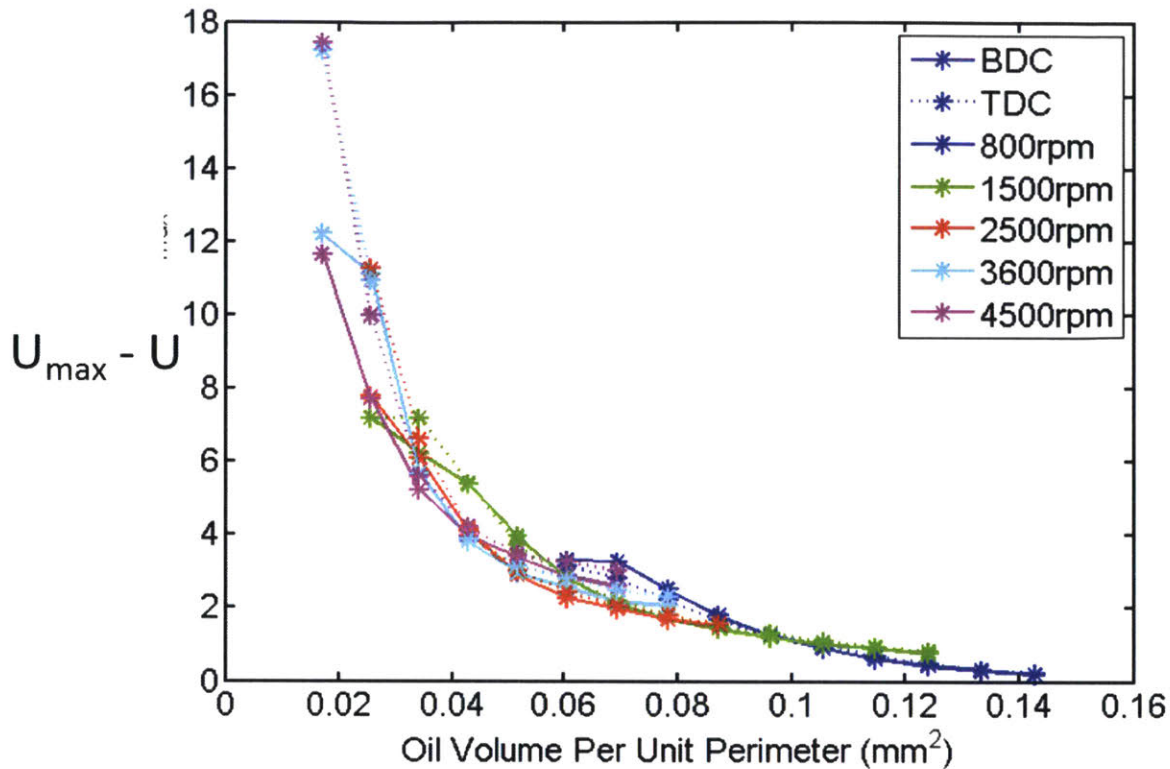
Figure 113 Timing of Bridging and Accumulated Oil Volume [58]

So far, there is still no direct method to calculate the accumulated oil volume between the two lands of the TLOCR. In reality, there are two ways for the OCR to exchange oil in the region between the two lands with its surroundings. One is through the scraping and releasing oil by the two lands, as shown in Figure 114. The other way is through the drain slots or holes on the TLOCR. Thus predicting the oil accumulation volume between the two lands is not straightforward and is beyond the scope of the current work. Here we propose a simplified assumption to predict the accumulation volume between the two lands. First, we assume the region between the two lands is closed from the groove. The second assumption is that the accumulation volume per length is uniform along the circumference. The consequence of these two assumptions is that the inflow and outflow to this region is balanced at the steady state. Correspondingly, through post-processing, we iterate to solve the accumulation volume that gives the same outflow volume as the inflow within a cycle as shown in Figure 115. When the trailing-land of the TLOCR is fully-flooded all the time (which is equivalent to -180 crank angle degree before BDC of the start timing of bridging during the down-stroke in Figure 115), the outflow of the oil from the volume between the two lands reaches its maximum. As a result, the net flow into this region becomes negative (as shown in Figure 115) and the oil accumulation decreases, postponing the start

timing of bridging. On the other hand side, when the trailing land of the TLOCR is starved all the time (which is 0 crank angle degree before BDC of the start timing of bridging during the down-stroke in Figure 115), the outflow of the oil to the region between the two lands reaches it minimum and correspondingly the net flow becomes positive (as shown in Figure 115). In this situation, the oil accumulation in this region increases which advances the start timing of bridging. Thus, when we iterate the start timing of the bridging, there should exist a timing that the net flow into the region between the two lands is zero and the oil accumulation becomes invariant from cycle to cycle. In the case shown in Figure 115, this timing is 90 crank angle degree before the bottom dead center.

Accumulation between the OCR two lands
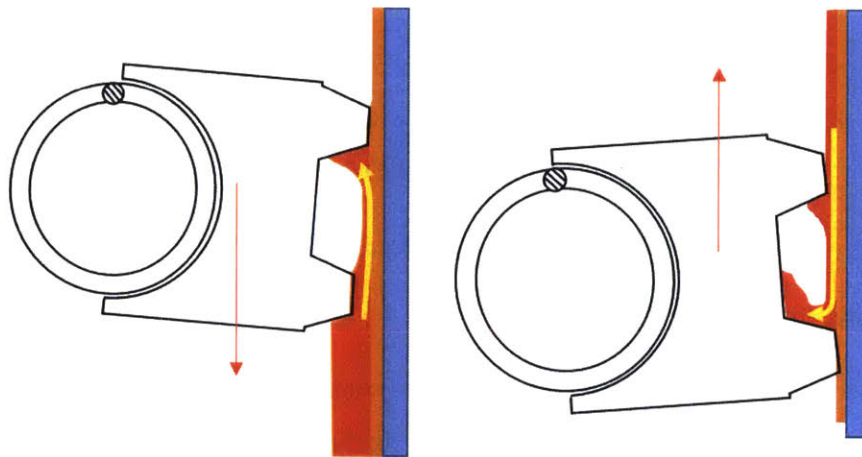
Release on the liner
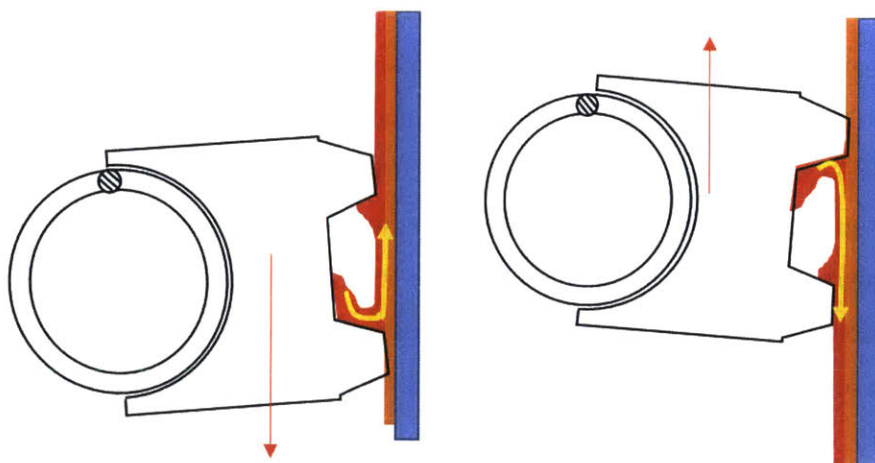
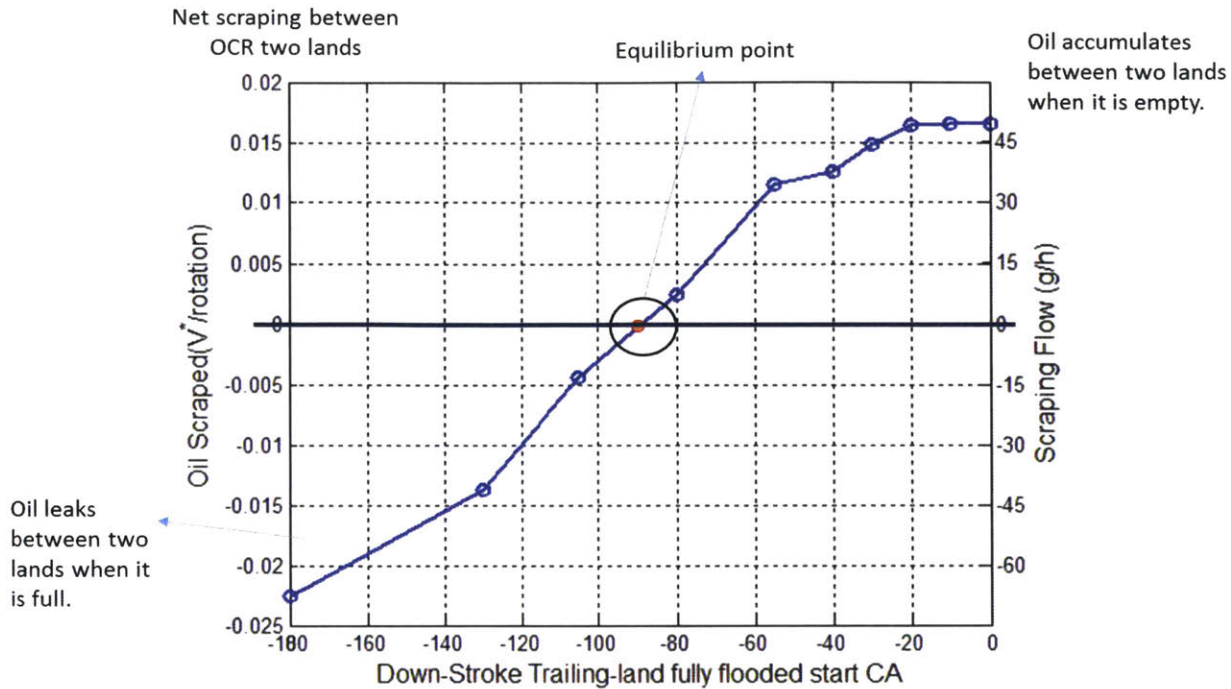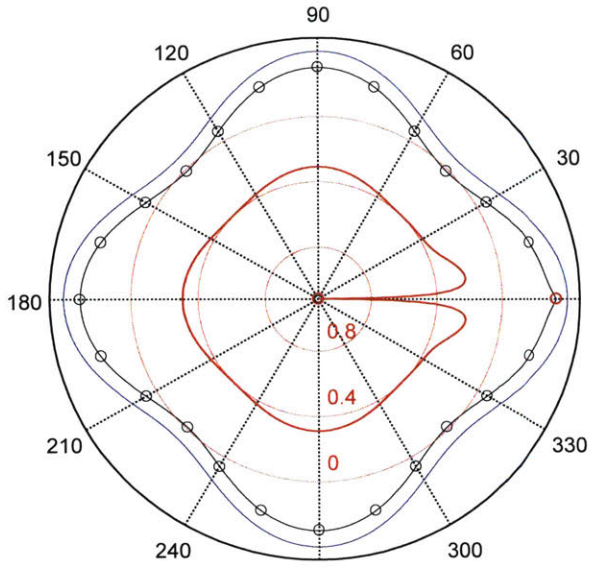*Figure 114 Scraping and Release Oil for a Twisted OCR*

Figure 115 Oil Net Flow Rate as a Function of Start Timing of Bridging around BDC
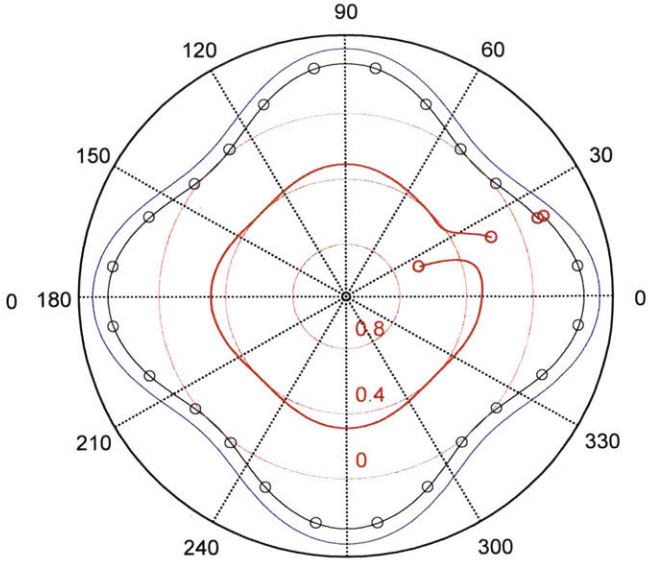
5.5.2. The Effect of Gap Positions

Ring gap can be seen as two free ends and does not have constraint from the other side which is different from the rest part of the ring. As a result, the ring may have singular behavior here. Piston rings have been observed to rotate during engine operation, meaning that any ring gap position is likely to occur. Therefore, there is a great interest of understanding the region near the ring gap.
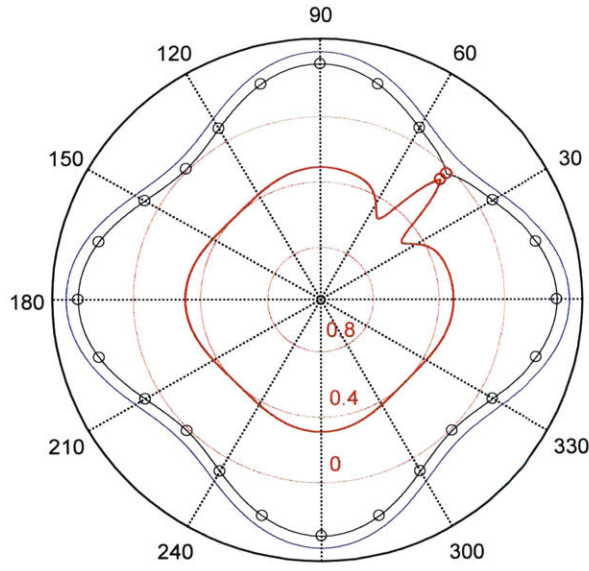
To study the behavior of the ring gap, Baelden rotated an OCR in a distorted bore with a single 4th order distortion of $5\mu m$ magnitude and calculated the equilibrium of the ring for each position [45]. His results are shown in Figure 116. In Figure 116, the blue curve represents the distorted bore, the black curve is the distorted ring on which the circular dots are the nodes of the ring elements and the two red circular dots are the ring gap ends and the red one is the contact pressure. Larger contact pressure occurs at the positions when the red curve bends inwards and smaller when the red curve bends out wards. From the results, one can find that the ring gap can have larger contact at both ends, or lose contact at both ends, or lose contact at one end and have larger contact at the other. The behavior of the ring gap is really dependent on the local geometry of the distorted bore and it is difficult to give an easy conclusion.
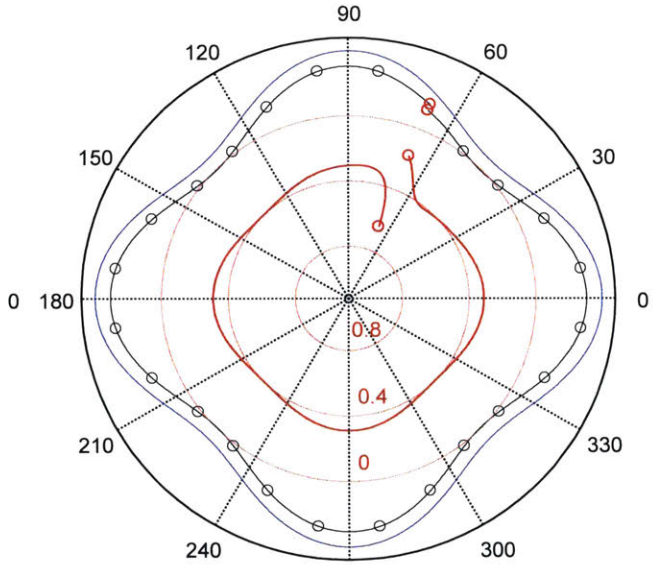
$P_{t1}=1.4$ N.mm^{-1} $P_{t2}=1.4$ N.mm^{-1}

$P_{t1}=0.2$ N.mm^{-1} $P_{t2}=0.7$ N.mm^{-1}

$P_{t1}=0.1$ N.mm^{-1} $P_{t2}=0.1$ N.mm^{-1}

$P_{t1}=0.7$ N.mm^{-1} $P_{t2}=0.2$ N.mm^{-1}
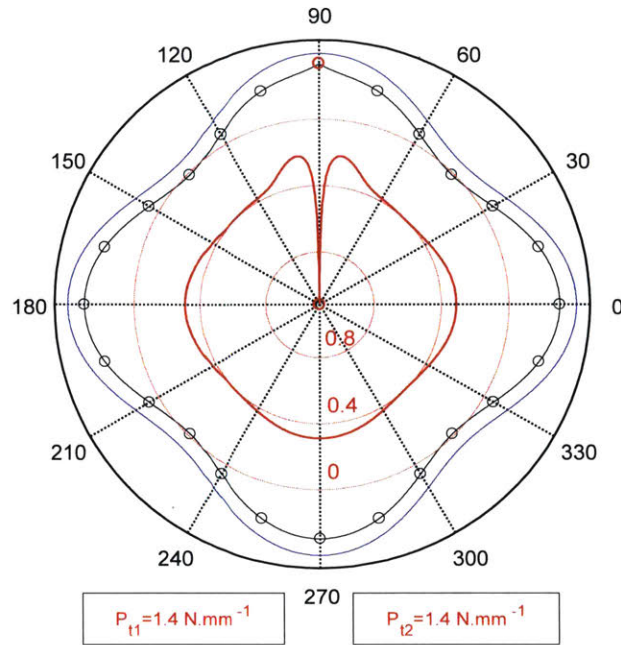
163

Figure 116 Rotation of a Ring in a Distorted Bore [45]

5.5.3. The Effect of Bore Distortion on Oil Transfer around TLOCR

In this and following sections, we will study the effects of different design and operating parameters on oil transfer around TLOCR. The engine used in the calculation has a bore diameter of 82.5mm and a stroke of 92.8mm. Figure 117 demonstrates the ring parameter and its cross section, piston tilt and bore deformation. Piston tilt was calculated using P2M model developed by Bai and Totaro [17] [56]. It has a magnitude order of 0.2 degree. The bore distortion was based on the FEA of a real engine. Certain modifications were made not to disclose the exact information while ensuring the relevance of the data. Bore deformation has a 0th order up to $200\mu m$, 2nd order up to $50\mu m$, 3rd order up to $15\mu m$ and 4th order up to $10\mu m$. The oil control ring gap is set to be aligned with the thrust side of the bore and the position is fixed in the circumferential direction during the calculation.
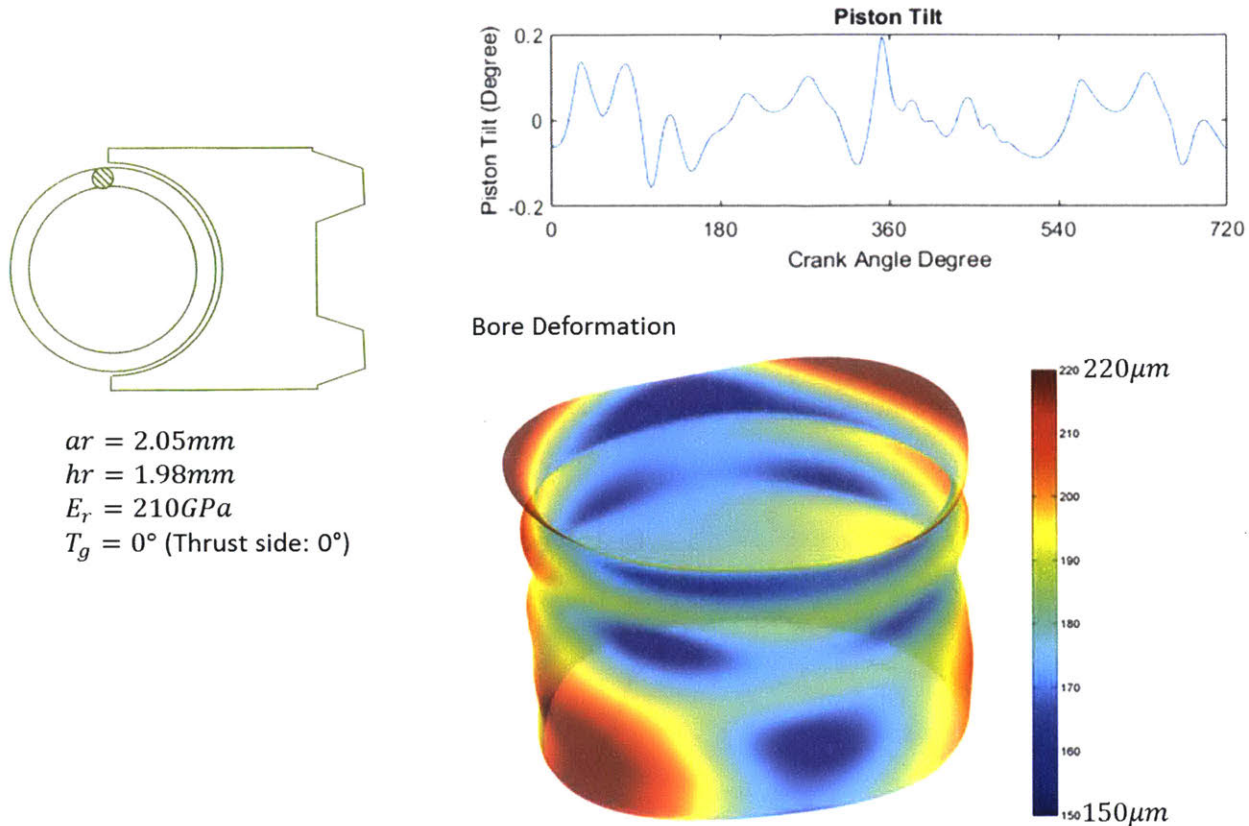
Figure 117 Calculation Set-up for TLOCR Oil Transfer

$ar = 2.05mm$
$hr = 1.98mm$
$E_r = 210GPa$
$T_g = 0°$ (Thrust side: 0°)

In this section, we will examine the effect of bore distortion on oil control of the TLOCR. To do such a study, a series of calculation was run with no bore distortion, normal bore distortion shown in Figure 117 and doubled bore distortion.

First, the oil control of the TLOCR is defined with two quantities. The first is the thickness of the oil left on the liner during down-strokes. This oil film thickness will lubricate the top two rings and represents the most critical function of the TLOCR. Particularly, the top ring under high cylinder pressure may either conform to the bore better than the TLOCR or allow less oil to pass than the OCR. The second is up-scraping of the oil on the liner by the upper land during up-strokes. This quantity is significant as it represents the net oil transfer to the upper regions. Some of the oil scraped by the upper land can flow to the piston third land and the rest is dropped on the liner at TDC to interact with the top two rings. Eventually, these two quantities will be the boundary conditions for the models dealing with the oil transport in upper areas. Furthermore, one will see that the first oil control quantity is important in the upper part of the liner and the second lower part.

Correspondingly, two kinds of conformability between the TLOCR and the liner are defined here. The first is circumferential conformability which can be interpreted as how the ring neutral axis deforms to adapt to the distorted bore. Loss of circumferential conformability is equivalent to the loss of contact of the TLOCR both lands (as shown in Figure 118). This conformability is determined by the moment of inertial to the cylinder axial direction, z. The second conformability is axial conformability. When the TLOCR loses its axial conformability, only one of its lands loses the contact to the liner while the other still stays in contact. It occurs when the TLOCR has a relatively large angle to the liner (usually caused by the tilted groove), as shown in Figure 119. This conformability is determined by the torsion constant of the ring.
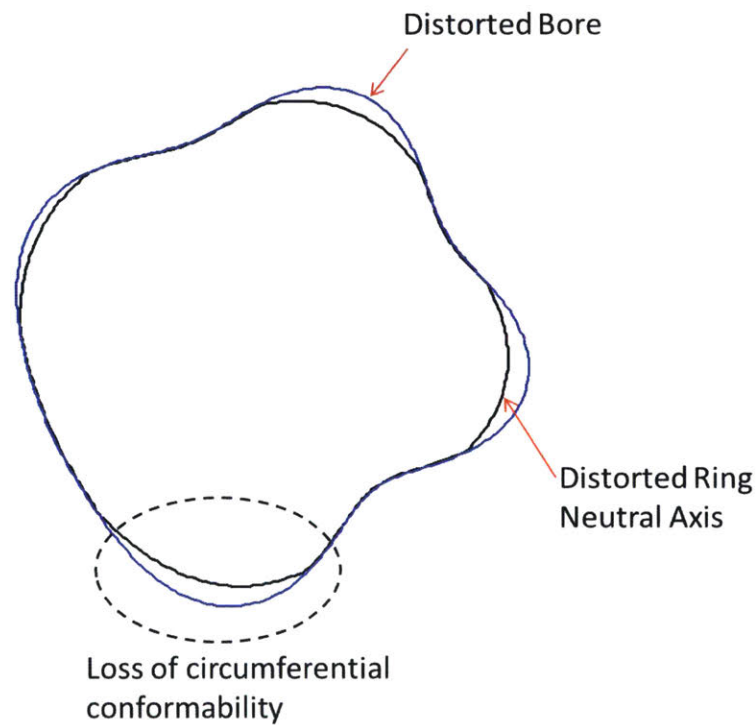

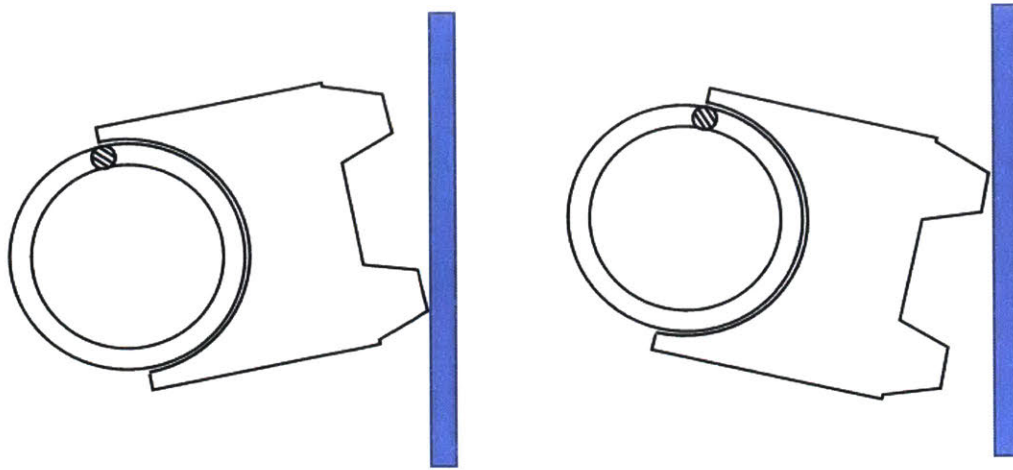*Figure 118 Loss of TLOCR Circumferential Conformability*

Figure 119 Loss of TLOCR Axial Conformability

Figure 120 shows the results of oil film thickness left by the TLOCR on the liner during the intake stroke at three representative locations along the circumference. The engine speed is 650rpm and the ring tension in tangential force (Ft) is 10N. The y-axis is the axial position of TLOCR inside the engine. Zero corresponds to the position of the top ring at the top dead center and the positive direction is pointing upwards. The x-axis is the oil film thickness in microns. From left to the right are the results of the oil film thickness on the liner left by the TLOCR at the thrust side, the anti-thrust side and the pin side of the bore. When reaching BDC, bridging occurs between the TLOCR two lands to give upper-land fully-flooded oil supply condition, which, combined with the effect of piston tilt, results in thick oil film thickness on the liner on the anti-thrust side.

Ring gap (which is set to be at the thrust side) can be seen as two free ends and does not have constraint from the other side which is different from the rest part of the ring. As a result, the impact of ring structure dynamics is magnified here. The results shown in Figure 120 suggest that bore distortion affects ring-liner lubrication of the TLOCR by changing its structural conformability to the bore. With the increase of bore distortion, the ring is more and more difficult to conform to the bore and the oil film thickness becomes thicker. This effect is more obvious around the ring gap area as shown in the left plot in Figure 120. Bore distortion has negligible effect on ring dynamic twist. Thus, around the bottom dead center when bridging wets the trailing land, oil film thickness almost remains the same as changing bore distortion.
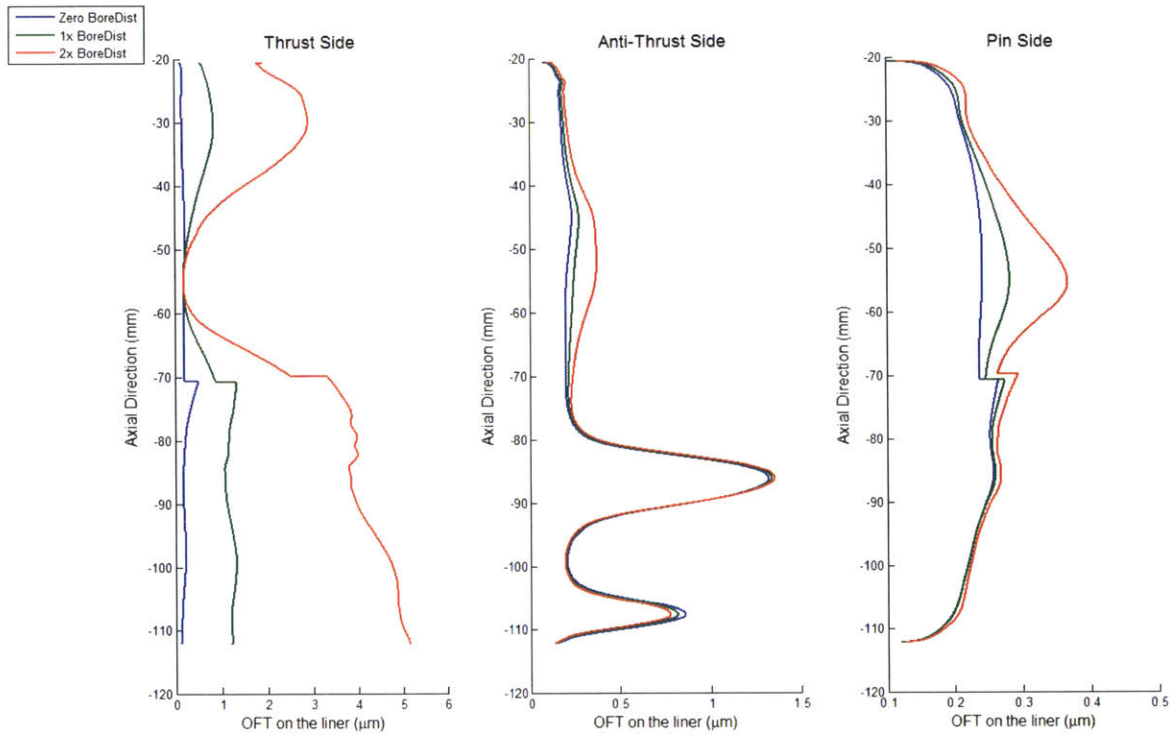
Figure 120 Oil Film Thickness on the Liner with Different Bore Distortion during Intake Stroke

Figure 121 shows the oil film thickness distribution along the circumference (0 is the thrust side and 180° is the anti-thrust side) on the liner after the TLOCR at different axial positions (z=-30mm early in the down stroke; -55mm mid-stroke; z=-85mm late in the down stroke; z=0 is the TDC of the top ring) during the intake stroke. The ring tension is 10N and the bore distortion is the original one. The solid blue line is the clearance between the lower land and the liner, the dash blue line is the clearance between the upper land and the liner and the orange line is the oil film thickness on the liner after the TLOCR. Since the distance between the upper land and the lower land is 1.3mm, during the intake stroke the lower land always comes earlier than the upper land. However, this distance is much smaller compared to the stroke and the small difference between the arriving timing of the two lands at the same axial position can be neglected most of the time. For the first plot in Figure 121, the oil film thickness on the liner is half of the smaller clearance between the two lands and the liner since the oil film left by the lower land is the only oil supply to the upper land. In first plot, it is obvious that the piston has a positive tilt such that around the anti-thrust side the lower land has larger clearance than the upper land while at the thrust side the upper land has larger clearance than the lower land. Both two lands are able to control the oil film on the liner. As a result, the oil film thickness is controlled to

168

sub-micron level though most part of the ring does not have a good axial conformability to the liner. Around the thrust side, the ring loses its circumferential conformability due to the existence of the ring gap. Neither of the two lands stays in contact with the liner and thick oil film is allowed to pass the TLOCR. From the plot, it is clear that the gap effect is localized, since the gap size is small compared to the circumference. The second plot can be explained similarly but in this plot the two ends of the gap stay in contact with the liner. As explained in Section 5.5.2, the behavior of the ring gap is highly dependent on the local geometry of the distorted bore. For the last plot in Figure 121, the oil film thickness on the liner is half of the clearance between the upper land and the liner because at this position bridging brings additional oil to the liner and causes the upper land fully flooded. From the plot, we can clearly see that with a negative piston tilt the ring has a larger upper land clearance around the anti-thrust side which leaves thick oil film on the liner. Around the thrust side, the ring loses the circumferential conformability to the liner due to the existence of the ring gap and localized thick oil film is observed on the liner.
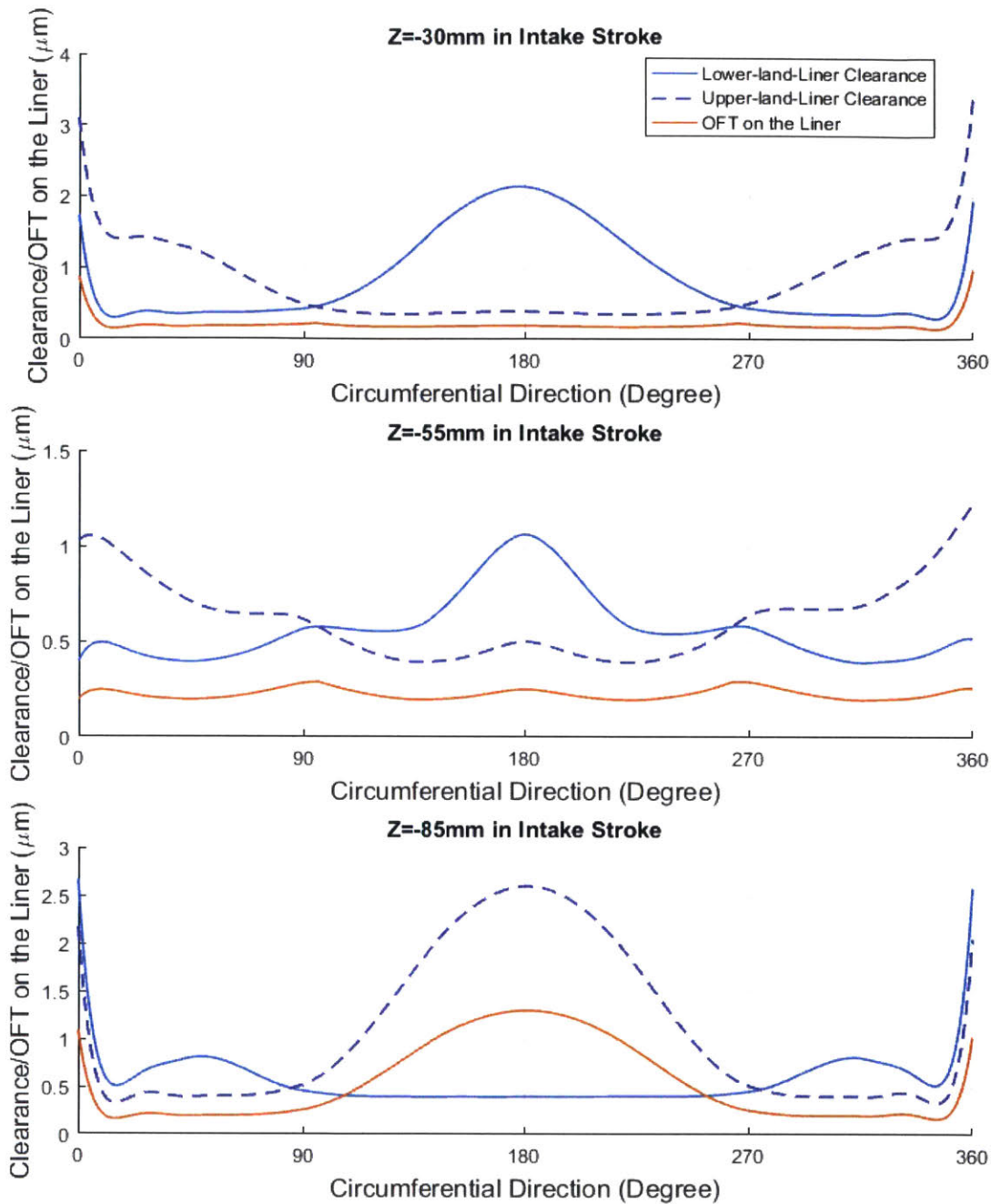
Figure 121 OFT after TLOCR at Different Axial Positions in Intake Stroke

To examine the up-scraping rate, we recognize that after TDC during a down-stroke, the trailing land is starved and the oil film thickness is determined by the smaller clearance between the two lands and the liner. Thus, up scraping is difficult to occur (Figure 122) in the upper part of the liner when the TLOCR travels back in the ensuing up-stroke. It needs to be emphasized that this conclusion is based on the assumption that the oil film left on the liner by the TLOCR during down-strokes is not affected by the

passage of the top two rings. This assumption is in general true except in the expansion stroke under high load conditions when the top ring can redistribute the oil film on the liner. This secondary effect will be studied carefully in future work when a mass-conserved sub-model for the top two rings hydrodynamic lubrication is employed. However, when the ring is approaching the bottom dead center, the trailing land becomes fully-flooded due to bridging and tilted groove may lead to thick oil film and up scraping tends to happen here (Figure 122). On the other hand, the cylinder pressure tends to be lowered substantially when the top ring travels in the lower part of the liner, thus direct scraping by the top ring is unlikely. As a result, oil film thickness left by the OCR on the liner in the lower part of the liner becomes not important, and emphasis should be put on the study of oil up scraping.
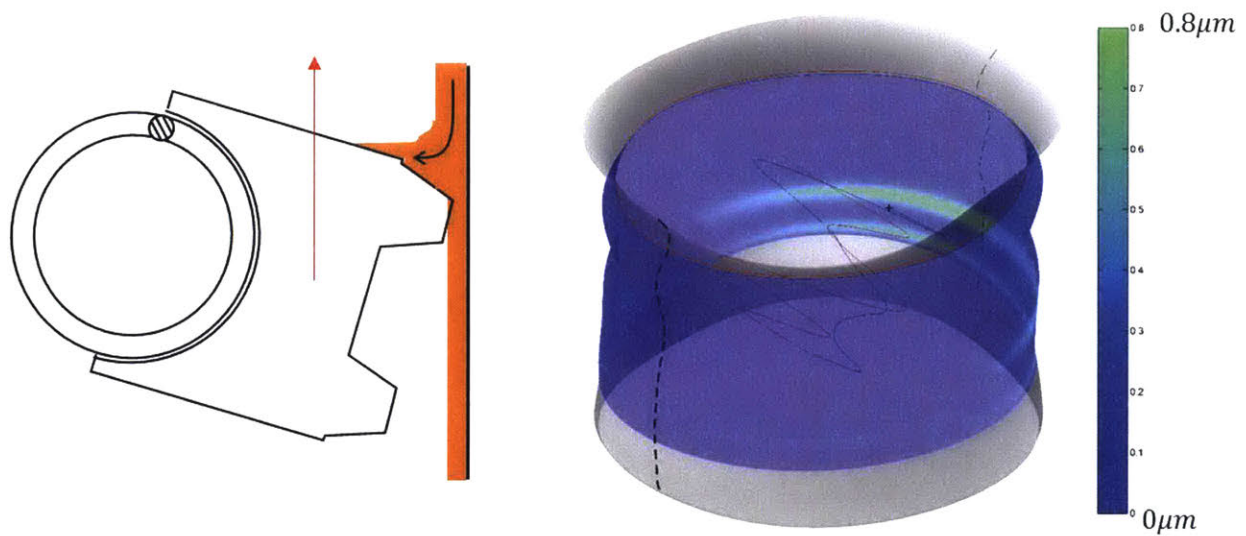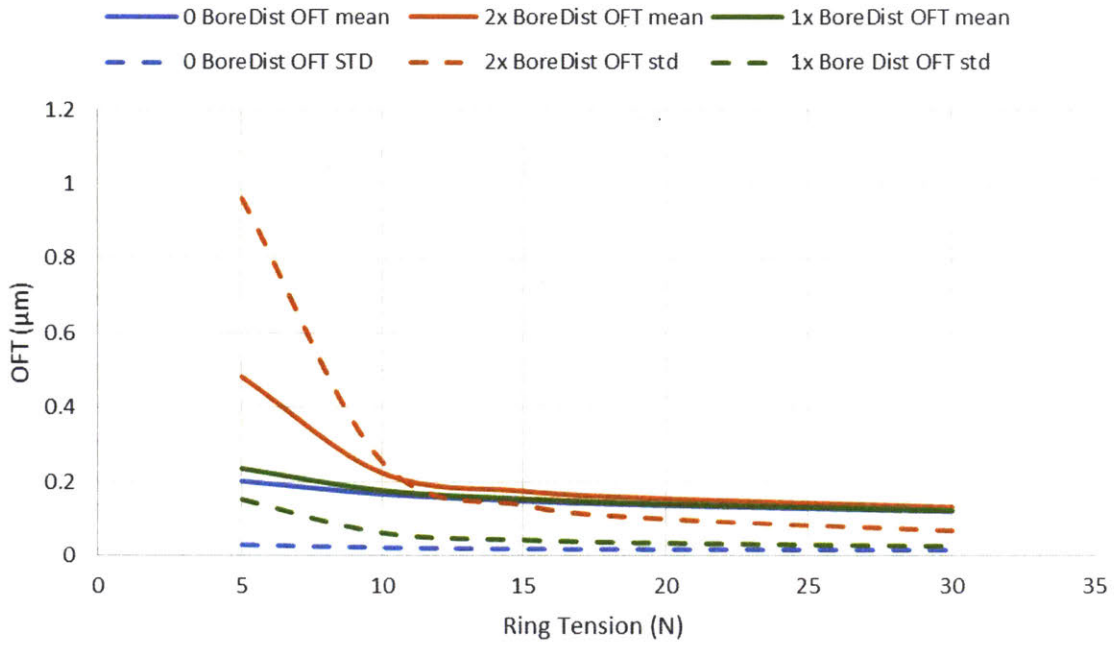

Figure 122 Up-Scraped Oil Film Thickness by TLOCR in Compression Stroke

Based on the above discussion, the results of oil film thickness around the top dead center and the TLOCR up-scraping rate with different ring tensions and bore distortions are summarized in Figure 123. In the upper plot, solid lines are the results of the average oil film thickness around the top dead center as a function of ring tension and dashed lines are the results of its standard deviation as a function of ring tension. Increase of ring tension not only decreases the oil film thickness which is suggested by Equation 4.2 and Equation 5.7, but also improves the capability of the ring to adapt to the cylinder geometry as discussed in Section 3.4, thus decreasing the variance of the oil film thickness caused by non-conformability. When increasing bore distortion, we can find that higher ring tension is required to control the oil film thickness and its variance. When the bore distortion is zero, there is still a very small variance which is introduced by change of piston tilt and sliding speed between the ring running surfaces and the liner. The lower plot shows the results of the average rate of oil scraped by the TLOCR

upper land during the compression and the exhaust strokes as a function of ring tension. According to previous discussion, OCR up-scraping rate is mainly determined by the change of ring relative angle to the liner. Increase of ring tension can help TLOCR conform to the liner better between the two lands since it increases the contact force to the land that tends to stay with the liner and provides counter-balance twisting moment. Therefore, increase of ring tension leads to a decrease of up-scraping rate. The effect of bore distortion on ring dynamic twist is insignificant, so it is difficult to make a difference in up-scraping rate.
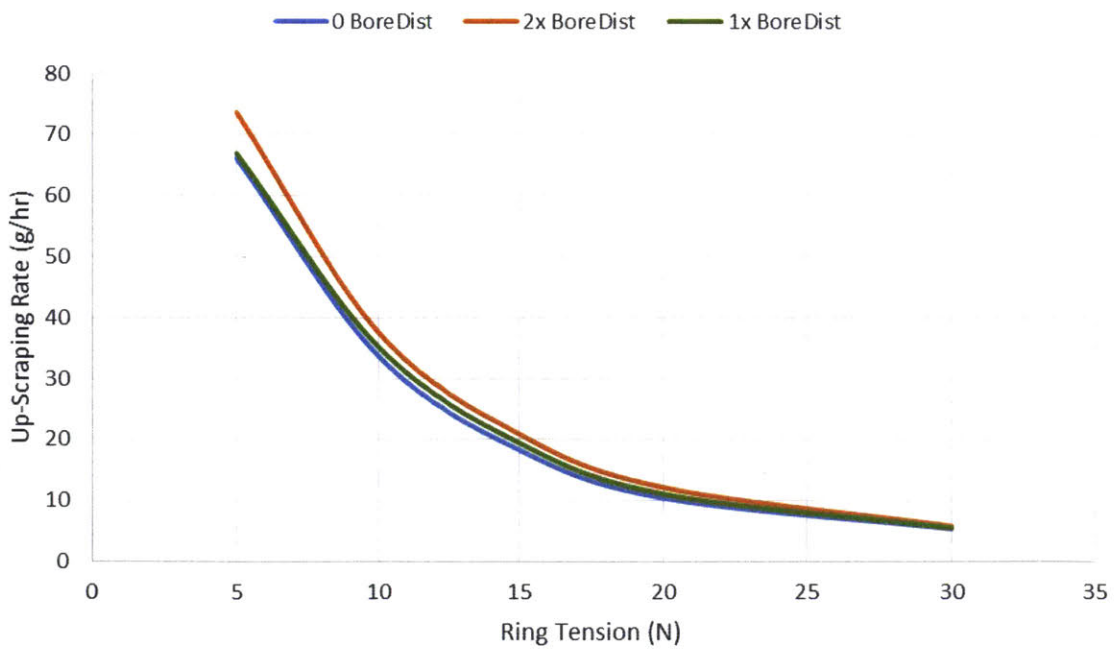
Figure 123 Oil Film Thickness and Up-Scraping Rate with Different Bore Distortions and Ring Tensions

5.5.4. The Effect of Piston Tilt on Oil Transfer around TLOCR

A similar analysis is conducted on the effect of piton tilt in this section. The same engine is used for calculation. We change the level of piston tilt by changing the clearance between the piston skirt and the liner. Piston tilt is aggregated with larger clearance. Figure 124 shows 3 different levels of piston tilt used in the analysis.
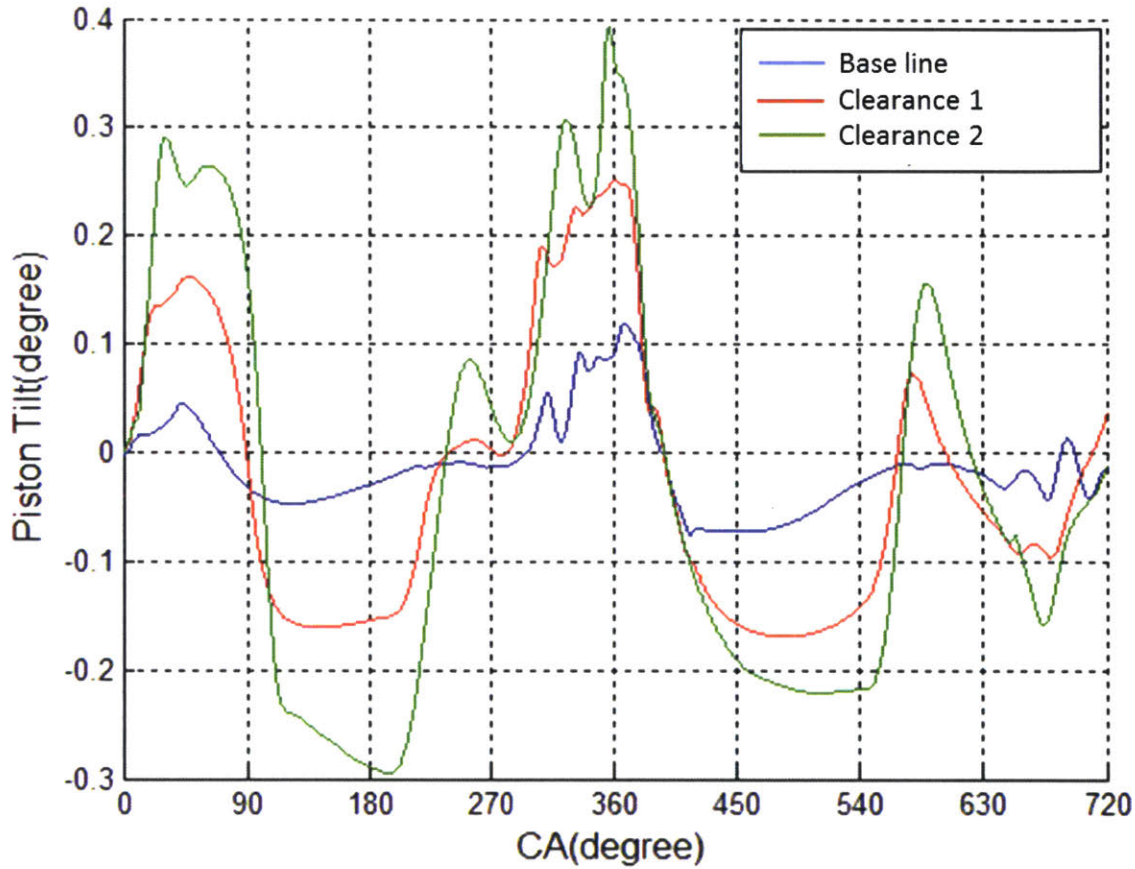

Figure 124 Three Different Patterns of Piston Tilt

The ring gap is still aligned with the thrust side of the bore and its position is fixed during the calculation. The ring tension is 10N and the engine speed was changed to 2000rpm. Again, we will examine the two quantities of TLOCR oil control, namely, the oil film thickness left on the liner during early part of down-strokes, and the up-scraping by the upper land in the lower part of the stroke.

Figure 125 shows the results of oil film thickness on the liner left by the TLOCR with different levels of piton tilt. Since piston tilt does not impact much on ring-liner circumferential conformability in the early part of the down-strokes so that the oil film thickness of the three levels of piston tilt is very close with

174

each other. However, when the ring is approaching to BDC, the trailing land becomes fully-flooded due to bridging and thus the piston tilt becomes important. Change of piton tilt not only affects the start timing of bridging but also impacts the oil film thickness allowed to pass the OCR.
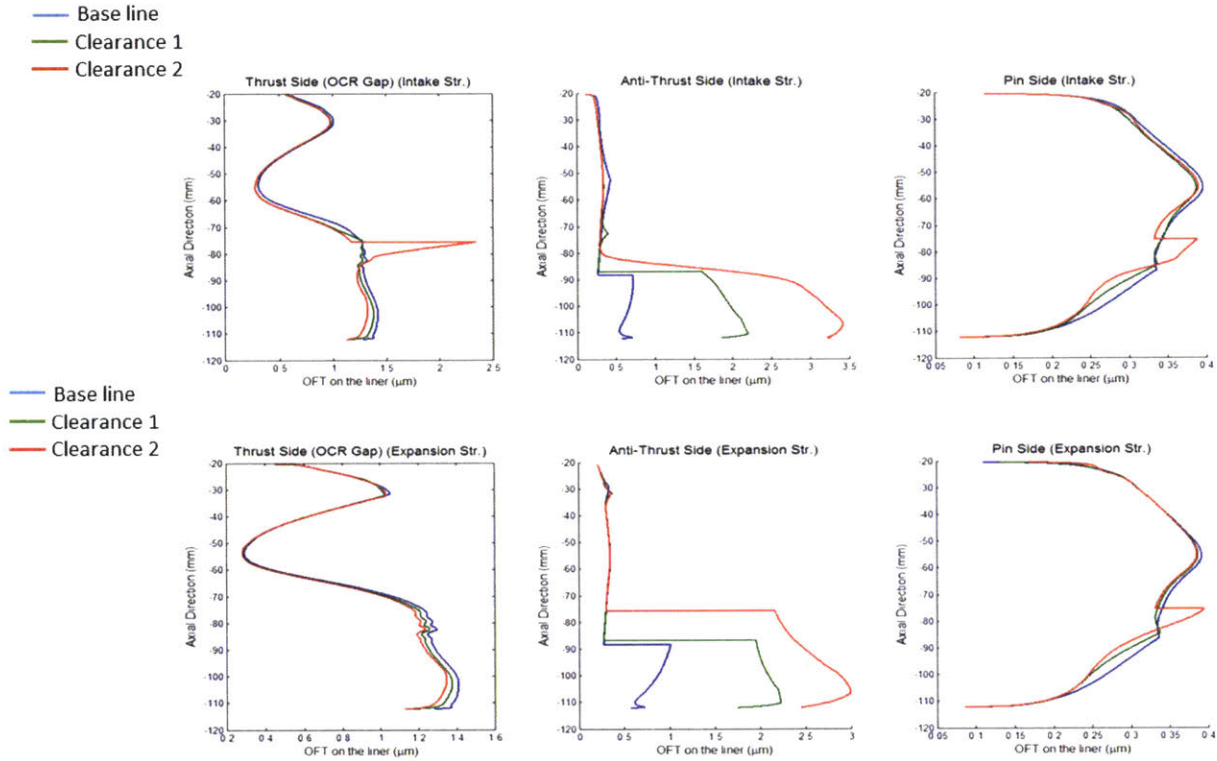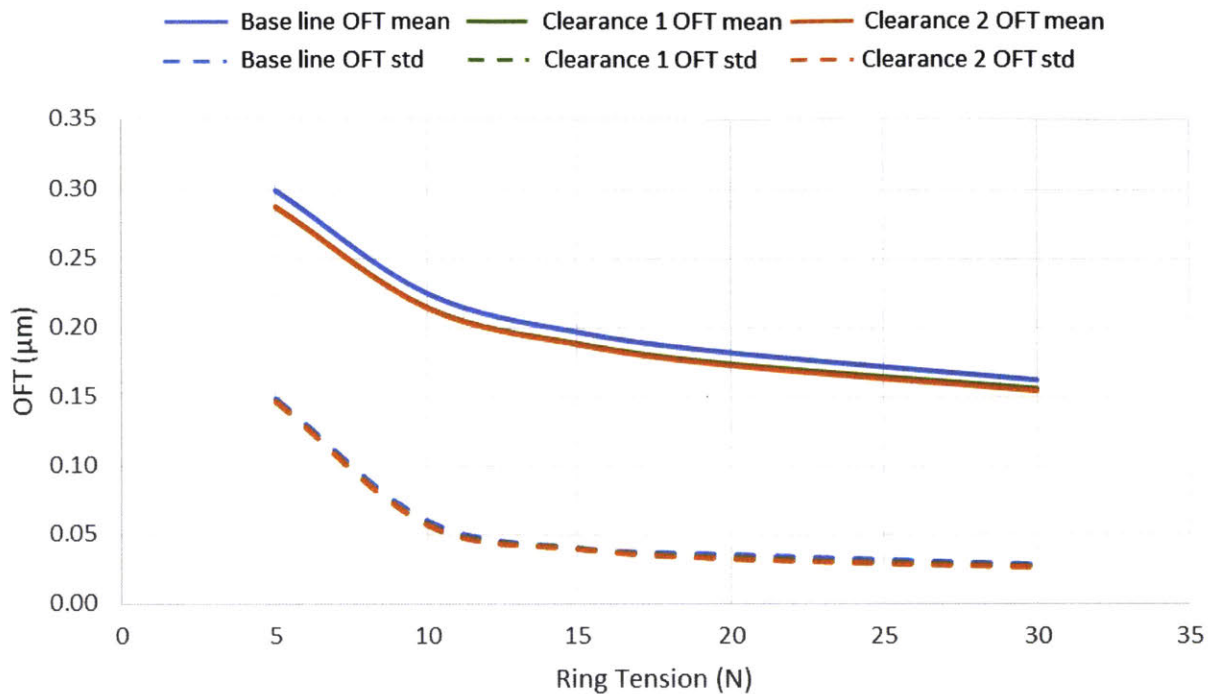

Figure 125 Oil Film Thickness on the Liner with Different Patterns of Piston Tilt during Intake and Expansion Strokes

Figure 126 shows the results of oil film thickness in the early part of the stroke and TLOCR up-scraping rate with different ring tensions and levels of piston tilt. In the upper plot, solid lines are the results of the average oil film thickness around the top dead center as a function of ring tension and dashed lines are the results of its standard deviation as a function of ring tension. As we expect, change of piston tilt does not really change the oil film thickness and its variance around the top dead center, since it has negligible impact on ring-liner circumferential conformability. The lower plot shows the results of the average OCR up-scraping rate during compression and exhaust strokes as a function of ring tension. Change of piston tilt significantly changes ring relative angle with the liner and it is obvious that an increase of piston tilt results in a larger up-scraping rate.
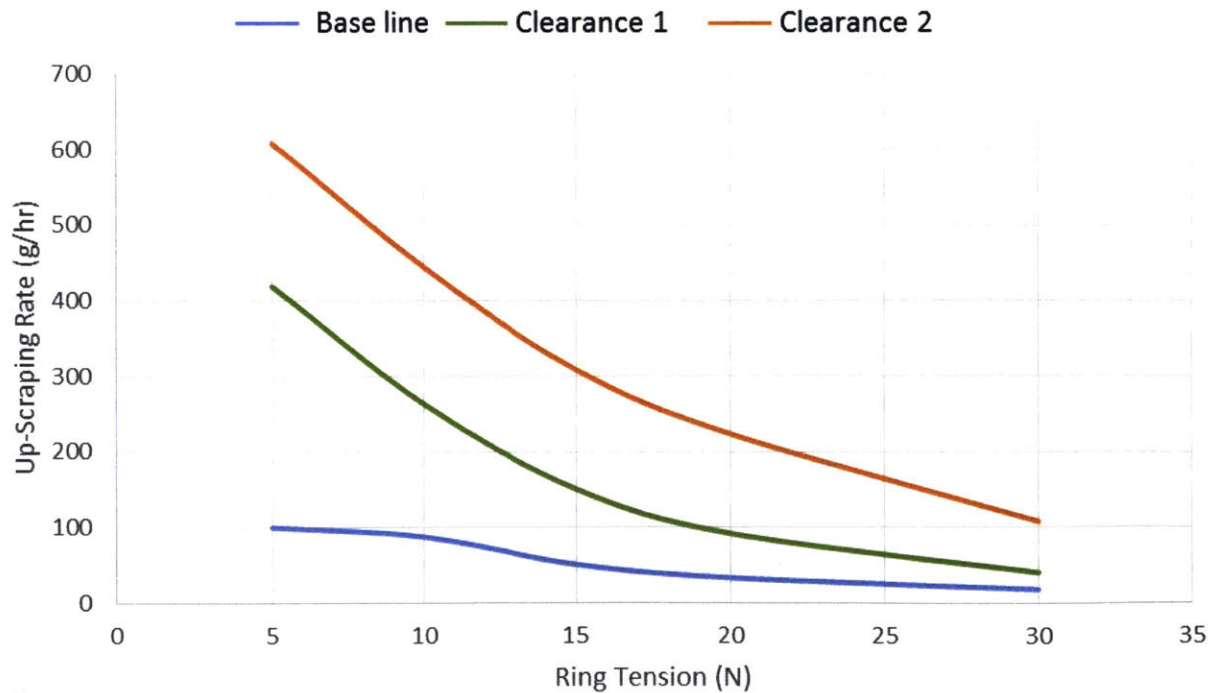
Figure 126 Oil Film Thickness and Up-Scraping Rate with Different Patterns of Piston Tilt and Ring Tensions

5.5.5. Constant Contact Pressure and Constant Ring Land-Width

In automotive industry, many efforts are made to reduce the ring tension of OCR without increase of oil consumption. One of the common methods used by the industry is to reduce the ring tension and ring land width at the same time to keep the same unit pressure applied to each land. As Equation 4.2 and Equation 5.7 imply, when the ring land is in contact with the liner, it is the unit pressure that determines the oil film thickness. Another design direction to accompany with tension reduction is to use a smoother liner as the same or less oil film thickness can be reached with smoother liner and less ring tension [8]. Thus, we are going to apply the calculation on the same engine but with a smoother liner.
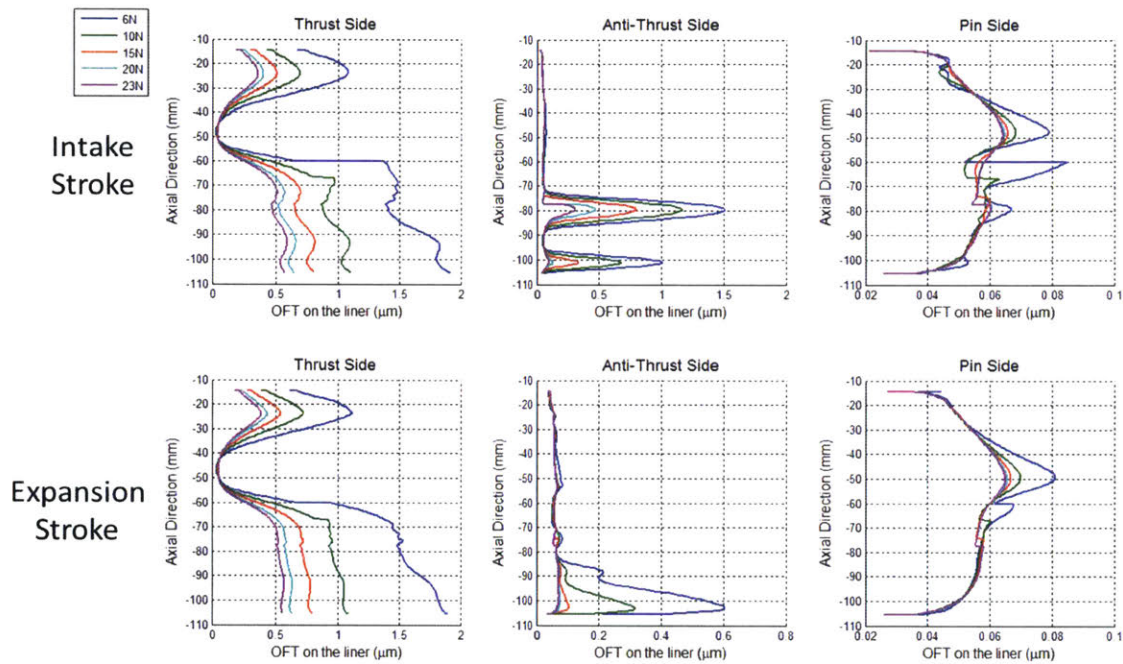

Figure 127 Oil Film Thickness on the Liner with Different Ring Tensions

Figure 127 shows the results of oil film thickness on the liner with different ring tensions. The ring land width is adjusted to keep the same unit pressure applied when ring tension is changed. The results clearly show that we are able to maintain almost the same level of oil film thickness on the liner when reducing ring tension but keeping the same unit pressure, as long as the ring conforms to the liner and the trailing land is starved. However, as discussed before, ring tension is very important to both ring-liner circumferential conformability and axial conformability. As a result, reducing ring tension but keeping the same unit pressure cannot help the ring have the same ability to resist a loss of contact due to ring structural deformation. We can find this problem around ring gap area and lower stroke, where

the ring tends to conform to the liner badly and the trailing land becomes fully flooded. The oil film thickness increases incredibly in these areas with a decrease of ring tension.
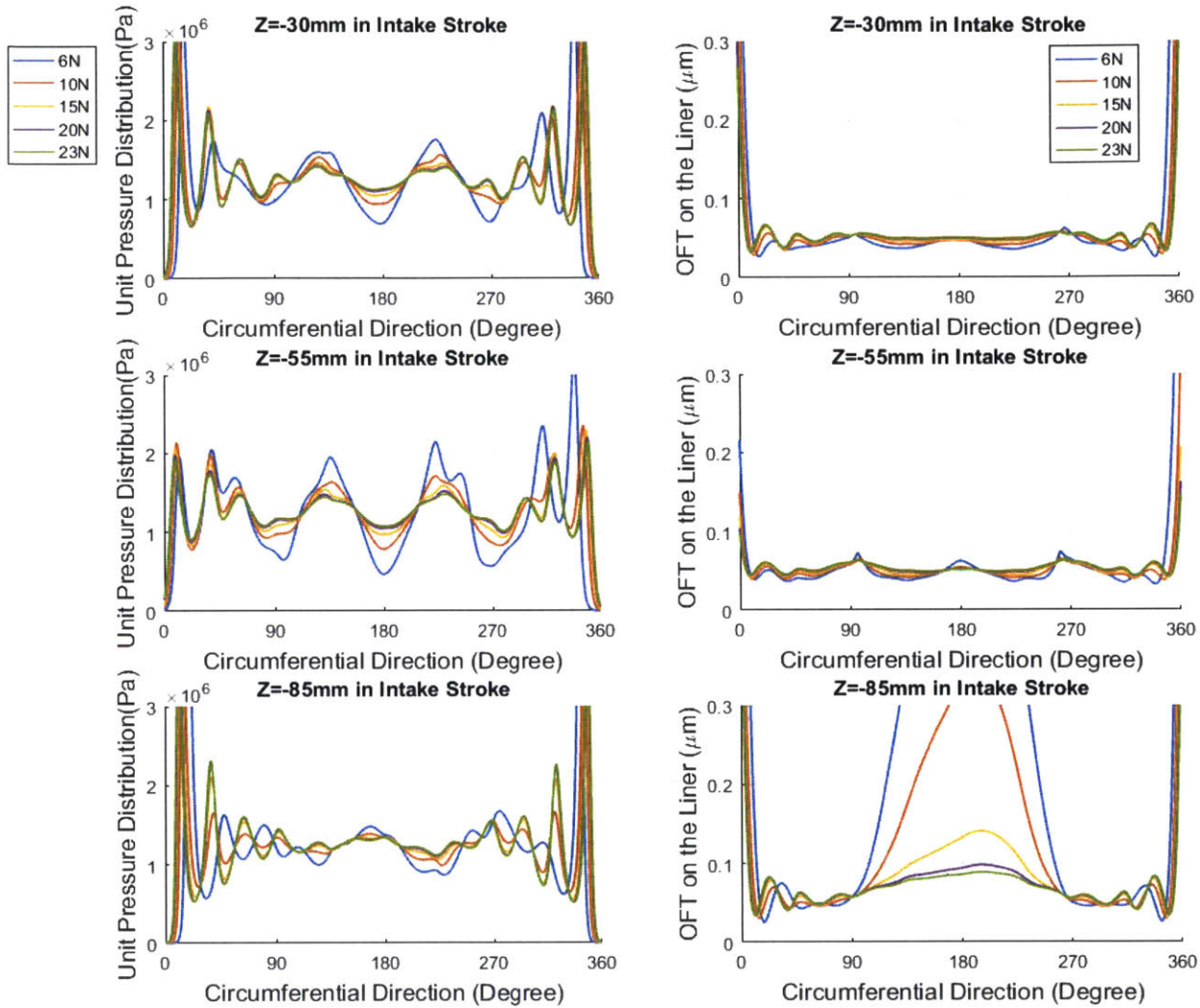

Figure 128 Unit Pressure and OFT Distribution along the Circumference

Figure 128 shows the distributions of the unit pressure and the oil film thickness along the circumference (0 is the thrust side and 180° is the anti-thrust side) at different axial positions (z=-30mm early in the down stroke; -55mm mid-stroke; z=-85mm late in the down stroke; z=0 is the TDC of the top ring). If there is no bore distortion or piston tilt, the unit pressure should be $\frac{6N}{0.06mm*2*D_b/2} =$

$\frac{10N}{0.1mm*2*D_b/2} = \frac{15N}{0.15mm*2*D_b/2} = \frac{20N}{0.2mm*2*D_b/2} = \frac{23N}{0.23mm*2*D_b/2} = 1.2 \times 10^6 \ Pa.$ We can see that the

pressure distributions along the circumference are around this number but with high order variance

though the bore distortion only has up to 4th order. It is because the ring relative angle to the liner changes both magnitude and direction along the circumference which results in different clearances between the two lands and the liner, and the correlations between the pressure (both hydrodynamic pressure and asperity contact pressure) and the clearance are not linear. In addition, the ring gap also causes non-linear behavior around the gap area. All these non-linear factors combined together lead to a high order variance of the unit pressure. However, if we look at the ring neutral axis deformation as shown in Figure 129, it actually follows the distorted geometry of the bore which matches our expectation as discussed in Section 3.5. The oil film thickness is mostly dependent on the unit pressure, so the distributions of the oil film thickness are very close to each other among all the ring tensions. However, higher ring tension improves both circumferential and axial conformabilities of the TLOCR which leads to a smaller variance. The different behaviors at the anti-thrust side in the late down-stroke and around the gap area are explained above, but from Figure 128 we can see that the gap effect is localized.
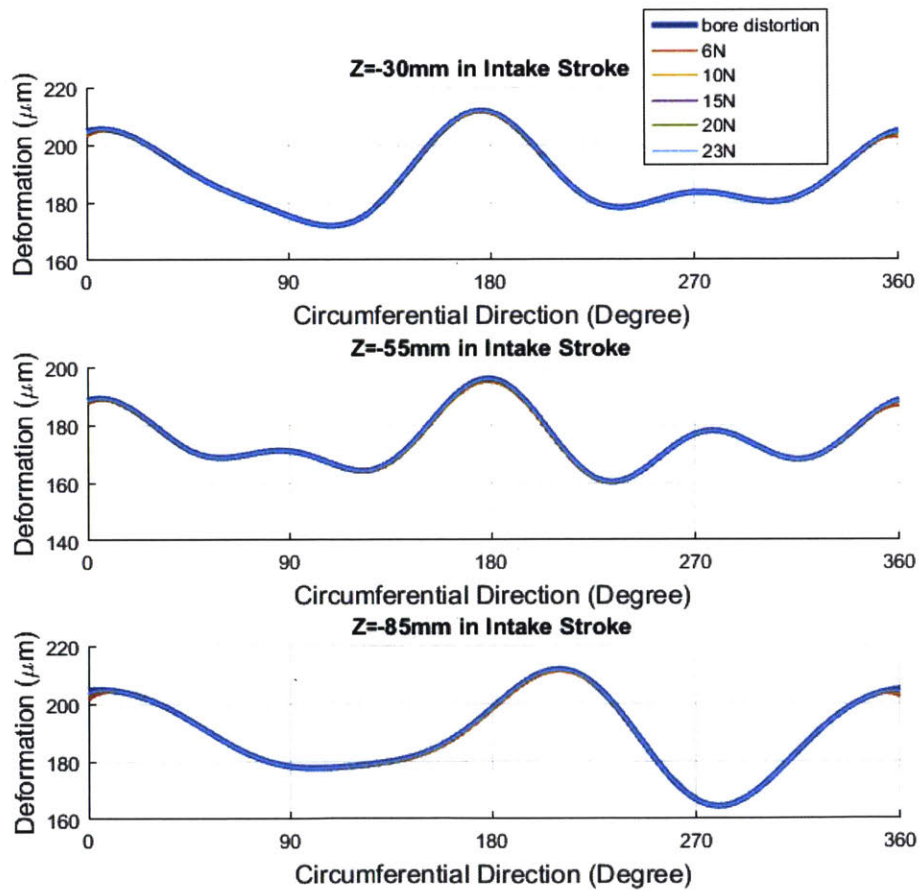

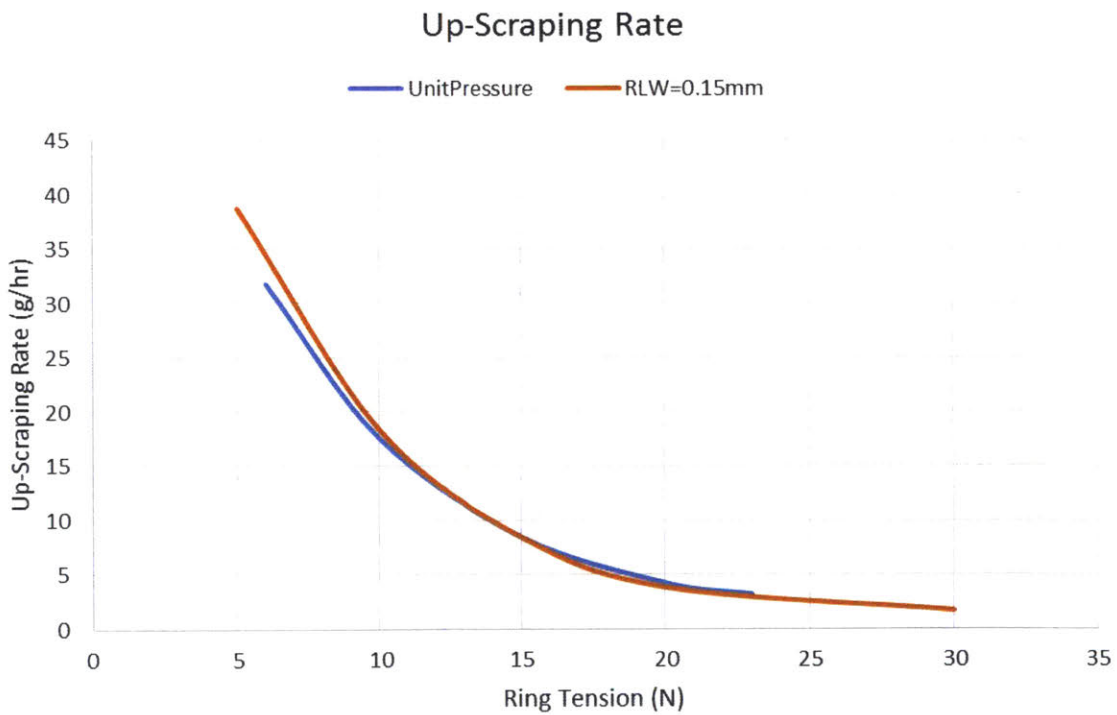Figure 129 Bore Distortion and Ring Neutral Axis Deformation at Different Axial Positions
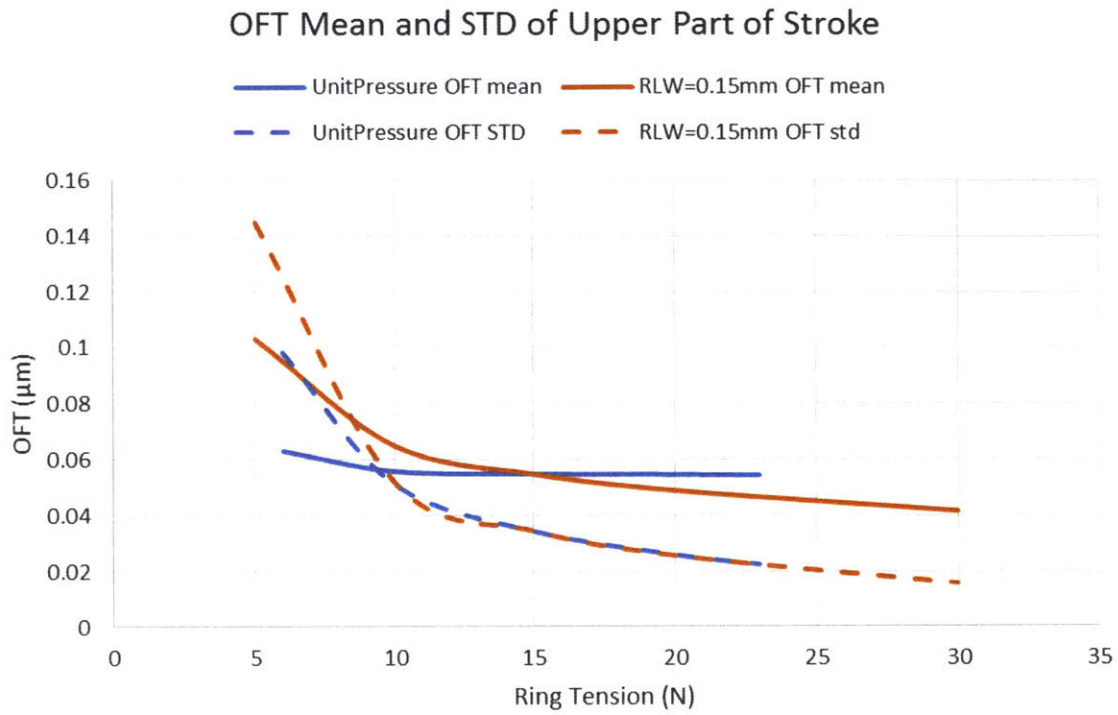
OFT Mean and STD of Upper Part of Stroke

Up-Scraping Rate

Figure 130 Comparison between Constant Unit Pressure and Constant Ring Land Width

Figure 130 shows the results of oil film thickness on the liner around the top dead center and its

standard deviation as a function of ring tension and the OCR up-scraping rate as a function of ring

tension. There are two cases in this figure. One is keeping the same unit pressure applied to each land (blue lines) and the other is keeping the same ring land-width (orange lines). As mentioned earlier, the oil control of the TLOCR is defined with two quantities. The first is the thickness of the oil left on the liner during a down-stroke. The second is up-scraping of the oil on the liner by the upper land during an up-stroke. Figure 130 shows that the first oil control quantity is largely determined by the unit pressure within the range of reasonable ring tension, and the second (up-scraping) is determined by the ring tension, which implies that the structural level behavior is dominant. As a result, to keep a constant unit pressure when ring tension is reduced is a good idea to maintain similar oil film thickness as long as the ring conforms to the liner, but people still need to find other ways to control oil transport caused by non-conformability and scraping.

5.6. Oil Transport by the Top Two Rings

Several calculations were completed on a production gasoline engine to study the oil transport by the top two rings with an integration of both local and global processes. The global factors include bore distortion, piston secondary motion, ring structural deformation and inter-ring gas pressure, et al. The oil supply to the top two rings is mostly determined by the oil film thickness on the liner left by the OCR. This part of oil supply to the top two rings is a result of the TLOCR circumferential conformability and axial conformability (Section 5.5) and could be treated as a global factor as well. Local force is generated with boundary conditions dependent on the global factors and local processes. In addition to the oil film thickness left by the OCR that is fed into the top two rings, bridging can bring excessive oil from the piston lands to the liner and change the oil supply to the top two rings locally. Another local deviation of the oil content from the oil film left by the oil control ring is the addition of the fuel, which is one of the sources for fuel dilution and local excessive wear on the liner.

The baseline of the calculation is the case that the engine is running with normal conditions and bridging in some conformed area by the top two rings. Then we add few fuel spots to the oil film before the compression stroke at some random positions on the liner to study the fuel-oil dilution effect. Finally, we run the third calculation on an engine with extraordinary bore distortion with bridging in the non-conformed area by the top two rings and study the oil transport with the combination of global and local processes. The goal of presenting these results is to show the basic and unique capabilities of the model.

5.6.1. Calculation Set-up

The results of ring twist and land pressures described in Section 4.9.1 are used for the lubrication of the top two rings under the same conditions. In order to study the effect of bridging at the piston 3rd land on ring-liner lubrication, an additional $10\mu m$ oil film with a width of 10^0 along the circumference was put at the pin side (90^0 away from the thrust side) of the liner around the top dead center and the bottom dead center in the intake and expansion strokes (the two red stripes in Figure 131). Therefore, this amount of the oil by-passed the OCR and was directly fed into the second ring.
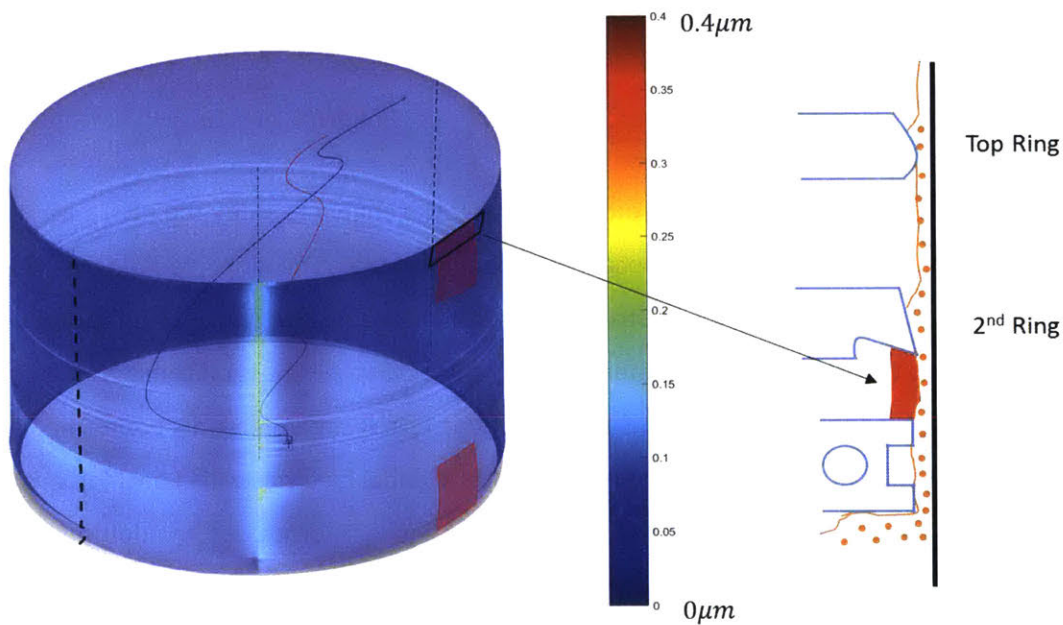

Figure 131 Additional Oil on the Liner from Bridging

5.6.2. Sample Results

Figure 132, Figure 133 and Figure 134 demonstrate the oil film thickness on the liner after the OCR, the second ring and the top ring in the intake stroke. Zero degree of the circumferential direction represents the thrust side of the liner and the reference point of the axial direction is set to be the position of the top ring at the top dead center. In the three figures, the bolded dashed line on the liner marks the thrust side and correspondingly the light dashed line represents the anti-thrust side. The red curve inside the cylinder shows the piston tilt during the down-stroke and the blue curve inside the cylinder shows the piston tilt during the up stroke. The curve towards the anti-thrust side implies that the crown land of the piston tilts towards the anti-thrust side, equivalent to a positive piston tilt. The curve towards the thrust

side implies that the crown land of the piston tilts towards the thrust side, equivalent to a negative piston tilt.

From the results, it is very obvious that the oil film thickness on the liner left by the ring pack is mainly determined by the OCR. The OCR has a relatively large ring tension and small stiffness which help it stay in contact with the liner. Furthermore, the profiles of its two lands are flat, so it has to utilize the gradient of the surface micro geometry to generate hydrodynamic pressure. As a result, the OCR is able to control the oil film thickness to a roughness level. However, at the two ends of the ring gap, the OCR loses constraint from the other side. Then, depending on the local bore distortion, the ring may either not conform well at the gap location with relatively thicker oil film thickness is observed around 45 degree of the circumferential direction (the position of the OCR gap), or have higher level contact as discussed in Section 5.5.2.

The oil film thickness left by the OCR is the major oil supply to the top two rings. Therefore, though the top two rings sometimes have poor conformability with the liner, the oil film thickness that is allowed to pass the top two rings is still limited to the inter-asperity level as long as there is no other oil supply, as shown in Figure 135 and Figure 136. Figure 136 plots the bore distortion, the second ring neutral axis deformation, the ring-liner minimum clearance and the oil film thickness after the second ring at 40CAD (-19.5mm in axial direction). It clearly shows that around the second ring gap position (225° away from the thrust side) the second ring loses the conformability to the liner but the oil film thickness left at that position is limited by the oil supply from the TLOCR. In Figure 135 and Figure 136, some non-conformability between the top two rings and the liner around the top dead center is introduced by a discontinuity of oil supply at the pin side (from sub-microns oil film thickness to $10\mu m$ oil film thickness).

As discussed before, besides the oil film thickness left by the oil control ring, some local behavior such as bridging can also provide additional oil supply to the top two rings. In this calculation, $10\mu m$ oil film with a width of 20° along the circumference is fed into the second ring at the pin side (90° away from the thrust side) around the top dead center and the bottom dead center, which leads to a fully-flooded boundary condition of the second ring. The second ring is lifted locally due to an increase of hydrodynamic pressure and leaves thick oil film on the liner (Figure 133 and Figure 136). When the top ring slides down and encounters this thick oil film, it scrapes some oil from the liner with the help of the pressure force in the top ring groove (Figure 134) but relatively thick oil film (roughly $0.3\mu m$) is still left on the liner.
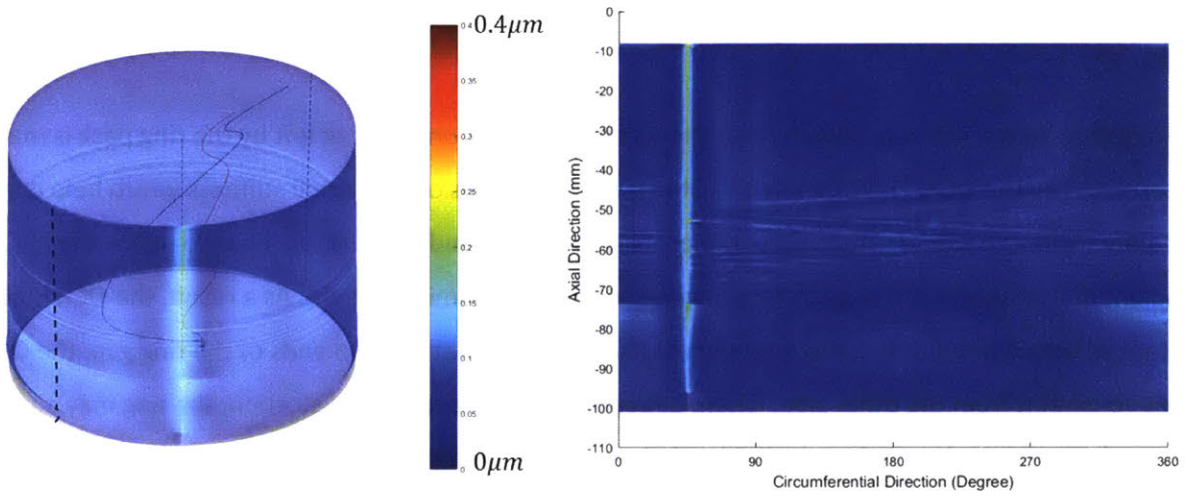
183

Figure 132 the Oil Film Thickness on the Liner after the OCR in the Intake Stroke
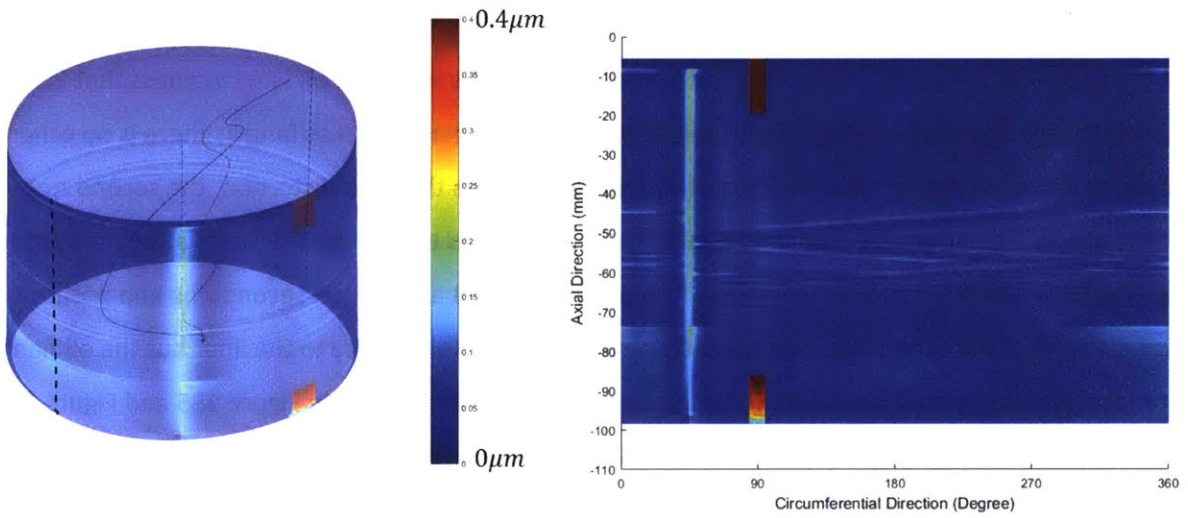

Figure 133 the Oil Film Thickness on the Liner after the Second Ring in the Intake Stroke
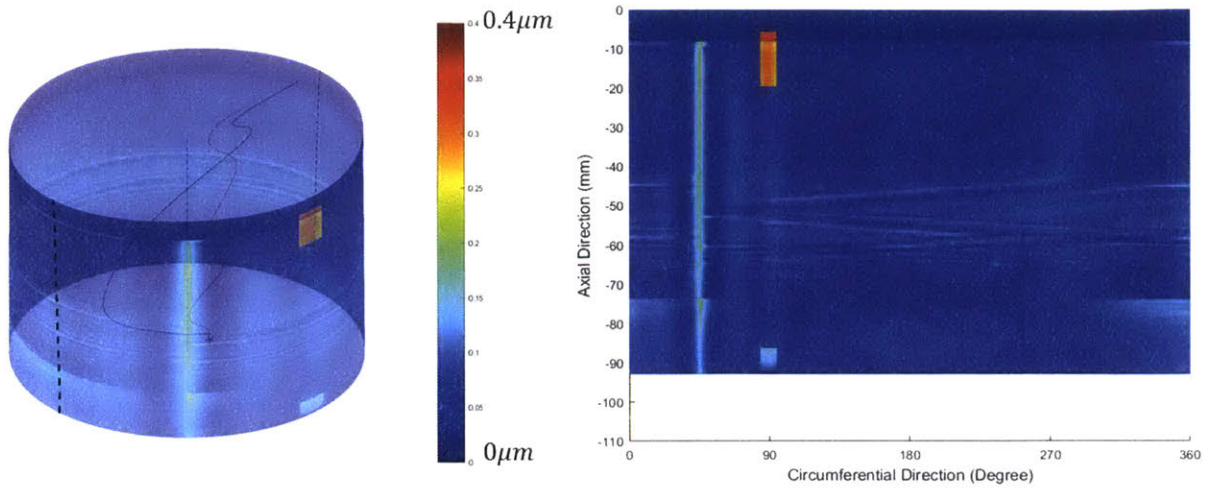
Figure 134 the Oil Film Thickness on the Liner after the Top Ring in the Intake Stroke
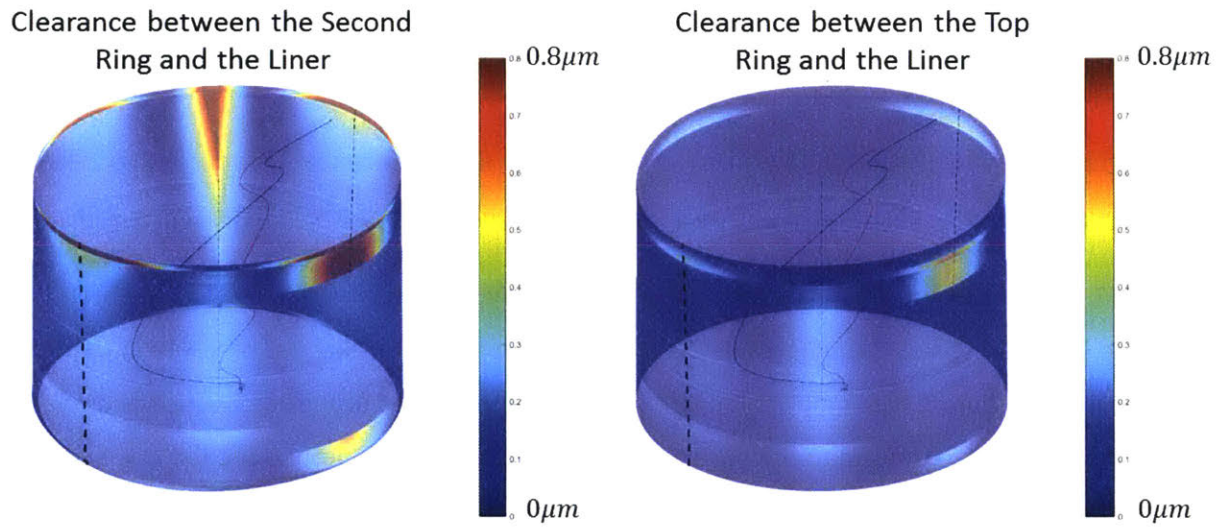

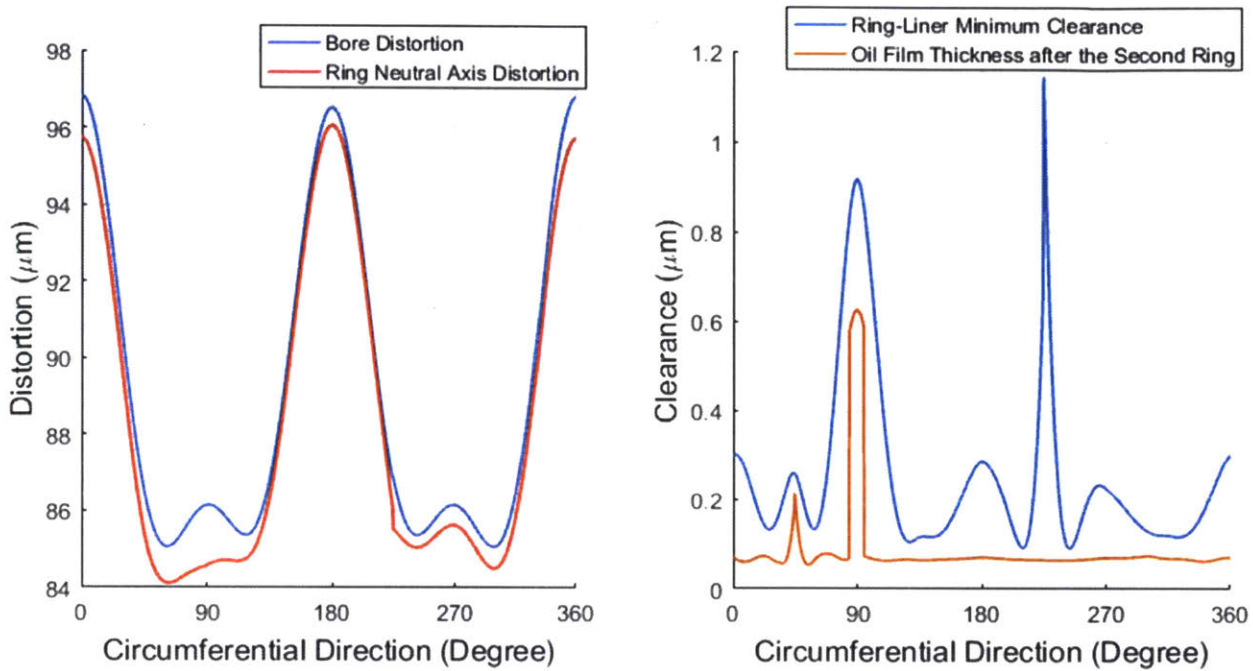*Figure 135 the Minimum Ring-Liner Clearance of the Top Two Rings*

Figure 136 Second Ring Ring-Liner Geometry and Oil Film Thickness at 40CA (-19.5mm in Axial Direction)

Figure 137, Figure 138 and Figure 139 show the results of the oil film thickness on the liner after the top ring, the second ring and the OCR respectively in the compression stroke. Gas pressure in the top ring groove is raised during the compression stroke since it is connected to the combustion chamber, and helps the top ring to conform to the bore distortion. The thick oil film around the top dead center that was left during the intake stoke is up-scraped. The difference of the oil film thickness passing the top ring during the intake and the compression strokes at the pin side is plotted in Figure 141.

At the end of the compression stroke, thick oil film thickness is left on the liner by the OCR around the anti-thrust side. Figure 81 shows that at the end of the compression stroke, the OCR has a large negative angle relative to the liner at the anti-thrust side, causing a loss of contact of the OCR trailing land. At the same time, bridging happens between the OCR two lands and thick oil film is allowed to pass the trailing land with a fully-flooded boundary condition, as shown in Figure 140. However, this thick oil film is difficult to contribute to oil consumption because when the OCR moves downwards during the expansion stroke, the oil will be scraped from the liner and flow into the piston chamfer below the OCR.
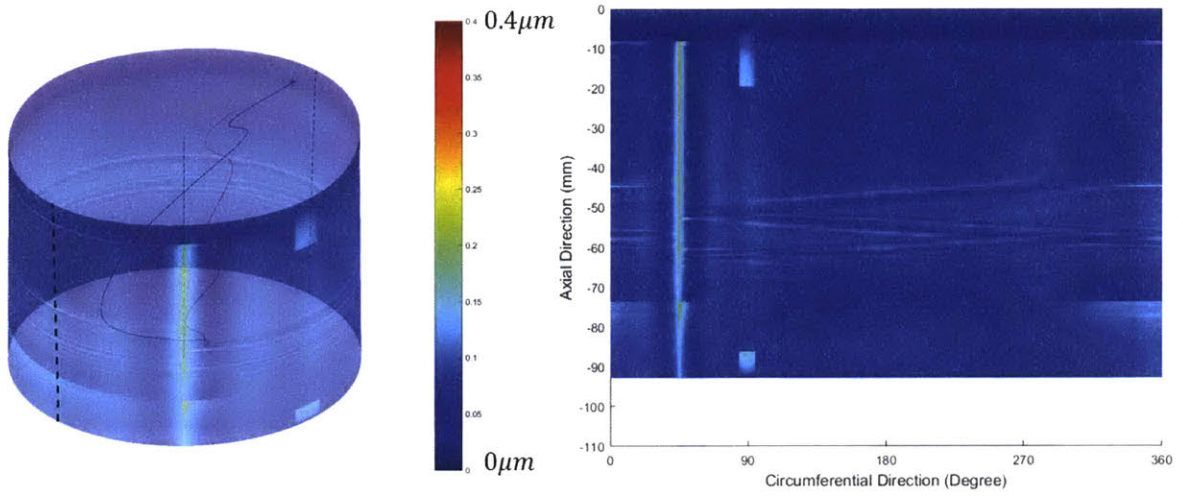
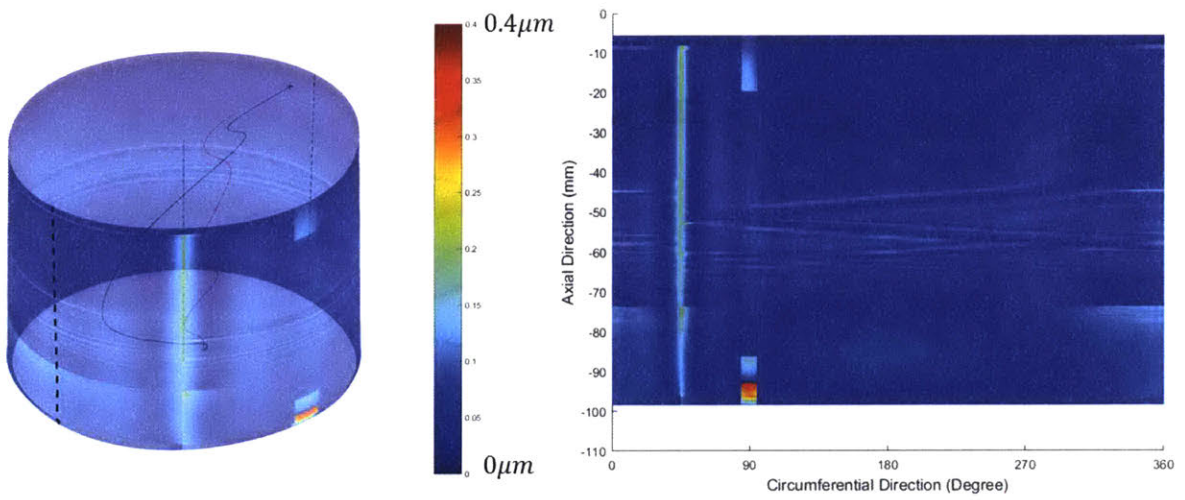*Figure 137 the Oil Film Thickness on the Liner after the Top Ring in the Compression Stroke*

Figure 138 the Oil Film Thickness on the Liner after the Second Ring in the Compression Stroke
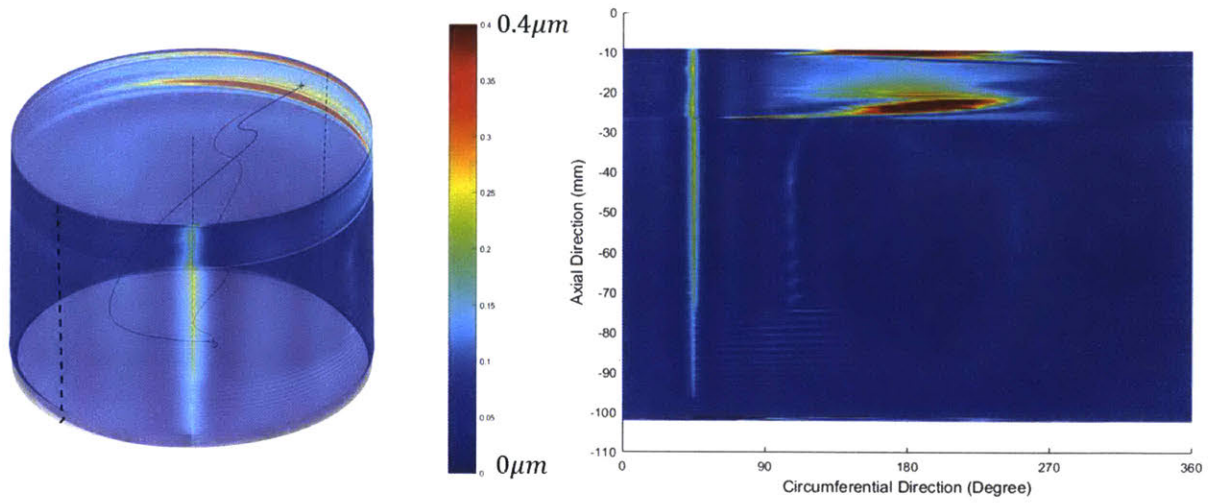
Figure 139 the Oil Film Thickness on the Liner after the OCR in the Compression Stroke
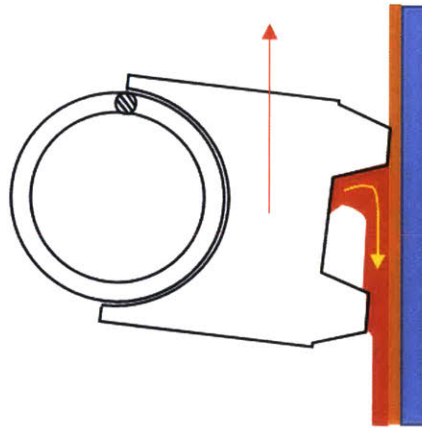

Figure 140 Fully Flooded Trialing Land of the TLOCR before TDC in the Compression Stroke
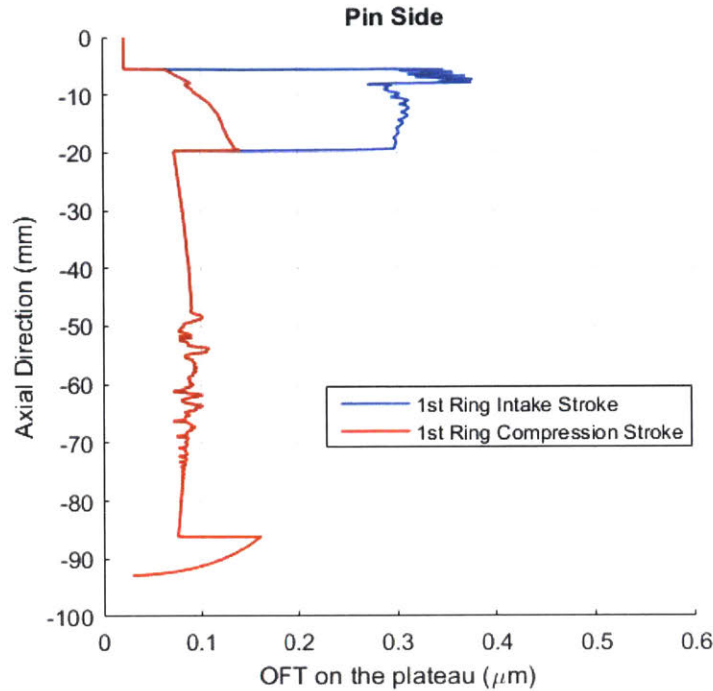
Figure 141 the Oil Film Thickness on the Liner (Pin Side) after the Top Ring in the Intake and the Compression Strokes

Figure 142, Figure 143 and Figure 144 demonstrate the oil film thickness on the liner after the OCR, the second ring and the top ring respectively during the expansion stroke. The overall oil film thickness is still determined by the OCR. However, compared to the intake stroke, the surrounding gas pressure of the ring pack is high. As a result, the excessive oil fed into the second ring due to bridging is scraped by the top two rings and only limited amount is left on the liner. At the circumferential position of 45°, all the three rings leave high oil film thickness on the liner. It is because the OCR gap is set to be at this position and around the gap area the OCR does not conform to the liner and leaves relatively high oil film thickness which is fed into the top two rings. However, the film thickness is not large enough to provide fully flooded boundary condition. Therefore, based on the assumption of Equation 5.17 the top two rings will not change the oil film thickness left by the OCR.
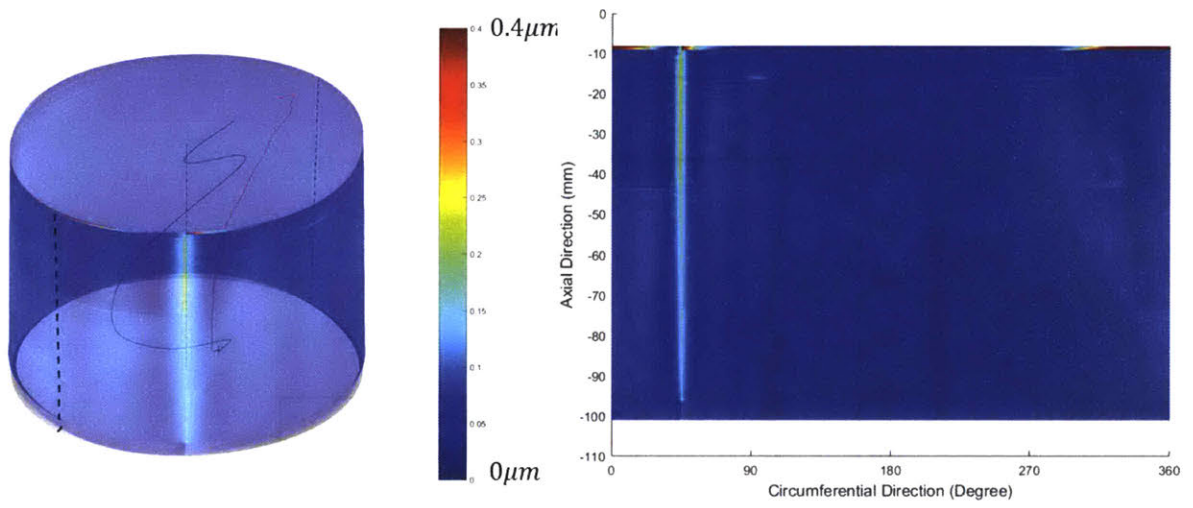
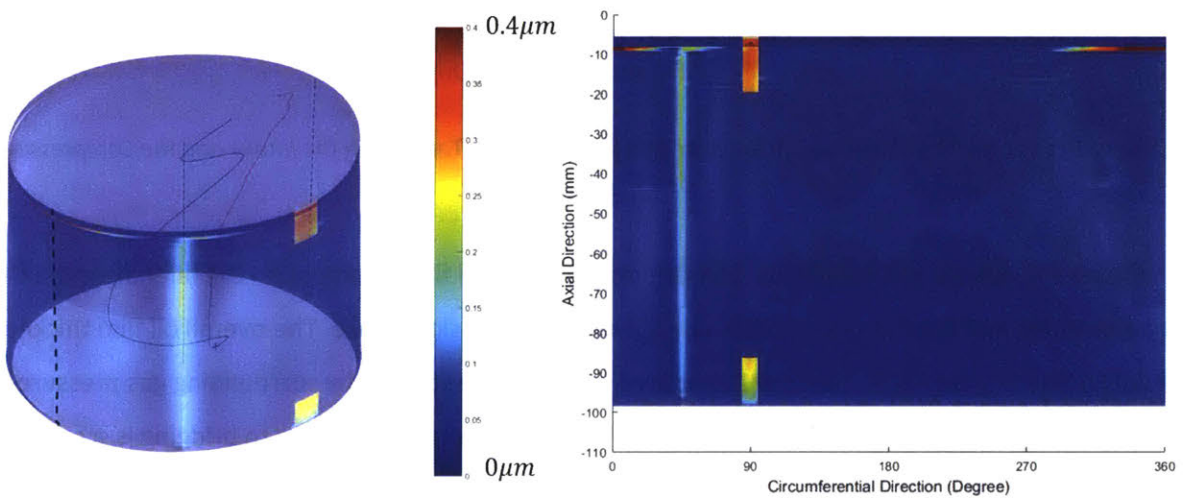*Figure 142 the Oil Film Thickness on the Liner after the OCR in the Expansion Stroke*

Figure 143 the Oil Film Thickness on the Liner after the Second Ring in the Expansion Stroke
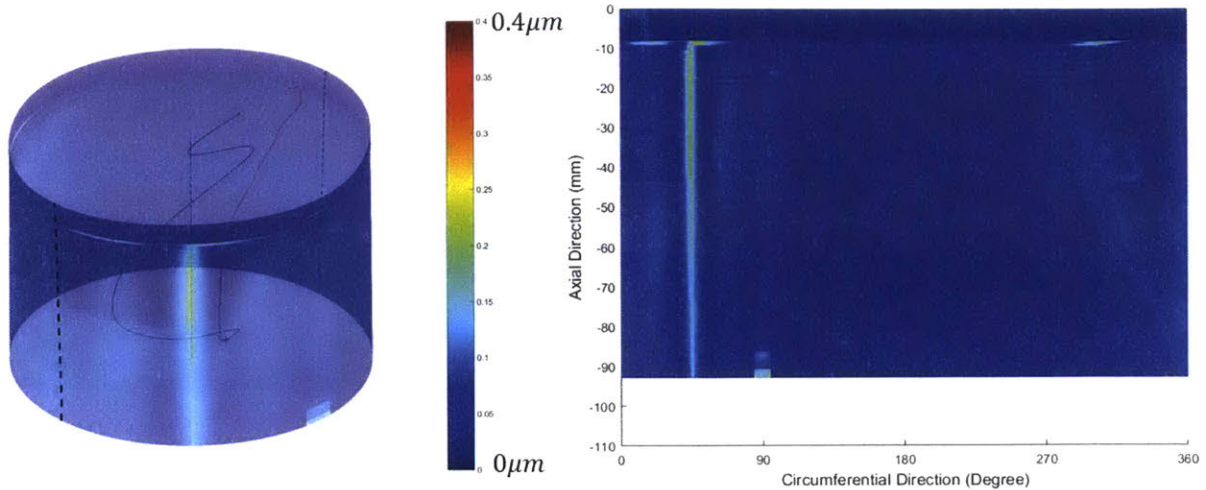
Figure 144 the Oil Film Thickness on the Liner after the Top Ring in the Expansion Stroke

Figure 145, Figure 146 and Figure 147 demonstrate the oil film thickness on the liner after the top ring, the second ring and the OCR respectively during the exhaust stroke. In the expansion stroke, the ring pack had good conformability to the liner due to an increase of surrounding pressure. Thus, sub-microns oil film was left on the liner even with bridging in the piston 3rd land. Then when the ring pack moves upwards during the exhaust stroke, the top two rings have starved boundary condition in most of the time. As a result, the oil film thickness on the liner after the top two rings during the exhaust stroke is very close to the oil film thickness left on the liner during the expansion stroke. Around the top dead center, some thick oil film is left by the OCR at the anti-thrust side of the liner, which is caused by the OCR dynamic twist and bridging between the two lands. This thick oil film will be down scraped by the OCR when it moves back during the intake stroke.
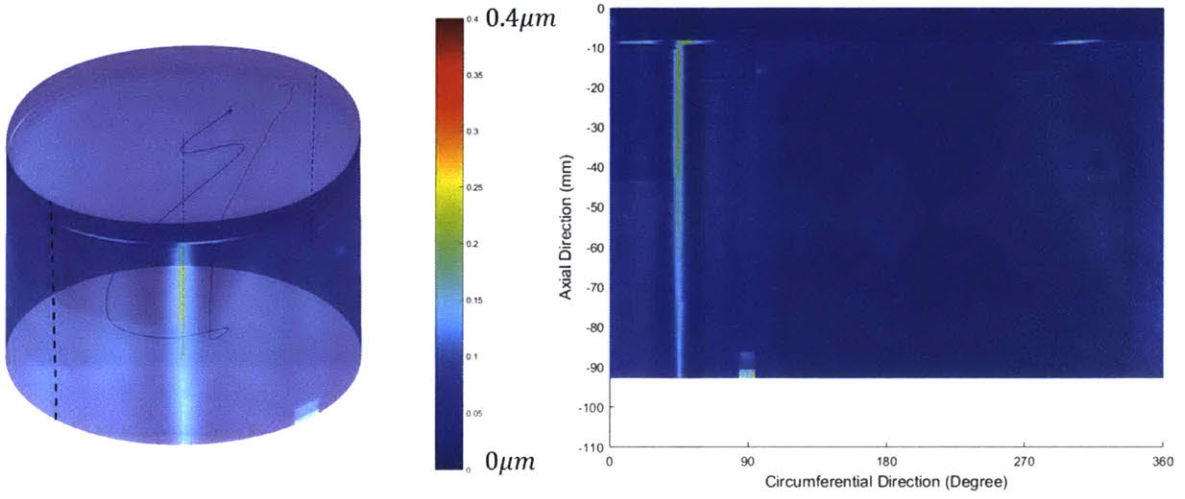
Figure 145 the Oil Film Thickness on the Liner after the Top Ring in the Exhaust Stroke
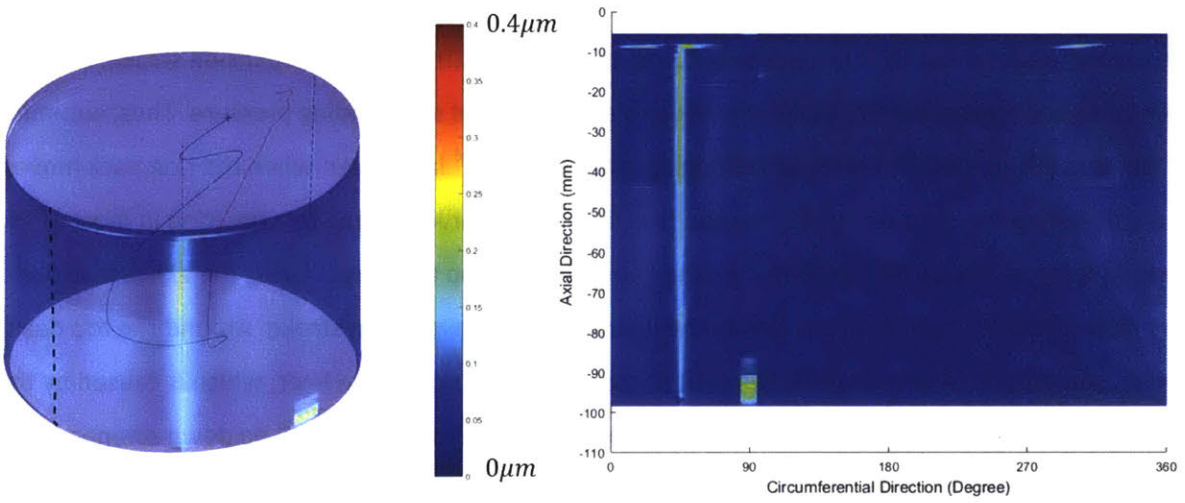
Figure 146 the Oil Film Thickness on the Liner after the Second Ring in the Exhaust Stroke
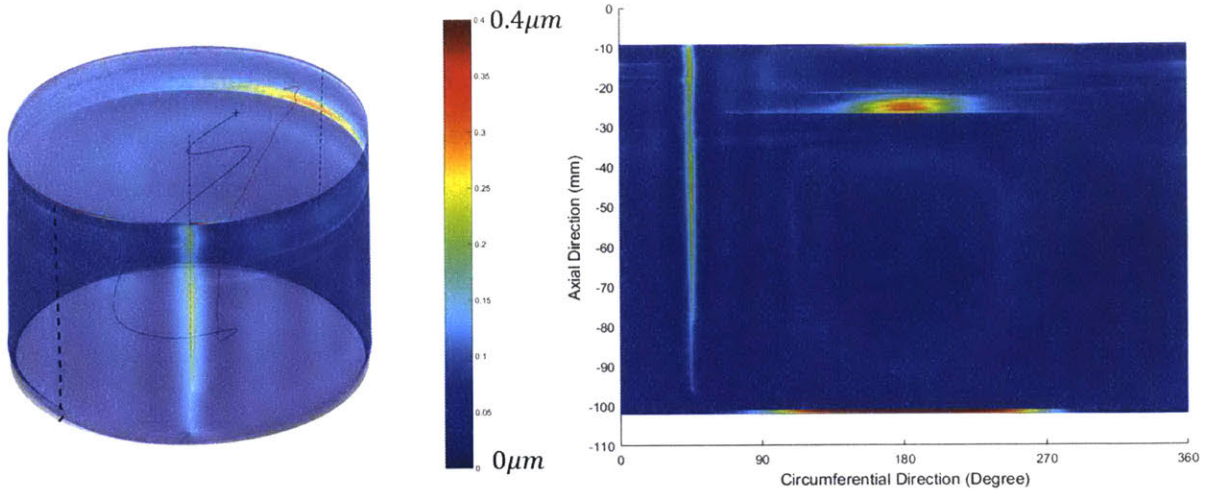
Figure 147 the Oil Film Thickness on the Liner after the OCR in the Exhaust Stroke

5.6.3. The Effect of Fuel Deposition to the Oil Layer

Local oil film exposed to the combustion chamber change is composition and thickness with deposition of the fuel. In a direct injection engine, fuel is directly injected inside the combustion chamber during the intake stroke and it is very likely that some of the fuel is sprayed onto the cylinder wall. The fuel droplets on the cylinder wall form a fuel layer over the oil film then experiences evaporation and diffusion with the oil layer. For a typical of 10's microns of fuel thickness, one can find that there is still certain amount of fuel/oil mixture left when the top ring comes back in the compression stroke [59] as shown in Figure 148.
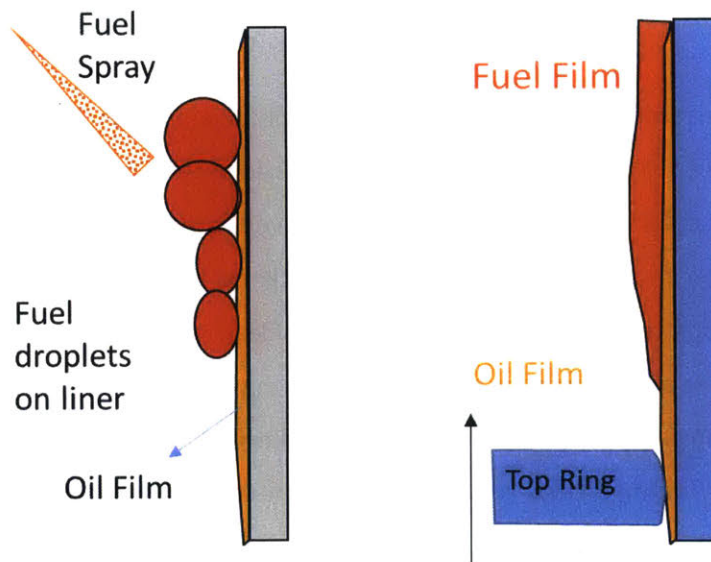
Figure 148 The Formation of Fuel Film on the Liner

In the remaining fuel/oil mixture, there are much more amount of fuel species than oil's. Since the viscosity of the fuel is roughly 1 percent of the viscosity of the oil, locally the mixture will have a huge drop of viscosity compared to the adjacent oil film. When the top ring moves upwards during the compression stroke, it will up scrape the mixture and oil may flow to the crown land with the scraped mixture layer.
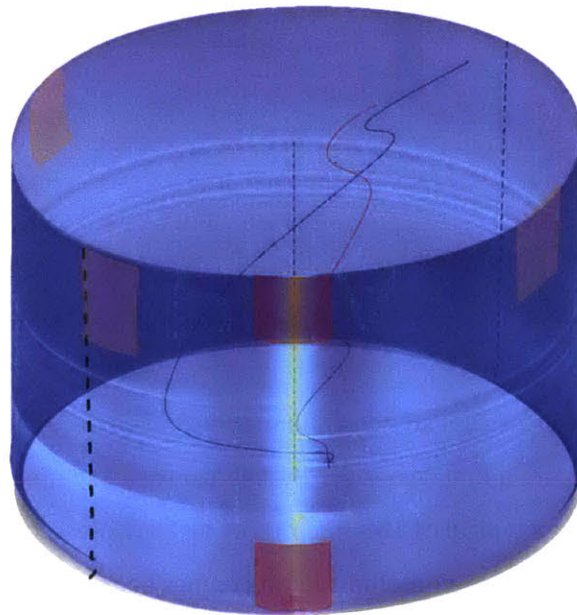
Figure 149 the Positions of Fuel Layer on the Liner

In the calculation, three stripes of fuel layer were artificially added onto the liner around the thrust side (0°) and two pin sides (90° and 320°) after the top ring had passed in the intake stroke. The position of the bridging that happened in the piston 3rd land was moved to an angular position of 45°, as shown in Figure 149. Figure 150 shows the result of the oil film thickness on the liner after the top ring in the intake stroke. The bright rectangular stripes around the top dead center and the bottom dead center correspond to the bridging area. In this case, the oil film on the liner introduced by bridging is not very thick because the top ring has a relatively good conformability with the liner at this position during the intake stroke. Thus, very limited oil may be up-scraped by the top ring associated with the bridging phenomenon.

Figure 151 shows the result of the oil film thickness on the liner after the top ring in the compression stroke. The fuel layer has already been added to the liner, so when the top ring moves upwards, it encounters the fuel film. In Figure 151, three dark stripes correspond to the positions where the fuel layer was added. Since the viscosity of the mixture decreases due to lube-fuel dilution, the oil film thickness becomes thinner locally. Figure 152 demonstrates the difference of the oil film thickness passing the top ring during the intake and the compression strokes at the pin side (90°), which implies that a significant portion of oil is up-scraped with the mixture by the top ring.
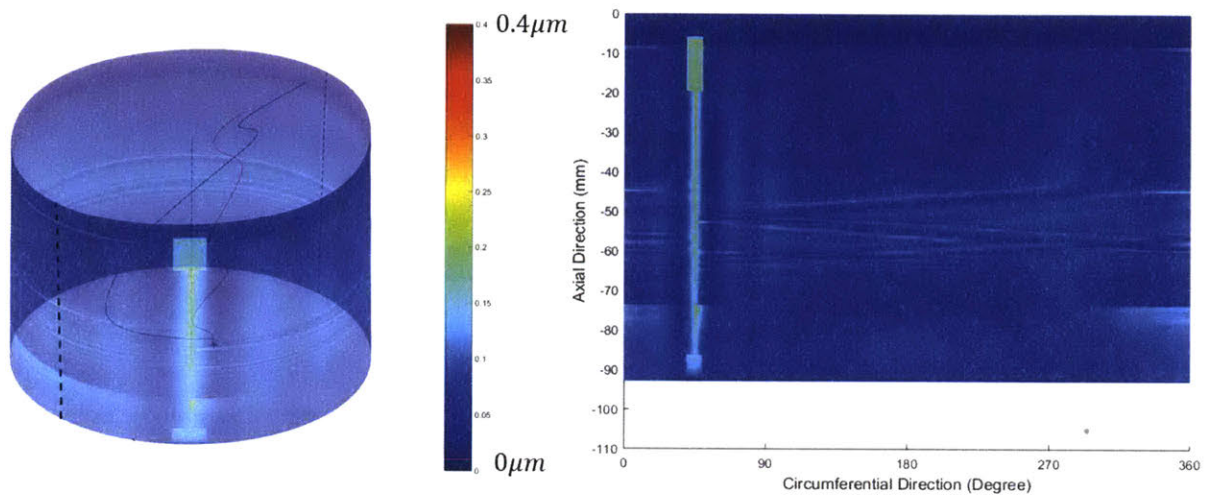
Figure 150 the Oil Film Thickness on the Liner after the Top Ring in the Intake Stroke
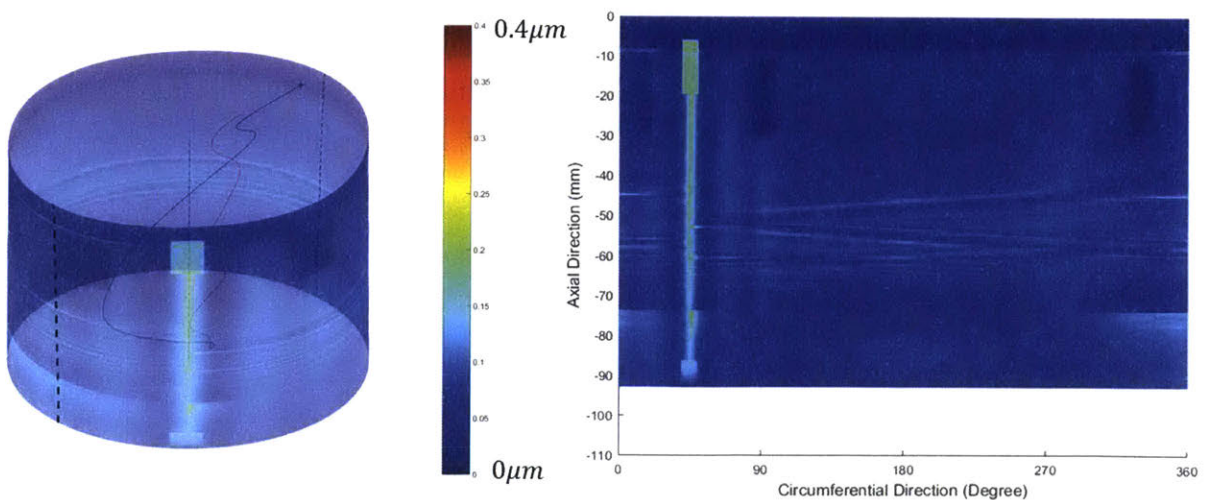
Figure 151 the Oil Film Thickness on the Liner after the Top Ring in the Compression Stroke with Added Fuel Film
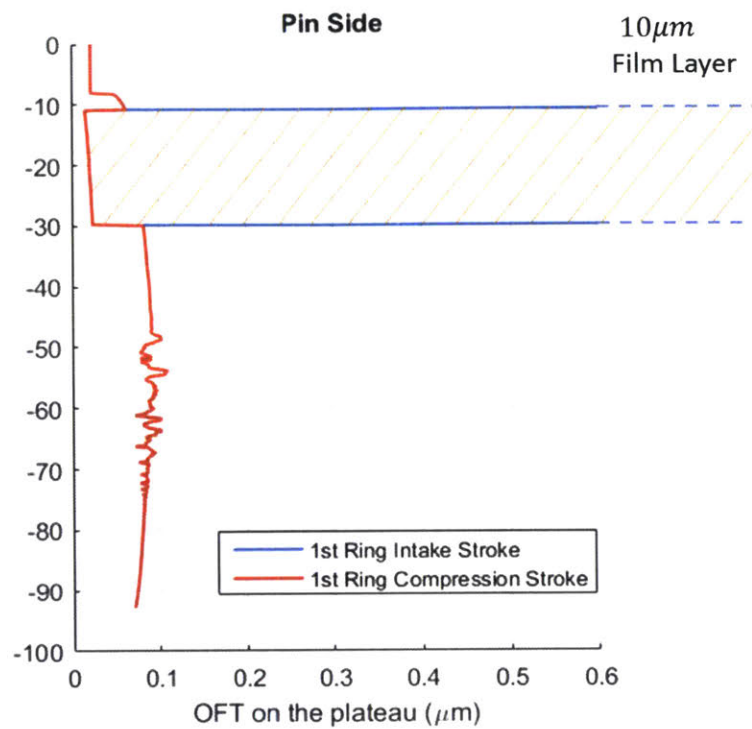
Figure 152 the Oil Film Thickness on the Liner (Pin Side, 90°) after the Top Ring in the Intake and the Compression Strokes

With fuel diluted, the viscosity of the oil film decreases to almost 1% of the original value. Thus, at the spots where the fuel is mixed into the oil film, higher direct asperity-contact pressure is expected. Figure 153 shows the local difference of the dry contact force distribution between the oil film and the mixture film. Three spikes of contact force happen at the positions where the fuel is added to the oil film.
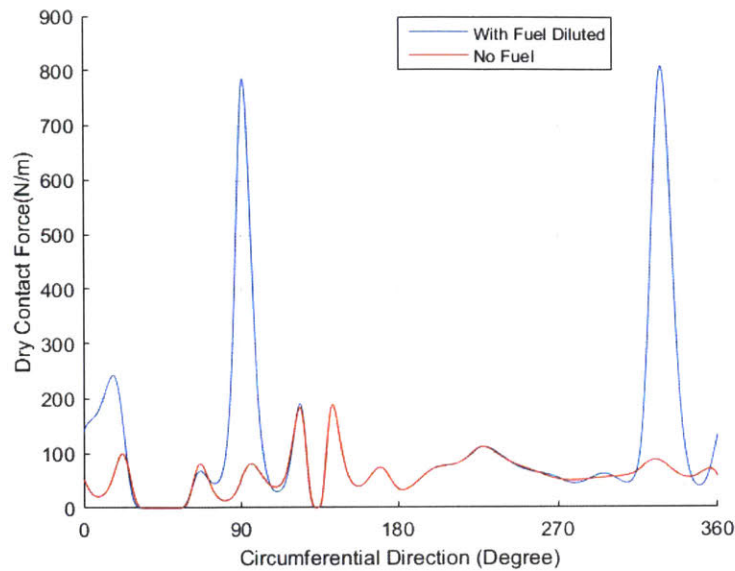
Figure 153 Difference of Dry Contact Force Distribution between the Oil Film and the Mixture Film

5.6.4. Sample Results for Extraordinary Bore Distortion

In the above examples, given bore distortion and the ring pack design, there was not much net oil transfer from the liner to the upper regions even with bridging from the piston 3rd land. The oil film thickness on the liner was in the order of sub-microns and the oil that potentially might be up scraped by the top ring during the compression stroke was also limited. In this section, we will present an example with an artificially enlarged bore distortion to show how oil transport is affected by global and local processes under this condition.

For the new bore distortion, the 2nd order and 4th order bore components are magnified by 4 times with a magnitude up to $40 \mu m$ and $20 \mu m$ correspondingly. The other parameters are kept the same. The positions of the bridging area are moved back to the pin side (90° from the thrust side) in comparison of 45° from the thrust side in the last section.

Figure 154, Figure 155 and Figure 156 demonstrate the oil film thickness on the liner after the OCR, the second ring and the top ring in the intake stroke. Though the bore distortion is magnified, the OCR is flexible enough to keep contact with the liner except for the gap area, and the oil film thickness on the liner is still well controlled at a level of sub-microns. As explained in previous sections, the ring gap tends to lose contact with the liner due to a loss of constraint, so in Figure 154 a thick oil film thickness left on the liner by the OCR is observed around the OCR gap area (this is true when the OCR gap is at the given position; the OCR gap may have higher level contact if it is at other positions). Figure 155 and Figure 156

show that part of the thick oil film caused by the loss of contact between the OCR gap and the liner is scraped by the top two rings.

The pressure force and the ring tension acting on the top two rings are not sufficient to deform the rings to adapt to the cylinder geometry in the intake stroke (Figure 157), but the oil supply to the top two rings is controlled by the OCR so the oil film thickness that passes the top two rings almost remains the same as that left by the OCR except for the bridging area. Within the bridging area, thick oil film is brought to the liner and allowed to pass through the large ring-liner clearance.

Figure 154 the Oil Film Thickness on the Liner after the OCR in the Intake Stroke

Figure 155 the Oil Film Thickness on the Liner after the Second Ring in the Intake Stroke

198

Figure 156 the Oil Film Thickness on the Liner after the Top Ring in the Intake Stroke
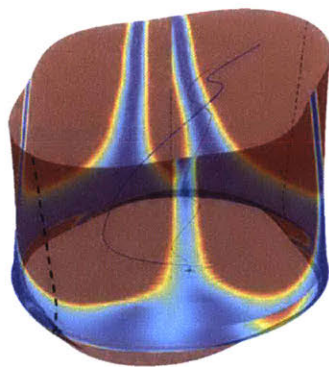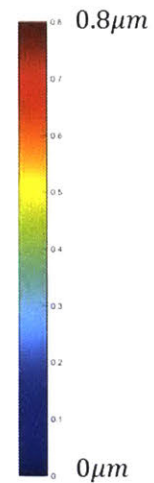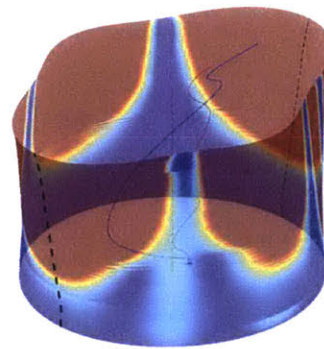
Figure 157 the Minimum Ring-Liner Clearance of the Top Two Rings

Figure 158, Figure 159 and Figure 160 show the results of the oil film thickness on the liner after the top ring, the second ring and the OCR respectively in the compression stroke. The conformability between the top ring and the liner improves with the help of a rising pressure in the top ring groove. In this case, since the thickness of the oil film left on the liner caused by bridging during the intake stroke was several microns, a significant amount of oil is up-scraped by the top ring due to the difference of its conformability to the liner between the intake and the compression strokes. The difference of the oil film thickness passing the top ring during the intake and the compression strokes at the pin side is demonstrated in Figure 161.

At the end of the compression stroke, thick oil film thickness is left on the liner by the OCR around the anti-thrust side, which is caused by the OCR dynamic twist and bridging between the two lands. This is similar to what was observed in the previous example.
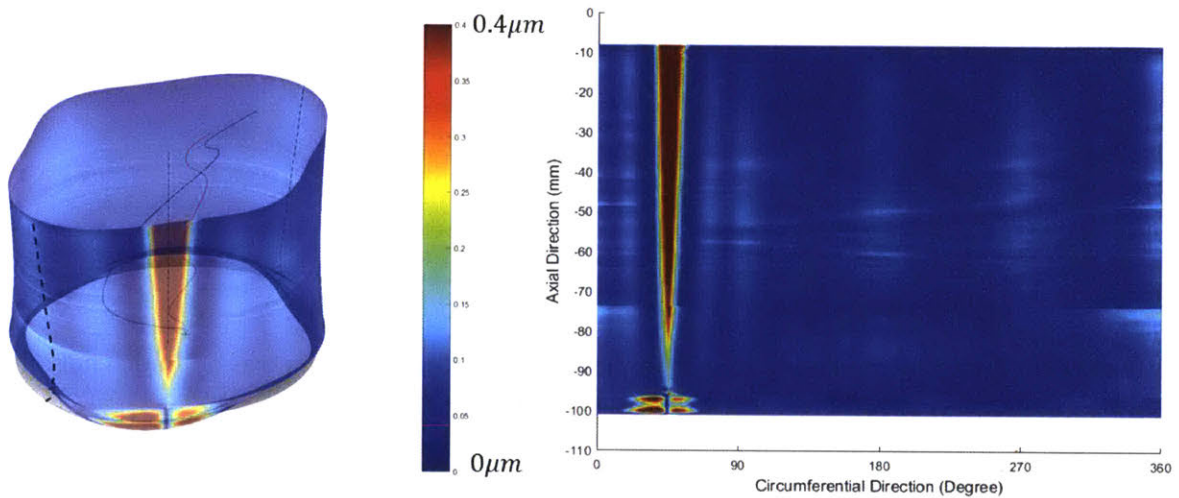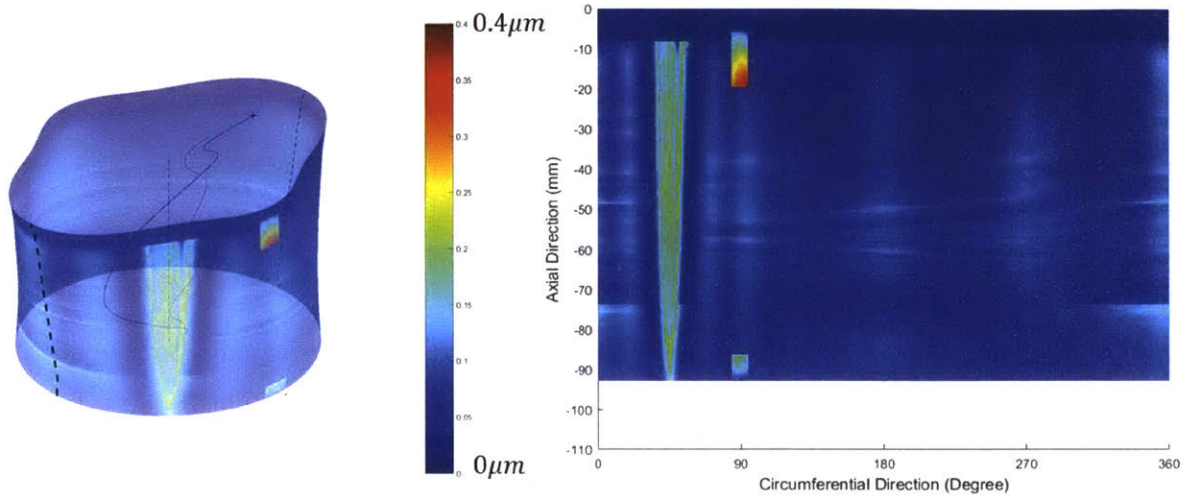

Figure 158 the Oil Film Thickness on the Liner after the Top Ring in the Compression Stroke
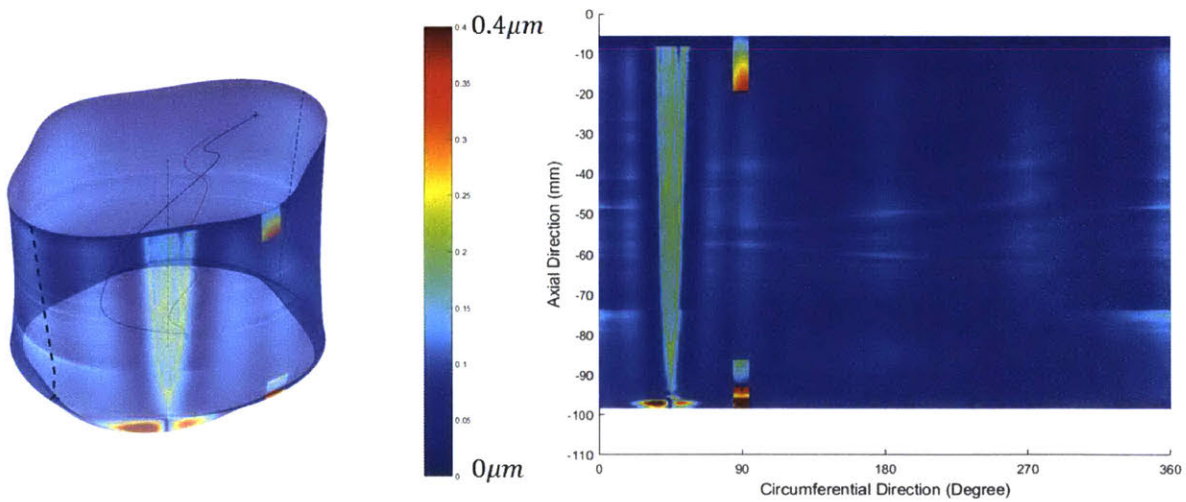
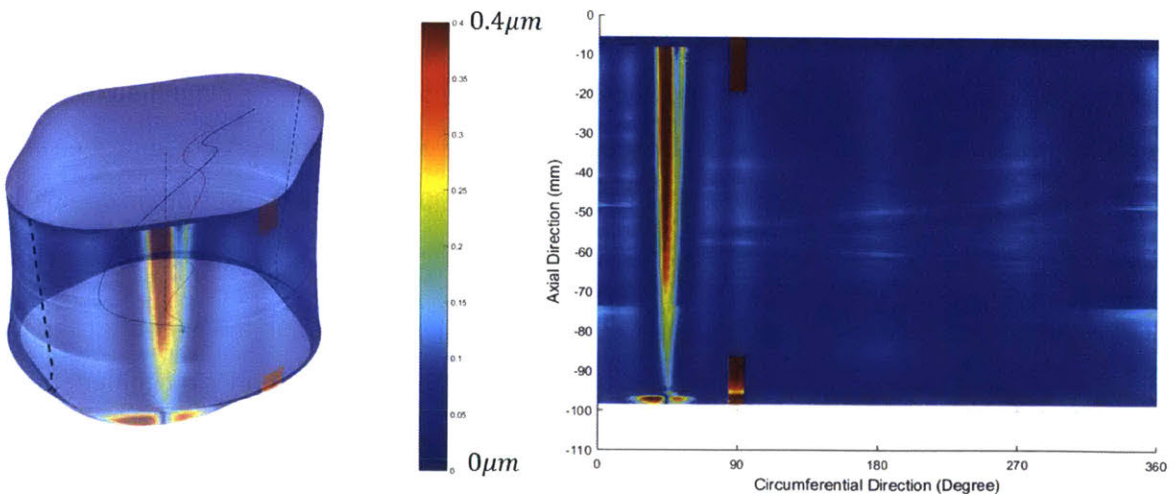*Figure 159 the Oil Film Thickness on the Liner after the Second Ring in the Compression Stroke*
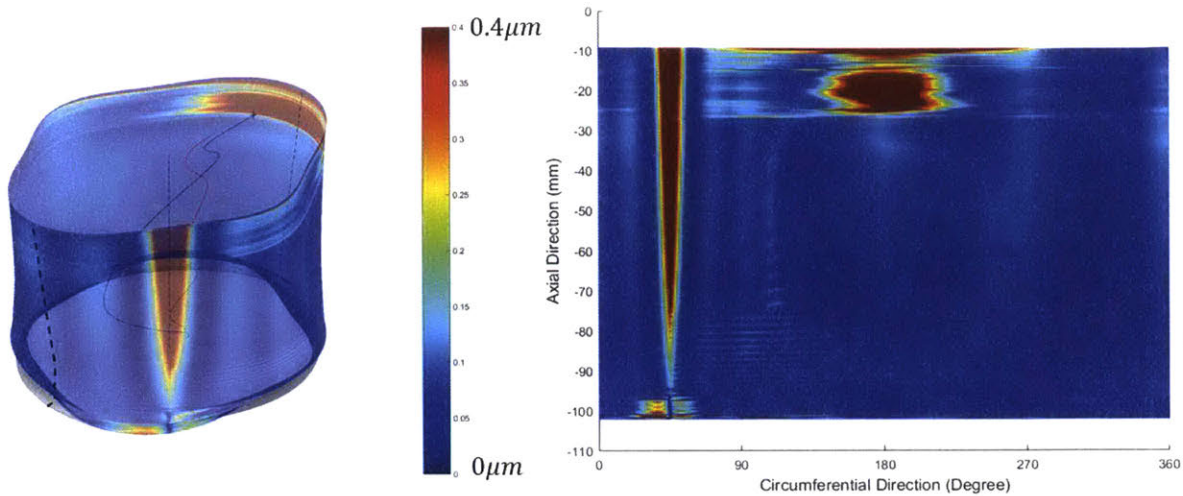
Figure 160 the Oil Film Thickness on the Liner after the OCR in the Compression Stroke
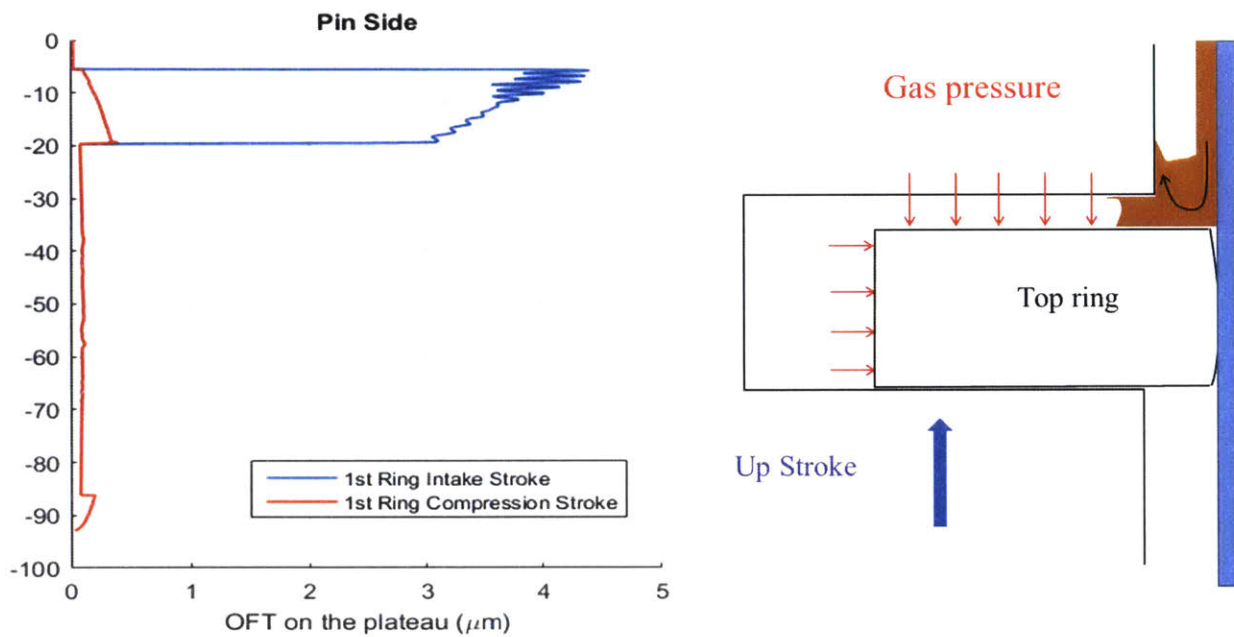
Figure 161 the Oil Film Thickness on the Liner (Pin Side) after the Top Ring in the Intake and the Compression Strokes

Figure 162 to Figure 164 show the oil film thickness on the liner after the OCR, the second ring and the top ring respectively during the expansion stroke. Figure 165, Figure 166 and Figure 167 demonstrate the oil film thickness on the liner after the top ring, the second ring and the OCR respectively during the exhaust stroke. The behavior of the ring pack in the expansion and exhaust strokes is very close to what was demonstrated in the previous example and similar explanations can be applied here.
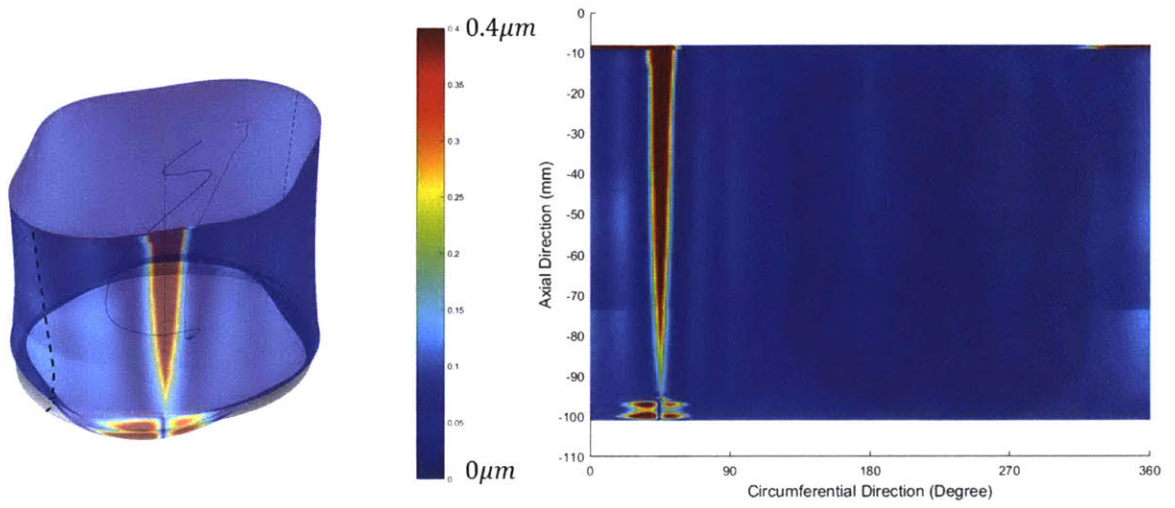
Figure 162 Oil Film Thickness on the Liner after the OCR in the Expansion Stroke
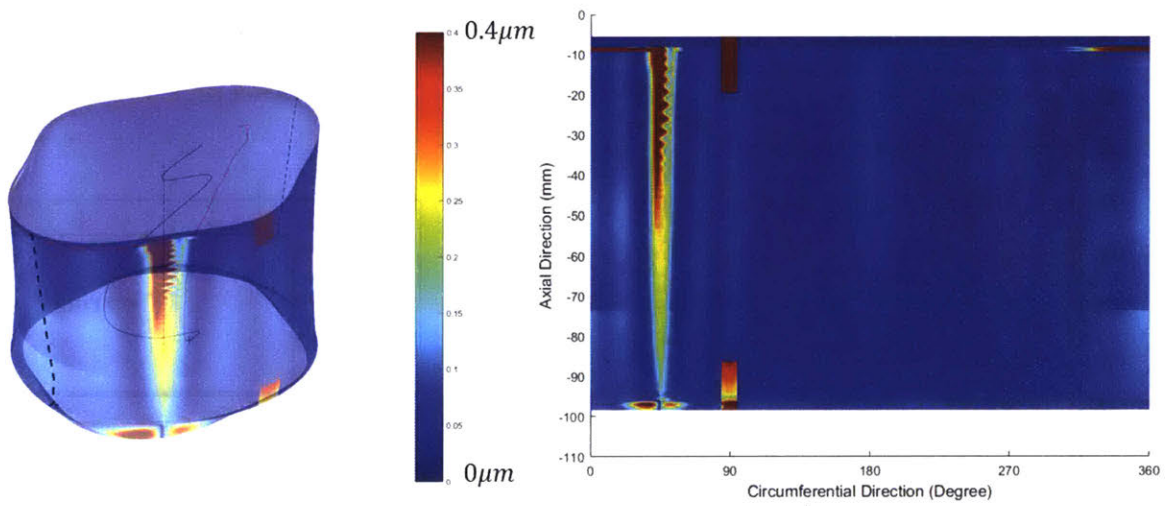
Figure 163 Oil Film Thickness on the Liner after the Second Ring in the Expansion Stroke
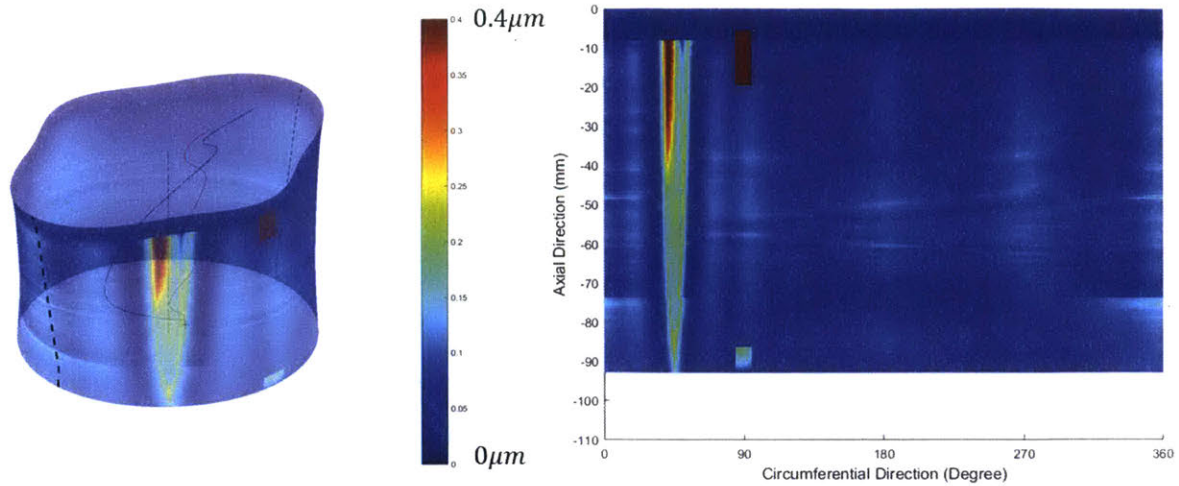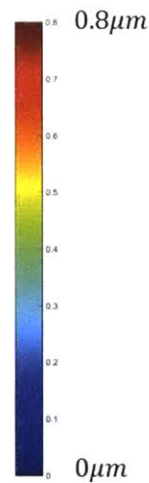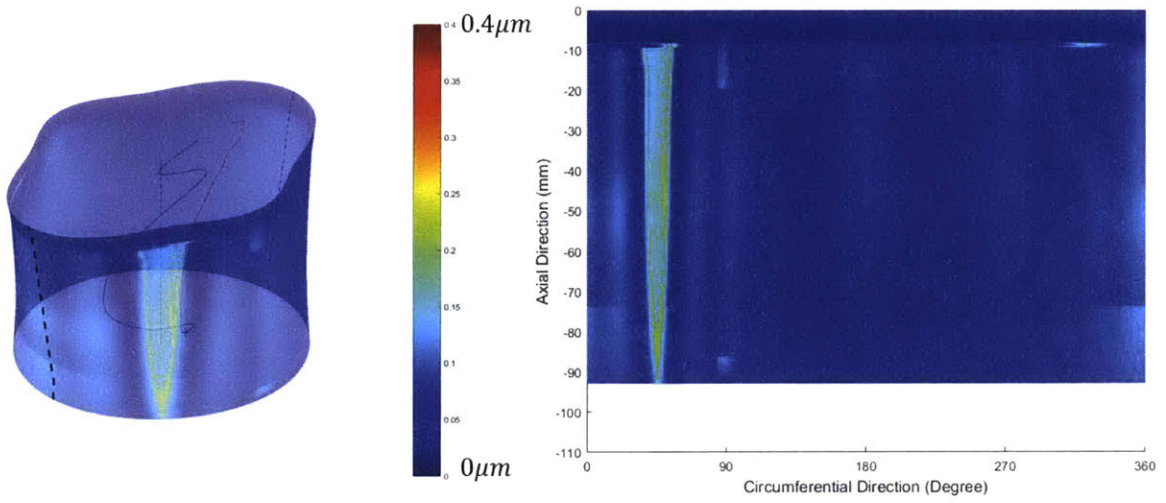
Figure 164 Oil Film Thickness on the Liner after the Frist Ring in the Expansion Stroke
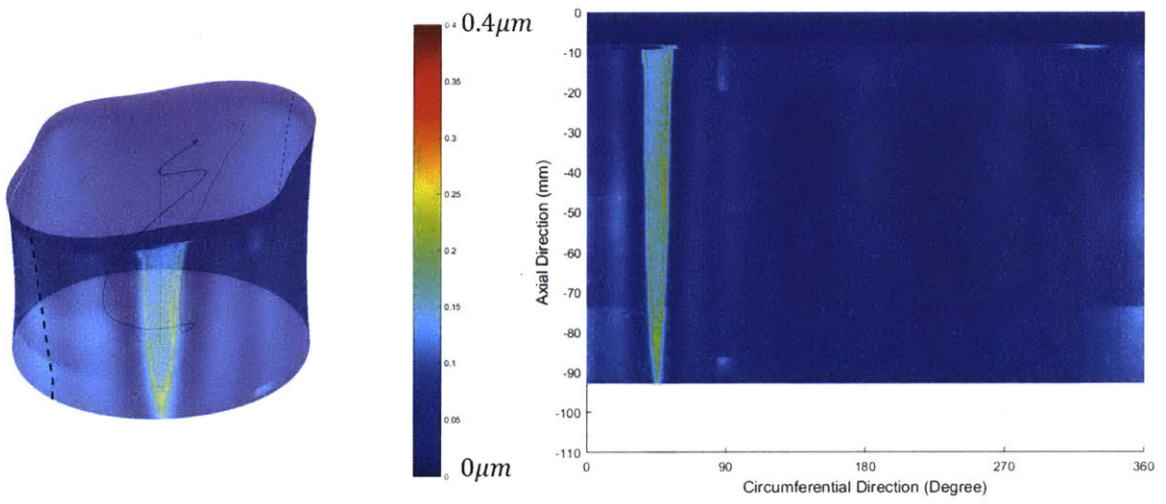
Figure 165 Oil Film Thickness on the Liner after the Top Ring in the Exhaust Stroke
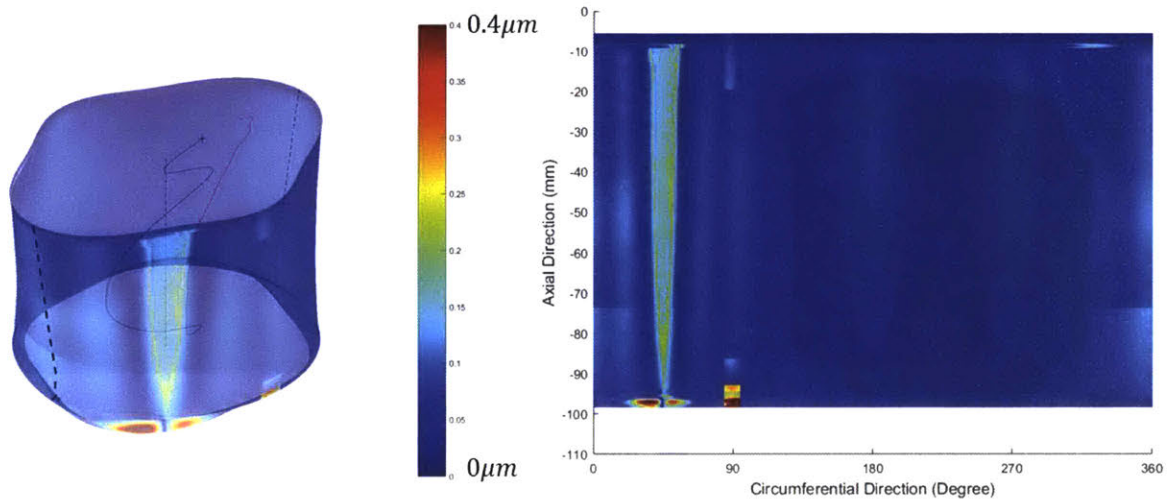
Figure 166 Oil Film Thickness on the Liner after the Second Ring in the Exhaust Stroke
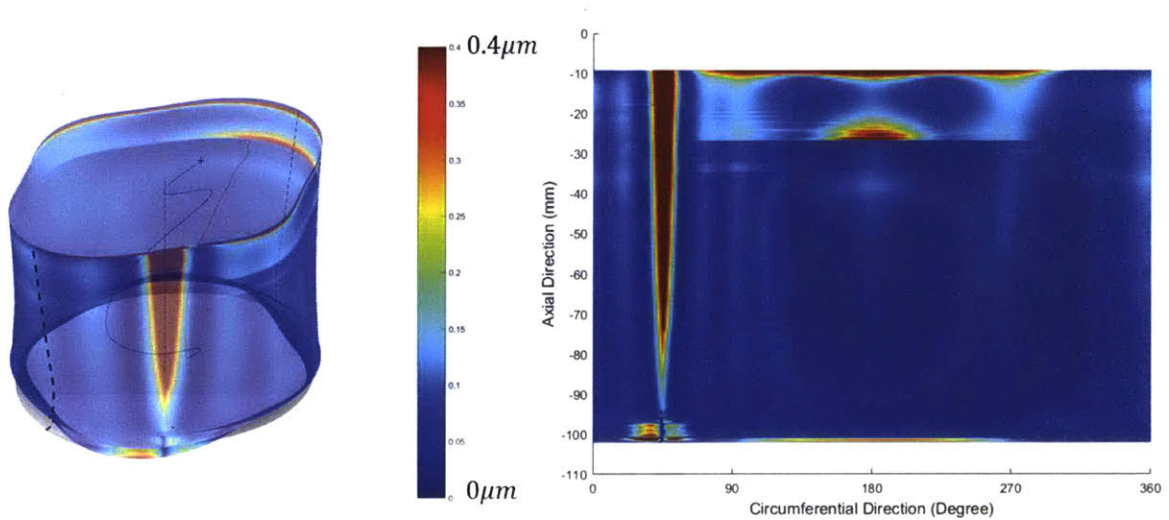
Figure 167 Oil Film Thickness on the Liner after the OCR in the Exhaust Stroke

5.7. Conclusion

The oil supply to the piston ring pack is mainly controlled by the OCR through the clearances between the ring lands and the liner. At the structural level, the clearances are determined by ring-liner conformability along the circumference and ring-liner axial conformability. Ring-liner circumferential conformability is a result of bore distortion and ring cross section stiffness in z (axial) direction, and the ring-liner axial conformability a result of piston tilt due to secondary motion, local slope of the bore distortion profile along the axial direction, and the ring torsion constant. Furthermore, when the oil supply to the trailing land of the OCR is starved, the oil film thickness left by the OCR is determined by the smaller clearance between the two lands and the liner. However, when the oil supply to the trailing

204

land of the OCR is fully flooded due to bridging between the OCR two lands, it is the clearance between the trailing land and the liner that determines the oil film thickness. If the axial non-conformability is mainly caused by the piston dynamic tilt, a larger trailing land clearance is present at either thrust or anti-thrust side to allow more oil to leak out of the OCR. As discussed in Section 5.5, there are two important quantities regarding to the oil control of the TLOCR: the first is the thickness of the oil left on the liner during down-strokes; the second is up-scraping of the oil on the liner by the upper land during up-strokes. In the upper part of the liner, the trailing land is starved during a down-stroke, so up-scarping is difficult to occur in the ensuing up-stroke. Thus, the thickness of the oil left on the liner becomes important and the bore distortion is the most critical factor to be considered for the oil control of the OCR in this area. On the other hand, in the lower part of the liner the trailing land may become fully flooded during a down-stroke due to bridging and up-scraping tends to occur here. As a result, emphasis should be put on the study of oil up scraping, and piston secondary motion becomes the most critical factor.

The oil supply to the top two rings is largely controlled by the OCR. Therefore, though sometimes they may have bad conformability to the liner due to bore distortion, the oil film left on the liner after the top two rings is still limited due to limited oil supply. However, local phenomena such as bridging or lube-fuel dilution can disturb local oil supply. Bridging brings excessive oil film to the liner that is fed into the top two rings directly. Then, when the top two rings do not have good conformability to the liner, e.g., during the intake stroke, a thick oil film is left on the liner. In the ensuing compression stroke, conformability between the top ring and the liner is improved by the gas pressure in the top ring groove and the thick oil film is scraped from the liner to the piston crown land. Therefore, the conformability of the top two rings in the TDC area of the ring pack is more critical to the net oil transfer to the crown land due to the conformability difference there between different strokes.

Fuel may be sprayed on to the liner in the intake stroke and mixes with the oil film. The mixed film has a thickness on the order of $10\mu m$ and has a much smaller viscosity compared to the oil film, which significantly reduces hydrodynamic pressure generation ability between the ring and the liner. Thus, when the top ring moves upwards in the compression stroke, it will up scrape the mixed layer and has a more severe contact. Polished spots are observed on the running surface of the top ring, corresponding to the fuel-lube mixture on the liner.

In most of the time, the oil film thickness on the liner is limited to a sub-micron level which is reasonable because if the oil film thickness on the liner is too thick, for example reaching micron level,

the top ring can scrape it from the liner with the help of the gas pressure. The oil picked by the top ring has a high possibility of flowing into the combustion chamber and contributing to oil consumption. In this case, the oil consumption will be much larger than what is measured from the experiments.

Oil transfer from the liner and interaction between the fuel and lubricant occur locally. Yet, the local clearance is a result of local lubrication and global balance. The present model makes it possible to combine the local and global effects and to realistically examine the integral effect of all the critical design and operating parameters such as bore and piston distortion, piston secondary motion, ring stiffness, profiles, and roughness. Certainly, the additional oil and fuel supply boundary conditions have to come from other sources. Nonetheless, one can use the current model to investigate the impact of the bridging area and fuel coverage area, which is controlled by other processes. Being able to do so not only represents a major step forward to quantifying the effects of relevant parameters to oil consumption, but also helps us determine the significance and needed accuracy of the related oil transport modeling.

6. Conclusions

The transport of gas, oil, as well as lubrication in the piston ring pack needs a resolution of the ring dynamics at global and local levels. Particularly, the oil transport and leakage through each ring occurs locally while the gas pressures and ring dynamics most likely are determined by global balance. In this work, a multi-length-scale ring pack model was, for the first time, successfully assembled. This model bears its fundamental values to truly reflect the integral results of all the relevant mechanisms from structural balance to local oil flows and asperity contact details. The significance of the current work is that the model demonstrated such an integration of all the length scales is possible for a cycle model with a reasonable computation cost. With the current model, one can realistically investigate the effects of all kinds of piston and bore distortion as well as piston secondary motion, bridging, and lube-oil dilution on gas sealing, oil transport and lubrication. A prediction of oil leakage through the ring-groove interfaces needs an improvement of oil flow sub-model. Furthermore, this model alone cannot predict oil consumption as the local oil supply boundary conditions need separate efforts to resolve oil transport and distribution at longer time scales. Nonetheless, the present work represents a necessary step to comprehend and optimize the piston ring pack.

6.1. Summary of the Models

From Chapter 2 to 5, the curved beam finite element method has been extended to the top two rings based on Baelden's TLOCR curved beam model [45] and three models have been developed to facilitate the analysis of piston rings. The static model which is a stand-alone module conducts many useful analyses without involvement of ring dynamics such as free-shape and contact force distribution relations, ring interaction with a distorted bore (commonly called conformability analysis), ring-liner and ring-groove interaction with elevated gas pressures. The ring dynamics model simulates the piston ring pack dynamic behavior and inter-ring gas pressure in engine cycles. The ring-liner lubrication model simulates oil transport through the ring-liner interface based on the boundary conditions from the ring dynamics model such as inter-ring gas pressure and ring dynamic twist (as shown in Figure 168).

3D Curve Beam Finite Element Models

Structural Model and Static Analysis

- Curved Beam Finite Element Model
- Ring Closing Model
- Free Shape Calculation
- Ring-Liner Conformability
- Ring-Groove Conformability
- Ring Twist Angle
- Ovality Calculation

Dynamic Analysis

Ring-Pack Dynamics

- 3-D Ring Displacements
- Ring-Liner Interaction
- Ring-Groove Interaction
- Gas Flow in all Directions
- Inter-Ring Gas Pressure

Pressure ➔
Twist

Ring-Liner Lubrication

- In-Plane Displacement
- Oil Film Thickness
- Oil Scraping
- Hydrodynamic Correlation
- Ring-Liner Friction

Figure 168 Connections among the Models

As shown in Figure 169, to solve the ring deformation/dynamics at each crank angel using Equation 2.112 we need to know the constraints of the distorted environment given by bore distortion, groove distortion and piston secondary motion. The ring deformation together with the bore/groove distortion and piston secondary motion gives the clearances between the piston rings and the liner and the clearances between the piston rings and the grooves which are needed in the calculation of the ring-liner and ring-groove interactions. To solve Equation 2.112, we also need to know the gas pressure to calculate the pressure force. Gas pressure can be solved using Equation 4.1 with two boundary conditions: the combustion chamber pressure and the crank case pressure. Solving Equation 4.1 requires the information of all the clearances of the gas flow paths which are dependent on the ring deformation. As a result, in the model we need to couple Equation 2.112 and Equation 4.1 and solve them iteratively.

In the ring-liner lubrication model, we simulate the oil transport via the ring-liner interface by solving the oil film thickness on the liner. We first solve the piston ring pack in plane deformation using Equation 5.5 which needs the ring twist angle and inter-ring gas pressure from the ring dynamics model as boundary conditions. With the ring deformation and the constraint of bore distortion, we should be able to get the clearances between the rings and the liner. Similar to the ring dynamics model, the ring-liner clearances are the inputs for the calculation of the ring-liner interaction which implies that Equation 5.5 has to be solved iteratively. Given the ring-liner clearances and the oil supply boundary

conditions, the oil film thickness left on the liner after the piston ring pack can be calculated using the oil flow models.
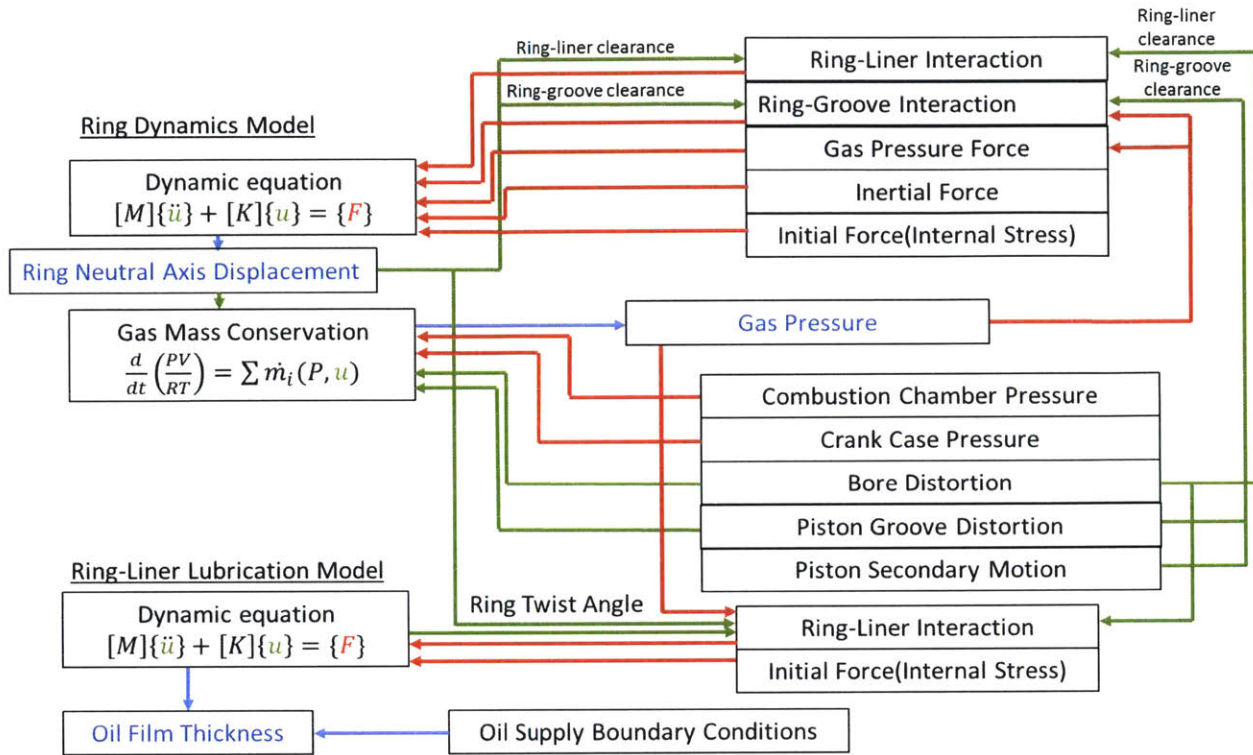
Figure 169 Algorithm of the Model

6.2. Conclusions

As discussed in Section 1.2, oil transport and ring structure dynamics are the results of combined global and local processes with different length scales (ranging from sub-micron level to several millimeters). Particularly, the oil transport and leakage through each ring occurs locally while the gas pressures and ring dynamics most likely are determined by global balance. In this work, the curved beam finite element method is used to integrate all the relevant mechanisms at their proper length scales which differentiates it from the conventional straight beam method, since it enables the separation of the structural mesh from local grids of ring-liner and ring-groove interactions using shape functions. Therefore, the current model allows realistic investigation of all the important factors to gas sealing, oil transport and lubrication: ring structural response, bore distortion, groove distortion, piston secondary motion, gas pressure, ring-groove pumping, bridging, fuel-lube dilution, ring profile and inter-asperity contact and hydrodynamic behavior. Furthermore, with the separation of the ring structural mesh and local contact grid, this model can be treated as a framework of ring structural response with assembled

different sub-models, which brings flexibility to improve the model by upgrading the current sub-models or adding new ones without changing its big structure.

Though the current model is able to truly reflect the integral results of all the relevant mechanisms from structural balance to local oil flows and asperity contact details, it has limitations due to simplified sub-models. For example, the current model for oil flow through the ring-groove interfaces is not mass conserved and thus is not able to predict the oil pumping rate. Moreover, as shown in Section 5.3.5, the current ring-liner lubrication model uses the correlations based on steady or quasi-steady results to calculate the ring-liner hydrodynamic behavior. As a result, the associated oil flow model is not able to capture the unsteady effect on the oil film thickness left by the piston ring pack. It also needs to be pointed out that this model alone cannot predict oil consumption as the additional oil and fuel supply boundary conditions have to come from other sources which need separate efforts to resolve oil transport and distribution at longer time scales. Nonetheless, the present work demonstrates such an integration of all the length scales is possible for a cycle model with reasonable computation efficiency and helps the industry to understand the mechanisms of the oil consumption and finally optimize the power cylinder system with lower development cost.

The current model shows that there are two important quantities related to oil control of the TLOCR: the first is the oil film thickness on the liner during a down-stroke and the second is the up-scraping of the oil on the liner by the upper land during an up-stroke. The first one is controlled by the circumferential conformability between the TLOCR and the distorted bore which is important in the upper part of the liner and is mainly affected by the bore distortion. This value needs to be controlled to roughness level. Otherwise, the top ring with the help of the cylinder pressure can directly scrape the excessive oil left by the OCR to either the crown or second land. The second value is controlled by the axial conformability of the TLOCR which is important in the lower part of the liner and is determined by the piston tilt. Some of the up-scraped oil can flow to the piston third land and the rest is dropped on the liner at TDC to interact with the top two rings.

The circumferential conformability of the top two rings also plays an important role in the oil consumption. The oil supply to the top two rings is largely controlled by the OCR. Therefore, though sometimes they may have bad conformability to the liner due to bore distortion, the oil film left on the liner after the top two rings is still limited due to limited oil supply. Bridging can bring excessive oil to the liner with sufficiently large oil accumulation on the piston lands. If the bridging happens at the conformed area of the top two rings, the top two rings especially the second ring will down scrape the

excessive oil from the liner, preventing oil leakage further to the upper part of the piston. However, if bridging occurs where the top two rings are badly conformed to the distorted bore, e.g., during the intake stroke, a thick oil film is left on the liner. In the ensuing compression stroke, conformability between the top ring and the liner is improved by the gas pressure in the first ring groove and the thick oil film may be scraped from the liner to the piston crown land.

Fuel with much smaller viscosity may be sprayed on to the liner in the intake stroke and mixes with the oil film, which significantly reduces hydrodynamic pressure generation ability between the ring and the liner. Thus, when the top ring moves upwards in the compression stroke, it will up scrape the mixed layer and has a more severe contact. However, the quantity of the oil up-scraped with the mixture needs more sophisticated model to calculate.

6.3. Future Work

Oil transport and oil consumption in the ring pack of internal combustion engines is an ongoing topic of research. This thesis provides the frame work of modeling oil transfer in the ring pack system based on the curved beam finite element method. This frame work has established the basis to integrate both global and local behaviors of oil transport. With the current model, one can study the oil transport through the ring-liner interface with given oil supply boundary conditions such as bridging and fuel-lube dilution.

As discussed earlier, the current model is not able to predict the oil flow through the ring-groove interfaces, which is one critical oil transfer path in the ring pack. Neither can the model reflect the unsteady effect on the oil film thickness change on the liner by the piston ring pack which in some occasions may be the main contributor for net oil transfer from the liner to the piston. Further work integrating more accurate mass conserved sub-models for these two interfaces will enhance the model's ability to predict oil transfer rates with better fidelity.

The lube-fuel dilution in this model is addressed by a naïve method that it only reduces the viscosity in the mixture layer by 99%. A more complete lube-fuel interaction and vaporization model is useful to study species transport and quantify the amount of oil up-scraped by the top ring from the liner in the mixture.

In the future, with more experiments and more study of oil transport, some other new local phenomena may be found important to oil consumption at the ring-liner and ring-groove interfaces. This frame work gives flexibility to add these new features.

Further effort is needed to improve the numerical efficiency and robustness. In the current model, a small time step (0.01CAD) is required to control the robustness. Drastic changes of the pressure generation mechanisms and gas flow rates when a ring moves to or leaves the vicinity of the flanks are the main physics reasons for a small time step. However, a better strategy for initial guess and Newton's iteration may allow larger time steps to succeed.

References

[1]   D. E. Richardson, "Review of power cylinder friction for diesel engines," *Journal of engineering for gas turbines and power,* vol. 122(4), pp. 506-519, 2000.

[2]   T. Tian, "Dynamic Behaviors of Piston Rings and Their Practical Impact. Part 1: Ring Flutter and Ring Collapse and Their Effects on Gas Flow and Oil Transport," *Proc IMechE, Part J: Journal of Engineering Tribology,* vol. 216, pp. 209-227, 2002.

[3]   R. Rabute and T. Tian, "Challenges involved in Piston Top Ring Designs for Modern SI Engines," *ASME Transaction - JOURNAL OF ENGINEERING FOR GAS TURBINES AND POWER,* vol. 123, pp. 448-459, 2001.

[4]   T. Tian, L. B. Noordzij, V. W. Wong and J. B. Heywood, "Modeling Piston-Ring Dynamics, Blowby, and Ring-Twist Effects," *ASME Transaction - JOURNAL OF ENGINEERING FOR GAS TURBINES AND POWER,* vol. 120, pp. 849-854, 1998.

[5]   H. Kenneth, P. Andersson and A. Erdemir, "Global energy consumption due to friction in passenger cars," *Tribology International,* pp. 221-234, 2012.

[6]   L. L. Ting, "Development of a Reciprocating Test Rig for Tribological Studies of Piston Engine Moving Components - Part I: Rig Design and Piston Ring Friction Coefficients Measuring Method," *SAE Technical Paper,* no. 930685, 1993.

[7]   L. L. Ting, "Development of a Reciprocating Test Rig for Tribological Studies of Piston Engine Moving Components-Part II: Measurements of Piston Ring Friction Coefficients and Rig Test Confirmation," *SAE Technical Paper,* no. 930686, 1993.

[8]   K. Liao, "Factors Affecting Piston Ring Friction," Ph.D. Thesis, the Department of Mechanical Engineering, Massachusetts Institute of Technology, Cambridge, MA, 2013.

[9]   M. Nakada, "Piston and Piston Ring Tribology and Fuel Economy," in *International Tribology Conference*, Yokohama, 1993.

[10] P. B. Shell, "Relationship between oil consumption, deposit formation and piston ring motion for single-cylinder diesel engines," *SAE Paper,* no. 920089, 1992.

[11] R. Munro, "Emissions Impossible-The Piston & Ring Support System," *SAE Technical Paper,* no. 900590, 1990.

[12] J. H. Johnson, S. T. Bagley, L. D. Gratz and D. G. Leddy, "A review of diesel particulate control technology and emissions effects-1992 horning memorial award lecture," *SAE technical paper,* no. 940233, 1994.

[13] C. Drury and S. Whitehouse, "The effect of lubricant phosphorus level on exhaust emissions in a

field trial of gasoline engine vehicles," *SAE Technical Paper,* no. 940745, 1994.

[14] F. Ueda, S. Sugiyama, K. Arimura, S. Hamaguchi and K. Akiyama, "Engine oil additive effects on deactivation of monolithic three-way catalysts and oxygen sensors," *SAE Technical Paper,* no. 940746, 1994.

[15] S. S. V. Przesmitzki, "Characterization of oil transport in the power cylinder of internal combustion engines during steady state and transient operation," Ph.D. Thesis, the Department of Mechanical Engineering, Massachusetts Institute of Technology, Cambridge, MA, 2008.

[16] E. B. Senzer, "Oil transport inside the oil control ring grove and its interaction with surrounding areas in internal combustion engines," Ph.D. Thesis, the Department of Mechanical Engineering, Massachusetts Institute of Technology, Cambridge, MA, 2012.

[17] D. Bai, "Modeling Piston Skirt Lubrication in Internal Combustion Engines," Ph.D. Thesis, the Department of Mechanical Engineering, Massachusetts Institute of Technology, Cambridge, MA, 2012.

[18] T. Fang, "Computations and Modeling of Oil Transport between Piston Lands and Liner in Internal Combustion Engines," Master Thesis, the Department of Mechanical Engineering, Massachusetts Institute of Technology, Cambridge, MA, 2014.

[19] B. B. P. Thirouard, "Characterization and modeling of the fundamental aspects of oil transport in the piston ring pack of internal combustion engines," Ph.D. Thesis, the Department of Mechanical Engineering, Massachusetts Institute of Technology, Cambridge, MA, 2001.

[20] S. Przesmitzki, A. Vokac and T. Tian, "An Experimental Study of Oil Transport between the Piston Ring Pack and Cylinder Liner," *SAE Technical Paper,* no. 2005-01-3823, 2005.

[21] J. Prescott, "the Bending of Thin Rings," *Automobile Engineer,* vol. 9, no. 130, pp. 295-302, 1919.

[22] H. W. Swift, "Elastic deformation of piston rings," *Engineering,* vol. 163, pp. 161-165, 1947.

[23] E. Dragoni and A. Strozzi, "Analysis of a split ring inserted into a circular housing," *The Journal of Strain Analysis for Engineering Design,* vol. 21, no. 2, pp. 59-70, 1986.

[24] R. Müller, "Zur Frage des Formfüllungsvermögen von Kolbenringen in von der Kreisform abweichenden Bohrungen gleicher Umfangslänge," *MTZ,* vol. 31, pp. 79-82, 1970.

[25] V. V. Dunaevsky, "Analysis of distortions of cylinders and conformability of piston rings," *Tribology transactions,* vol. 33, no. 1, pp. 33-40, 1990.

[26] V. V. Dunaevsky, S. Alexandrov and F. Barlat, "Analysis of three-dimensional distortions of the piston rings with arbitrary cross-section," *SAE Technical Paper,* no. 2000-01-3453, 2000.

[27] V. V. Dunaevsky, S. Alexandrov and F. Barlat, "Fundamentals for analysis of threedimensional distortions of the piston rings," in *the ASME Internal Combustion Engine Division,* 2000.

[28] V. V. S. F. Dunaevsky and S. Alexandrov, "Development of conformability model of piston rings with consideration of their three-dimensional torsional distortions and Fourier series representation of cylinder bore geometry," *SAE Technical Paper,* no. 2002-01-3131, 2002.

[29] V. Dunaevsky and J. Rudzitis, "Clarification of a semi-empirical approach in Piston ring-cylinder bore conformability prediction," *Journal of tribology,* vol. 129, no. 2, pp. 430-435, 2007.

[30] E. Tomanik, "Piston ring conformability in a distorted bore," *SAE Technical Paper,* no. 960356, 1996.

[31] E. Tomanik, "Improved Criterion for Ring Conformability Under Realistic Bore Deformation," *SAE Technical Paper,* no. 2009-01-0190, 2009.

[32] T. Tian, "Modeling the Performance of the Piston Ring-Pack in Internal Combustion Engines," Ph.D. Thesis, the Department of Mechanical Engineering, Massachusetts Institute of Technology, Cambridge, MA, 1997.

[33] T. Tian, "Dynamic Behaviors of Piston Rings and Their Practical Impact. Part 2: Oil Transport, Friction, and Wear of Ring/Liner Interface and the Effects of Piston and Ring," *Proc IMechE, Part J: Journal of Engineering Tribology,* vol. 216, pp. 229-247, 2002.

[34] M. Namazian and J. B. Heywood, "Flow in the Piston-Cylinder-Ring Crevices of a Spark-Ignition Engine: Effects on Hydrocarbon Emission, Efficiency and Power," *SAE Paper 820088,* 1982.

[35] R. Keribar, Z. Dursunkaya and M. F. Flemming, "An Integrated Model of Ring Pack Performance," *ASME Transaction - JOURNAL OF ENGINEERING FOR GAS TURBINES AND POWER,* vol. 113, pp. 382-389, 1991.

[36] B. L. Ruddy, B. Parsons, D. Dowson and P. N. Economou, "The Influence of Thermal Distortion and Wear of Piston Ring Groove upon the Lubrication of Piston Rings in Diesel Engines," in *Leeds-Lyon Symposium on Tribology.,* Lyon, 1979.

[37] M. A. Ejakov, H. Schock and L. Brombolich, "Modeling of Ring Twist For an IC Engine," *SAE Technical Paper,* 1998.

[38] Y. Hu, H. S. Cheng, T. Arai, Y. Kobayashi and S. Aoyama, "Numerical Simulation of Piston Ring in Mixed Lubrication - A Nonaxisymmetrical Analysis," *ASME Journal of Tribology,* vol. 116(3), pp. 470-478, 1994.

[39] M.-T. Ma, I. Sherrington and E. H. Smith, "Analysis of lubrication and friction for a complete piston-ring pack with an improved oil availability model: Part 1: Circumferentially uniform film," *Proceedings of the Institution of Mechanical Engineers, Part J: Journal of Engineering Tribology,* vol. 211(1), pp. 1-15, 1997.

[40] M.-T. Ma, I. Sherrington and E. H. Smith, "Analysis of lubrication and friction for a complete piston-ring pack with an improved oil availability model: Part 2: Circumferentially variable film," *Proceedings of the Institution of Mechanical Engineers, Part J: Journal of Engineering Tribology,* vol.

211(1), pp. 17-27, 1997.

[41] L. Liu and T. Tian, "A three-dimensional model for piston ring-pack dynamics and blow-by gas flow," in *ASME 2004 Internal Combustion Engine Division Fall Technical Conference*, 2004.

[42] L. Liu and T. Tian, "Modeling piston ring-pack lubrication with consideration of ring structural response," *SAE Technical Paper,* no. 2005-01-1641, 2005.

[43] L. Liu, "Modeling the performance of the piston ring-pack with consideration of non-axisymmetric characteristics of the power cylinder system in internal combustion engines," Ph.D. Thesis, the Department of Mechanical Engineering, Massachusetts Institute of Technology, Cambridge, MA, 2005.

[44] C. Baelden and T. Tian, "A Dual Grid Curved Beam Finite Element Model of Piston Rings for Improved Contact Capabilities," *SAE International Journal of Engines,* vol. 7, no. 2014-01-1085, pp. 156-171, 2014.

[45] C. Baelden, "A multi-scale model for piston ring dynamics, lubrication and oil transport in internal combustion engines," Ph.D. Thesis, the Department of Mechanical Engineering, Massachusetts Institute of Technology, Cambridge, MA, 2014.

[46] Y. Li, H. Chen and T. Tian, "A deterministic model for lubricant transport within complex geometry under sliding contact and its application in the interaction between the oil control ring and rough liner in internal combustion engines," *SAE Technical Paper,* no. 2008-01-1615, 2008.

[47] H. Chen, Y. Li and T. Tian, "A novel approach to model the lubrication and friction between the twin-land oil control ring and liner with consideration of micro structure of the liner surface finish in internal combustion engines," *SAE Technical Paper,* no. 2008-01-1613, 2008.

[48] H. Chen, "Modeling the lubrication of the piston ring pack in internal combustion engines using the deterministic method," Ph.D. Thesis, the Department of Mechanical Engineering, Massachusetts Institute of Technology, Cambridge, MA, 2011.

[49] Y. Li, "Multiphase oil transport at complex micro geometry," Ph.D. Thesis, the Department of Mechanical Engineering, Massachusetts Institute of Technology, Cambridge, MA, 2011.

[50] Y. Liu, "Developing an approach utilizing local deterministic analysis to predict the cycle friction of the piston ring-pack in internal combustion engines," Master Thesis, the Department of Mechanical Engineering, Massachusetts Institute of Technology, Cambridge, MA, 2013.

[51] S. P. Timošenko, Strength of Materials: Elementary Theory and Problems, D. Van Nostrand Company, 1940.

[52] A. N. Pressley, Elementary differential geometry, Springer Science & Business Media, 2010.

[53] L. Liu, T. Tian and R. Rabute, "Development and Applications of an Analytical Tool for Piston Ring Design," *SAE Technical Paper,* no. 2003-01-3112, 2003.

[54] J. A. Greenwood and J. H. Tripp, "The contact of two nominally flat rough surfaces," *Proceedings of the institution of mechanical engineers,* vol. 185, no. 1, pp. 625-633, 1970.

[55] D. Bai, "Modeling Piston Skirt Lubrication in Internal Combustion Engines," Ph.D. Thesis, the Department of Mechanical Engineering, Massachusetts Institute of Technology, Cambridge, MA, 2012.

[56] P. Totaro, "Modeling Piston Secondary Motion, Skirt Lubrication and Applications," Master Thesis, the Department of Mechanical Engineering, Massachusetts Institute of Technology, Cambridge, MA, 2014.

[57] E. Zanghi, "Analysis of oil flow mechanisms in internal combustion engines via high speed Laser Induced Fluorescence (LIF) spectroscopy," Master Thesis, the Department of Mechanical Engineering, Massachusetts Institute of Technology, Cambridge, MA, 2014.

[58] T. Fang, Private Communication, 2014.

[59] V. T. Kalva, "Modeling the Evolution of Composition of the Fuel and Lubricant Mixture on the Cylinder Wall in Internal Combustion Engines," Master Thesis, the Department of Mechanical Engineering, Massachusetts Institute of Technology, Cambridge, MA, 2017.